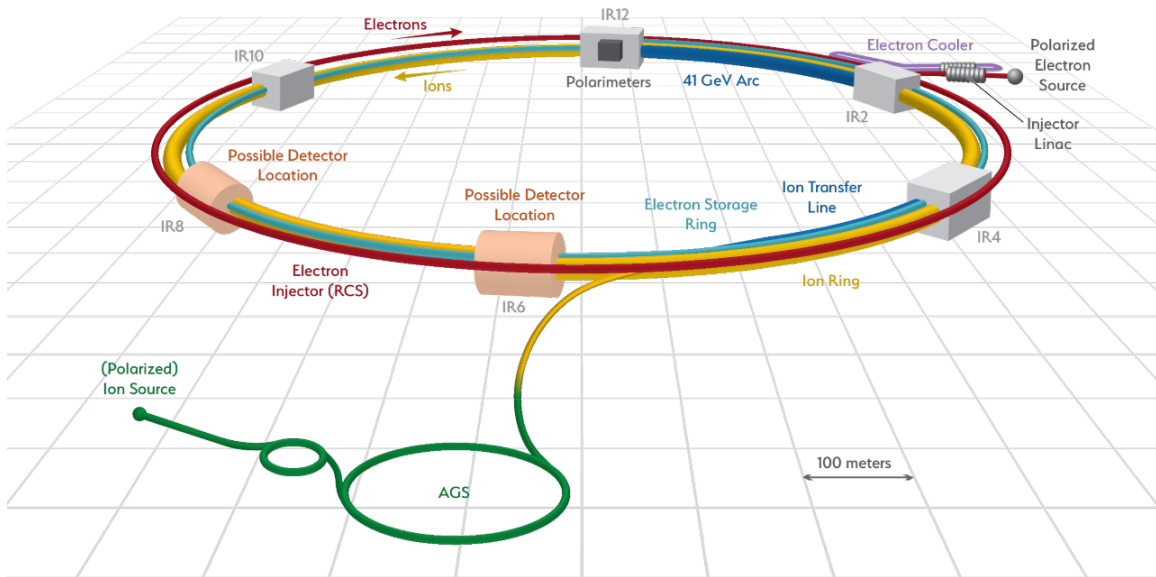


August 2019

An Electron-Ion Collider Study

Brookhaven National Laboratory



For more technical details please contact Dr. F. Willeke
(willeke@bnl.gov)

Editor:

J. Beebe-Wang

Contributors:

(All BNL staff members unless otherwise noted)

A. Arno, E. Aschenauer, K. Bane¹, G. Bassi, E. Beebe, J. Beebe-Wang, Y. Belyavina, I. Ben-Zvi, J. S. Berg, M. Blaskiewicz, A. Blednykh, S. Binello, J. M. Brennan, S. Brooks, K. Brown, F. Craner, W. Cheng, W. Christie, A. Deshpande², T. D'Ottavio, K.A. Drees, J. Epstein, M. Fallier, S. Fazio, A. Fedotov, N. Feege², P. K. Feng, W. Fischer, A. Flores, C. Folz, N. Franco, C. J. Gardner, D. Gassner, E. Gianfelice-Wendt³, W. Guo, Y. Hao, D. Hatton, A. Hershcovitch, C. Hetzel, D. Holmes, D. Hseuh, H. Huang, R. Hulsart, W. Jackson, J. Jamilkowski, F. Karl, J. Kewisch, A. Kiselev, P. Kolb, R. Lambiase, C-J. Liaw, C. Liu, H. Lovelace III, T. Ludlam, Y. Luo, M. Mapes, I. Marneris, B. Martin, A. Marusic, G. McIntyre, E. McSweeney, F. Meot, J-L. Mi, R. Michnoff, T. Miller, M. Minty, C. Montag, D. Morrison, J. Morris, M. Musgrave⁴, S. Nemesure, D. Padrazo, B. Page, R. B. Palmer, M. Paniccia, B. Parker, S. Peggs, A. Petrone, R. Petti, S. Polizzo, V. Ptitsyn, O. Rahman, V. Ranjbar, D. Raparia, J. Reich, J. Ritter, G. Robert-Demolaize, P. Sampson, J. Sandberg, J. Scaduto, W. Schmidke, S. Seletskiy, T. Shafan, J. Skaritka, V. Smalyuk, K. Smith, G. Stupakov¹, S. Tepikian, R. Than, C. Theisen, P. Thieberger, D. Trbojevic, N. Tsoupas, J. Tuozzolo, T. Ullrich, R. Venugopalan, S. Verdú-Andrés, E. Wang, G. Wang, G-M. Wang, W-T. Weng, F. Willeke, H. Witte, Q. Wu, A. Wund, B. Xiao, T. Xin, W. Xu, W. Yu, A. Zaltsman, A. Zelen-ski, W. Zhang, Z. Zhao, P. Zurita

¹SLAC National Accelerator Laboratory

²Stony Brook University

³Fermi National Accelerator Laboratory

⁴The Massachusetts Institute of Technology

Disclaimer

This report was prepared as an account of work sponsored by an agency of the United States Government. Neither the United States Government nor any agency thereof, nor any of their employees, nor any of their contractors, subcontractors, or their employees, makes any warranty, express or implied, or assumes any legal liability or responsibility for the accuracy, completeness, or any third party's use or the results of such use of any information, apparatus, product, or process disclosed, or represents that its use would not infringe privately owned rights. Reference herein to any specific commercial product, process, or service by trade name, trademark, manufacturer, or otherwise, does not necessarily constitute or imply its endorsement, recommendation, or favoring by the United States Government or any agency thereof or its contractors or subcontractors. The views and opinions of authors expressed herein do not necessarily state or reflect those of the United States Government or any agency thereof.

Notice: This manuscript has been authored by employees of Brookhaven Science Associates, LLC under Contract No. DE-SC0012704 with the U.S. Department of Energy. The publisher by accepting the manuscript for publication acknowledges that the United States Government retains a non-exclusive, paid-up, irrevocable, world-wide license to publish or reproduce the published form of this manuscript, or allow others to do so, for United States Government purposes.

Executive Summary

The Electron Ion Collider (EIC) will open exciting new frontiers for research in nuclear physics and quantum chromodynamics. In a comprehensive White Paper [1] the U.S. nuclear physics community, with worldwide support, has compiled a detailed description of the potential for such a facility to realize, at a fundamental level, important new understanding and discoveries regarding the nature of visible matter in our universe. The 2015 DOE/NSF Long Range Plan for Nuclear Science [2] recommends an EIC as the next new facility to be initiated for the field, and the 2018 National Academies of Sciences, Engineering, and Medicine report, "An Assessment of U.S.-Based Electron-Ion Collider Science" [3] states, "In summary, the committee concludes that an EIC is timely and has the support of the nuclear science community. The science that it will achieve is unique and world leading and will ensure global U.S. leadership in nuclear science as well as in the accelerator science and technology of colliders."

The key requirements for such a facility, laid out in the above documents and articulated in the National Academies report are:

- Center-of-mass energy range from ~ 20 to 100 GeV, upgradable to ~ 140 GeV
- Ion beams from deuterons to the heaviest stable nuclei
- High luminosity, on the order of 10^{33} to $10^{34} \text{ cm}^{-2} \text{ sec}^{-1}$
- Spin-polarized ($\sim 70\%$ at a minimum) electron and proton/light-ion beams
- One or more interaction regions which integrate the detectors into the collider to preserve extensive kinematic coverage

Brookhaven National Laboratory (BNL) is proposing eRHIC as the electron ion collider. The design meets the requirements listed above for an EIC with a cost-effective implementation that takes advantage of the existing infrastructure and accelerator components of the RHIC ion-ion collider. An electron storage ring is planned to be added to the RHIC complex to enable electron-proton (e-p) collisions at center-of-mass energies (E_{CM}) ranging between 20 GeV and 140 GeV with luminosity well above $10^{33} \text{ cm}^{-2} \text{ sec}^{-1}$ over the range from 40 GeV to 140 GeV, and a top of luminosity at $E_{\text{CM}} = 105$ GeV of $10^{34} \text{ cm}^{-2} \text{ sec}^{-1}$.

Ion beams ranging from deuterons to uranium nuclei will be available. For collisions of electrons with protons and light ions (deuterons and ^3He nuclei), both beams will be spin

polarized with polarization of $P \geq 70\%$. The design of eRHIC has been developed in a joint effort by nuclear physicists and accelerator scientists, enabling large-acceptance experiments with unprecedented resolving power in the domain of quarks and gluons.

This eRHIC Preliminary Conceptual Design Report (pCDR) provides the reference design that will serve as a guiding document for the eRHIC team and the foundation for a subsequent proposal. The primary result of the pCDR is to show that the eRHIC concept is technically feasible, is consistent with the anticipated cost expectations for an EIC, and will deliver the performance needed to support the full scientific program recommended in the DOE/NSF Long Range Plan and assessed by the National Academies committee.

In close coordination with the nuclear science community, the pCDR includes a description of essential experimental measurements and a general detector concept to guide the design of the interaction regions. This element of the pCDR is aimed at motivating the interest of experimenters, theorists, and detector builders. The eRHIC facility includes the capability for two large multipurpose colliding beam detectors.

All of the key facility requirements, including the availability of e-p collisions up to a center-of-mass energy of 140 GeV, and the scaled equivalent for electron-ion collisions, will be met with this design, requiring no further upgrades.

The full-performance luminosity for e-p collisions can be achieved via strong cooling of the proton beam utilizing the technique of coherent electron cooling (CeC). This is a novel approach, currently under study at BNL and elsewhere, that has not yet been demonstrated. Thus, in parallel, we have developed alternative measures for achieving the maximum luminosity goal which depend only on established technology. These are described in Appendix ???. Without cooling or alternative measures, the luminosity for e-p collisions at $E_{CM} = 105 \text{ GeV}$ is $3.3 \times 10^{33} \text{ cm}^{-2} \text{ sec}^{-1}$, still well within the required range for this key performance measure.

The eRHIC pCDR, in concert with the National Academies committee findings on the EIC scientific program, is intended to facilitate a DOE Critical Decision 0; i.e. to declare a mission need for an electron ion collider supported by a technical plan to realize such a facility. DOE Critical Decision 1 (CD-1) will be based on a Conceptual Design Report, along with numerous CD-1 required planning documents, and will be developed with explicit DOE Office of Nuclear Physics support. The eRHIC pCDR demonstrates a feasible way forward along this path.

Contents

Executive Summary	iv
1 eRHIC Overview	1
1.1 Physics Case of the Electron-Ion Collider	1
1.2 Overview of the eRHIC Electron Ion Collider	3
1.3 eRHIC Design Concept	8
1.4 Beam Parameters and Luminosity	10
1.5 Beam-Beam Dynamics	13
1.6 Layout of the Interaction Region	15
1.7 Spin Rotators	19
1.8 Electron Storage Ring Design	21
1.9 Hadron Ring Design	31
1.10 Electron Injection Complex	37
1.11 Hardware Systems of the eRHIC	42
1.12 Overview Summary	55
2 EIC Physics and Requirements for Machine Design	57
2.1 Introduction	57
2.2 The Science Goals of the EIC and the Machine Parameters	59
2.3 Summary of Machine Design Parameters for the EIC Physics	73
2.4 Scientific Requirements for the Detectors and IRs	75
2.5 Scientific Requirements for the Detectors	76
2.6 Scientific Requirements for the Interaction Regions	78

3 eRHIC Design	91
3.1 Beam Parameters, Luminosities and Complex Layout	91
3.2 Interaction Region Development	105
Glossary of Acronyms	G-1
References	R-1

Chapter 1

eRHIC Overview

1.1 Physics Case of the Electron-Ion Collider

In the decades since the discovery of quarks, experiments in nuclear and particle physics have led to a fundamental theory of strong interactions —quantum chromodynamics (QCD) —that describes an extraordinary richness of nature at the subatomic level. The visible mass of matter in our universe the atoms and molecules that constitute the galaxies, planets, and life itself is made up of a dynamic substructure of quarks bound together by force-carrying gluons in complex systems internal to the protons and neutrons of atomic nuclei. An understanding of how the properties of matter originate from the deeply fundamental constituents of QCD is a primary goal of nuclear physics and the central motivation for an Electron-Ion Collider (EIC).

To date, a global program of precision measurements with high energy spin-polarized particle beams has begun to quantify how the intrinsic spins and orbital momenta of quarks, anti-quarks, and gluons each contribute to the characteristic spins of observed particles, but the mechanism by which this complex system results in the characteristic spin $\frac{1}{2}$ of the nucleon is not yet understood. The EIC concept is designed with the capability to answer this question.

Neutrons and protons bound inside atomic nuclei exhibit collective behavior that reveals the QCD substructure under extreme conditions. We now know, through laboratory experiments with high energy heavy ion collisions at RHIC [4] and the CERN LHC [5], that at temperatures and densities similar to those of the nascent universe moments after the Big Bang nuclear matter is transformed to a plasma of quarks and gluons. The strongly coupled “perfect fluid” property of this quark-gluon plasma [6] came as a remarkable surprise, and has brought widespread interest to the study of condensed matter of the strong force, and the understanding that the formation and evolution of this extreme phase of QCD matter is dominated by the properties of gluons at high density.

The most energetic nuclear collisions, including electron-proton collisions at HERA [7], established the dominance of gluons in the structure of nuclear matter when probed at

high energies. This arises from the property that gluons, unlike their electromagnetic analogue (the photon), can interact directly with each other. Like quarks, gluons can interact through a “color” charge. The energy of self-interaction among the gluons accounts for a significant fraction of the nucleon mass. In collisions at higher and higher energies the density of gluons seen in the nucleon increases rapidly and without apparent limit. While this rise must saturate at some point, this saturation of the gluon density has not been observed yet, and its mechanism is of fundamental interest. It is widely conjectured that such a saturated gluonic state may have universal properties for all strongly interacting particles in nature. The EIC, through high energy collisions of electrons with heavy nuclei, is expected to enable detailed studies of this extraordinary state of matter.

In the last two decades, nuclear physicists have developed new phenomenological tools to enable remarkable tomographic images of the quarks and gluons inside protons and neutrons. These tools are being utilized and will be further enhanced at the upgraded 12 GeV CEBAF [8] at JLab and the COMPASS [9] experiment at CERN. Applying these new tools to study the transition of matter from being dominated by quarks to being governed by gluons will require the higher energy and beam polarization of an EIC.

In light of these advances and discoveries, a worldwide community of scientists has come together over the past several years to articulate the key science questions for a next-generation facility, the EIC, and to broadly specify its performance requirements, at many international conferences and workshops. Following an intensive ten-week workshop held at the University of Washington’s Institute for Nuclear Theory (INT) in 2011, a summary White Paper, published initially in 2014 and updated in 2016 [1] presents the science case for an EIC, including some “golden measurements” and the accelerator and detector concepts required to achieve them.

Addressing these studies, the Department of Energy’s Nuclear Science Advisory Committee, in its Long Range Plan for U.S. Nuclear Physics completed in 2015 [2], acknowledged the “qualitative leap in technical capabilities” required for the EIC, and identified an electron ion collider as “the highest priority new facility construction following the completion of FRIB”. In 2018 this program was endorsed by the National Academies of Sciences Committee on U.S. Based Electron Ion Collider Science Assessment [3], stating:

“An EIC can uniquely address three profound questions about nucleons - neutrons and protons, and how they are assembled to form the nuclei of atoms:

- How does the mass of the nucleon arise?
- How does the spin of the nucleon arise?
- What are the emergent properties of dense systems of gluons?”

These questions call for an EIC with capabilities that far exceed any current or past colliding beams accelerator facility:

- A collider with a range of center-of-mass energies E_{CM} from 20 to 140 GeV will enable a kinematic reach well into the gluon-dominated regime;

- Highly polarized ($\approx 70\%$) electron, proton, and light nuclear ion beams (for example, deuterons, or ^3He) are planned for a comprehensive study of the nucleon structure including their spin: The electron beam brings to bear the unmatched precision of the electromagnetic interaction as a probe, while polarized nucleon beams are needed to determine the correlations of sea quark and gluon distributions with the nucleon's spin. High values of polarization reduce the uncertainties in determination of these correlations;
- High collision luminosity 10^{33} to $10^{34} \text{ cm}^{-2}\text{sec}^{-1}$ over a broad range in E_{CM} will enable precise determination of confined momentum and spatial distributions of sea quarks and gluons in nucleons and nuclei;
- Ion beams from deuteron to the heaviest nuclei (gold or uranium) of the EIC will provide access to the regime of saturated gluon densities and to understand how color propagates through nuclear matter.

In this document we present the plan for eRHIC, Brookhaven's proposal for realizing the EIC. The eRHIC proposal provides a design that fully utilizes the existing RHIC facility to produce hadron beams, including high-intensity polarized proton beams, and takes advantage of recent technical advances to provide a powerful, cost-effective new facility that fully meets the requirements for a compelling and lasting research program, with high potential for new discovery, as spelled out in the community White Paper and described below in Section 2.2.

1.2 Overview of the eRHIC Electron Ion Collider

The EIC eRHIC takes advantage of the entire existing Relativistic Heavy Ion Collider (RHIC) facility with only a few modifications, and with cost implications that are small on the scale of the eRHIC project. The well-established beam parameters of the present RHIC facility are close to what is required for the highest performance of eRHIC. The addition of an electron storage ring inside the present RHIC tunnel will provide polarized electron beams for collisions with the polarized protons or the heavy ions of RHIC.

The eRHIC design must satisfy the requirements of the science program while having acceptable technical risk, reasonable cost, and a clear path to achieving design performance after a short period of initial operating time. The strategy for arriving at an optimum design that meets these requirements led to the eRHIC design.

The storage ring based design meets or even exceeds the requirements referenced in the Long Range Plan [2], including the upgraded energy reach:

- Center-of-mass energy (E_{CM}) of 20 to 140 GeV¹; the long range plan requires ≈ 20 to 100 GeV.

¹The upper limit of the center of mass energy range can only be extended by a significant additional investment in RF equipment; the lower limit is softer and is given by the ability to detect low energy deep inelastic scattered electrons; there is no hard restriction from the accelerator other than reduction in luminosity

- A luminosity of up to $10^{34} \text{ cm}^{-2} \text{ sec}^{-1}$; the long range plan requires 10^{33} to $10^{34} \text{ cm}^{-2} \text{ sec}^{-1}$.
- High polarization of electron and light ion beams with arbitrary spin patterns, with time-averaged polarizations of $\approx 70\%$, as required by the Long Range Plan.
- Beam divergences at the interaction point and apertures of the interaction region magnets that are compatible with the acceptance requirements of the colliding beam detector.
- Collisions of electrons with a large range of light to heavy ions (protons to uranium ions); the long range plan requires ions as heavy as uranium.
- Two interaction regions.

The RHIC tunnel complex incorporates two large experimental halls with full infrastructure for two major collider detectors. These are at the 6 o'clock position², where the RHIC STAR detector [10] is currently operating, and the 8 o'clock position, home of the RHIC PHENIX detector [11] (see Figure 1.1). The design described here allows for two eRHIC detectors, but initially only one will be implemented. In this report, we describe in detail the interaction region (IR) configuration for a large, general-purpose detector in one of these areas (6 o'clock), which could fulfill the requirements for the full range of EIC science questions described above and in Chapter 2. Our plans for eRHIC include the capability for two such detectors.

The scientific requirements, calling for high luminosity and near-complete angular coverage by the detector, result in an IR lattice that produces a significant degree of chromaticity (energy sensitivity of the beam optics). The nonlinear sextupole fields needed to compensate for this effect generally limit the dynamic aperture and need to be well optimized to provide sufficient beam lifetime. Calculations motivated by experience at HERA [12] indicate that adding an identical second IR can be achieved without further reduction of the dynamic aperture (see Section ??). We thus plan for detectors at both the IR6 and IR8 positions. The forces acting on the particles in each beam, which are introduced by the collective charges of the opposing beam, respectively, and the corresponding dynamical implications are called "beam-beam effects". In order to avoid unacceptably large beam-beam effects in the case of two experiments, the collider would be operated in a mode where each of the two experiments sees one-half of the bunch crossings; i.e., each experiment receives 1/2 of the total luminosity (see Section ??).

Highest luminosities can only be achieved by implementing strong cooling of the ion and proton beams to counteract emittance growth by intrabeam scattering (IBS) [13] associated with the corresponding small beam emittances. Cooling of hadron beams with beam energies up to 275 GeV requires novel cooling techniques that are currently being developed and tested in an R&D program at BNL [14].

²RHIC is composed of six sextants separated by six 200 m long straight sections with a potential collision point in the center. These six straight sections are denoted as 2, 4, 6, 8, 10, and 12 o'clock, or IR2 to IR12, with IR12 being the Northern-most IR

The design satisfies all requirements while the beam dynamics limits are not exceeded. In particular, the design parameters remain within the limits for maximum beam-beam tune-shift parameters (hadrons: $\xi_p \leq 0.015$; electrons: $\xi_e \leq 0.1$) and space charge parameter (≤ 0.06), as well as beam intensity limitations. The outline for the eRHIC electron ion collider is shown in Figure 1.1.

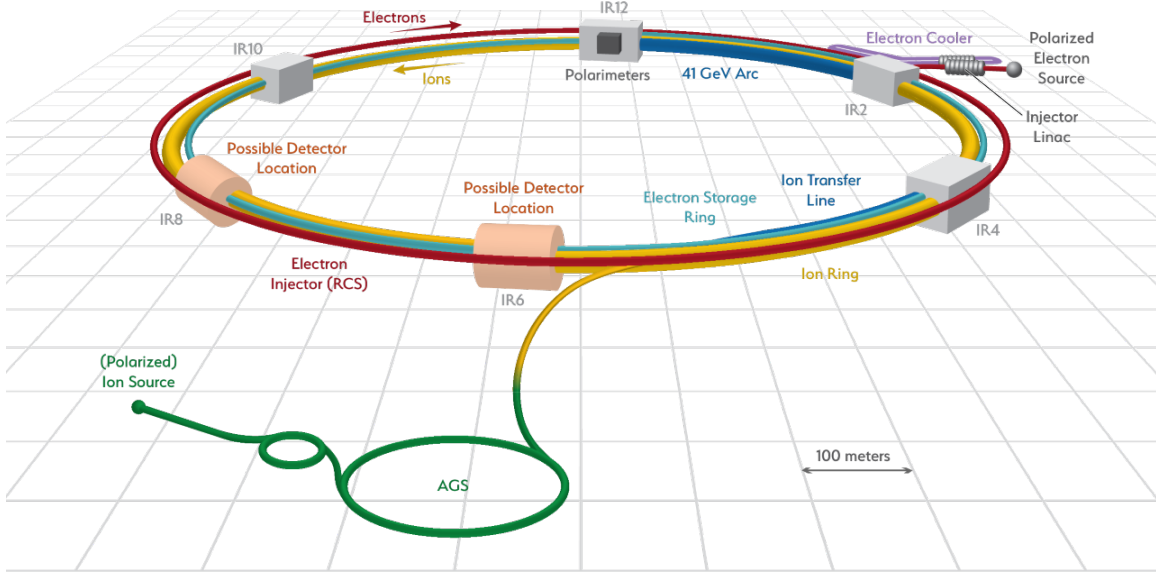


Figure 1.1: Schematic diagram of the eRHIC layout.

Polarized electron bunches carrying a charge of 10 nC are generated in a state-of-the-art polarized electron source. The beam is then accelerated to 400 MeV by a linear accelerator (LINAC). Once per second, an electron bunch is accelerated in a rapid cycling synchrotron (RCS), which is also located in the RHIC tunnel, to a beam energy of up to 18 GeV and is then injected into the electron storage ring, where it is brought into collisions with the hadron beam. The spin orientation of half of the bunches is anti-parallel to the magnetic guide field. The other half of the bunches have a spin parallel to the guide field in the arcs. The Sokolov-Ternov [15] effect will depolarize these electron bunches with a time constant of 30 min (at the highest energy of 18 GeV). In order to maintain high spin polarization, each of the bunches with their spins parallel to the main dipole field (of which there are 145 at 18 GeV) is replaced every six minutes. The polarization lifetime is larger at lower beam energies and bunch replacements are less frequent.

The highest luminosity of $L = 1 \times 10^{34} \text{ cm}^{-2} \text{ sec}^{-1}$ is achieved with 10 GeV electrons colliding with 275 GeV protons ($E_{\text{CM}} = 105 \text{ GeV}$). The high luminosity is achieved due to large beam-beam parameters, a flat shape (or large aspect ratio σ_x/σ_y) of the electron and hadron bunches at the collision point, and the large circulating electron and proton currents distributed over as many as 1160 bunches. Table 1.1 lists the main design parameters for the beam energies with the highest peak luminosity.

Table 1.1: Maximum luminosity parameters.

Parameter	hadron	electron
Center-of-mass energy [GeV]	104.9	
Energy [GeV]	275	10
Number of bunches	1160	
Particles per bunch [10^{10}]	6.9	17.2
Beam current [A]	1.0	2.5
Horizontal emittance [nm]	9.6	20.0
Vertical emittance [nm]	1.5	1.2
Horizontal β -function at IP β_x^* [cm]	90	43
Vertical β -function at IP β_y^* [cm]	4.0	5.0
Horizontal/Vertical fractional betatron tunes	0.305/0.31	0.08/0.06
Horizontal divergence at IP $\sigma_{x'}^*$ [mrad]	0.103	0.215
Vertical divergence at IP $\sigma_{y'}^*$ [mrad]	0.195	0.156
Horizontal beam-beam parameter ξ_x	0.014	0.073
Vertical beam-beam parameter ξ_y	0.007	0.1
IBS growth time longitudinal/horizontal [hr]	3.4/2.0	-
Synchrotron radiation power [MW]	-	9.0
Bunch length [cm]	6	2
Hourglass and crab reduction factor [16]	0.86	
Luminosity [$10^{34} \text{ cm}^{-2} \text{ sec}^{-1}$]	1.0	

At the lower center-of-mass energies, the beam sizes need to be increased and/or the beam intensities have to be decreased to keep the beam-beam tune shift below the maximum allowed value. At a higher center-of-mass energy, which is achieved by increasing the electron energy to 18 GeV, the electron beam intensity has to be reduced to limit the synchrotron radiation power loss to 10 MW. Figure 1.2 shows the peak luminosity versus center-of-mass energy that will be achieved in eRHIC. In the case of collisions between electrons and ions, the electron-nucleon luminosity is lower, but event rates comparable to the electron-proton case are achieved.

We need to separate the electron and hadron beams quickly after collisions. In order to avoid parasitic crossings, without introducing separator magnets and the associated generation of synchrotron radiation, the beams collide under a crossing angle of 25 mrad. Collisions with a crossing angle reduce the overlap region of the two beams thereby reducing the luminosity by an order of magnitude. In addition, with a crossing angle, the transverse beam-beam forces depend strongly on the longitudinal position of the particles which generates strong synchro-betatron resonances that affect the beam lifetime and stability. These

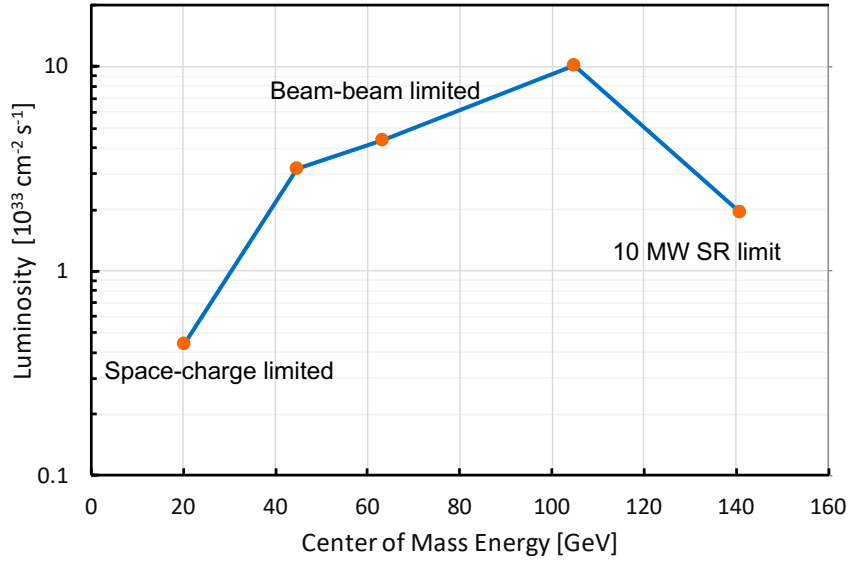


Figure 1.2: eRHIC electron-proton peak luminosity versus center-of-mass energy (E_{CM}). The luminosity for low E_{CM} is limited by the beam-beam interaction; at high E_{CM} , the luminosity is limited by the electron beam intensity and the total synchrotron radiation power. A maximum power of 10 MW is chosen to limit operational costs. This is not a technical limit but a design choice. (Solid lines connecting the dots are inserted to guide the eye.)

crossing angle effects are avoided by employing crab crossing [17] using crab cavities. Compensation of the crossing angle by crab cavities is a proven technology that has been demonstrated routinely in the electron-positron collider KEKB [18], and crab crossing is planned for the high luminosity upgrade of the large hadron collider (LHC).

The main elements of eRHIC that have to be added to the existing RHIC complex are:

- A low frequency photocathode gun delivering 10 nC bunches of polarized electrons at 1 Hz
- A 400 MeV normal-conducting S-band injector LINAC
- A 400 MeV to 18 GeV rapid cycling synchrotron (RCS) in the RHIC tunnel
- A high intensity, spin-transparent electron storage ring with up to 18 GeV beam energy in the RHIC tunnel with superconducting RF cavities
- A high luminosity interaction region with 25 mrad crossing angle, crab cavities and spin rotators that allows for a full acceptance detector; a second interaction region is possible and feasible
- A 150 MeV energy recovery LINAC that provides continuous electron beams for strong hadron cooling

- A small number of additional buildings to house additional RF power stations and the electron injector.

The eRHIC electron storage ring design is using established and existing technologies from high intensity electron storage rings such as the B-factories of KEK [18] and SLAC [19], as well as from modern synchrotron light sources.

1.3 eRHIC Design Concept

The eRHIC pre-conceptual design provides a path towards a machine with a nominal luminosity of up to $10^{34} \text{ cm}^{-2} \text{ sec}^{-1}$. The overall concept is to base the design, to a large extent, on existing technologies which will greatly reduce the technical risk. This is expected to result in reduced project costs, rapid commissioning, and will provide usable physics data soon after project completion. A design version with somewhat reduced luminosity (“moderate luminosity”) is discussed as well in the context of design risk mitigation (see Appendix ??). For commissioning and initial operation, we consider even more modest parameters that are, however, still within the range of requirements of the White Paper on the EIC [1] (see Appendix ??).

In the following we will describe the parameters for the maximum performance that we are referring to as nominal parameters, which are summarized below:

- The design peak luminosity reaches up to $1.0 \times 10^{34} \text{ cm}^{-2} \text{ sec}^{-1}$, depending on center-of-mass energy (see Figure 1.2). The electron energy and the luminosity at energies $E_e \geq 10 \text{ GeV}$ is limited by the power of the synchrotron radiation. A total synchrotron radiation power of 10 MW is considered a reasonable upper limit. This allows a beam energy of 18 GeV together with a luminosity which is still 19% of the maximum luminosity at 10 GeV.
- The center-of-mass energy from 20 to 140 GeV is realized by proton energies that range from 41 to 275 GeV, and by electron energies up to 18 GeV. RHIC magnets are capable of exceeding the present maximum operational energy of 255 GeV since some magnets that presently limit the beam energy will no longer be needed in eRHIC. The lowest eRHIC proton energy is 41 GeV. This is limited by the need to synchronize the revolution frequency with the electron beam.
- Both electron and hadron beams will be spin polarized with flexible spin patterns. Proton polarization is part of the present RHIC program and can be carried over as-is to eRHIC. The capability of light ion polarization (helions and deuterons) will be added by upgrading the Siberian snakes (this sequence of magnets which suppress spin depolarizing resonances have been first described in Reference [20]) and ion sources, and by improved polarimetry. The electron beam polarization will be enabled by full-energy injection of polarized electron bunches with the desired spin direction (up or down) and frequent electron bunch replacement to ensure a high degree of polarization.

- A transverse momentum detection acceptance for scattered protons from 200 MeV/c to 1.3 GeV/c in at least one transverse plane is realized by limiting the divergence angle of the proton beam at the interaction point (IP). Proton β -functions at the IP are chosen such that 50% of all scattered protons with a transverse momentum of 200 MeV/c can be detected by forward detectors close to the beam (“Roman Pots”), which limits the achievable luminosity in this configuration. Increasing this lower limit of detectable transverse momentum allows us to decrease the horizontal β -function at the IP substantially, thus increasing the maximum luminosity by a factor of two or more. As the cross section increases steeply with decreasing scattering angle, it is sufficient to operate in this mode for only a short amount of time ($\approx 10\%$), which then has only a correspondingly small impact on integrated luminosity.

The basic assumptions of this design are:

- The electron ring is installed in the existing RHIC tunnel to minimize civil engineering efforts, and it has the same circumference as RHIC.
- The layout described here admits two interaction regions (IR) and two interaction points (IP). However, the second IR has not yet been integrated into the lattice design and the dynamic aperture assessment is yet to be completed. In case of operation with two collision points, the luminosity is maximized as half of the electron and hadron bunches collide in one of the two interaction points and the other half of the particles collide in the second IP. Luminosities and beam-beam parameters quoted are based on a single beam-beam interaction per turn. In operations with two detectors, each will receive half of the luminosity (see Section ??).
- Electron and hadron beams have identical beam sizes at the interaction point. The beams are flat and the horizontal beam size is larger than the vertical one. At the interaction point, the two beams intersect at a full crossing angle of 25 mrad in the horizontal plane. The resulting luminosity loss will be largely restored by tilting the bunches around the vertical axis in the IP (perpendicular to the crossing plane) by half the crossing angle using transversely deflecting RF resonators, so-called crab cavities, in the hadron ring. This is mandatory for hadron bunches. Crab cavities in the electron ring are needed as well to avoid synchro-betatron resonances excited by the collision crossing angle in the electron beam, though their pure geometric effect is negligible.
- Hadron beam parameters are a moderate extrapolation of what has been achieved at RHIC, with one exception: the number of bunches is increased from 111 to up to 1160. The total proton current, however, is increased only by a factor of three. Injection and acceleration will be done with 290 bunches. At the maximum beam energy in storage mode, the bunches will be adiabatically split in two steps into 1160 bunches. Note that in the absence of strong hadron cooling, a maximum luminosity of $0.43 \times 10^{34} \text{ cm}^{-2} \text{ sec}^{-1}$ is achievable with 580 bunches (see Appendix ??).
- A rapid cycling synchrotron (RCS) located inside the RHIC tunnel serves as a polarized full-energy injector for the electron storage ring.

- The maximum electron beam-beam parameter does not exceed $\xi_e = 0.1$, a level that has been routinely achieved at the B-factories KEKB [18] and PEP-II [19]. The electron ring will be operated near the integer betatron resonance to mitigate the beam-beam effect while simultaneously minimizing the impact of systematic depolarizing spin resonances.
- The RF power required to replace the power of the synchrotron radiation emitted by the beam is 10 MW. This corresponds to a linear synchrotron radiation power load of 4 kW/m, which is equivalent to 37 W/mm² in the arcs. This linear load is less than half of the corresponding value for PEP-II [19] and KEKB [18]. There is no principle hard limit of the RF power but 10 MW is considered a practical upper limit.

1.4 Beam Parameters and Luminosity

The luminosity of an electron-proton collider is given by

$$L = H \cdot f_b \cdot \frac{N_p N_e}{4\pi\sigma_x\sigma_y}, \quad (1.1)$$

where N_p and N_e are the number of hadrons and electrons per bunch, respectively, f_b is the bunch frequency, and σ_x and σ_y are the RMS beam sizes (assuming they are the same for both beams) given by the electron or proton beam emittances $\varepsilon_{x,y}$ and β -functions at the interaction point (IP) $\beta_{x,y}^*$ as

$$\sigma_{x,y} = \sqrt{\varepsilon_{x,y}\beta_{x,y}^*}. \quad (1.2)$$

H is a factor reflecting the impact of the hourglass effect (the impact of the variation of the beam cross section along the length of the bunch in collisions) and residual effects of the compensated crossing angle. With the bunch length being close to the vertical β -function at the IP, the factor H remains above 0.8. For eRHIC, the current limits are taken as 1.0 A for the protons and 2.5 A for the electrons based on the PEP-II [19] operation with 2.1 A at 9 GeV and 3.2 A at 3 GeV.

The numbers of particles per bunch $N_{e,p}$ are constrained by the beam-beam tune shift parameters induced by the bunches upon each other,

$$\xi_{x,y,e,p} = \frac{r_{e,p}}{2\pi} \frac{N_{p,e}}{\gamma_{e,p}\epsilon_{e,p}} \frac{1}{1 + K_{y,x}}, \quad (1.3)$$

where $r_{e,p}$ are the classical radii of the electrons or protons, respectively, and

$$K_y = \frac{\sigma_y}{\sigma_x} = \frac{1}{K_x}. \quad (1.4)$$

Combining these two equations and thereby eliminating the emittances yields

$$L = \frac{1}{e^2 \sqrt{r_e \cdot r_p}} \frac{1 + K_y}{\sqrt{K_y}} (\gamma_e \gamma_p I_e I_p)^{1/2} \left(\frac{\tilde{\zeta}_{ex} \tilde{\zeta}_{ey} \tilde{\zeta}_{px} \tilde{\zeta}_{py}}{\beta_{xe}^* \beta_{ye}^* \beta_{xp}^* \beta_{yp}^*} \right)^{1/4}. \quad (1.5)$$

In this form, the luminosity is expressed by the limiting factors, the beam currents I_e and I_p , the beam-beam tune-shift parameters $\tilde{\zeta}_{x,y,e,p}$, the β -functions at the IP, and the beam size ratio K_y . We see that for flat beams, $K_y \ll 1$, one gets a significant enhancement factor of the luminosity as compared to round beams ($K_y = 1$). For this reason, the beam parameters are optimized around a value of $K_y = 0.08$ which enhances the luminosity by a factor of ≈ 1.5 as compared to a round beam scenario.

Colliding beam experience at RHIC suggests the beam-beam parameters $\tilde{\zeta}_p$ for the protons are bounded by beam stability considerations at values of $\tilde{\zeta}_p \approx 0.015$, while the electrons can, with sufficient synchrotron radiation damping, reach $\tilde{\zeta}_e = 0.1$ according to experience at the B-factories. Beam currents are assumed to be limited by the bunch current values achieved in RHIC [21] and by total beam currents achieved in PEP-II [19].

High luminosity obviously requires small values of the β -functions at the IP. There are a number of constraints which limit the β -functions:

- For flat beams, the vertical β -function at the IP is smaller than the horizontal one. The vertical β -function is limited by the length of the proton bunch via the hourglass effect. The proton bunch length in turn is limited by intra-beam scattering. The minimum value is about 5 cm for the highest luminosity case with 1160 bunches.
- An important part of the EIC physics program is the measurement of the spatial distribution of the gluon density of the hadrons. This requires detection of protons that are scattered under a small angle. The acceptance for such low transverse momentum scattered protons (low- p_t) depends strongly on the horizontal divergence of the beam at the IP and gives rise to another limitation for the horizontal β -function and K_y . The horizontal divergence is proportional to $1/(\beta_{xp}^*)^{1/2}$. In order to accept scattered particles with $p_t = 200$ MeV/c, the horizontal β -function of the hadron beam should be about 1 m. The design values are $\beta_{xp}^* = 90$ cm and $\beta_{yp}^* = 4$ cm.
- Small β -functions at the interaction point (IP) imply large β -functions in the strong final focus quadrupoles. Very large β -functions in quadrupoles cause a strong effect on the tune and the optics for off-energy particles, referred to as chromatic effects. Chromaticity needs to be compensated to provide sufficient space for a stable working point for the beam in-between nonlinear resonances. Chromaticity correction is accomplished by nonlinear sextupole fields in the accelerator arcs. This in turn introduces a dynamic aperture limit and increases the width of nonlinear resonances to be avoided by reducing the tune footprint. Sufficient beam lifetime requires a minimum dynamic aperture. Beyond a certain value of chromaticity, the stability requirements for the beam cannot be fulfilled. This threshold value depends on other parameters such as phase advance per arc FODO cell and number of sextupole families. An ap-

proximate rule is that the IR chromaticity should not contribute more than about one third to the total natural chromaticity.

In summary, the general concept of achieving high luminosity is the same as that for e^+e^- colliders:

Luminosity is increased by running with the highest beam currents, using flat beams, low emittances, and low β -functions at the IP. Focusing magnets are installed as close as possible to the IP. The beam current is distributed over many, closely spaced bunches, while the charge per bunch is relatively low. These choices mandate a crossing angle collision geometry.

Table 1.1 in Section 1.2 shows the beam parameters for the highest luminosity. The highest luminosity is achieved for an electron beam energy of 10 GeV and for a proton beam energy of 275 GeV. Both the β^* and emittances of both protons and electrons are larger in the horizontal plane than in the vertical plane, resulting in flat beam profiles at the IP. Unequal emittances are natural for the electrons in a storage ring. For protons, however, the beam first needs to be pre-cooled at low energies using electron cooling. Subsequently, kicker noise is applied in the horizontal plane to increase the horizontal emittance to its desired value. Experimentally, it is known that such emittance asymmetries can be stable in RHIC for long storage times.

Maximum luminosity is achieved with an electron beam energy of 10 GeV and a proton beam energy of 275 GeV which corresponds to a center-of-mass energy of 105 GeV. For larger electron energies, the rapidly increasing synchrotron radiation power scales with the electron energy to the 4th power, $P \propto E_e^4$. This requires reducing the electron current by the same factor to keep the total synchrotron radiation power below the limit of 10 MW. At the highest electron energy of 18 GeV, the electron current is only 0.26 A—nine times smaller than the maximum value. The loss in luminosity is mitigated by decreasing the number of bunches by a factor of four and adjusting the transverse beam parameters. The increase of electron beam emittance, which scales as E_e^2 , is compensated by increasing the phase advance in the arcs from 60° per FODO cell³ to 90° per FODO cell. The overall result is that the luminosity is reduced by a factor of five as compared to the maximum value achieved at 10 GeV electron energy.

These considerations result in the luminosity versus center-of-mass energy as shown in Figure 1.2. The parameters shown in Table 1.1 are derived under the assumption that the proton beam emittances will remain constant at the very small values of $\epsilon_x = 9.6$ nm and $\epsilon_y = 1.5$ nm. However, the dense hadron beam is subject to substantial emittance growth due to intrabeam scattering (IBS). IBS must be counterbalanced by strong cooling of the hadron beam to maintain emittances and bunch length over a reasonable amount of time. This time needs to be much larger than the time it takes to replace a depleted hadron beam. Several schemes for strong cooling are considered that promise to yield sufficiently fast cooling rates to balance emittance growth at the operational parameters of eRHIC. One of these schemes, called “Coherent Electron Cooling” [22], is being tested experimentally.

³A FODO cell is a lattice structure with alternating gradient quadrupole magnets between the bending magnets

Strong cooling is discussed further in Section 1.9.6.

As already mentioned in Section 1.3, the design must enable detection of scattered protons with a minimum transverse momentum of $p_t = 200 \text{ MeV}/c$, which at a hadron beam energy of 275 GeV corresponds to a scattering angle of $730 \mu\text{rad}$. The RMS divergence of the proton beam at the IP must not exceed one tenth of this minimum scattering angle, $\sigma' \leq 73 \mu\text{rad}$. This requirement, however, may be violated in the vertical plane, provided the beam divergence in the horizontal plane meets the requirement. A horizontal RMS beam divergence of $56 \mu\text{rad}$ allows detection of 50% of all scattered protons with a transverse momentum of $200 \text{ MeV}/c$. eRHIC will be operated for a short time, say 10% of the time, with a large β_x^* that results in this low divergence and thus provides high acceptance at the expense of reduced luminosity. For the vast majority of the time, about 90 %, eRHIC will be operated at small β_x^* for high luminosity but reduced acceptance. Because of the large cross section for small p_t , in a short amount of time, a large amount of data can be collected so that there is eventually an equal amount of data at all p_t values from $200 \text{ MeV}/c$ to $1.3 \text{ GeV}/c$. This scenario substantially increases the effective luminosity of the facility.

So far we have only discussed electron-proton collisions. Most of the considerations discussed in this section apply to ions with only a few exceptions which are addressed below. Ions are characterized by the number of nucleons, A , and the electrical charge $Z \cdot e$, with $A \approx 2.5Z$. The beam-beam tune-shift of the electrons that is assumed to be at the maximum tolerable value for the collision parameters with protons is proportional to Z (for protons $Z = 1$). In order to maintain the electron tune-shift value in collisions with ions, the number of ions per bunch, N_i has to be reduced by a factor Z . The beam-beam tune shift for the hadrons is also proportional to Z but is inversely proportional to A . Thus the ion beam-beam tune shift is reduced approximately by a factor of 2.5 for a constant number of electrons. In principle, we could benefit from the reduced tune-shift and increase the number of particles in the electron bunch by a factor of 2.5. However, this would increase the electron beam current by a factor of 2.5, which is deemed too high. In conclusion, the electron-ion luminosity is reduced by a factor of Z . However, most of the cross sections in electron-ion collisions will increase by a factor of A compared to electron-proton cross sections. Therefore, the event rate of electron-ion collisions is expected to increase by a factor of approximately 2.5 in electron-ion collisions as compared to electron-proton collisions in eRHIC. A full luminosity parameter table is shown in section 3.1.1. Note that heavy ion beams will be unpolarized.

1.5 Beam-Beam Dynamics

The eRHIC approach to achieving stable beam-beam interactions is similar to the HERA approach: Each beam is assumed to reach the same beam-beam tune shift values as they did when colliding with a beam of the same species. The beam-beam tune shift as discussed in Section 1.4 is an established measure of characterizing the strength of the highly nonlinear interaction of the two beams.

However, for eRHIC, this approach is applied on a higher level of beam-beam strength

than for HERA, as will be discussed in Section ???. The total beam-beam tuneshift values of electrons with two collision points in HERA are about the same as for one collision point in eRHIC. For this reason, comprehensive simulation studies have been performed to ensure that the beams remain stable in collisions and that the hadron beam does not suffer from unacceptably fast emittance growth when colliding with the electron beam. Long term slow emittance growth is investigated by so called weak-strong beam-beam simulations. With this method one beam is considered static in its transverse and longitudinal dimensions. This is the equivalent of treating it as a static external field. The other beam is described by individual particles that are launched in phase space and whose trajectories are tracked in a complete dynamic model over a large number of turns. This study did not reveal any unacceptable hadron beam emittance growth for the operational parameters of eRHIC.

The other effect that might compromise the performance of an electron-ion collider is a strong coherent interaction between the two beams. Such interactions have been observed occasionally in HERA but could not be studied systematically. If such a coherent beam-beam instability occurs, the hadron beam transverse phase space will filament quickly, which corresponds to a strong effective emittance growth. This would render the hadron beam useless for high luminosity collision operations.

This issue was investigated for eRHIC parameters using so-called strong-strong beam-beam simulations. Both beams are described by super-particles in a complete dynamical model. The particle distributions at the collision point are used to generate a realistic beam-beam force. Much mathematical finesse is required to suppress artificial noise due to the fact that the number of super-particles is much smaller than the number of particles in a real beam. These methods are not well suited to investigate long term stability of the beam but are designed to describe short term strong dynamic effects.

The simulations for eRHIC performed with the computer codes BBSS [23] and Beam-Beam3D [24] indeed revealed a coherent instability such as observed in HERA. A clear instability threshold has been found for beam-beam tune shift values of the hadron beam which are twice as large as the eRHIC design parameters. Figure 1.3 shows the result of this simulation.

A particular complication of the beam-beam effect arises from crab crossing as the “crabbed” bunch exhibits residual deviations from a straight line due to the sinusoidal crab cavity field. According to simulations, this deviation must be small compared to the transverse beam size to avoid hadron emittance growth.

The conclusion of the beam-beam dynamics study is that while the eRHIC beam-beam parameters are fairly aggressive, the simulations predict stable beams in collisions with only small long term emittance growth.

Further studies are still in progress at this stage of the eRHIC design, for example imperfect compensation of the crossing angle and residual dynamic effects such as synchro-betatron resonances, as well as imperfection and spurious dispersion in the crab cavities. Some of these effects are described in more detail in the body of this pre-conceptual design study.

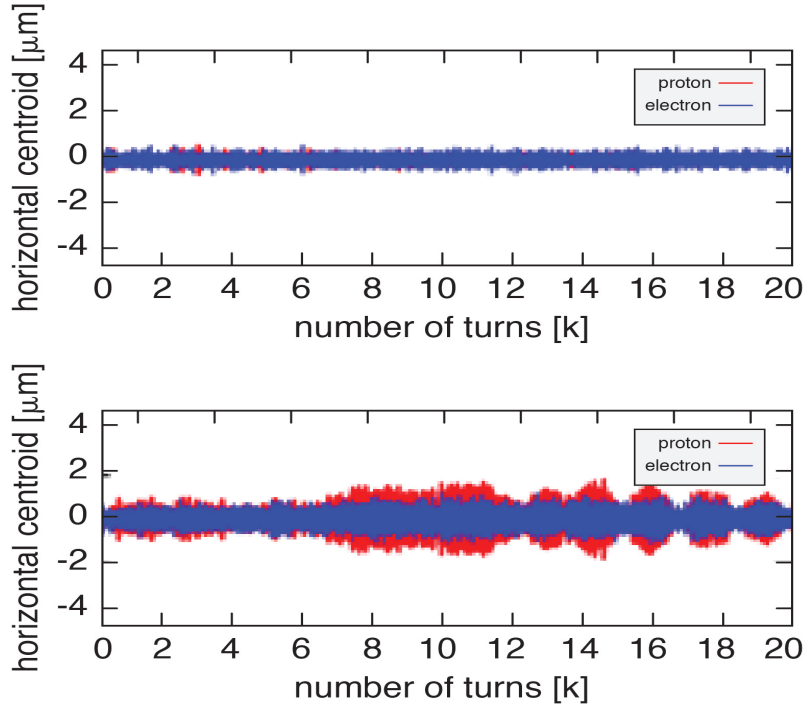


Figure 1.3: Coherent beam-beam instability as seen by strong-strong beam-beam simulations using the code BBSS. The number of protons in the upper plot is at 1.6 times the eRHIC design value of 10^{11} ; the resulting motion is still stable. In the lower plot, the number of protons is increased to twice the design value. In this case both beams perform unstable betatron oscillations. Such oscillations will blow up the hadron emittance.

1.6 Layout of the Interaction Region

The layout of the interaction region (IR) fulfills the following requirements:

- To achieve small beam cross sections and high luminosity, the beams are strongly focused at the interaction point (small β^* of order a few centimeters) by low- β quadrupole magnets, also referred to as final focus quadrupoles.
- The final focus quadrupoles must have sufficient aperture for the large beam size at their location.
- Large contributions to the chromaticity, which is a set of parameters characterizing the energy sensitivity of the beam optics, are generated in the low- β quadrupoles. Chromaticity needs to be compensated by nonlinear sextupole fields which, in turn, limit the dynamic aperture. The eRHIC IR design balances small β^* and tolerable values of chromaticity.

- The EIC physics program requires a large acceptance of hadrons scattered under very small angles off the collision point. The low- β quadrupoles have a large aperture so that scattered hadrons and neutrons can be detected by detector elements placed further downstream.
- The beam divergence and therefore the minimum β^* is restricted to enable detection of forward scattered protons with transverse momenta as small as $p_t = 200 \text{ MeV}/c$. These particles are then outside the 10σ proton beam envelope and are detectable by near-beam detectors, so-called “Roman Pots,” which are placed on the forward hadron beam pipe.
- The beams collide under a crossing angle of 25 mrad to separate the electron and proton beams quickly, to avoid parasitic collisions, and to provide space for a neutron detector in the forward⁴ direction and the luminosity detector in the forward electron direction. An important factor is the large bunch frequency of up to 99 MHz, which corresponds to only ten nanoseconds bunch spacing, required for high luminosity. The crossing angle effects, in particular the reduced overlap of the two beams and excitation of synchro-betatron resonances, must be compensated for by using so-called crab cavities —transverse RF resonators that kick the head and the tail of the proton and electron bunches in opposite directions in the plane of the crossing angle. These cavities are placed at a horizontal betatron phase advance of $\pi/2$ from the interaction point (IP) on both the rear and the forward side, forming a 180° bump. This causes the bunches to be tilted in-between the crab cavities in the horizontal plane by exactly half the crossing angle at the IP, and provides (ideally) the same collision geometry as head-on collisions, thereby avoiding synchro-betatron coupling.
- Strong synchrotron radiation generated by the electron beam can destroy sensitive detector equipment and make data-taking impossible. Therefore, the electron beam must not experience dipole fields in the interaction region (IR), certainly not on the forward side upstream of the IP. This is another strong reason why the two beams must collide at a crossing angle. Synchrotron radiation generated in the low- β quadrupoles on the electron-upstream side (the forward side of the IR) should be absorbed on the rear side of the IR as far as possible from the detector to minimize backscattered photons. This requires an extra large aperture for the electron low- β quadrupole magnets on the downstream side of the IP.
- Both the light hadron (protons, deuterons, ^3He) and electron beams are spin polarized. Polarization is only stable if the polarization direction coincides with the direction of the guide field in the arcs. In collisions, the spins are oriented longitudinally. Thus, the IR design accommodates pairs of spin rotators that accomplish longitudinal spin at the IP and vertical spin in the arcs. The spin rotators in the hadron ring already exist and are unchanged in this design. The spin rotators for the electron beam consist of two pairs of strong solenoids with quadrupole magnets in-between each pair, which are tuned such that the x - y coupling by the two solenoids cancels. This

⁴The IP separates the IR into a forward and a rear side or direction. The forward side is the side of the proton beam coming from the IP and the rear side is the side of protons going to the IP.

set of four solenoids is required on each side of the IP. The beam transport between the rotators is “spin transparent.” This means the magnetic fields in quadrupole magnets experienced by a particle performing betatron and synchrotron oscillations cancel between the spin rotators. This translates into beam optics spin matching conditions.

- The IR layout must provide room for a luminosity monitor on the rear side. This monitor detects hard γ -rays that are generated in the Bethe-Heitler process and exploited for luminosity measurement. The dipole magnet bending the electrons away from the path of the γ beam is at the same time a spectrometer magnet.
- On the forward proton side, a neutron detector is required. A dipole magnet bends the hadron beam away from the collision axis to provide space for this element.

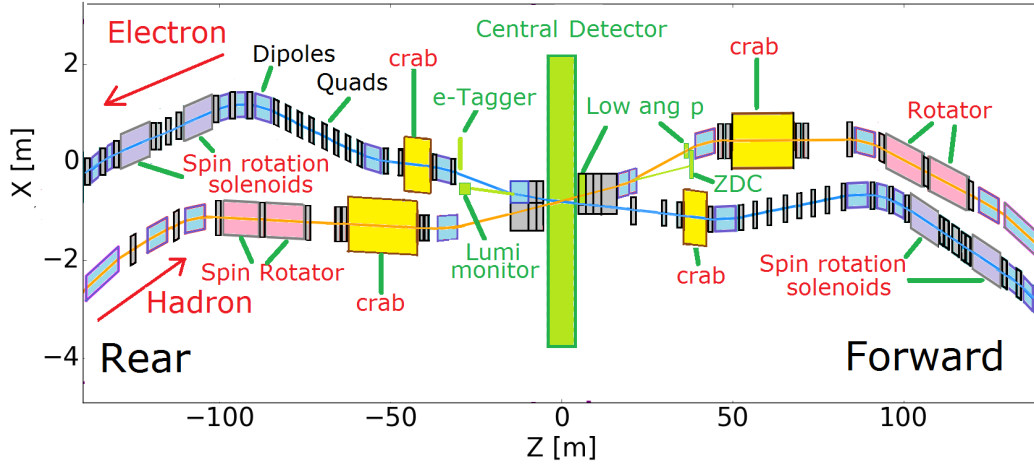


Figure 1.4: Schematic layout of the interaction region (top view, as simulated for high divergence, no cooling). Beams cross at an angle of 25 mrad. Note the length scales for the horizontal and vertical axis are very different. The IR design integrates focusing magnets for both beams, luminosity and neutron detectors, electron taggers, spectrometer magnets, near-beam detectors (Roman pots for hadrons), crab cavities, and spin rotators for both beams. The two beams are focused by quadrupole doublets. On the hadron-forward side, there are separate focusing magnets which are partially longitudinally interleaved. The first quadrupole magnet for electrons is integrated into a hadron spectrometer dipole. On the rear side, hadrons and electrons are focused by quadrupoles which are installed side-by-side in the same cryostat. The maximum β -functions in the IR for hadrons of 2000 m remain within the operating range of RHIC, while the maximum β -functions for electrons remain below 860 m.

Figure 1.4 shows a schematic of the top-view of the IR with 25 mrad beam crossing angle which satisfies all these conditions. For high luminosities, the β -functions at the IP are required to be as small as possible. In the case of 10 GeV electrons colliding with 275 GeV hadrons, the β -functions are $\beta_{x,e}^* = 43$ cm, $\beta_{y,e}^* = 5$ cm, $\beta_{x,p}^* = 90$ cm, and $\beta_{y,p}^* = 4$ cm (see Table 1.1). To avoid generation of an excessive amount of chromaticity generated in the low- β quadrupoles, these magnets should be placed as close as possible to the interaction

point. Special quadrupole magnets are needed to focus the two beams with the conditions and constraints mentioned above.

On the forward side, electron and hadron quadrupole magnets are partially interleaved. The first magnet is a room temperature spectrometer magnet with a very large aperture; located inside the aperture of the spectrometer magnet there is an electron quadrupole, which is shielded from the dipole field by an anti-dipole magnet. Further downstream the electron beam is shielded from the strong fields of the superconducting hadron quadrupoles by return yokes with designated cut-out regions which provide a field-free region for the electron beam. A strong dipole magnet is required on this side of the IP to steer the hadron beam away from the path of neutrons that are detected in the downstream neutron detector placed in this area as well.

On the rear side, the superconducting focusing magnets for electrons and protons are installed side-by-side in the same cryostat. The cross-section of the first quadrupoles on the hadron-rear side is shown in Figure 1.5. A steel return yoke shields the electron beam from the field of the hadron quadrupole magnets. Electron quadrupoles have an extra large aperture to provide sufficient space for the synchrotron radiation fan generated by the forward-side quadrupoles and must be absorbed further downstream, far away from sensitive detector components. The electron beam is steered away from the path of γ -radiation created by electron-hadron scattering (Bethe-Heitler), which is used to measure luminosity. The bending magnet acts as a spectrometer magnet for deep-inelastically scattered electrons with low Q^2 . These are tagged as part of the luminosity measurement.

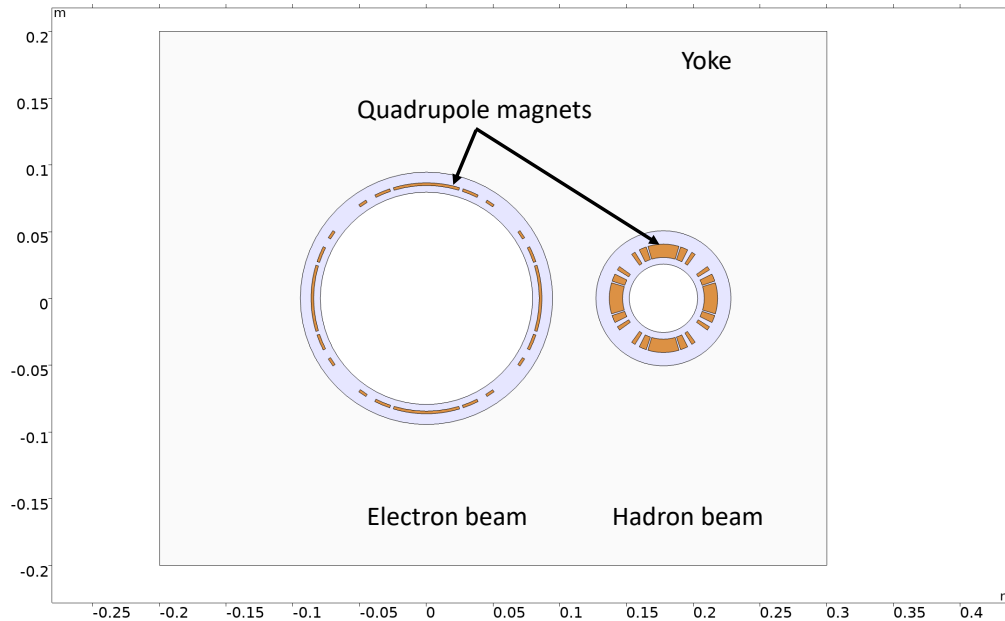


Figure 1.5: Cross section through the first low- β quadrupole cryostat on the hadron rear side (electron forward side). The two superconducting magnets, one for hadrons (left) and one for electrons (right), are separated by a common return yoke structure.

The maximum β -functions in the low- β quadrupoles for protons are $\hat{\beta}_{x,p} = 700$ m and $\hat{\beta}_{y,p} = 2000$ m, respectively. For electrons the corresponding numbers are $\hat{\beta}_{x,e} = 860$ m and $\hat{\beta}_{y,e} = 645$ m. The two beam lines are relatively close, so the early magnets of both beams need to have limited outside radial dimensions, outside of which the fields must be low. On the forward side, the apertures for the hadron magnets are considerably larger than required by the circulating hadron beam to provide sufficient clearance for scattered hadrons from the IP to be detected further downstream. For further details of IR magnet properties see Section 3.2.1.

1.7 Spin Rotators

Spin polarization of electron and hadron beams is preserved in beam storage if the spin orientation in the arcs of the accelerator is vertical. In collision, both electron and hadron spins are required to be in the longitudinal direction. In order to rotate the electron spin from the vertical direction in the arcs to the longitudinal direction, a set of magnets called spin rotators are required and need to be integrated into the interaction region. A second spin rotator, which rotates the spin back into the vertical direction, is required after the beam passes the interaction point. Spin rotators are an integral part of the interaction region and are associated with a number of beam optics conditions as discussed below.

The ends of the arcs surrounding the detectors in IR8 and IR6 accommodate the spin rotators. The proton spin rotators are identical to the ones presently used in RHIC, which are based on helical dipole magnets. Spin rotators based on helical magnets have been successfully used for polarized protons in RHIC [25, 26]. A helical magnet design leads to smaller orbit excursion compared with a design based on regular dipoles. The eRHIC electron spin rotators must operate over a large energy range, up to 18 GeV. Since the orbit excursion in the dipole magnets (either regular or helical) scales inversely with the beam energy, a HERA-type rotator would lead to 1 m orbit excursions of 5 GeV electrons [27]. Furthermore, the synchrotron radiation power per meter produced by 18 GeV eRHIC electrons is considerably larger than that generated by the 27.5 GeV electrons in HERA, due to the much larger electron current. Reducing the linear power load requires further increasing the rotator length and, correspondingly, the orbit excursion. Therefore, the most practical solution consists of a spin rotator based on strong solenoid magnets. Solenoidal Siberian snakes have been used in electron accelerators operating in the 0.5 GeV to 1 GeV range [28].

The spin rotators for electrons are based on interleaved solenoids and bending magnets. Each of the long and short solenoid modules contains a solenoid (split into two half-sections), and five quadrupoles that compensate the impact of the strong solenoidal fields on beam optics and transverse coupling and are required to satisfy the spin matching conditions. The lengths of the solenoids are chosen such that the maximum magnetic field required is 7 T. The settings for the magnetic fields of the solenoids to achieve longitudinal polarization of the electron beam depend on the beam energy. Optimization of the solenoidal spin integrals led to the parameters listed in Table 1.2.

The optics functions through the IR are shown in Figure 1.6. The set of β -functions describing this coupled case is given in Mais-Ripken parameterization [29]. Betatron coupling functions are limited to the rotator insertions, which are also made dispersion-free.

Table 1.2: Spin rotator parameters.

Parameter	Short solenoid module	Long solenoid module
Field integral range [T · m]	20-34	4-122
Solenoid length [m]	5.4	18.
Solenoid spin rotation angle at 18 GeV	32°	116°
Location in the RHIC tunnel	RHIC dipole 9-10	RHIC dipole 6-8

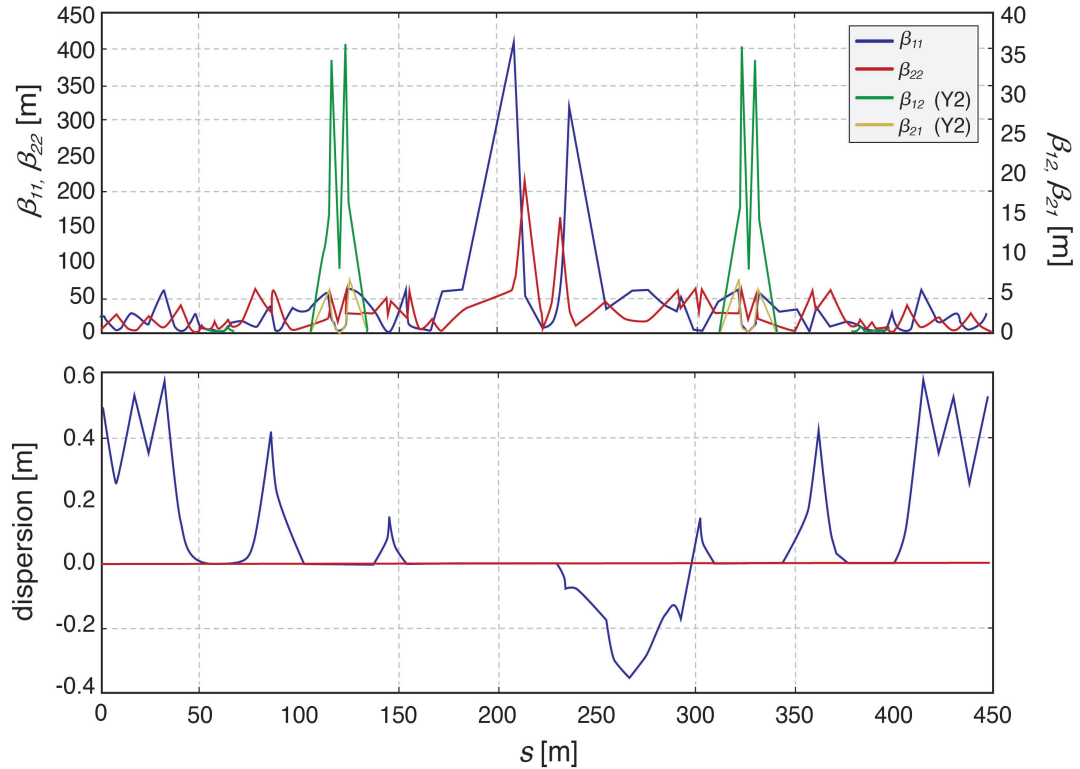


Figure 1.6: 18 GeV electron beam optics in the colliding straight section with the interaction region, the matching sections, the spin rotators, and dispersion suppressors. In the center of the plot is the interaction point (IP) with large values of the β -functions on both sides. The additional β peaks, in this plot denoted by $\beta_{1,2}$ and $\beta_{2,1}$, are caused by the coupled β -functions that vanish outside the rotator. These are drawn on a different scale, shown on the right hand side of the plot.

1.8 Electron Storage Ring Design

1.8.1 Storage Ring Overview

The electron storage ring is located in the existing RHIC tunnel, in the same plane as the ion ring, and has a circumference of 3833.940 m that matches the proton revolution time at 133 GeV, an energy that balances the orbit offsets required for maintaining the revolution time at 100 GeV and 275 GeV, see Section 1.9 Like the ion ring, it consists of alternating inner and outer arcs in order to have the same revolution time as the ion ring. Figure 1.7 shows a tunnel cross section with the two existing RHIC ion rings, the electron ring, and the rapid-cycling synchrotron.

As in the present RHIC, there are six arcs separated by six approximately 200 m long straight sections with a potential interaction point (IP) in the middle. These straight sections are denoted by their geographical positions as IR2 to IR12, with IR12 being in the North.

The ring is organized as follows:

- Straight section IR 6: colliding beam detector with hadron/electron low- β section, spin rotators and crab cavities.
- Straight section IR 10: superconducting RF systems, hadron beam abort.
- Straight section IR 12: polarimetry, damper systems, special instrumentation, electron injection and extraction.
- Straight section IR 2: electron source and pre-injector LINAC, strong hadron cooler facility.
- Straight section IR 4: hadron injection, warm hadron RF.
- Straight section IR 8: 2nd colliding beam detector, spin rotators and crab cavities.

The average arc radius is 380 m, with a dipole bending radius of $\rho = 290$ m. The lattice in the arcs and the non-colliding utility straights is composed of FODO cells. Each of the main dipoles in the arcs consists of three individual bending magnets, a short, 0.594 meter long magnet in the center between two longer ($l = 3.253$ m) magnets, thus forming super-bends.

In this configuration, the amount of synchrotron radiation can be controlled to ensure sufficient radiation damping for all beam energies between 5 and 18 GeV, thereby providing sufficient damping decrements in support of the anticipated strong beam-beam parameters of $\xi_{x,y} \leq 0.1$ (see below). In addition, the split magnets produce the desired beam emittance at 5 GeV beam energy. Each arc of the electron ring is composed of 16 identical FODO cells. Each half cell consists of a 0.6 meter long quadrupole, a 0.5 meter long sextupole, a 7.4 meter long dipole triplet, and a 0.25 meter long dipole corrector. The drift

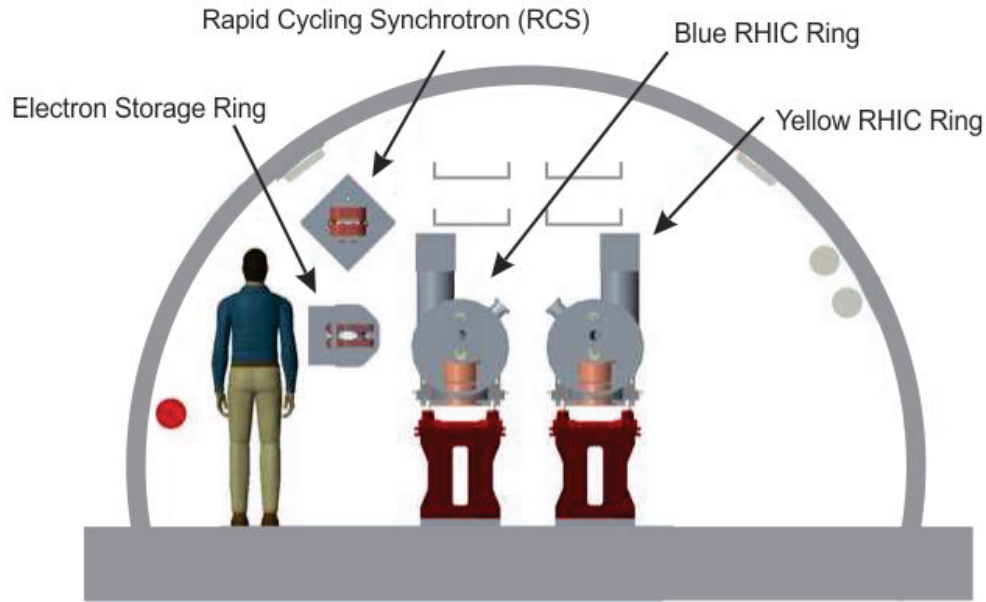


Figure 1.7: Schematic view of the location of the electron storage ring in the tunnel arcs. The Rapid Cycling Synchrotron injector is mounted above the collider ring plane.

spaces between the individual magnets are slightly different for the inner and outer arcs to account for the difference in the average bending radius. Figure 1.8 shows the layout of one arc FODO cell. At both ends of each arc, two additional FODO cells with individually powered quadrupoles are used to match the optical functions between the straights and the arc, and to suppress the dispersion in the straight sections. A missing-magnet scheme eases the dispersion matching.

The specific horizontal emittances required at different energies are realized by a combination of FODO cell phase advances in the arc, and utilizing the super-bends, while the vertical emittance is controlled by applying a vertical dispersion bump. At a beam energy of 18 GeV, the phase advance per arc FODO cell is set to 90° , while at 5 and 10 GeV it is reduced to 60° . The vertical phase advance is set to the same value in order to maximize the dynamic aperture [2]. These different phase advances require a flexible chromaticity correction scheme, based on four families for a FODO cell phase advance of 90° and 6 families for a 60° phase advance. The parameters of the beam optics of the arcs for different beam energies are shown in Table 1.3.

A large number of constraints have to be fulfilled to match the interaction region into the arcs. The small β -functions at the IP result in large β -functions in the low- β quadrupoles.

The horizontal β -functions are intentionally large at the crab cavities in order to lower the required cavity voltage. Together with the large β -functions in the final focus quadrupoles, these contribute significantly to the chromaticity. The solenoid spin rotators induce betatron coupling. This coupling is compensated by splitting each solenoid into two individual magnets with a system of five individually powered quadrupoles between them. Spin

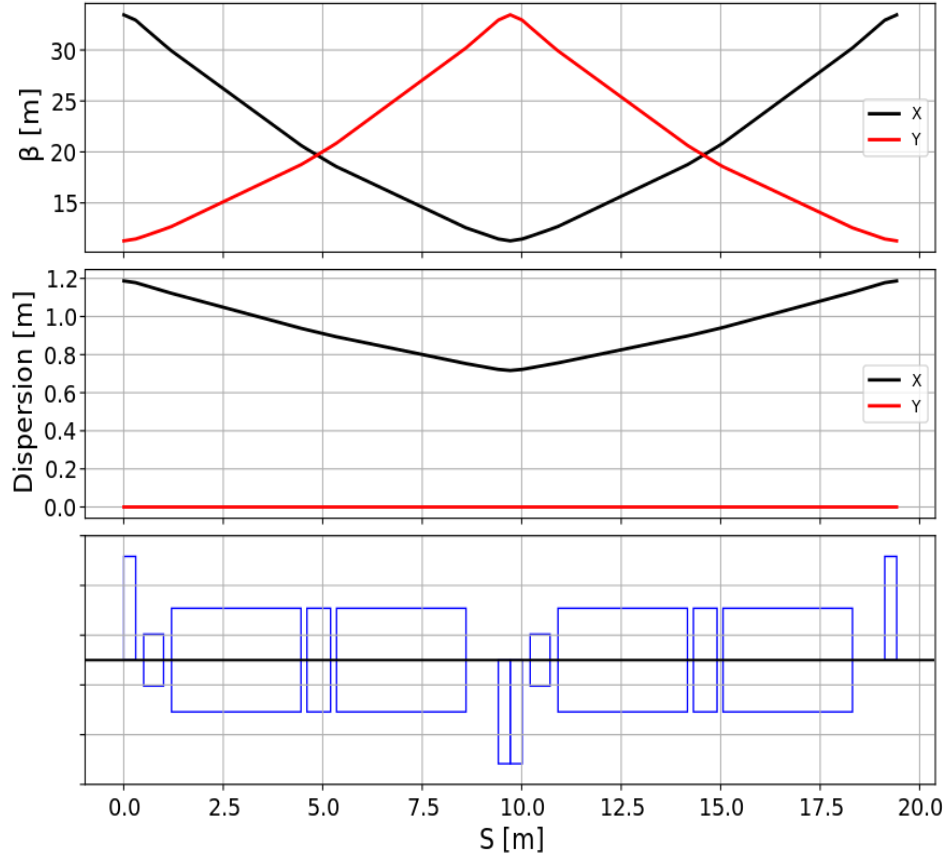


Figure 1.8: One arc FODO cell for an outer arc cell. The lengths of individual components are to scale.

matching is accomplished by adjusting the independent quadrupole circuits in the interaction region. Figure 1.6 shows the colliding straight section with the interaction region, matching section, dispersion suppressors, and spin rotators.

1.8.2 Maintaining Radiation Damping and Emittance Control for 5 GeV Electron Beams

Radiation damping allows the electron beam to have a large beam-beam tune shift. While sufficient radiation to allow a large beam-beam tune shift is produced at higher energies, simply scaling down the dipole fields for lower energies does not result in sufficient radiation damping to allow for the same large beam-beam tune shift. The radiation damping for 11 GeV still corresponds to the damping decrement $\delta = 1/(f_c \cdot \tau_{x,y})$ of KEKB, where

Table 1.3: Parameters of the electron storage ring (eSR) beam optics in the arcs for different beam energies. At the lowest energies $E_e < 10$ GeV, the short dipole in each half-cell is reversed, thus creating a super-bend. This increases radiation damping and damping decrement, provides the required beam emittances, and prevents the bunch length from becoming too short.

Parameter	5 GeV	10 GeV	18 GeV
Phase advance per cell [degrees]	60	60	90
Horizontal emittance [nm]	20	20	24
Relative energy spread [10^{-4}]	6.8	5.8	10.9
Transverse damping time [turns]	5480	4650	720
Natural chromaticity x/y	-96.2/-89.5	-96.2/-89.5	-101.2/-99.6
Momentum compaction factor [10^{-3}]	2.5	2.5	1.2
Quadrupole strength k_{QF} [m^{-2}]	0.175	0.175	0.248
Quadrupole strength k_{QD} [m^{-2}]	0.175	0.248	0.248
Hor./Vert. sextupole families/sextant	3	3	2
Arc β_x^{\max} [m]	33.4	33.4	32.9
Arc β_y^{\max} [m]	33.4	33.4	32.9
Arc maximum dispersion [m]	1.24	1.24	0.67
Quadrupole aperture requirement x/y [mm]	30/30	30/30	30/30

$\tau_{x,y}$ denotes the horizontal and vertical damping time and f_c is the revolution frequency.

The solution to this is to place three dipoles, instead of a single dipole, between the arc quadrupoles. At energies of 10 GeV and above, all three dipoles have the same field. At the lowest energy (5 GeV), the central dipole will have a higher field (0.46 T) and reversed polarity. This will increase synchrotron radiation sufficiently to reduce the transverse damping times to 50 msec which gives a damping decrement comparable to that realized in KEKB. This arrangement will also increase the beam emittance close to the 10 GeV value whereas the total synchrotron radiation power is less than half the 10 GeV value (3.2 MW). Figure 1.9 shows schematically the dipole configuration and orbits at different energies.

There are three impacts associated with this scheme:

- The orbits are different for each energy, requiring wider dipoles and a wider vacuum chamber.
- The additional drifts between dipoles reduce the dipole packing fraction, leading to additional undesirable synchrotron radiation losses at higher energies due to the higher required dipole fields.
- Higher dipole fields are required for the center dipole when operated at 5 GeV.

The parameters of the electron storage ring are summarized in Table 1.4.

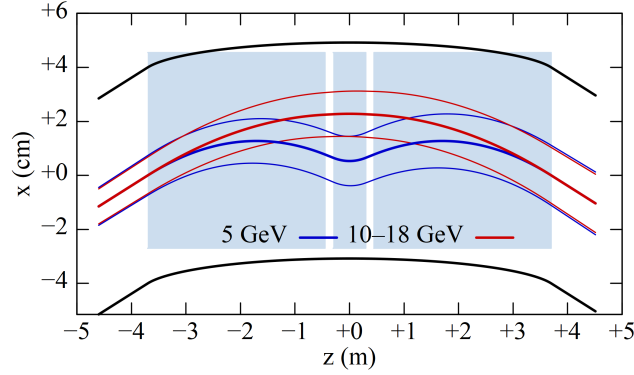


Figure 1.9: Schematic view of beam orbits and 10σ envelopes in the split dipole magnets for various beam energies.

Table 1.4: Parameters of the electron storage ring lattice.

Parameter	Value
Path length in dipoles per half-cell [m]	7.4
Bend angle [mrad]	25.5
Number of split dipoles in the entire ring	192
Drift space between split dipoles [m]	0.15
Transverse Damping decrement [10^{-4}]	1.3 - 10.6
Minimum Beam Energy [GeV]	5
Length of strong center dipole [m]	0.594
Field strength of center dipole [T] at 5 GeV, 18 GeV	-0.456, 0.248
Max. Difference between 5 GeV and 18 GeV orbits [mm]	14
Length of weak and long dipole [m]	3.253
Field strength of center dipole [T] at 5 GeV, 18 GeV	0.113, 0.248

1.8.3 Electron Spin Polarization in the Storage Ring

The collision of longitudinally polarized electrons is a key requirement of the electron-ion collider, and a large effort has been undertaken to ensure good polarization of the electron beam during collision operation. The evolution of beam polarization in electron storage rings is defined by two processes related to synchrotron radiation, namely Sokolov-Ternov self-polarization and depolarization caused by synchrotron radiation quantum emission. The self-polarization process leads to a slow buildup of electron polarization in the direction opposite to the vertical guiding field, up to a maximum level of 92.4% in an accelerator without spin rotators and with sufficiently weak spin resonances. However, the presence of spin rotators, super-bends, and strong spin resonances reduces the equilibrium polarization level. An important quantity is also the self-polarization time, which has a strong

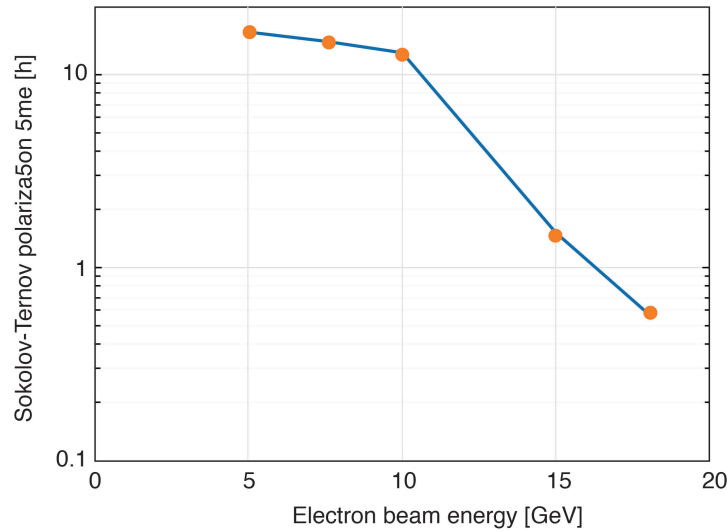


Figure 1.10: Sokolov-Ternov electron spin polarization time as a function of electron beam energy. The depolarization for spin parallel to the magnetic guide field due to the Sokolov-Ternov effect becomes important for beam energies well above 10 GeV. At 18 GeV, electron bunches with polarization in the direction of the guide field have to be replaced every six min.

dependence on the beam energy. The self-polarization time as a function of beam energy for an eRHIC storage ring placed in the present RHIC tunnel is shown in Figure 1.10. The calculation takes into account the split dipole structure which enhances the synchrotron radiation at energies below 10 GeV. Nevertheless the self-polarization time is quite long over the entire energy range, except approaching 18 GeV where it drops to about 30 minutes. This demands a full energy polarized electron injector, so that the electron beam is injected into the storage ring with high polarization ($\approx 85\%$). One benefit of the long self-polarization time is that spin patterns containing bunches of opposite polarization orientation can be efficiently used.

The HERA collider had a successful electron spin program with an electron energy of 27.5 GeV. Electrons collided with hadrons in three interaction points (one of them was a fixed target) that required three pairs of spin rotators [30]. The polarization was between 45 and 55%, limited by the slow Sokolov-Ternov time (24 min) and the low rate of reliable polarization measurements in presence of slow drifts of the closed orbit. Essential for the success of spin operations in HERA was a spin matched optics between spin rotators around each interaction point (IP). Spin matching requires a set of beam-optical conditions where the small spin rotations experienced during betatron and synchrotron oscillations due to the fields of the focusing magnets and solenoids cancel for all particles in the beam, thus zeroing spin rotations to linear order in transverse and longitudinal phase space variables. Spin matching for eRHIC includes the effects of all quadrupole, dipole, and solenoid fields (see Sections ?? and ?? for details).

Another important element of high polarization in HERA was the introduction of har-

monic orbit bumps [27] in the lattice to cancel the driving terms of spin imperfection resonances by residual dipole fields due to orbit distortions in the arc. It was also essential that the betatron tunes were chosen close to the integer resonance $Q_{x,y} = 48.08, 48.12$, as far away as possible from the half integer depolarizing resonance. The plans for high electron polarization operation in eRHIC are based on the successful HERA spin program.

The main challenge of spin dynamics in the eRHIC storage ring is to preserve the high polarization level of the injected beam, which implies that beam energies must be chosen far from spin resonance conditions. The required time scale of polarization preservation is defined by the time interval between electron bunch replacements. Depolarizing effects are dominated by spin diffusion caused by the quantum nature of synchrotron radiation emission. In the presence of synchrotron radiation related spin diffusion the equilibrium polarization is described by the Derbenev-Kondratenko formula [31]. The depolarizing time τ_{dpl} is defined by the diffusion rate of the beam energy spread and the sensitivity of the stable spin solution \vec{n} to the particle energy,

$$\frac{1}{\tau_{\text{dpl}}} \approx \frac{1}{2} \left\langle \left| \gamma \frac{\partial \vec{n}}{\partial \gamma} \right|^2 \frac{d(\delta\gamma/\gamma)}{dt} \right\rangle_{\theta} \quad (1.6)$$

where γ is the relativistic factor and the averaging inside the angle brackets is performed over the accelerator azimuth θ and over the beam phase space. The strength of depolarizing effects generally increases as E^7 , thus making it more difficult to maintain high polarization in storage rings at higher energies [32]. The accelerator technology used to achieve high polarization at high energies includes highly efficient orbit correction, beam-based alignment of beam position monitors relative to quadrupole field centers, and harmonic spin matching [32]. The control of betatron coupling is also essential to maintain high levels of polarization. These tools mitigate the effects of imperfection spin resonances and their synchrotron sidebands. In addition, the intrinsic resonances must be narrow enough to preserve high polarization, at least at energies far enough away from spin resonance conditions.

As discussed above, the eRHIC storage ring uses split dipoles to increase the damping decrement at lower energies. Such enhanced synchrotron radiation increases the spin diffusion rate. Thus, careful attention has been paid to the possibility of enhanced depolarization at lower energies.

Similarly, the effect of beam-beam interactions on polarization requires consideration. One concern is the large electron beam-beam tune spread that might effectively widen the intrinsic spin resonances. In HERA, the effect of beam-beam interactions on polarization was not critical. However, in case of positron-proton collisions, it was observed that non-colliding positron bunches had a smaller polarization in collision mode because the tunes were optimized for colliding bunches. For electron-proton collisions, the opposite effect was observed [33]. This observation, however, raises a concern for the eRHIC polarization. The beam-beam tune shift is about the same in eRHIC compared to HERA (taking the sum of the beam-beam tuneshifts from the two interaction points in HERA which is to be compared with a single collision per turn in eRHIC). Moreover, the amplitude dependent

tune shift for large amplitude particles needs to be carefully considered. This beam-beam tune spread might push a significant part of the electrons away from ideal tunes for good polarization.

The spin tracking study for eRHIC indicates that the polarization levels at 18 GeV electron beam energy in eRHIC will be at least similar to the polarization levels achieved in HERA. At lower energies, significantly higher polarization levels are expected.

Polarization tuning to eliminate imperfection resonances is expected to be easier in eRHIC than it was in HERA. A much more efficient polarimeter design and the frequent injection of fully polarized bunches is expected to speed up the tuning process by a factor 10-100 compared to HERA.

1.8.4 Electron Storage Ring Dynamic Aperture

The dynamic aperture of the electron storage ring is critical. With their maximum β -functions of ≈ 860 m a single interaction region contributes approximately 30% to the natural chromaticity. A phase advance of 90° per FODO cell is required to achieve the desired horizontal beam emittance of 20 nm for 18 GeV beam energy. At 10 GeV, where the highest luminosity is achieved, the optimum betatron phase advance in the arcs is 60° per FODO cell. The total natural chromaticity including one IR is $\xi_{x,y} \approx -100$. At 18 GeV, the interaction region contributes chromaticities of $\xi_{x,y}^{\text{IR}} \approx -30$. The dynamic aperture for on-momentum particles is maximized by using a two-family sextupole correction scheme to set the chromaticities to $\xi_{x,y} = +1$. However, the large off-momentum β -beat generated by the low- β quadrupole magnets causes a large nonlinear chromaticity that deteriorates the off-momentum dynamic aperture. The strategy to recover off-momentum dynamic aperture is two-fold:

- Achieve as much intrinsic compensation of $(\Delta\beta_{x,y}/\beta_{x,y})/(\Delta p/p)$ by optimized betatron phase advances between the sources of chromaticity. However, this is constrained by the spin matching conditions and the special phase advances between crab cavities and IP.
- Arrange the sextupoles in the arcs in families which are tuned to create an off-momentum β -beat that cancels the off-momentum β -beat from the IR, while avoiding the generation of nonlinear resonance driving terms.

In addition, sextupoles in the dispersion-free straight sections, called "geometric sextupoles," may be used to minimize residual contributions to driving terms of nonlinear resonances.

The six eRHIC arcs consist of 16 regular periodic FODO cells and have, at each end, three FODO cells for dispersion matching, which are not identical to the regular cells. For the 60° optics for a beam energy of 10 GeV, a scheme with a structure of 32 sextupole magnets (16 horizontally focusing and 16 vertically focusing ones) per arc is applied. They are powered in three horizontal and three vertical families, labeled by $A_{h,v}$, $B_{h,v}$, and $C_{h,v}$. Vertically

focusing sextupoles are interleaved with the horizontal ones; the scheme is the same. Sextupoles belonging to the same family are always spaced by 180° . This implies that driving terms for off-momentum β -beat accumulate over the sextupoles of the same family and thereby maximize the potential for compensation of the β -beat from the IR. The contributions to nonlinear driving terms from sextupoles of the same family, however, cancel, so that non-linear effects are only created in higher order. Since the β -wave generated in the IR arrives at each arc with a different phase, the sextupole families need to be re-optimized in each individual arc.

This scheme produces an on-momentum dynamic aperture of $\pm 22\sigma_x$ and provides a momentum aperture of $12\sigma_p$. These values are believed to provide sufficient margin to accommodate magnetic imperfections and effects of misalignment. An additional margin is provided by non-chromatic sextupoles in the straight section, which have not yet been optimized. Figure 1.11 shows the dynamic aperture for different values of the relative momentum offset $\Delta p/p$ in the (x, y) plane.

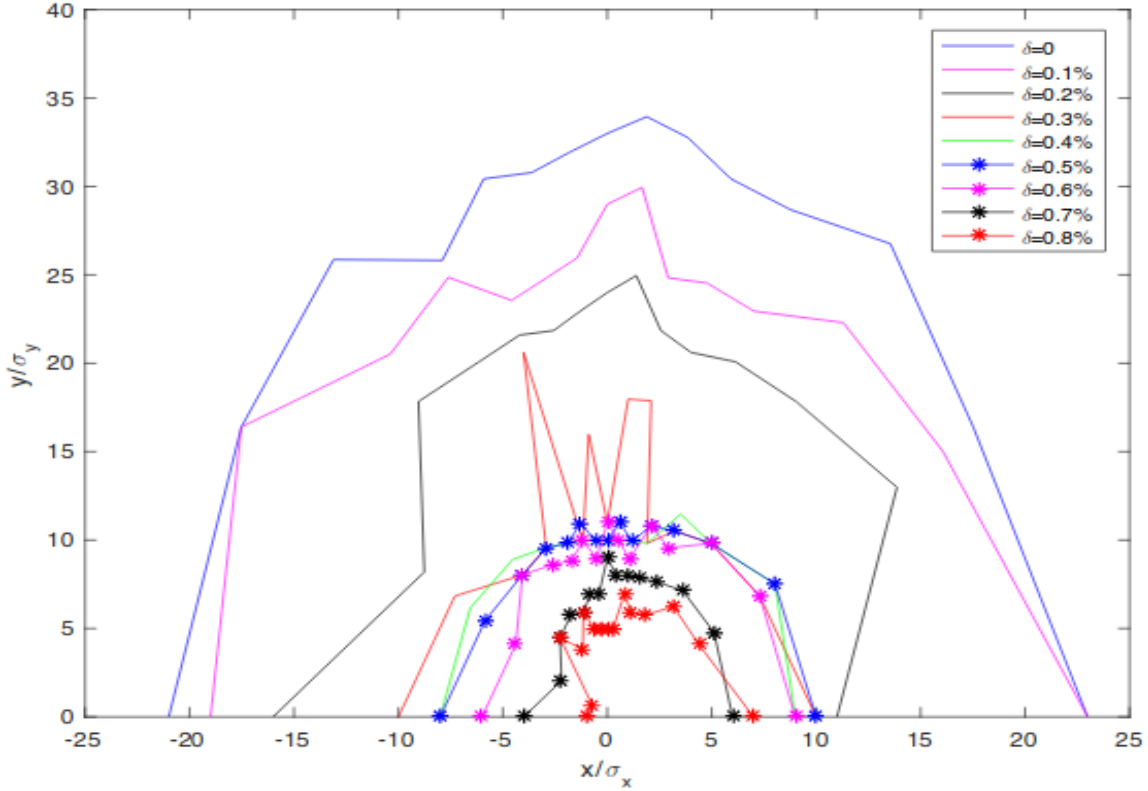


Figure 1.11: Dynamic aperture in the (x, y) plane for different values of the momentum offset $\Delta p/p$.

The beam optics for 18 GeV with a phase advance of 90° requires a different strategy. With a phase advance of 90° , two sextupoles in neighboring cells (horizontally focusing or vertically focusing, respectively) will generate an off-momentum β -beat if the two strengths are different. Sextupoles in successive pairs with the same strengths will add to this β -beat.

However, there is no control over the phase of that β -beat. For this reason, the phase of the beat which comes from the IR needs to arrive with the correct phase at the first sextupole in the regular arc.

The betatron phase needs to be optimized between the six arcs in order to enable all sextupoles for correction of second order chromaticity. Alternatively, one can arrange that the first arc corrects only the cosine-like part of the β -beat and the next arc which would be spaced by a horizontal and vertical betatron phase difference from the first arc of $(2k + 1)\pi/4$ (k integer) to correct the sine-like component of the β -beat (phase referring always to the first regular sextupole in the arc adjacent to the IR). The 18 GeV lattice is not fully optimized yet and is not further discussed. In case of unexpected difficulties, it will be possible to run with a 60° lattice at this energy which would result in some luminosity loss.

1.8.5 Collective Effects in the eRHIC Electron Storage Ring

We have considered coherent instabilities, intrabeam scattering, and Touschek scattering. Emittance growth times due to intrabeam scattering in the electron storage ring are of order minutes, much longer than the 50 msec radiation damping times. Touschek lifetimes are hours —much longer than the bunch replacement time required to compensate polarization loss. Coherent instabilities in the electron ring have been studied using a modified version of TRANFT [34], which was used during the design of NSLS-II. The code has evolved to simulate both single bunch and coupled bunch instabilities by tracking typically five bunches and assuming a uniform fill pattern. This allows one to use a few times 10^5 simulation particles per bunch when doing coupled bunch calculations.

Table 1.5: Electron Beam Parameters for $|Z/n| = 0.1 \Omega$. A uniform fill of 630 bunches was assumed for coupled bunch effects.

Parameter	5 GeV	10 GeV	18 GeV
RF voltage ($h = 7560$) [MV]	12	24	68
γ_t	31	31	41
V_{synch} [MV]	1.3	3.6	38
N_e [10^{10}]	26	42	40
$\sigma(p)/p$ ($Z/n=0$) [10^{-4}]	6.8	5.5	10.9
$\sigma(p)/p$ ($Z/n=0.1$) [10^{-4}]	7.5	5.6	10.9
σ_s ($Z/n=0.1$) [mm]	9.6	7.5	8.7

Simulations were done for 5, 10, and 18 GeV, and the results are summarized in Table 1.5. The code tracks three dimensions but the longitudinal and a single transverse dimension are subjected to wake forces. The other transverse dimension is included so that the beam beam force has the right distribution. The calculation includes the short range re-

sistive wall wake scaled from NSLS-II, coherent synchrotron radiation, and narrow band impedances. The dominant narrow band transverse impedance is from resistive wall and was modeled as a low frequency resonator. The main longitudinal HOM is from the RF cavities.

The beam-beam force was sufficient to damp transverse coupled bunch modes, and a longitudinal damper with a gain of $Im(Q_s) = .001$ was able to suppress the coupled bunch longitudinal oscillations. It is envisioned that one would use a transverse pickup in a dispersive region with closed orbit subtraction and a filter to notch out the betatron oscillations. The beam-beam parameter was set to 0.1 initially but values as low as 0.075 were found sufficient to stabilize the electrons.

After dealing with the longitudinal coupled bunch modes the threshold intensity was set by the resistive wall instability. The beam parameters in Table 1.5 are stable against resistive wall and no third harmonic RF system was used. The momentum spreads and bunch lengths listed in the last two lines include some small impedance induced spread but the momentum spread is only slightly larger than the $Z/n = 0$ result.

The ion instability has been studied as well. A computer code has been written and, as with impedance driven instabilities, the beam-beam force is the dominant transverse damping mechanism. The code is still being benchmarked against analytic estimates, Elegant and data but we are confident the results fairly good. We find that H2 is not a problem for any reasonable pressure. For carbon monoxide we found maximum partial pressures. For 20 ns bunch spacing with 599, 55 nC electron bunches, a partial pressure of 0.31 nTorr was stable. For 10 ns bunch spacing with 1160, 28 nC electron bunches, a partial pressure of 0.12 nTorr was stable. We note that these are averaged over the electron storage ring, and not peak values. This appears challenging, but reasonable.

1.9 Hadron Ring Design

1.9.1 Lattice Design

The present RHIC and its injector complex remain, for the most part, unchanged when becoming a part of eRHIC. In particular, the arcs with their superconducting magnet structure will remain the same as the present RHIC. Some modifications are necessary or desirable. eRHIC hadrons will circulate in the “Yellow” ring while the “Blue” ring will remain in place as well. The sextant between IR6 and IR4 of the Blue ring will serve as a transfer line and the beam will be injected in IR4. New injection kickers with faster risetime will be placed in IR4. Some modification of the RF system is necessary to accommodate the 290 bunches at injection and to accomplish the splitting into 1160 bunches. Space for more RF cavities will be provided in IR4 and IR10. The non-colliding straight sections (utility straights) will be simplified by removing the DX magnets⁵, in order to simplify the

⁵DX separator dipoles on each side of each IP put the two hadron beams of present RHIC onto the common head-on collision orbits. The D0 dipoles at the entrance of the quadrupole triplets put the two RHIC beams

geometry and provide space for the electron ring crossover from inner to outer arcs and vice versa. Studies are underway to investigate whether the D0 magnets can be removed as well. The sextant between IR2 and IR12 of the Blue ring will be used to circulate low energy hadrons at 41 GeV which then have the same revolution time as electrons, despite their reduced velocity.

1.9.2 Keeping the Hadron Revolution Frequency Constant for All Beam Energies

Proton and ion beams are not ultra-relativistic in the energy range of an electron-ion collider. In eRHIC, the proton beam energy is chosen to vary between 41 GeV and 275 GeV. If the beam orbit was the same, the revolution time would vary by 3.3 nsec between these two beam energies. In order to maintain synchronization with the ultra-relativistic electrons, the hadron orbit will be shortened by up to 94 cm for the lowest hadron energies (41 GeV).

This is accomplished in the following way:

The hadrons circulate counterclockwise in the Yellow ring. In the arc between IR2 and IR12, the high energy beam (in the 100 to 275 GeV energy range) travels in the outer arc (part of the Yellow ring), while the 41 GeV beam passes through the inner arc (part of the Blue ring). The inner and outer arc radii differ by 88 cm, and an inner sextant is 94.2 cm shorter than an outer one. This path length difference allows for synchronizing 41 GeV hadron beams with the electrons. For energies of 100 GeV and higher, the outer arc between IR2 and IR12 is used. If the beam passes through the quadrupole centers, a proton beam of 133 GeV would be synchronized with the electron beam. For the beam energies 275 GeV and 100 GeV the synchronization is accomplished by +14 mm and -14 mm radial shifts, correspondingly, which is well within the acceptance of the 80 mm diameter vacuum chamber. A 41 GeV, proton beam is synchronized by using the inner arc between IR2 and IR12.

The corresponding modifications to the RHIC lattice are only relatively minor. This requires some rearrangement of the bus system. The “Blue” ring sextants used for injection and low energy running must be powered with reversed polarity. The superconducting magnets of RHIC are protected by cold diodes which in principle must be reversed. However, an analysis shows that at less than 20% of maximum magnet excitation, this protection is not required. Thus modification of the RHIC lattice and magnet system for eRHIC are fully reversible and are accomplished with relatively little effort.

1.9.3 Hadron Ring Dynamic Aperture

The strong focusing of the hadrons at the collision point causes maximum β -functions in the low- β quadrupoles of $\beta_x = 700$ m and $\beta_y = 2000$ m. The contribution to the natural chromaticity generated in one IR amounts to $\xi_x = -30$ and $\xi_y = -40$, which is 20%

on near-parallel orbits.

of the contributions from the arcs. This implies a large contribution of the chromaticity generated in the interaction region that must be compensated by sextupoles in the arcs in order to confine the tune footprint of the hadron beam to remain within the space between nonlinear resonance lines. As discussed above, the strength of these resonances is enhanced by the nonlinear field, and the resonance-free space in the tune diagram shrinks. As addressed before, there is a maximum amount of IR chromaticity and corresponding tune footprint which can be accepted. This chromaticity limit is determined by numerical particle tracking to verify that the dynamic aperture is sufficiently large. The numerical simulations also include the impact of field errors of the superconducting magnets, the magnets in the interaction regions, and imperfections such as magnet misalignment.

The dynamic aperture is defined as the maximum betatron amplitude at which particles are stable over a given number of turns. The long-term dynamic aperture converges to the boundary between regular and chaotic motion. Experience with RHIC operations indicates that relevant dynamic aperture simulations require tracking over 10^6 turns. The stability of a particle is assessed by the analysis of the trajectories over 10^6 turns, which allows one to characterize a trajectory as stable or unstable.

The results of such simulations show that the dynamic aperture of the eRHIC hadron ring amounts to 10σ at injection and 6σ at high luminosity operation. The simulation includes the beam-beam effect in weak-strong approximation. These are the same values as obtained for present RHIC.

1.9.4 Electron Cloud Effects

Electron clouds are a serious concern for the ion ring with 1160 bunches and 0.6×10^{11} particles per bunch. Electrons produced in the beam vacuum chamber by ionization of the residual gas by the beam may get accelerated by the following bunches and hit the vacuum chamber wall, thereby releasing more electrons from the wall. This mechanism can create an electron avalanche that builds up rapidly as the bunch train passes by. The consequences include high cryogenic losses and beam instabilities. Next to beam current and bunch parameters, the key parameter that determines the seriousness of the electron cloud effect is the secondary emission yield (SEY, number of emitted electrons from the surface per incident electron) of the vacuum chamber material. We assume that the stainless steel beam pipe of RHIC will be coated with copper and that we will be able to improve the secondary emission coefficient by scrubbing the surface by beam operation to the level achieved in the LHC [35]. An initial simulation using the computer code CSEC [36] and a model for the wall parameters in the scrubbed LHC showed dangerous electron clouds both for the LHC and for eRHIC, with LHC being slightly worse. Due to lack of a liner, eRHIC requires a stronger suppression of the electron cloud mechanism than LHC in order to keep the cryogenic load within tolerable limits of $P_{\text{load}} \leq 1 \text{ W/m}$. This is planned to be achieved by an additional layer of coating consisting of amorphous carbon. For electron clouds we are collaborating with CERN in understanding and reproducing their results. In the end we know that electron clouds in the LHC are difficult but tractable. There is currently no reason to believe otherwise for eRHIC.

1.9.5 Intra-beam Scattering

The effect of multiple Coulomb scattering of charged particles off each other inside a bunched beam, taking into account the Lorentz boost, is known as Intra-Beam Scattering (IBS) [13]. This causes emittance growth in all oscillation planes of the beam. This effect limits the high beam density needed for high luminosities, and it affects the luminosity lifetime and the average luminosity. Beam parameters must be chosen to achieve an IBS growth time of several hours given the beam setup time of typically one hour, unless the emittance growth can be overcome by strong active cooling of the beam. Table 1.6 lists the beam parameters and calculated IBS growth times for the eRHIC design parameters of protons at 41 GeV, 100 GeV, and 275 GeV.

Table 1.6: eRHIC proton beam parameters.

Parameter	41 GeV	100 GeV	275 GeV
Bunch intensity [10^{10}]	2.6	6.9	6.9
RMS Horizontal normalized emittance [mm mrad]	1.9	4.0	2.8
RMS Vertical normalized emittance [mm mrad]	0.45	0.22	0.45
Longitudinal bunch area [eV sec]	0.2	0.4	0.7
RF frequency [MHz]	197	591	591
RF voltage [MV]	10.5	16.1	28
RMS momentum spread [10^{-4}]	10.4	9.0	6.6
RMS bunch length [cm]	7.5	7	6
Longitudinal emittance IBS growth time [hours]	3.8	2.	3.4
Horizontal emittance IBS growth time [hours] (without coupling)	3.4	2.3	2.0

For the high luminosity parameters as listed in Table 1.6, beam growth due to IBS is significant, and strong cooling is required to maintain the beam density and the luminosity over a reasonable store time of at least several hours. These parameters are based on reuse of the existing 197 MHz RHIC RF system, and the addition of a new 591 MHz RF system for the hadron ring. The results are based on complete decoupling of horizontal and vertical betatron motion. This is also essential to maintain unequal emittances in the horizontal and vertical plane. Very good vertical orbit control is also mandatory to avoid any significant vertical dispersion. With strongly suppressed vertical dispersion, there will be no significant emittance growth due to IBS in the vertical plane.

1.9.6 Hadron Ring Strong Beam Cooling

Highest luminosity in an electron-ion collider can only be achieved by introducing a strong beam cooling mechanism that counteracts IBS, which would otherwise cause a rapid increase of emittance and reduction of luminosity. Moreover, the hadrons that gained large transverse and longitudinal amplitudes by IBS experience a strong nonlinear beam-beam force imposed by the electron beam that would enhance halo formation and experimental backgrounds. Thus, with the parameters required for high luminosity, the hadron beam would quickly become unusable without cooling and would have to be replaced frequently. As the turn-around time of superconducting RHIC is about one hour due to the magnetic cycle of the RHIC main magnets and spin rotators and the filling time at injection, the increase of peak luminosity above a certain level of performance would lead to a reduction of average luminosity.

The eRHIC High Luminosity parameters (see Tables 1.1 and 1.6) were selected to have an IBS growth time $\varepsilon / (d\varepsilon/dt)$ of no less than two hours in order to ease the requirements on the hadron cooler.

Stochastic cooling is a well established cooling mechanism for hadrons that was pioneered at RHIC for bunched ion beams. It is used very successfully for cooling of gold beams in RHIC operations and has enhanced the luminosity significantly. It would work, in principle, for protons at high energies, but the cooling rates at typical intensities of eRHIC proton bunches fall short of the need by orders of magnitude because of bandwidth limitations of beam pick-up and kicker magnets.

Electron cooling with a DC electron beam is a standard cooling mechanism for hadron beams that works well at low hadron energies up to a few GeV. For large hadron energies of multi-GeV, however, this cooling method becomes quite weak as the cooling time scales strongly with the beam energy as $\gamma^{5/2}$, with γ being the relativistic factor of the hadrons. Furthermore, the electrons have to have the same relativistic factor as the hadrons and DC electron energies of tens of MeV are not available. Using bunched electron beams accelerated by an RF LINAC would mitigate this. However, the cooling of 275 GeV hadron beams is still extremely challenging with incoherent electron cooling and the effort in cooling installation becomes unrealistically large because of large required electron beam currents on the order of amperes.

For this reason we need to consider more advanced approaches for strong hadron cooling. A novel method of hadron cooling that promises to work at very high hadron beam energies has been proposed [22]. This method, which is called “coherent electron cooling”, uses an electron beam to pick up the longitudinal Schottky noise of the hadron beam, and subsequently amplifies the signal by sending the electron beam through a free electron laser. The strongly micro-bunched electron beam is then merged with the hadron beam with proper timing. The electron beam then acts as a kicker to reduce the energy spread of the hadron beam. Recently, a variant of this method has been proposed, which achieves the micro-bunching by sending the beam through a chicane or a series of chicanes with optimized R_{56} [37]. This method has limited amplification of the signal but reaches extremely large bandwidth. A proof-of-principle experiment on a low energy RHIC ion beam is un-

derway that aims at demonstrating coherent electron cooling with FEL amplification [14].

Figure 1.12 shows the layout of the proposed coherent electron cooling system for eRHIC, designed to support the storage of hadron beams required for luminosities in the range of $10^{34} \text{ cm}^{-2} \text{ sec}^{-1}$. An electron beam generated by a superconducting RF gun is injected into an energy-recovery superconducting LINAC that provides an energy gain of 150 MeV. The fully accelerated electron beam of 150 MeV is injected onto an orbit that overlaps with the orbit of the eRHIC hadron beam in the straight section of IR2 over a distance of 50 m, which is called the “modulator section”. After this first common section, the hadron beam propagates through a section with an appropriately tuned $R_{56} = \lambda_{\text{FEL}} / (\Delta p/p)_{\text{RMS}}$ to separate particles with positive and negative energy deviation by a longitudinal distance corresponding to the width of the micro-bunch peak of the electron beam. The hadron beam path length is increased by a chicane which extends over a large fraction of the straight section.

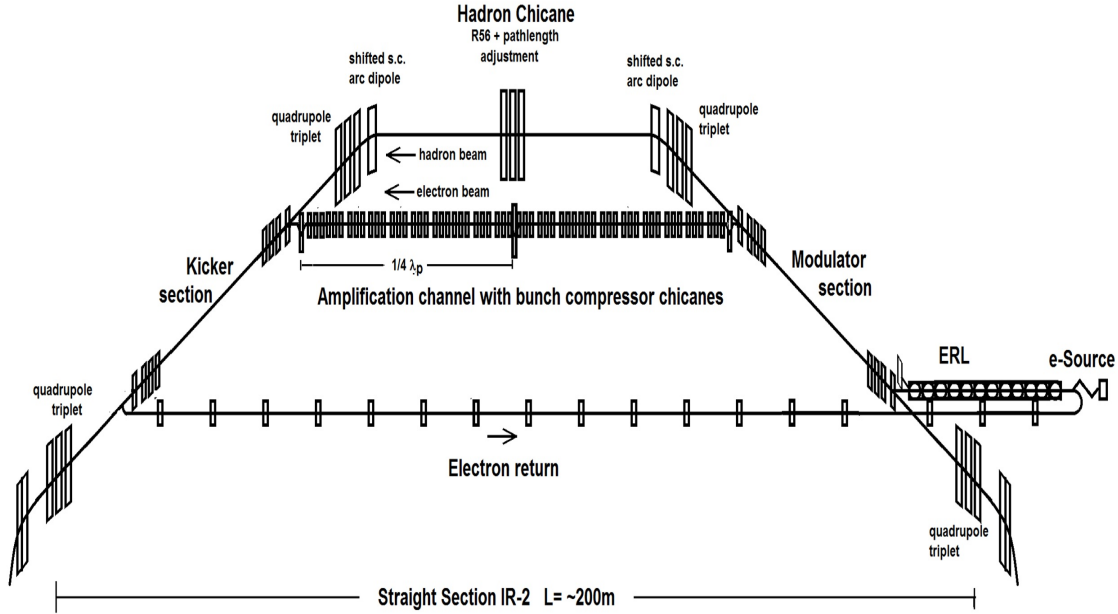


Figure 1.12: Schematic of the layout of the eRHIC strong hadron cooling facility. Note that the vertical scale has been stretched by a factor of $\simeq 50$.

The electron beam is energy-modulated, due to residual fluctuating space charge forces from the hadron beam. The electron beam passes then through an isochronous chicane where the energy modulation, caused by the hadron beam density fluctuation, is transformed into a micro-bunching of the electron beam. The density modulation of the electron beam is then amplified by a mechanism exploiting plasma oscillations: After one quarter plasma oscillation wavelength, the density modulation is transformed into a, now, even larger energy modulation, which, after a second chicane, is turned into a stronger den-

sity modulation. The present stage of the development proposes two amplification stages to produce a sufficiently strong electron density modulation. The electron beam is again launched onto the hadron orbit, thereby overlapping with the hadron beam with carefully adjusted phase. Hadrons with higher energy will be ahead of the electron micro-bunch and will be decelerated. Hadrons with lower energy will trail behind the electron micro-bunch and will be accelerated. The energy spread of the hadrons will thus be reduced after this “kicker” section. Cooling times of ≈ 1 h are envisioned. Table 1.7 summarizes the parameters of eRHIC coherent cooling.

Table 1.7: Parameters of the eRHIC coherent electron cooling.

Parameter	Value
Hadron energy range [GeV]	41-275
Electron beam energy [MeV]	22-150
Electron beam current [mA]	100
Electron charge per bunch [nC]	1
1st R_{56} [m]	2.4
2nd R_{56} [m]	2.4
3rd R_{56} [m]	2.4
Plasma amplification stages	2
Length of the modulator section [m]	40
Length of the kicker section [m]	40
Cooling time [h]	≈ 0.25

1.10 Electron Injection Complex

1.10.1 General Considerations

The requirements on the electron injector complex are driven by the need for polarized electrons in electron-ion collisions. The electron polarization should be close to 80%. To suppress systematic errors of the detectors it is necessary to have two electron spin polarization directions simultaneously present in the same store.

In principle, electron polarization in a storage ring builds up by the Sokolov-Ternov effect: Spin flips are induced in the process of emitting synchrotron light photons. Spin flips from spin that is parallel to the magnetic dipole field to spin that is antiparallel when emitting photons are slightly more likely than the opposite spin flip. The differential flip rate leads to a slow buildup of polarization antiparallel to the magnetic dipole field. Unfortunately, the polarization build-up time is much too slow to be of practical use at eRHIC electron energies.

Consequently, the spin polarization for eRHIC electron beams must be produced at the source and must be preserved during the acceleration process.

The bunches that are polarized parallel to the magnetic guide field are subject to slow depolarization by the Sokolov-Ternov effect in the storage ring. At 18 GeV operation, a bunch replacement rate of once per six min for each individual bunch in the storage ring is required to keep the time-averaged level of polarization at a level of $\approx 70\%$, assuming an initial polarization of the freshly injected bunches of 85% . Thus the injector has to provide a new bunch about every second to maintain good polarization of all 290 bunches. At 10 GeV and 5 GeV, the depolarization time is much longer and the bunch replacement rate can be reduced by a factor of at least five.

The RCS injector will deliver electron bunches which are 85% spin polarized at beam energies up to 18 GeV. In the storage ring the highest bunch charge of 27.5 nC is required for operation at 10 GeV and below. For 18 GeV operation a bunch charge of 11.7 nC is more than sufficient. In order to reach the storage ring bunch intensity of 27.5 nC at 10 GeV five 5.5 GeV bunches from the injector need to be accumulated in one storage ring bucket. Thus, at maximum the injector has to deliver 12 nC at a 1 Hz rate. These bunch charge and rate requirements are sufficient for operation at all energies with and without hadron cooling, as shown in Table 1.8.

Table 1.8: Requirements for the electron injector.

Parameter	5 GeV	10 GeV	18 GeV
Ext. E_k from source ($\gamma = 1.27$) [keV]		350	
LINAC energy gain [MeV]		400	
Normalized electron emittance after LINAC [μm]	20	20	55
Emittances at RCS extraction $\varepsilon_x/\varepsilon_y$ [nm]	20/2	20/1.2	24/2
Bunch charge in storage ring [nC]	27.5	27.5	11.7
Number of bunches in storage ring	1160	1160	290
Bunch charge in source and RCS [nC]	5.5	5.5	11.7
Repetition rate [Hz]		2	
Bunch replacement period [min]	48.5	48.5	2.4
Bunch replacement period (polar. req.) [min]	70	59	3.1

The electron injection complex consists of the following elements:

- Electron gun with a Ga-As photo-cathode.
- Low energy transfer line (0.4 MeV).
- Electron S-band LINAC (400 MeV).

- Medium energy transfer line (400 MeV).
- Rapid Cycling Synchrotron (0.4 to 18 GeV) in the RHIC tunnel.
- High energy transfer line (up to 18 GeV).

1.10.2 Polarized Electron Source

The requirement for the polarized eRHIC source is a charge of 3 to 12 nC of 85% polarized electrons at a rate of 2 Hz and a normalized transverse emittance of 10 to 55 μm . This requirement satisfies the needs for all operation modes of the storage ring.

Polarized electron beams are obtained from special photo-cathodes. The most common material which has been used successfully in the last 30 years is Ga-As alloy. Strained Ga-As cathodes which are irradiated with UV laser light of 780 nm yield high polarization of the extracted electron beam and a high quantum efficiency ($QE \geq 1\%$) when coated with a mono-layer of Cs.

The polarized electron gun of the Stanford Linear Collider (SLC) which was developed in the 1980s provided a reliable performance delivering up to 20 nC [38] of polarized electrons (70 to 75% polarization) at 120 Hz repetition rate. In principle, the eRHIC injector could be based on the SLC gun. However, to exploit the technical development which has occurred in the last three decades, a dedicated eRHIC gun is being developed which promises higher beam energy, longer cathode lifetime, higher reliability, and larger polarization ($\geq 80\%$). A comparison of gun parameters is shown in Table 1.9.

Table 1.9: Electron source parameters.

Project	RF Frequency [GHz]	σ_s [psec]	Bunch Charge [nC]	Energy [MeV]	Emittance [μm]	$\Delta\gamma/\gamma$ [%]	Cathode Material
SLC 5 mJ, 845 nm Laser	DC	2000	9 ... 16	0.12	15	1.5	Ga-As
eRHIC 5 mJ, 780 nm Laser	DC	2000	3 ... 12	0.35	10 ... 55	2	Ga-As super lattice

A new gun geometry based on the “inverted gun” scheme has been designed. The design is optimized for a high extraction voltage of 350 keV and low electron beam loss. For good cathode lifetime and high reliability, excellent vacuum conditions are needed in the gun, the extraction line, and the tune-up beam dump. A prototype of this beam line has been built and tested. A load lock system for installation of prepared and activated cathodes into the gun has been designed. A prototype of this system is available and has been tested.

1.10.3 Rapid Cycling Synchrotron

Full energy injection of polarized electron bunches is accomplished by a Rapid Cycling Synchrotron (RCS) in the RHIC tunnel which accelerates the electrons from the 400 MeV LINAC to up to 18 GeV for injection into the storage ring. The synchrotron has a repetition rate of up to 2 Hz and a total ramping time of 100 msec. The most important design feature of the synchrotron is spin transparency - the preservation of spin polarization during acceleration - up to the full energy of 18 GeV. This is accomplished by enforcing a high lattice periodicity P . The RHIC tunnel, however, only allows a lattice symmetry of six as it is composed of six arcs separated by six straight sections. This lattice design overcomes this constraint by configuring the straight section beam optics such that the transformation of beam coordinates through the straight section is an identity transformation. This also includes the electron spin. In order to suppress intrinsic depolarizing resonances, the periodicity P and the vertical betatron tune $Q_{y,\text{arc}}$, calculated by accounting for betatron phase advance in the arcs only, must fulfill the conditions:

$$P - Q_{y,\text{arc}} > a\gamma \quad (1.7)$$

and

$$Q_{y,\text{arc}} > a\gamma \quad (1.8)$$

where $a\gamma = 40.849$ is the spin tune with $a = 1.16 \times 10^{-3}$ being the anomalous magnetic moment of the electrons. This leads to the choice of $Q_{y,\text{arc}} \approx 50$ and $P = 96$, which is readily accomplished given the large arcs of RHIC. The lattice in the arcs is thus composed of 6×32 FODO cells with a betatron phase advance of $\pi/2$. A super-period consists of two FODO cells as there are two sextupole families per plane to compensate linear and nonlinear chromaticity. A special feature of one of the straight sections is that the rapid cycling synchrotron must pass around the colliding beam detector with a spin transparent chicane. At the peak energy of 18 GeV, the electrons suffer from an energy loss of 36 MeV/turn due to synchrotron radiation. The acceleration and radiation loss compensation is done by 5-cell superconducting 591 MHz RF cavities.

The synchrotron accelerates single bunches with a charge of 10 nC. With this amount of bunch charge, the electron beam remains below any collective instability threshold.

The concept of spin transparent acceleration was extensively simulated. The amount of depolarization during the acceleration was found to be only in the order of two percent. These simulations take into account an imperfect machine lattice. In order to obtain realistic estimates on the preservation of electron spin polarization, imperfections of quadrupole fields, typical betatron coupling, misalignment, and closed orbit errors, as well as sextupole fields for chromaticity corrections, have been introduced in the machine model.

Correction algorithms have been applied to adjust correction elements such as dipole correctors, tune correction quadrupoles, and skew quadrupoles. It is assumed that closed orbit excursions can be kept below 0.5 mm. It is further assumed that the betatron tunes during the ramp are kept within $|\Delta Q| \leq 0.01$ by applying tune feedback or pre-programmed time-dependent tune corrections. With this realistic machine model, simulations show

that the polarization is robust and resilient against residual imperfections (see Figure 1.13). These good polarization results are consistently obtained for a number of statistical error seeds.

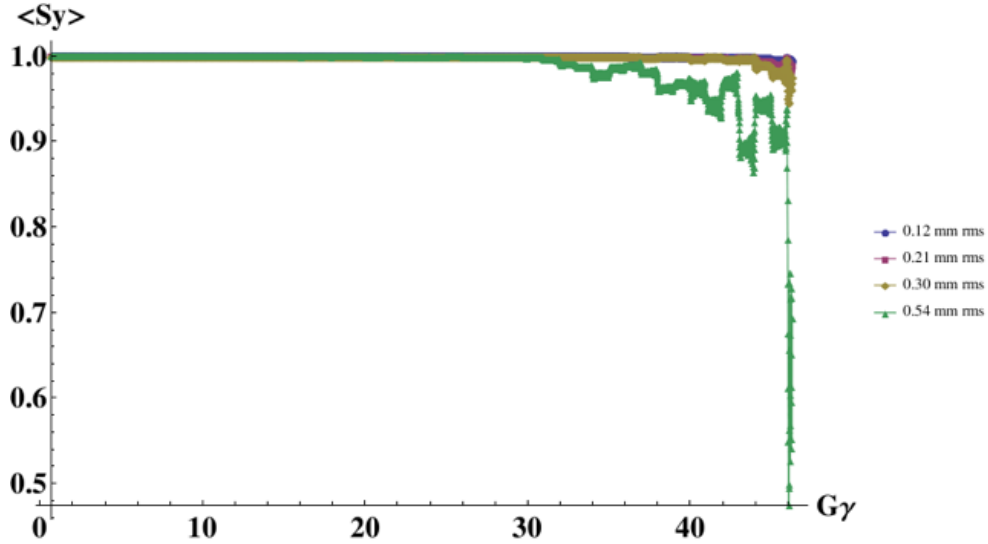


Figure 1.13: Electron spin polarization in the Rapid Cycling Synchrotron as a function of beam energy expressed in terms of spin tune $a\gamma$ during the ramp. Different colored curves indicate different RMS values of residual orbit distortions. Note the suppressed zero of the vertical scale.

1.10.4 Electron Injection

The requirement of arbitrary spin patterns in the electron ring coupled with radiative polarization necessitates regular bunch replacement. At an electron beam energy of 18 GeV, we plan to replace electron bunches on average every three minutes. With 290 bunches, this corresponds to half a second between injections. The electron injection is accomplished by a combination of fast and slow kickers and a pulsed eddy current injection septum in the horizontal plane.

The slow kickers form a closed two-bump. The first sine half-wave is used to extract a bunch with depleted polarization to create an empty bucket for the fresh bunch. It kicks a large fraction of the stored beam to transverse amplitudes close to the extraction septum. A fast kicker magnet, right next to the first slow bump kicker only kicks the bunch that will be extracted and is going to be replaced by a fresh, injected bunch. The additional kick allows the selected bunch to enter the extraction septum.

The second sine half-wave is for injection. The storage ring beam optics has a dispersion at the injection septum where the second slow bump has its maximum spatial excursion. The new bunch is extracted from the RCS with a slight energy offset with respect to the energy of the circulating beam in the storage ring. The energy offset times the dispersion equals

the distance of the bunch to be injected from the orbit of the circulating beam. This scheme results in injection without a transverse oscillation, but with a longitudinal oscillation. The offset of the injected beam, with respect to the closed orbit vanishes at locations where the dispersion is zero, which is, in particular, the case in the IR. The longitudinal injection oscillation will be eventually removed by radiation damping. The scheme is illustrated in Figure 1.14. We plan to replace each bunch that is kicked off this way in five steps of 5.5 nC each, thus accumulating in the longitudinal phase space.

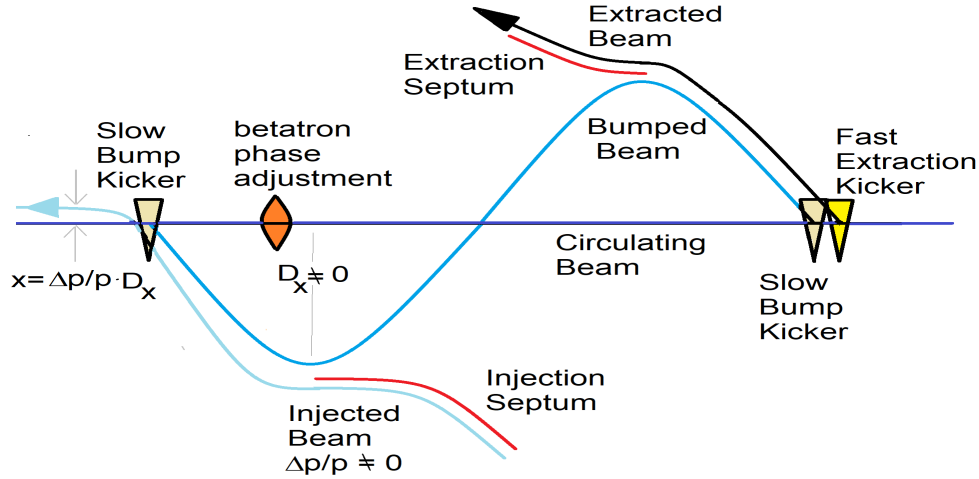


Figure 1.14: Electron injection and extraction scheme, based on one slow 360° kicker bump. The first sine half-wave is for extraction (right-hand side) and the second one for injection (left-hand side) which bring the stored beam within three horizontal RMS beam sizes ($\sigma_{\text{RMS}} = \sqrt{\epsilon_x \beta_x + D_x^2 \sigma_e^2}$) to the injection and extraction septum, respectively. The bumps rise in $13 \mu\text{sec}$ (one turn) and return to zero during the following $13 \mu\text{sec}$. The dispersion at the injection septum is non-zero. The beam to be injected has a slightly different energy than the stored beam and the distance between the center of the stored beam and the beam to be injected equals the dispersion times the relative energy difference between stored and injected beam. This way the beam is injected in the center of horizontal phase space but off-center in the longitudinal phase space. For extraction, a fast kick is required on top of the slow bump to kick the beam into the extraction septum.

1.11 Hardware Systems of the eRHIC

By far, the largest fraction of present-day RHIC will remain unchanged for eRHIC. There are only very few technical components of the hadron storage ring that need some upgrade for eRHIC operation. These will be discussed in the following sections. Much of the hardware of the new additional electron rings is based on well known accelerator technologies such as room temperature magnets and magnet power supplies. Established electron beam instrumentation technology can be carried over to eRHIC as well. Innovation is limited to

critical systems such as RF systems, vacuum systems and IR magnets. Only these critical subsystems will be described in the following sections.

The total power consumption of the the electron storage ring magnet system is a significant fraction of the increased operational power needs for eRHIC as compared to RHIC. Figure 1.15 shows the power consumption of eRHIC magnet systems.

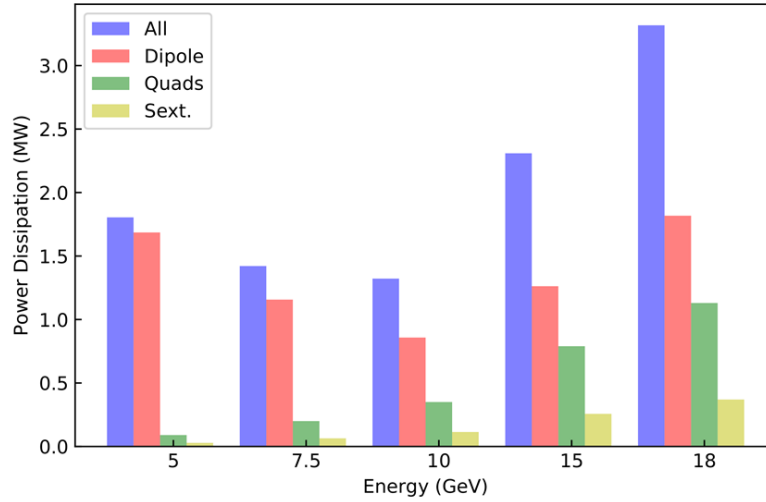


Figure 1.15: Power dissipation of storage ring magnets for operation energies 5 GeV to 18 GeV.

1.11.1 Hadron RF Systems

Hadron bunches extracted from the AGS will be received by the existing RF capture and acceleration system, modified from its RHIC operational frequency of 28 MHz to 24.6 MHz for eRHIC. Bunch train formation for maximum luminosity operation requires adiabatic splitting of the hadron bunches into four bunches via a two-stage bunch splitting scheme. This requires new normal conducting bunch splitting cavities, two each at 49.3 MHz and 98.5 MHz.

The existing RHIC 197 MHz system will be used to further compress the bunches before they can be accepted and compressed to the final store bunch length in a 591 MHz storage cavity system. The 591 MHz RF system will be superconducting, employing cryomodules identical to the RCS 591 MHz RF system. Two 591 MHz cavities will be required to squeeze the bunches to 6 cm bunch length, which requires a total RF voltage of 28 MV.

1.11.2 Hadron Injection Kicker

A new injection kicker system will be required to support single bunch transfers with a bunching frequency of 24.6 MHz. This kicker system must provide rise, flattop and fall times which total no more than the 24.6 MHz bunching period, or 40.7 ns, compared to the current RHIC bunching frequency of about 107 ns. Rise and fall times will need to be on the order of 10 ns, providing about 20 ns of flattop for the injected bunches. A total of 20 kicker units will span a length of ≈ 25 m. The new injection kickers will be placed in the IR-4 straight section. The corresponding updates of the magnetic elements in IR4 are only minor.

1.11.3 In-Situ Coating of the RHIC Beam Pipe

The high peak current of the eRHIC proton beam, with its large number of short, high intensity bunches, results in unacceptably high heat load of the cold stainless steel beam pipes in the superconducting RHIC magnets. To reduce this heat load to levels below 1 W/m, which can be compensated by the RHIC cryogenic system, the conductivity of the beam pipe must be increased. This will be accomplished by in-situ copper coating of the entire RHIC ring.

To prevent electron cloud buildup due to the short bunch spacing the secondary electron yield (SEY) of the beam pipe surface should be reduced below 1.2. Thorough “scrubbing” of the newly applied copper coating using a plasma discharge cleaning technique might accomplish that, but in order to reduce risk, it is also planned to apply a layer of amorphous carbon to safely reduce the SEY below the critical value.

1.11.4 Electron Storage Ring Vacuum System

The eRHIC Storage Ring vacuum system consists of 3.8 km of vacuum chamber separated into 36 vacuum sections. Each of the arc vacuum sections is comprised of eight arc FODO cells. Each FODO cell has two 7.4 meter long super-bends, each with a common vacuum chamber, and two 1.7 **fix number** meter long quadrupole chambers. The quadrupole chambers accommodate the quadrupole, sextupole and corrector magnets, the beam position monitors, synchrotron radiation masks, and pump ports. The individual chambers are separated by RF shielded bellows. There are also twelve vacuum sections for the 1.2 km of straight section and, in addition, twelve sections with specialized equipment, such as interaction region, RF-sections, and beam injection/extraction. The sections are separated by gate-valves that isolate the vacuum sections from each other.

The vacuum chambers are pumped by NEG-strips, NEG cartridges, titanium sublimation pumps and ion getter pumps. The vacuum system is designed for a pressure of 10 nTorr with full beam current of 2.7 A. The lifetime due to bremsstrahlung from scattering off the rest gas is larger than 20 hours for all beam energies from 5 GeV to 18 GeV.

The thermal load from synchrotron radiation hitting the beam pipe is considerable. A

total synchrotron radiation power of up to 10 MW is accommodated by the water-cooled vacuum chamber. On average, the vacuum chamber is exposed to a linear power density of 6 kW/m if the beam energy is between 10 and 18 GeV.

With the horizontal aperture of 80 mm, the emitted synchrotron radiation travels, on average, five meters before it hits the vacuum chamber. With a horizontal beam emittance of $\varepsilon_x = 24 \text{ nm}$ and an emittance ratio of $\kappa = \varepsilon_y/\varepsilon_x = 0.02$, the synchrotron radiation spot of the 18 GeV beam has a height of $h = 128 \text{ }\mu\text{m}$ when it hits the vacuum chamber. This corresponds to an average power density of 37 W/mm^2 . A material with good heat conductivity properties has to be chosen, which has, at the same time, good vacuum properties, good mechanical stability, and will allow standard manufacturing processes such as extrusion, welding, or brazing. Such a material is the Cu-Cr-Zr alloy, which has a heat conductance close to that of copper, as well as excellent manufacturability. In addition, this material has excellent yield strength and it is less costly than materials with comparable properties. Figure 1.16 shows a cross section of the vacuum chamber.

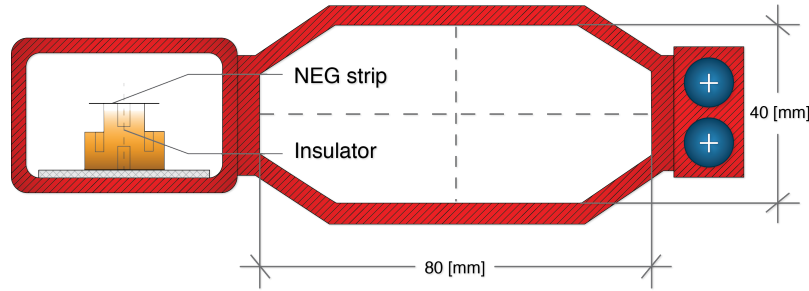


Figure 1.16: Cross section of storage ring vacuum chamber in dipole magnets.

With a cooling water velocity of 2 m/sec, the maximum temperature on the inner surface of the dipole chamber is about 100° C . Figure 1.17 shows the temperature distribution on the dipole chamber inner surface.

The chamber can be fabricated by extrusion. The pumping screen, flanges, and pump port will be attached to the chamber by tag welding without loss of the mechanical stability of the chamber material. The highest surface temperature is obtained at 5 GeV operation, when the center dipole is reversed in field direction and the field is increased to about twice the value for 18 GeV operation. In this case, the synchrotron radiation reaches the inside of the quadrupole vacuum chamber where the pump screen is located. At this location, there is no cooling and the temperature reaches up to 210° C .

The gas load in the vacuum chamber is dominated by desorption of molecules from the chamber wall by synchrotron radiation photons (Photon Stimulated Desorption - PSD). The photon flux at 10 GeV with a beam current of 2.7 A (worst case) is $8.1 \times 10^{17} \times E/\text{GeV} \times I/\text{mA} = 2 \times 10^{22} \text{ Torr} \cdot \text{l} \cdot \text{m}^{-1} \cdot \text{sec}^{-1}$. A desorption coefficient in the order of $\eta = 1 \times 10^{-6} \text{ molecules/photon}$ is assumed to be achieved after some conditioning. The desorbed gas load is then $1.3 \times 10^{13} \text{ molecules}/(\text{sec} \cdot \text{m})$ or $4 \times 10^{-7} \text{ torr} \cdot \text{l}/\text{sec} \cdot \text{m}$. The lin-

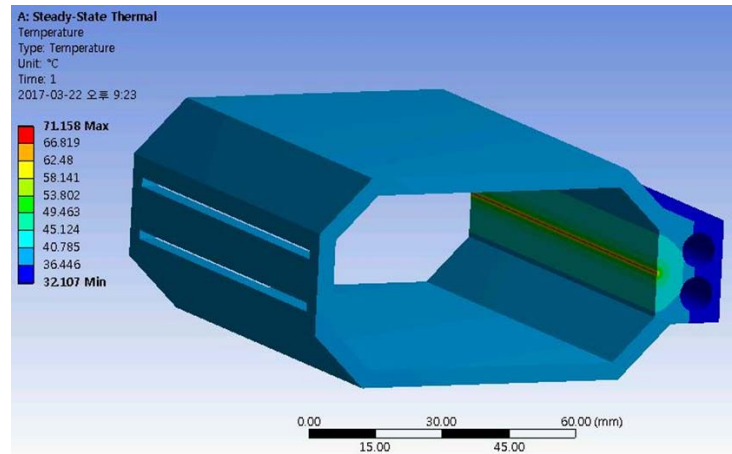


Figure 1.17: Analysis of the temperature distribution of the dipole chamber exposed to the full synchrotron radiation power.

ear pumping speed is designed to be $100 \text{ l/sec} \cdot \text{m}$ which results in a pressure of 4 nTorr . This capacity is achieved by pumping slots which cover 10% of the surface of the pump screen corresponding to a conductance of $200 \text{ l/sec} \cdot \text{m}$. Near the location of the quadrupole magnets, large lumped NEG cartridges and ion getter pumps are foreseen.

Due to the high beam currents, the RF-shielded bellows are a very critical element of the vacuum system design. The eRHIC design adapts the design that has been produced for the NSLS-II storage ring. The thermal contact of the sleeves is accomplished by fingers on the outside (see Figure 1.18). The NSLS-II design has shorter and wider fingers compared to the bellows designed for the Advanced Photon Source. The gaps in-between fingers are minimized to avoid heating of the fingers by RF power leaking through the gaps.

Another critical element of the vacuum design is the RF seal of flange connections. The pre-conceptual design choice is to use soft RF springs. These require careful assembly and alignment to avoid steps and discontinuities in the vacuum chamber, which could lead to considerable impedance and beam heating.

1.11.5 Electron Storage Ring RF System

One parameter that limits the luminosity of the eRHIC electron-ion collider is the design value for the synchrotron radiation loss in the electron storage ring. Up to 10 MW of RF power is required to replace the synchrotron radiation losses of the high current electron beam, with currents up to 2.5 A . The 38 MeV per turn energy loss at 18 GeV determines the

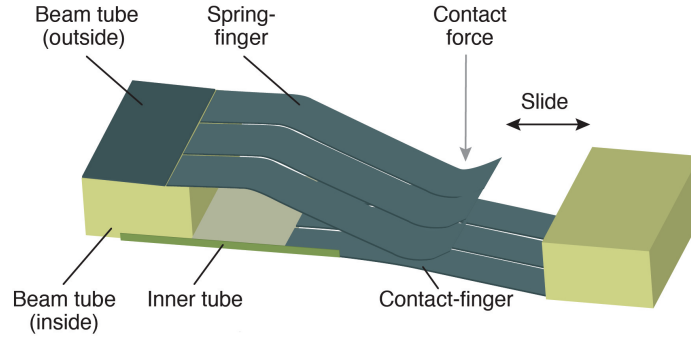


Figure 1.18: Schematic view of the bellow-finger concept.

maximum required peak RF voltage of 68 MV. The RF system is the most costly individual hardware sub-system of the electron complex of eRHIC and its components must be carefully optimized from both a performance and cost point of view in the earliest stage of the design. Table 1.10 summarizes some relevant parameters for 10 GeV and 18 GeV operations that determine the RF System.

Table 1.10: Summary of the eRHIC RF system requirements for 10 GeV and 18 GeV operations.

Parameter	10 GeV	18 GeV
Beam Current [A]	2.5	0.27
Energy Loss per Turn [MeV]	3.6	37.8
Synchrotron Radiation Power [MW]	10	10
Required RF Voltage [MV]	23.7	68

Superconducting RF cavities are chosen for reasons as follows:

- Operational cost saving. For 18 GeV operation, up to 10 MW of RF power are required at up to 68 MV (38 MV synchronous voltage) to replace beam energy lost to synchrotron radiation. For an SRF system, minimal RF power is dissipated by the cavity at any operating voltage, although it is of course an extremely important consideration for the cryogenic power load and system cost. The cryogenic wall power to support the SRF installation would be on the order of 300 kW, with all RF power available for the beam. A normal conducting RF system would require substantial additional power both to produce the required cavity voltage, and for cooling the cavities. A rough estimate of RF power required to drive normal conducting cavities (i.e. cavity ohmic loss) yields about 11 MW, based on a 2-cell structure with a Q_0 of 3.0×10^4 , a circuit (R/Q) of 100Ω per cell, and a voltage of 1 MV per cell, doubling overall CW RF power requirements compared with an SRF system, and adding the

additional 11 MW of cooling load to the water system.

- Superconducting cavities have a much higher stored energy and are therefore much better suited to handle heavy beam loading conditions.
- The impedances which drive coupled bunch instabilities are much lower than they would be for a normal-conducting cavity system with the same RF voltage.
- The much higher operating gradient of superconducting cavities (16 MV/m vs. 2 MV/m for normal-conducting cavities) leads to an installed system requiring much less longitudinal space than normal-conducting cavities.

Superconducting RF systems are used in most light sources, and for example the SuperKEKB electron-positron collider. Technical solutions for such cavity systems based on single-cell 500 MHz resonators exist. The designs are mature and the systems are, in principle, commercially available. The available systems are, however, not optimized for high energy beam applications such as eRHIC. While the systems would work technically, the solution would not be optimum from a cost point of view.

The eRHIC storage ring RF system is based on an optimized superconducting cavity concept:

- 2-cell, 591 MHz, single cavity cryomodules are designed for a more compact and cost effective RF structure.
- We are developing a variable, high power input coupler to provide optimal coupling across the wide range ($\times 10$) of loaded Q which results from the large range of operational cavity voltages in conjunction with the very high delivered beam power.
- RF power stations based on inductive output tube (IOT) amplifiers with high power RF combiner networks provide a cost effective, high reliability modular design requiring a relatively small footprint. It is anticipated that as solid state technology matures, power densities increase and costs decrease, such amplifiers may also offer a cost effective solution even at these very high power levels.

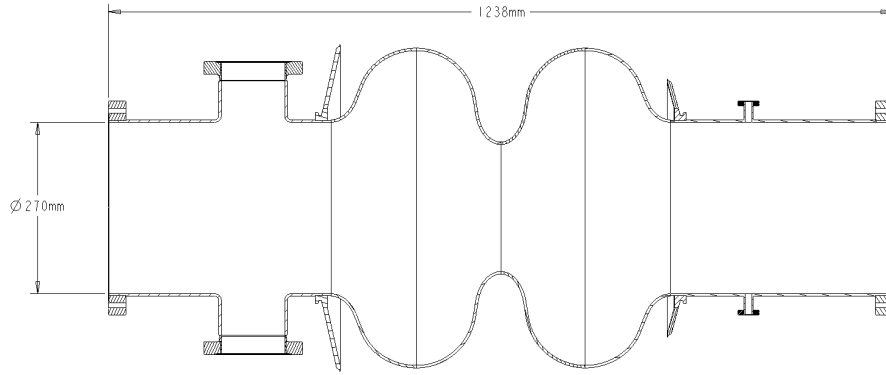
These design concepts lead to the parameters referenced in Table 1.11.

1.11.6 Superconducting RF Cavities

One 2-cell 591 MHz cavity is installed in each cryostat. The cavity shape has been optimized to suppress parasitic modes to the extent that the coupled-bunch instabilities associated with the residual higher order modes (HOMs) can be safely controlled by a multi-bunch damper system. The broad-band impedance of the cavity structure is sufficiently low so there is no issue with single bunch instabilities. The cavity shape is depicted in Figure 1.19 and the higher order mode structure is shown in Figure 1.20.

Table 1.11: eRHIC RF system parameters.

Parameter	Value
RF Frequency [MHz]	591
Number of cells per cavity	2
Number of cryostats	14
Maximum accelerating gradient [MV/m]	16
Total installed voltage [MV]	110
Maximum required RF voltage [MV]	68
Maximum power per input coupler [kW]	500
Number of input couplers per cryomodule	2
Total installed RF power [MW]	12.7
Number of RF transmitter stations	28
HOM power per cryomodule [kW]	80
HOM coupler type	beam-pipe SiC
Beam pipe absorbers per cryostat	4

**Figure 1.19:** Optimized shape of the 2-cell 591 MHz superconducting cavity for eRHIC.

Strong damping of higher order parasitic modes is important to achieve robust beam stability and to limit the required power of the broad-band damper system which actively stabilizes the beam. The choice made in the design of the eRHIC RF is to use warm, beam-pipe HOM absorbers located in the warm beamline sections adjacent to each cryomodule. The design is adapted from the ANL APS-U design, and benefits from the work of many

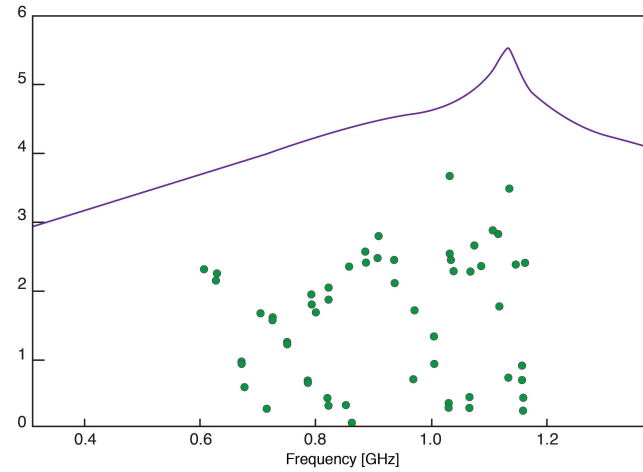


Figure 1.20: Longitudinal impedance of a single 2-cell cavity. The solid line is a Lorentzian fit of the envelope function; the dots are calculated using the code CST Microwave Studio [39]. The vertical axis is impedance in units of $k\Omega$.

labs. Figure 1.21 depicts the SiC absorber. Figure 1.22 shows a rendering of the 591 MHz cryomodule design.

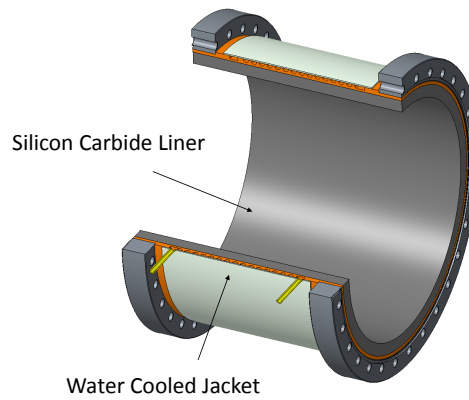


Figure 1.21: CAD model of the eRHIC SiC HOM damper.

1.11.7 High Power RF Input Couplers and Power Amplifiers

The power capability of the fundamental power input coupler (FPC) is an important parameter for the layout of the RF system, since it determines the minimum number of cryomodules needed to feed 10 MW RF power to the beam, compensate the substantial power

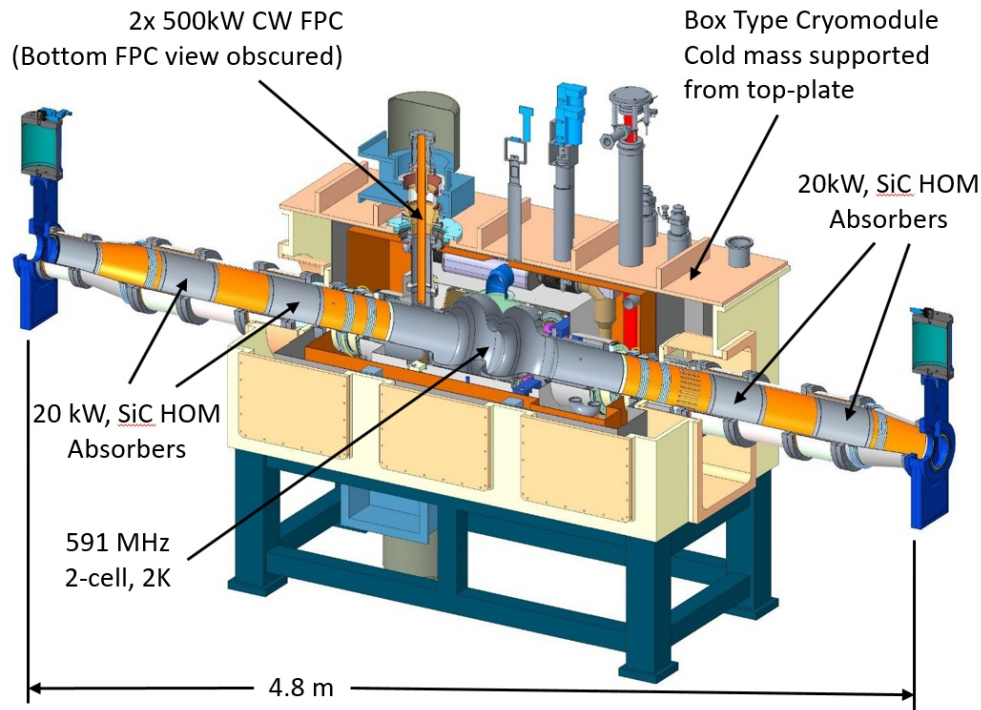


Figure 1.22: Cutaway view of the eSR 591 MHz cryomodule concept. Shown is the cryomodule, with a nominal valve to valve length of 4.8 m, including the adjacent warm spaces with four SiC beam pipe absorbers per cryomodule, beampipe tapers and gate valves. Shown also are the cryogenic feeds and the top RF input coupler, oriented vertically to save space in the IR.

lost to HOM generation and power extracted by a possible third harmonic RF system should it prove necessary. The choice was made to employ two 500 kW power couplers in each cryomodule, based on a fixed, 500 kW coupler designed and successfully tested on the superconducting photo-cathode gun developed at BNL. The eRHIC fundamental power coupler is a further development of this high power FPC. Operation at different electron beam currents and beam energies requires an optimized, variable coupling in order to avoid a large amount of reflected RF power. The optimum coupling varies by about a factor of 10 over the range of these operating parameters. For the worst case beam loading scenario at 10 GeV, installation of 14 cryomodules (28 power couplers) brings the expected maximum operating power of the couplers to just over 400 kW each, or 80% of design maximum.

RF power sources for the eRHIC electron storage ring cryomodules are based on high power units comprising multiple IOT transmitters and high power RF combiner networks. Each high power unit can deliver up to 500 kW of RF power, with two units required for

each cryomodule. The RF system includes a power margin of about 15%. Figure 1.23 shows a CAD-model of the eRHIC variable coupling high power input coupler.

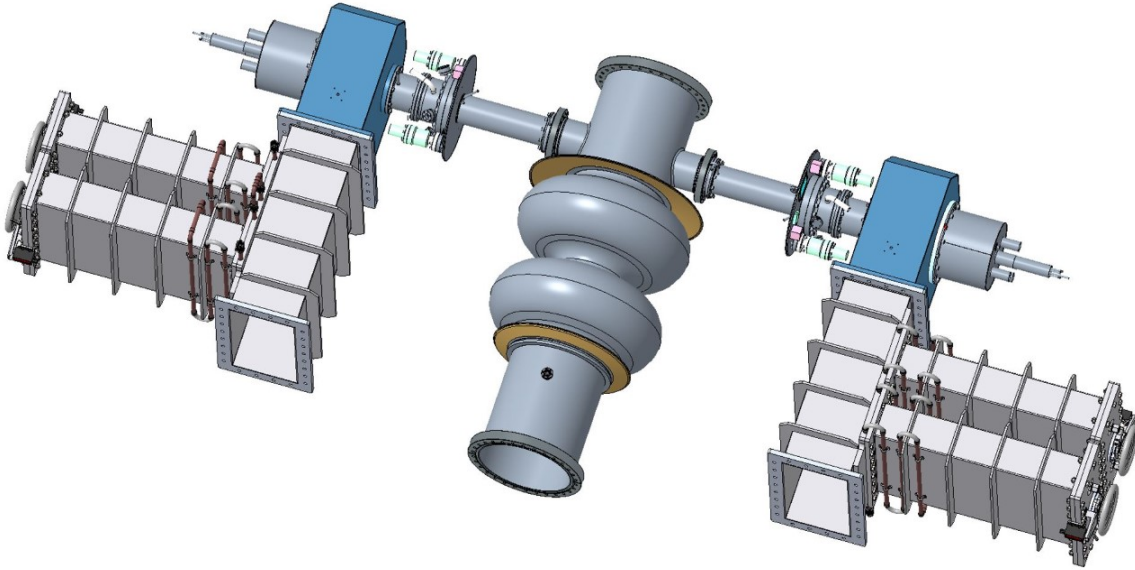


Figure 1.23: CAD model of the eRHIC 500 kW variable Q_{ext} power coupler. Two fixed coaxial couplers are shown attached to the cavity. The blue structures are the coax-waveguide doorknob transitions. These are attached to the waveguide tuner sections which are used to adjust the Q_{ext} of the couplers.

1.11.8 Crab Cavities

The eRHIC crab cavities, designed to operate at a frequency of 394 MHz, will be realized as superconducting Double Quarter Wave Crab Cavities (DQWCC). This cavity type, designed and developed at BNL for the LHC luminosity upgrade, has gone through a rigorous development program. The frequency of the LHC DQWCC devices is 400 MHz, conveniently close to the eRHIC DQWCC frequency, and thus serves to validate the expected performance of the eRHIC DQWCC.

At this time, a total of five LHC-style DQWCC have been built and tested with exceptionally good results: a proof-of-principle cavity built by Niowave Inc. for the BNL team and tested at BNL, two prototype cavities designed by BNL, built by Niowave through a LARP program, and tested at Jefferson Laboratory, and two prototype cavities of the same design built and tested at CERN. The BNL crab cavity team has been an active contributor to all the tests at JLab and CERN.

While the superconducting crab cavity is the most critical element of the crabbing system, there are many other auxiliary subsystems that are challenging and critical for the proper crabbing of the beam. These subsystems, which will be described in detail in this document, include the liquid helium tank, HOM dampers, fundamental power and pickup

couplers, mechanical cavity frequency tuner (comprising the dressed cavity, seen in Figure 1.24), as well as the crab cavity cryomodule. At this point all the subsystems mentioned have been built and successfully tested for the LHC DQWCC, and lessons learned from the LHC devices will be applied to the eRHIC DQWCC design.

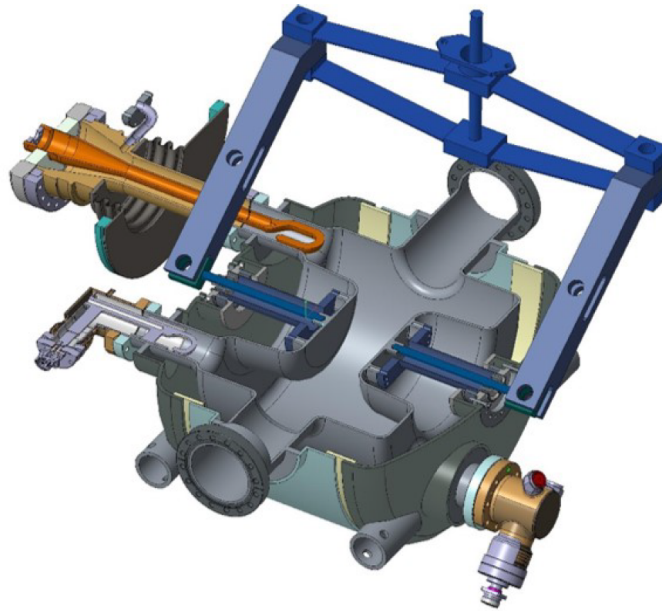


Figure 1.24: Cross section view of the eRHIC DQWCC showing the dressed cavity, with helium tank, couplers, and tuner.

The ultimate test of any accelerator cavity is its performance in the presence of beam. This is particularly true for hadron crab cavities, since there has never been any previous implementation of crab cavities in hadron accelerators. For this reason, a complete system, including two fully dressed DQWCC with all the couplers and tuners in a cryomodule, has been installed at CERN in the SPS accelerator, as shown in Figure 1.25. Beam tests commenced in April 2018, with active participation of BNL staff. During these tests no detrimental effects on the proton beam were observed.

1.11.9 Civil Construction and Infrastructure

An important feature of the Brookhaven eRHIC proposal is that, due to the significant existing RHIC infrastructure, a relatively small amount of new building square footage is required. There are 13 proposed new buildings totaling 145,00 square feet. At the present stage of the design, it is necessary to provide a new 70,749 sq. ft. building in the IR10 location to house RF power amplifiers and supporting equipment for the electron storage ring and the RCS. A new 21,000 sq. ft. facility will be constructed in the IR2 straight section to house the electron pre-injection LINAC and the strong hadron cooling electron ERL with

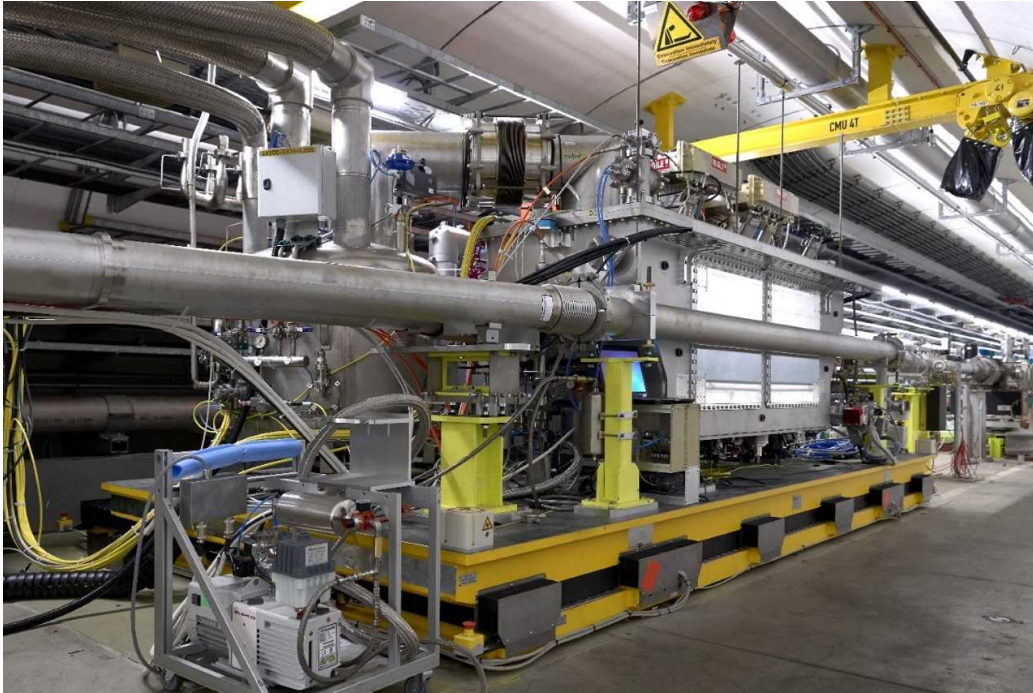


Figure 1.25: The LHC prototype twin DQWCC cryomodule installed in the SPS tunnel for beam tests (Photo Courtesy CERN).

their associated laser systems and other support equipment. Additional smaller buildings are required around the ring to house power supplies and other support equipment at locally optimized points. The existing central cryogenic plant will be used for cryogenic cooling for all of eRHIC, but additional cryogenic support facilities will be required to support 2 K cooling of new superconducting RF equipment in IRs 2, 10, and 6. The current operation of RHIC requires distributed cooling water systems located at or near the points of use. eRHIC will however require a significant increase in cooling water capacity for the electron storage ring vacuum chamber (10 MW) along with magnet and power supply cooling for the electron storage ring and RCS. Each building will also have HVAC requirements driven by the equipment and rack demand. The requirement for electron beam thermal stability will drive the design and installation of a new HVAC system for the tunnel. This system is currently envisioned to be an industrial ductless system to avoid the installation of large air ducting systems throughout the tunnel space. Existing site power is currently sufficient for the needs of eRHIC; however, the distribution system will require an upgrade to supply enough power to the new locations. A “ring bus” style distribution is envisioned for eRHIC, allowing for sections of the ring to be opened for maintenance operations without affecting downstream loads. A new 20 MVA main power transformer will be installed to support RF power demand. Backup power capacity will be installed in the form of two diesel generators along with distributed UPS systems where required.

1.12 Overview Summary

The eRHIC collider, as described in the pre-conceptual design provides collisions of electron and hadron beams stored in two storage rings: the Yellow ring of the Relativistic Heavy Ion Collider (RHIC) and a new electron storage ring with high luminosity of $L = 10^{34} \text{ cm}^{-2} \text{ sec}^{-1}$ over a center-of-mass energy range from 20 GeV to 140 GeV. The technical solution is based on accelerator physics and technology that is a moderate extrapolation of the state-of-the-art. Appendix ?? gives a detailed description of the hadron beams in the RHIC complex that are available for eRHIC. The required modifications of RHIC are few and relatively inexpensive on the scale of the entire project. The challenge of the design lies in its implementation into an existing tunnel with existing infrastructure at a reasonable cost, which will require very detailed planning. The final factor of two to three in luminosity requires strong hadron cooling, which will be realized by a novel scheme or by substantial extrapolation of existing technology. The main mitigation of the corresponding technical risk lies in the fact that a very respectable luminosity of up to $4.3 \times 10^{33} \text{ cm}^{-2} \text{ sec}^{-1}$ can be achieved without strong hadron cooling, a performance which would provide full access to the entire EIC physics program.

The electron injector complex consists of a polarized electron gun and 400 MeV S-band LINAC which will provide polarized electron bunches of 12 nC to the rapid cycling synchrotron in the RHIC tunnel. This large synchrotron is to be constructed with normal-conducting magnets and normal-conducting RF systems. The critical requirement is high spin transparency for the polarized beam. This has been taken into account by special design features and has been tested by extensive simulations.

The anticipated performance of the collider has been addressed by a comprehensive accelerator physics design study. The design allows for two large-solid-angle detectors utilizing the existing experimental areas now occupied by the RHIC detectors STAR and PHENIX/sPHENIX. Final parameters are chosen such that there is still a margin between the design values and values believed achievable. In that sense, the presented solution should be considered as robust and realistically achievable. While there are no components that require completely new technical concepts, several components are at state-of-the-art or slightly beyond present technology. The list of these components includes special superconducting magnets in the interaction regions with large apertures. Other advanced components are 2-cell superconducting cavities with 1 MW of input power and variable coupling of the forward power couplers. Strong hadron cooling requires a CW electron source which can reliably deliver 100 mA of beam current.

In conclusion, the presented eRHIC design based on an electron storage ring and its injectors added to the RHIC complex is an attractive, relatively low risk solution, which meets all requirements on an electron-ion collider at reasonable cost.

Chapter 2

EIC Physics and Requirements for Machine Design

2.1 Introduction

Half a century of investigations have revealed that the neutrons and protons (nucleons) that make up the atomic nucleus are composed of more basic constituents, the quarks and gluons, with their interactions mediated by the exchange of gluons. Their discovery has led to the development of the fundamental theory of strong interactions, quantum chromodynamics (QCD). QCD attributes the forces among quarks and gluons (collectively called partons) to their color charge. In contrast to quantum electrodynamics, where the force carriers (photons) are electrically neutral, gluons in QCD carry color charge and can self-interact.

As a consequence of QCD the internal structure of nucleons consists of a complex dynamical system of valence quarks immersed in a quantum sea of virtual quarks, antiquarks, and gluons, a system unlike any other heretofore observed in nature. The unique spin of the nucleon is not a simple sum of the spins of the valence quarks, but also includes significant contributions from this quantum sea. The mass of the nucleon is not the sum of its constituent partons (which is near zero), but emerges from interactions among the valence quarks, antiquarks, and gluons.

Understanding the structure of nucleons and nuclei, as well as their properties such as spin, mass, and nucleon-nucleon interactions from the properties and dynamics of quarks and gluons is a central goal of nuclear science. Decades of work in high energy physics and nuclear physics to probe the nature of matter at the QCD level has revealed a rich tapestry with many detailed answers, but the most fundamental questions remain unresolved, entailing many opportunities for new discoveries. The Electron Ion Collider (EIC) is conceived with unique capabilities to explore this new realm of discovery for understanding the fundamental role of QCD in the observed structure of matter.

The dynamical interactions between quarks and gluons have profound consequences, such

as the generation of the nucleon mass. They also result in a little explored domain of matter where gluons dominate the nuclear wavefunction. Hints of this domain have been seen in nuclear collisions at RHIC and the LHC where the nuclei collide at nearly the speed of light. Similar hints have been obtained from prior electron-proton scattering at HERA. The corresponding strong color fields are at the heart of many poorly understood emergent phenomena in QCD, such as confinement, properties of the quark gluon plasma, and the origin of nucleon spin. A quantitative study of matter in this domain of gluon dominance is a central goal of the EIC.

In the last two decades, nuclear physicists have developed new phenomenological tools that show promise of realizing tomographic images of the quarks and gluons inside polarized and unpolarized protons and neutrons. These tools are being utilized now and will be further refined in the next few years to study the valence quark region in the nucleon using the 12 GeV CEBAF at JLab and the COMPASS experiment at CERN. However, our knowledge of the nucleon will be far from complete without the investigation of the gluon dominated region within it. While high-energy polarized and unpolarized hadron-hadron collisions at RHIC and the LHC have initiated the exploration of this gluon-dominated regime, the EIC will complement these studies by simultaneously bringing the precision of the well-understood electromagnetic probe, polarized beams, and high energies to the study of the gluon dominated region.

As one increases the energy of the electron-nucleon collision, the deep inelastic scattering process probes regions of progressively higher gluon densities. However, the density of gluons inside a nucleon must eventually saturate to avoid an indefinite rise in the strength of the nucleon-nucleon interaction. How this exactly happens in QCD is unknown. Unambiguous evidence of this saturated gluon density has so far eluded us, although tantalizing hints at RHIC and the LHC have been observed. Experimental design limitations of the past are being specifically addressed in the design of the EIC in order to study this remarkable form of matter; this will be facilitated by electron collisions with heavy nuclei, where coherent contributions from many nucleons effectively amplify the probed gluon density.

The scientific goals and the machine parameters of the EIC were first agreed upon in deliberations at a community-driven program held at the Institute for Nuclear Theory (INT) [40]. They were further refined and summarized in the EIC White Paper [1]. The EIC science goals were set by identifying critical questions in QCD that remain unanswered despite the significant experimental and theoretical progress made over the past decades, and would remain unanswered unless the EIC is realized. Those science goals and the consequent machine parameters for the EIC were supported in the 2015 NSAC Long Range Plan (LRP) [2] leading to the recommendation for the EIC as the “highest priority new facility” to be constructed in the US by DOE’s Office of Nuclear Physics.

The eRHIC machine design (pre-CDR) presented in this document addresses all the scientific goals that were identified by the broader community [1, 2, 40, 41] as the most compelling questions in QCD that the future Electron Ion Collider must address. An independent assessment of the science of EIC was recently conducted by a panel convened by the National Academies of Sciences, Engineering, and Medicine [3]. The report strongly endorses this program, noting that it addresses profound scientific questions central to

nuclear physics research while also advancing U.S. leadership in accelerator science and technology.

2.2 The Science Goals of the EIC and the Machine Parameters

In this section, we present a few selected topics amongst the set of compelling questions in QCD that led to the recommendation for construction of an EIC in the NSAC process, and summarize the machine parameters that are needed to address them.

The key scientific questions that the EIC could address are:

1. How are the sea quarks and gluons, and their spins, distributed in space and momentum inside the nucleon? How do nucleon properties emerge from them and their interactions?
2. How do color-charged quarks and gluons, and jets, interact with a nuclear medium? How do the confined hadronic states emerge from these quarks and gluons? How do the quark-gluon interactions create nuclear binding?
3. How does a dense nuclear environment affect the quarks and gluons, their correlations and their interactions? What happens to the gluon density in nuclei? Does it saturate at high energy, giving rise to a gluonic matter with universal properties in all nuclei and even nucleons?

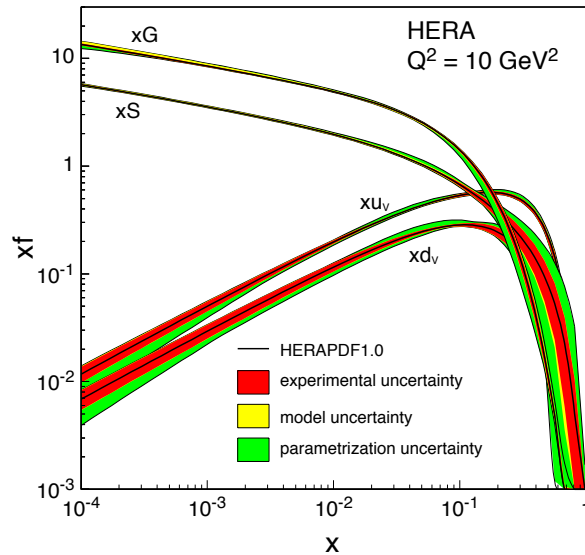


Figure 2.1: The gluon (xG), sea (xS) and valence quarks ($x u_v$ and $x d_v$) distributions as extracted from the data collected at HERA along with their uncertainties. Domination of gluons at $x \leq 0.1$ is evident.

Figure 2.1 depicts the parton distribution functions extracted from $e + p$ scattering data from the HERA collider at DESY. To leading order, these functions represent the probability density for finding a particle with a certain longitudinal momentum fraction x at resolution scale Q^2 . The plots show the valence quark, sea quark, and gluon distributions extracted from the data. The most surprising feature of this result was the rapid rise of the gluon distribution indicating that gluons dominate the proton's wavefunction at high energies or with decreasing x .

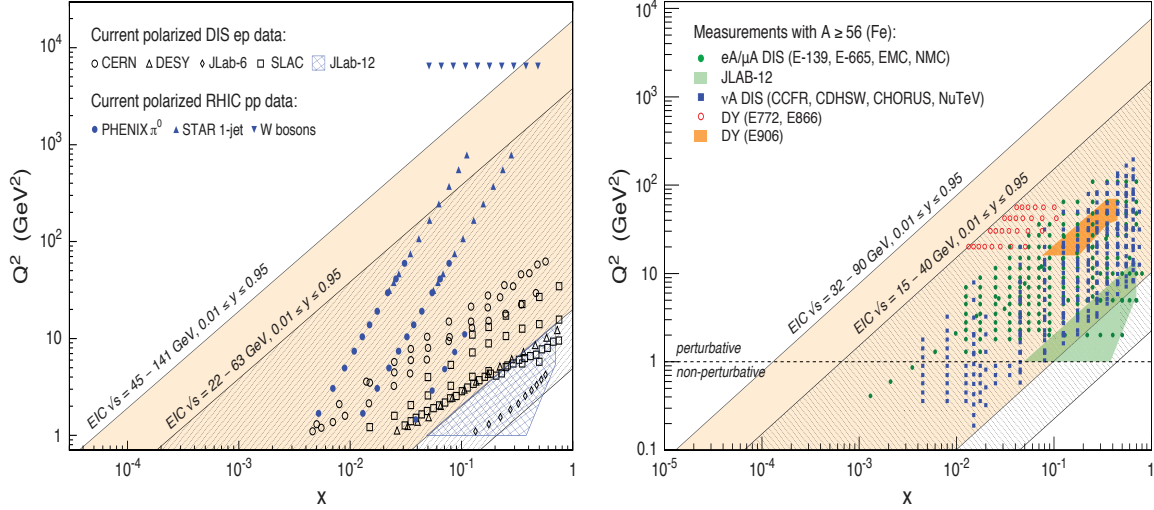


Figure 2.2: Left: The x - Q^2 range covered by the EIC with two different center-of-mass energy ranges in comparison with past and existing polarized $e + p$ at CERN, DESY and SLAC and $p + p$ experiments at RHIC. Right: the kinematic range in x - Q^2 for lepton-nucleus deep inelastic scattering and Drell-Yan (DY) experiments and future JLab12 experiments in comparison with the EIC.

The EIC design described in this document covers a center-of-mass energy range for the $e + p$ collisions of \sqrt{s} of 29 to 140 GeV. The kinematic reach in x and Q^2 , the momentum transferred by the electron to the proton, is shown in Figure 2.2. The diagonal lines in each plot represent lines of constant *inelasticity*, y , which represents the ratio of the virtual photon's energy to the incoming electron's, in the target rest frame. The variables x , Q^2 , y and s are related to each other by a simple equation $Q^2 = sxy$. Since the EIC is being designed to study the domain of gluon dominance in the proton, it has to have a substantial energy reach to access the low- x region ($x \propto 1/s$). The left figure shows the kinematic acceptance for polarized and unpolarized $e + p$ collisions, and the right figure shows the acceptance for $e + A$ collisions. Also shown for comparison is the reach of past and current fixed target facilities that acquire comparable data sets, and in case of the left plot, polarized $p + p$ collisions from RHIC. Note that there are no data from past or current experiments in the region of $x < 5 \times 10^{-3}$. The two figures establish that the EIC would, for the first time, allow us to explore significantly lower values of x where the role of gluon degrees of freedom is enhanced.

The details of the science case for the EIC have been presented in the EIC White Paper [1]. In what follows, we describe, in greater detail, the compelling scientific questions outlined above, and motivate the requirements for the machine parameters that would help us address these questions.

2.2.1 Nucleon Spin and Imaging

Nucleon Spin

Understanding the nucleon spin in terms of its components, quarks, anti-quarks, gluons, and the dynamics resulting from color interactions, has been an important goal for nuclear scientists over the past five decades. The nucleon spin can be split into its components [42]:

$$\frac{1}{2} = \frac{1}{2}\Delta\Sigma(Q_f^2) + \Delta G(Q_f) + L_{Q+G}(Q_f) \quad (2.1)$$

where $\Delta\Sigma$, ΔG , and L are the contributions from quark+anti-quarks, gluons, and their angular momentum to the nucleon spin. They are evaluated at a fixed scale Q_f and summed over the whole x range from 0 to 1. The discovery by the EMC experiment at CERN in the 1980s, that the quark and anti-quark spin alignment ($\Delta\Sigma$ in the above equation) could not explain the nucleon's spin, brought this fundamental issue into the limelight. Since then, numerous fixed target polarized electron/muon scattering experiments and polarized proton collisions at RHIC [43] have confirmed that the spin alignment of quarks+antiquarks, and gluons, in the covered kinematic region ($0.001 \leq x \leq 0.6$) does not explain the nucleon's spin, thus providing indirect evidence for a potential contribution from parton orbital angular momenta, L_{Q+G} . The largest uncertainties in $\Delta\Sigma$ and ΔG come from the unmeasured regions of $x < 5 \times 10^{-3}$, where no data exist. With measurements in this region, the EIC will provide precise measurements of $\Delta\Sigma$ and ΔG that will resolve the spin components of the proton [1, 41, 44].

Figure 2.3 illustrates the potential impact of the EIC on reducing the uncertainty in knowledge of the unmeasured region assuming \sqrt{s} range indicated in the figure. The EIC will significantly reduce the uncertainty in the knowledge of $\Delta\Sigma + \Delta G$ for $10^{-6} < x < 10^{-3}$ (y -axis), as well as in the contribution from orbital angular momentum in the range $10^{-3} < x < 1$ (x -axis). It is evident from this plot that the higher center-of-mass energy is required to make measurements for which the errors are much smaller than the individual contributions.

Machine Requirements For Polarized Inclusive Deep Inelastic Scattering

Double longitudinal spin asymmetry measurement requires measuring inclusive deep inelastic scattering (DIS) with longitudinally polarized electrons off longitudinally polarized protons. Typically, 70% beam polarization was assumed in the conducted simulations. Most studies were performed assuming a data set with integrated luminosity $L = 10 \text{ fb}^{-1}$, and it was shown in [41, 44] and references therein that the statistical uncertainties at this

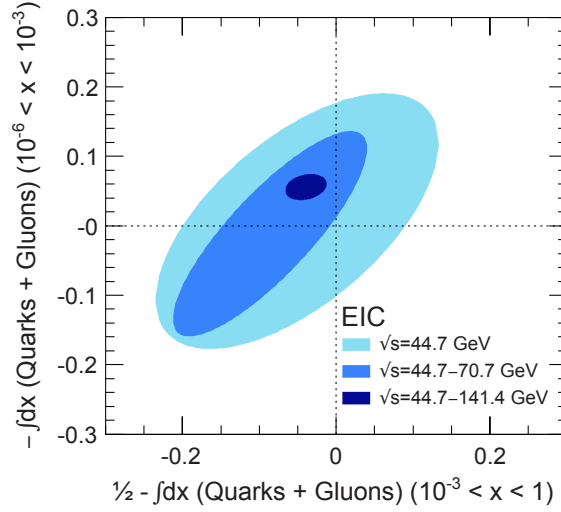


Figure 2.3: The impact of different center-of-mass energies on our knowledge of the sum of quark and gluons' helicity contributions in the range $10^{-6} < x < 10^{-3}$ (vertical axis) versus the contribution from the orbital angular motion in the range $10^{-3} < x < 1$ (horizontal axis). The calculations are shown at a fixed scale of $Q_f^2 = 10 \text{ GeV}^2$ [41].

luminosity are considerably smaller than the current theoretical uncertainties. Experimental systematic uncertainties, coming from polarization measurements and other (time dependent, detector related) false asymmetries in measurements would then have to be constrained to a few percent [45]. Similar measurements using polarized ^3He or deuteron are needed to obtain full flavor separation of the spin structure. The machine requirements are similar to the ones discussed for the proton except for the need of neutron rich polarized nuclear beams. In addition, this science program will need high center-of-mass energies and an integrated luminosity of at least 10 fb^{-1} .

Imaging The Confined Motion Of Quarks

DIS measurements in which hadrons are measured (in addition to the scattered electron), are commonly referred to as "Semi-Inclusive DIS" (SIDIS) measurements. Experiments with collisions of electrons on transversely polarized protons, deuterons (D), or helium (^3He) targets, have measured single spin azimuthal asymmetries for various identified hadrons over a broad range of kinematics. Similar effects have been observed and studied in singly polarized p+p collisions. The commonly accepted origin of these asymmetries are the correlations between the transverse momentum of quarks and their spin, as well as the spin of the parent nucleons. Therefore a full picture of the nucleon has to include the transverse momentum distribution of partons in addition to their longitudinal one.

SIDIS and polarized p+p measurements over the past decade, have allowed scientists to formulate a framework in which the measurements of single spin azimuthal asymmetries

for different identified hadrons are connected to the transverse momentum distribution (TMD) of partons, *i.e.*, their confined motion inside the nucleon. These TMDs incorporate the correlations between the motion of partons, their spin, and the spin of the parent nucleon. These correlations arise from spin-orbit coupling among the partons about which very little is known to-date. One can define eight types of TMDs [46] based on the different combinations of quark and nucleon spin combination, and a similar set of eight TMDs for gluons—all of which need to be mapped out if one is to gain full knowledge of the 3D momentum and spin structure of the nucleon.

The data sets used to constrain TMDs are currently more limited in x and Q^2 than the measurements shown in Figure 2.2 (left) used to constrain the helicity PDFs. With its polarized beams and high energy, the EIC will dramatically advance our knowledge of TMDs. One will be able to map out the 2+1 dimensional momentum structure of the different quark flavors and gluons inside nucleons over a wide region in x and Q^2 [1,47].

Figure 2.4 (left) depicts the transverse-momentum distribution of up quarks inside a proton moving in the z -direction (pointing out of the page) with its spin polarized in the positive y -direction. The colors represent the probability of finding the up quarks for the given momenta. The anisotropy in transverse momentum is described by the Sivers distribution function [1,48,49], which describes the correlation between the proton's spin direction and the motion of its quarks and gluons. While the figure is based on a preliminary extraction of this distribution from current experimental data, nothing is known about the spin and momentum correlations of the gluons and sea quarks. The achievable statistical precision of the quark Sivers function from EIC kinematics assuming an integrated luminosity of 10 fb^{-1} is shown in Figure 2.4 (right). Currently no data exist for extracting such a picture in the gluon-dominated region in the proton or in light nuclei. The EIC will be crucial to realize such a program.

Machine Requirements For TMD Measurements

Measurements of transverse momentum distributions require longitudinally and transversely polarized hadron beams colliding with (un)polarized electrons. Simulations to investigate the degree to which the EIC can constrain the Sivers function assumed 70% transverse polarization of the proton beam [1]. As mentioned earlier, semi-inclusive DIS implies the identification of final state hadrons in coincidence with the scattered electrons. There is already experimental evidence for flavor dependence, namely, a dependence on the type of quark involved in the collision, of the different TMDs. These measurements require that the hadron type in the final state be identified, in order to tag the flavor of the parton. To obtain a detailed understanding of the eight different quark and gluon TMDs, one needs to bin the experimental observables in multiple variables, such as x , Q^2 , y , p_t , and z simultaneously, where p_t is the hadron's transverse momentum and z is the momentum fraction of the final state hadron, both with respect to the virtual photon. Mapping the TMDs in multiple dimensions will require larger statistics than for inclusive measurements. To fully disentangle the flavor dependence of the various TMDs, it is important to collect data with neutron rich transversely polarized beams, such as ^3He or D with

equivalent experimental conditions. Each of these collider operating modes will need an integrated luminosity (or significant fraction) of 10 fb^{-1} . There is an obvious redundancy in the data sets. For example, unpolarized target conditions could be achieved by combining oppositely polarized longitudinal or transverse data sets, thus running the collider effectively for two physics programs simultaneously. However, despite such opportune simultaneity in data taking, it is anticipated that the systematic program of measurements essential for the complete mapping of TMDs will require large collective integrated luminosities (a couple of 10 fb^{-1}) for different targets and their spin orientation [1]. The wide range in $x - Q^2$ provided by the EIC is essential for mapping the TMDs. To explore gluon TMDs, access to the gluon dominated low- x region is critical and requires both high energy ($\sqrt{s} \geq 100 \text{ GeV}$) and a large luminosity [47, 50].

Imaging the Transverse Spatial Distribution of Partons

As in the case of the transverse momentum distribution of partons inside a hadron, we know little about what a hadron looks like in transverse spatial dimensions. Many of our expectations are solely based on models. In some cases, it is expected that at large- x , the quantum numbers of the hadrons come from the struck partons in the DIS measurement. As one goes to low- x , and gluon distribution begins to saturate, it's an interesting question of how gluons and sea quarks clump together in the hadron. At some yet unknown low- x a very high density gluon saturated region is reached [1, 41].

It is now possible to measure the transverse spatial distributions experimentally. The study of the spatial distribution of quarks and gluons requires a special category of mea-

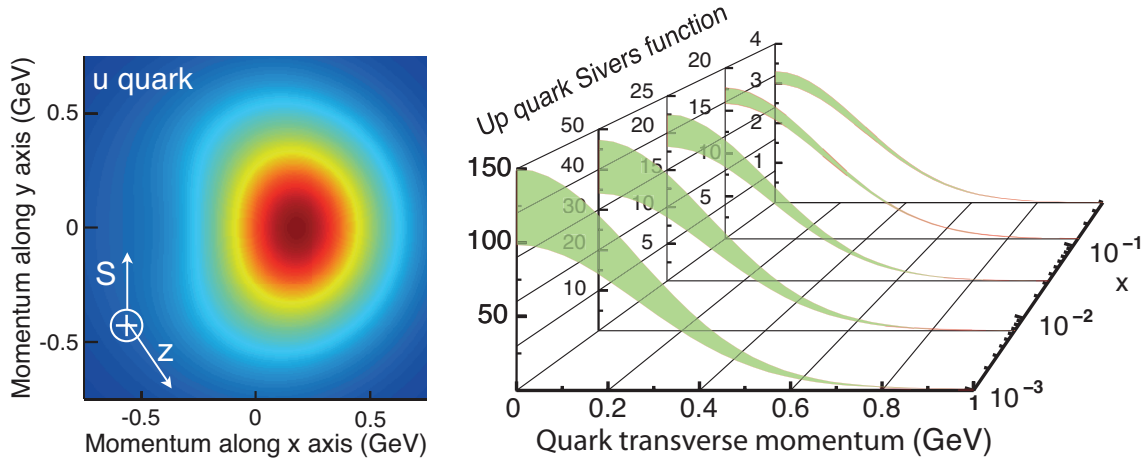


Figure 2.4: Left: The transverse momentum distribution of an up quark with longitudinal momentum fraction $x = 0.1$ in a transversely polarized proton moving in the z -direction, while polarized in the y -direction. The color code indicates the probability of finding the up quarks. Right: The transverse-momentum profile of the up quark Sivers function at five x values accessible to the EIC, and corresponding statistical uncertainties.

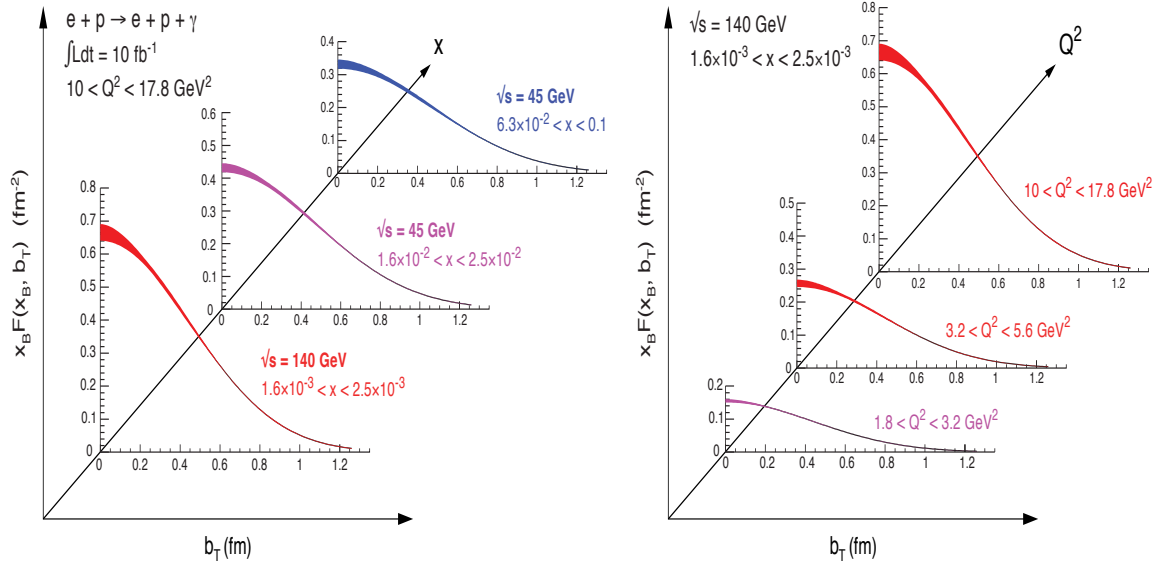


Figure 2.5: The projected precision of the transverse spatial distribution of partons obtained from the Fourier transform of the measurement of unpolarized DVCS cross section as a function of $|t|$ at the EIC for a targeted luminosity of 10 fb^{-1} at each center-of-mass energy. Impact parameter, b_T , is the distance from the center of the proton. Left: the evolution in x at a fixed Q^2 ($10 < Q^2 < 17.8 \text{ GeV}^2$). Right: the evolution in Q^2 at a fixed x ($1.6 \times 10^{-3} < x < 2.5 \times 10^{-3}$). The red and blue bands indicate extraction of spatial distribution only with high and low center-of-mass energies, respectively, while the purple band is accessible at both.

measurements, that of exclusive reactions. Examples are deeply virtual Compton scattering (DVCS) and deeply virtual vector meson (DVVM) production. In these, the proton remains intact after the electron has scattered off, and a photon or a vector meson is produced. Exclusivity demands that all final state products are detected. This includes the scattered electron, the produced photon or vector meson, and the scattered proton. The spatial distribution of quarks and gluons in these experiments is extracted from the Fourier transform of the differential cross section with respect to the momentum transfer, t , between the incoming and the scattered proton. The non-perturbative quantities that encode the spatial distributions are called Generalized Parton Distributions (GPDs) [51–53]. They are interesting to nuclear scientists not only because of their fundamental importance in non-perturbative QCD, but also because the second moment of particular sets of quark and gluon GPDs will give us information about total quark and total angular momentum of quarks and gluons in the proton [54]. This spatial distribution yields a picture of the proton that is complementary to the one obtained from the transverse-momentum distribution of quarks and gluons.

Currently, our knowledge of GPDs from DVCS is limited and is based on fixed target experiments at intermediate to high- x or at low- x from the HERA collider measurements. The high-energy, high-luminosity EIC will make a very significant impact on these measurements. It is anticipated that measurements made for protons in the range

$0.04 \lesssim t < 1.5 \text{ GeV}^2$ will enable maps of parton distributions all the way down to 0.1 fm [41, 55]. Such exclusive measurements performed on nuclei will enable us to gain a deeper understanding of the transverse quark and gluon distributions within.

Figure 2.5 shows the precision with which an EIC will provide transverse spatial distribution for quarks [41]. The red and blue bands are reachable only with high or low energy collider operations, respectively, while the purple band is reachable by both. To reach low- x and high- Q^2 the EIC needs to have the higher center-of-mass energy. The measurements were simulated using an integrated sample of 10 fb^{-1} . The uncertainties shown in this plot only account for statistics and experimental systematics, not for the systematic uncertainties associated with the extraction of these quantities from data. For more about the extraction of proton size, we refer to [1, 41, 55].

Machine Requirements for GPD Physics

It has been shown that an integrated luminosity of 10 fb^{-1} is sufficient to get to precise unpolarized spatial distribution functions. The continuous measurement of t from ~ 0.02 to about 1.5 GeV requires a careful design of the interaction region to detect the forward going protons scattered under small angles combined with a careful choice of the hadron beam parameters, *i.e.*, angular divergence and large acceptance magnets. A complete map of the spatial distributions of quarks and gluons including polarization effects, requires high polarization of hadron and lepton beams [1, 55].

2.2.2 Physics with High-Energy Nuclear Beams at the EIC

Precise knowledge of proton PDFs measured at HERA has been critically important for searches of physics beyond the Standard Model (BSM) at the LHC. When compared to our knowledge of parton distribution functions in the proton, our knowledge of nuclear PDFs (nPDF) is significantly more limited. Most of it comes from fixed target experiments in a region of intermediate to high- x as shown in Figure 2.2. Recently available data from the LHC have been included in nPDF extractions but have had limited impact on extracting nuclear PDFs [56]. High energy electron-nucleus collisions at the EIC will enable measurements of nuclear PDFs over a broad and continuous range in Q^2 all the way from photo-production ($Q^2 \sim 0$) to large Q^2 in the perturbative region. This will enable scientists to study the nPDFs with unprecedented precision. Precise knowledge of nPDFs will be crucial when searching for the transition between linear and non-linear evolution of the parton densities with change of the resolution scale of the probe. The latter saturation regime occurs at low x and low interaction scale Q^2 where the gluon densities are highest and the recombination of low- x gluons becomes increasingly important. In $e + A$ scattering such non-linearities are predicted to be more pronounced than in $e + p$ interactions [57] since the saturation scale Q_s^2 is expected to grow as $A^{1/3}$. As noted previously, exploring this intrinsically non-linear regime of QCD is a key science goal of the EIC. In addition, measurements with nuclear beams will allow us to investigate a wide range of questions, such as (i) whether color confinement in protons and nuclei is different, (ii) what is the

quark-gluon origin of short range nucleon-nucleon forces in the nuclei, and (iii) how the nuclear medium responds to colored and colorless probes. All these measurements require high energy beams of light and heavy nuclei. These measurements are discussed further below.

Nuclear Modification of PDFs and Their Precision Measurements

How parton distributions in nuclei are modified relative to those in the proton can be quantified by plotting their ratio normalized by the atomic number of the nucleus. The deviation of this ratio from unity is a clear demonstration that the nuclear parton distributions are not simple convolutions of parton distributions in the proton. A depletion of this ratio is often called shadowing, while an enhancement is dubbed anti-shadowing. The simulated data presented in this section was used in a study [58] that allowed additional flexibility in the fit function used to derive the gluon PDF in the nuclei. The ratio of gluon distribution in Pb to that in proton is plotted at two different values of Q^2 in Figure 2.6. The

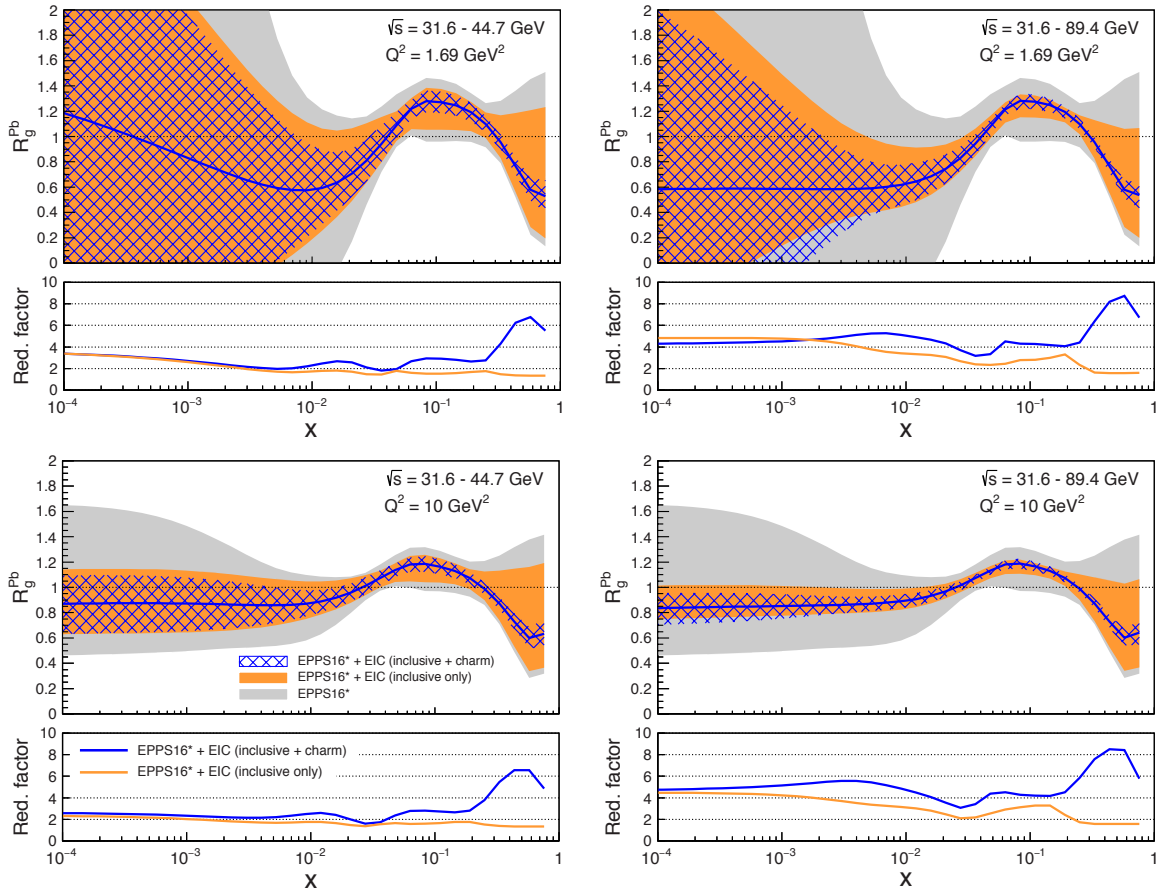


Figure 2.6: Nuclear PDFs improvements with the EIC.

grey bands indicate the current uncertainties in the nuclear PDFs, orange bands indicate the improvement we could expect from the inclusive data sets, and the hatched band indicates the further improvement one expects from the inclusion of charm quark production in this analysis. Clearly, the higher energy collider is more advantageous.

The reduced cross section $\sigma_{reduced}$ can be expressed in terms of the structure function F_2 and the longitudinal structure function F_L as:

$$\sigma_{reduced} = F_2(x, Q^2) - \frac{y^2}{1 + (1 - y)^2} \cdot F_L(x, Q^2) \quad (2.2)$$

While F_2 is sensitive to the momentum distributions of (anti)quarks and to gluons mainly through scaling violations, F_L has a larger direct contribution from gluons. An additional constraint on the gluon distribution at moderate to high- x comes from charm production driven by photon-gluon fusion. The fraction of charm production grows with the energy, reaching about 15% of the total cross section at the highest \sqrt{s} , thus permitting one to set a robust and independent constraint on the gluon distribution in nuclei at high- x [1, 41].

Figure 2.7 shows the reduced cross section for inclusive and charm production in $e + A$ scattering. The data were simulated using three different center-of-mass energies, 31.6, 44.7, and 89.4 GeV. The blue shaded region indicates the existing data, and grey bands indicate the uncertainty in the EPPS16 parametrization [56]. Note that the estimated exper-

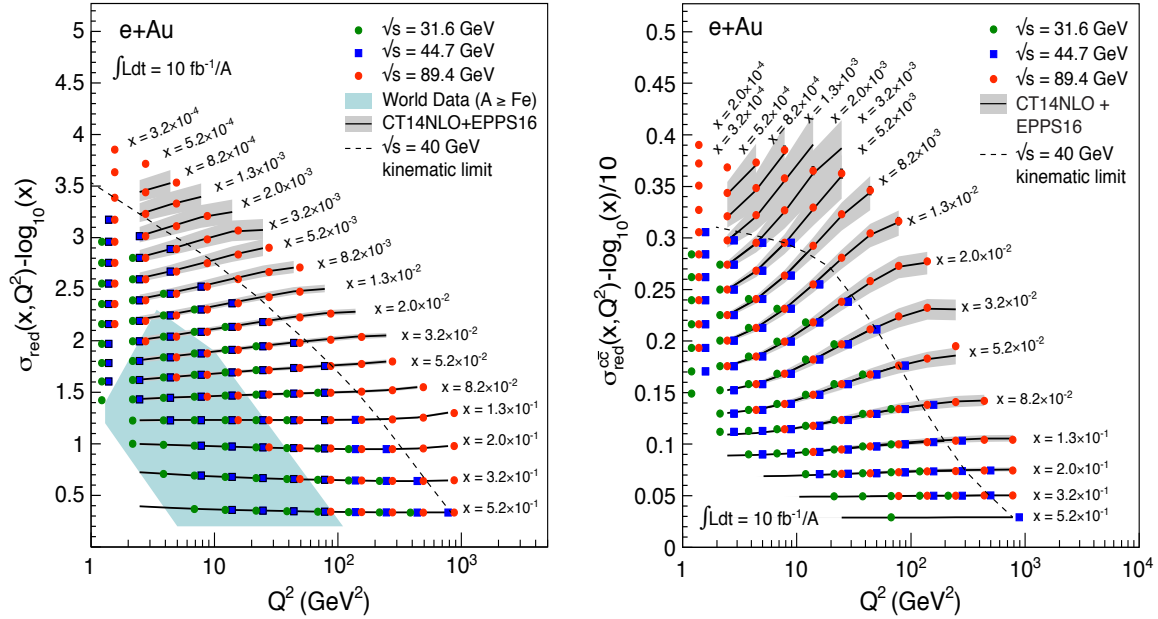


Figure 2.7: Reduced cross section for inclusive (left plot) and charm (right plot) plotted for x and Q^2 along with their uncertainties (shown in grey bands) from EPPS16 model. EIC simulated data are shown for different center-of-mass energy combinations. The blue band in the left plot shows the currently available data.

imental uncertainties on the data are very small compared to theory uncertainties, and the higher center-of-mass energy enables a broader range in (x, Q^2) , particularly in the low- x region where gluons dominate. Higher energies are clearly advantageous, and $10 \text{ fb}^{-1}/A$ combined for the data at all center-of-mass energies will be sufficient to make significant impact on our knowledge of nuclear PDFs.

Figure 2.8 shows F_L for inclusive (left) and for charm (right) calculations based on EPPS16 along with the uncertainties estimated at each energy. Note that the measurement of F_L requires one to operate the collider at several different center-of-mass energies. This simulation was performed with total of 10 fb^{-1} data over the combination of three center-of-mass energies [58]. The width of the gray bands reflects the current theoretical uncertainty in both cases and is wider than the statistical uncertainties from the simulations indicating that these uncertainty bands would be reduced significantly using future EIC data.

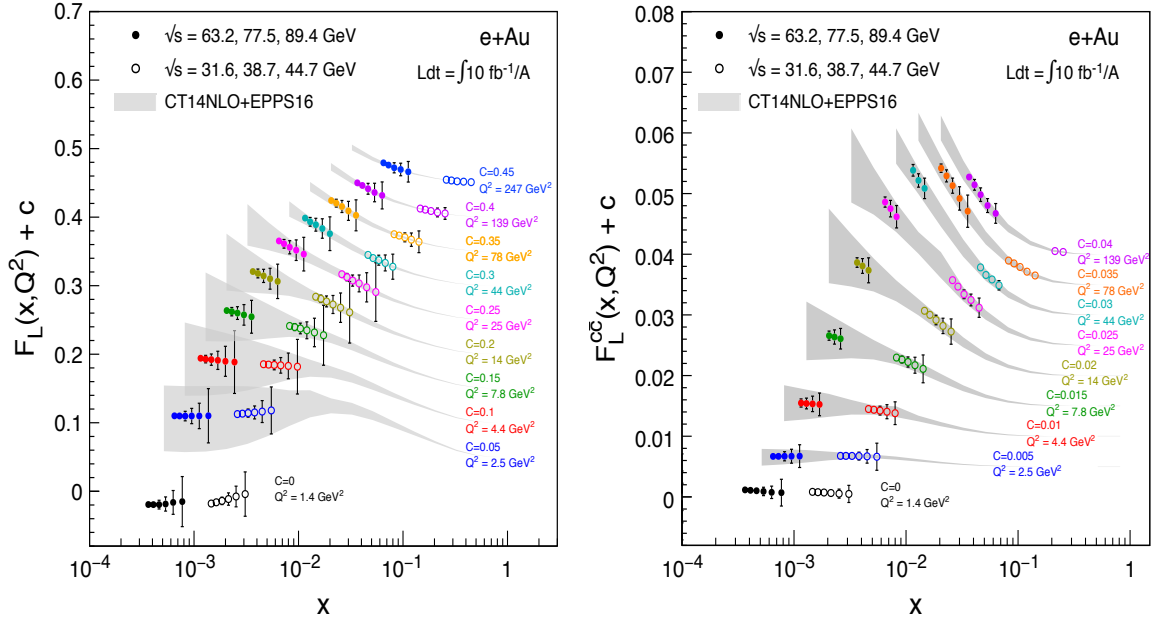


Figure 2.8: Inclusive F_L (left plot) and charm F_L^{cc} simulated data shown with the EPPS16 nuclear PDFs. Grey bands are uncertainties in the model, and the EIC data simulated with $10 \text{ fb}^{-1}/A$ are shown for three center-of-mass energies.

Machine Parameters For Precision Nuclear PDF Measurements

Based on the study presented above for inclusive DIS and charm cross section measurements, larger \sqrt{s} presents a significant advantage, as (i) a wider x Q^2 coverage can be explored and (ii) one reaches further in the region of gluon dominance. For precise high impact measurements an integrated luminosity of $10 \text{ fb}^{-1}/A$ is sufficient. In fact, beyond a few fb^{-1} , these measurements become systematics dominated [58] and more statistics will not affect the overall uncertainties.

Study of High Gluon Density Matter

A key feature of gluon saturation is the emergence of a momentum scale Q_S . If this scale is significantly larger than the QCD confinement scale Λ_{QCD} , the dynamics of strongly correlated gluons can be described using weak coupling many-body methods. The framework that enables such computations is called the Color Glass Condensate (CGC) [59]. The CGC predicts that $Q_S^2 \propto A^{1/3}$; thus, the novel domain of saturated gluon matter may be accessed sooner at a given energy in large nuclei. Unambiguous establishment of this novel domain, and its detailed study, is one of the most important goals of the EIC.

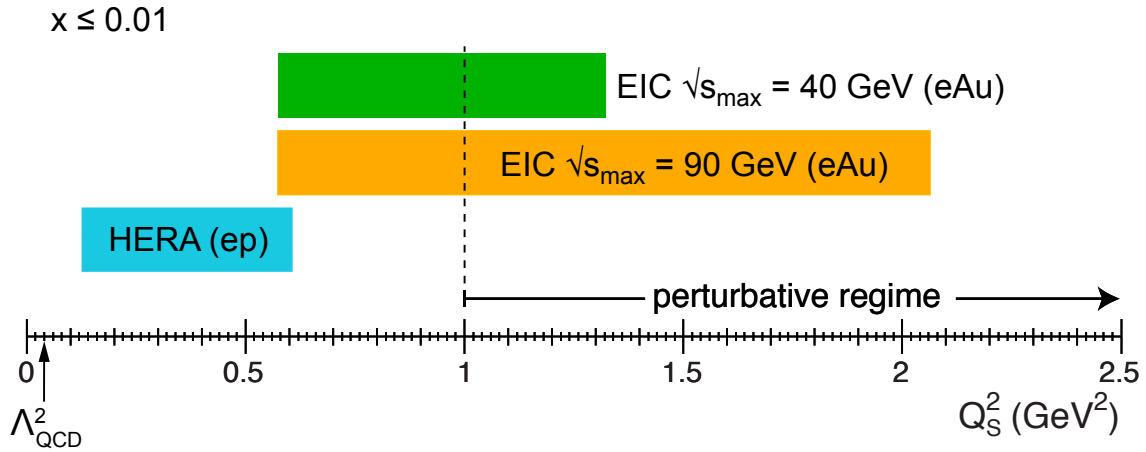


Figure 2.9: The accessible values of the saturation scale Q_S^2 at an EIC in $e + A$ collisions, assuming two different maximum center-of-mass energies and in $e + p$ collisions at HERA.

QCD predicts that the saturation of gluons is achieved precociously in large nuclei, *i.e.*, at larger values of x than in the proton since the saturation scale Q_S^2 is enhanced by approximately $A^{1/3}$. Figure 2.9 shows calculations for the saturation scales for the $e + A$ collisions assuming two different center-of-mass energies and for $e + p$ collisions at HERA. Perturbative calculations can be performed reliably in the higher Q^2 region to the right of the dashed vertical line. It is in this region where $Q^2 > Q_S^2$ that DGLAP evolution can be reliably compared with the saturation calculations. Clearly, the saturation scales achievable in both energy ranges at the EIC are significantly larger than those in $e + p$ although the \sqrt{s} energy for HERA was substantially larger. This enhancement of Q_S^2 in nuclei is a consequence of the high energy probe coupling coherently to all the partons along its path length in the nucleus. This figure makes the case that, to explore saturation phenomena reliably, one needs to have the largest nuclei at the highest affordable center-of-mass energy.

While there are multiple experimental signatures of saturation discussed in the literature [1], we only use two in this section to motivate the requirement for the energy of the collider; these are dihadron suppression and diffraction in $e + A$ collisions.

The dihadron correlation in the process $e + A \rightarrow e' + h_1 + h_2 + X$ refers to the angular correlations between two hadrons h_1 and h_2 . The angle between the two hadrons in the

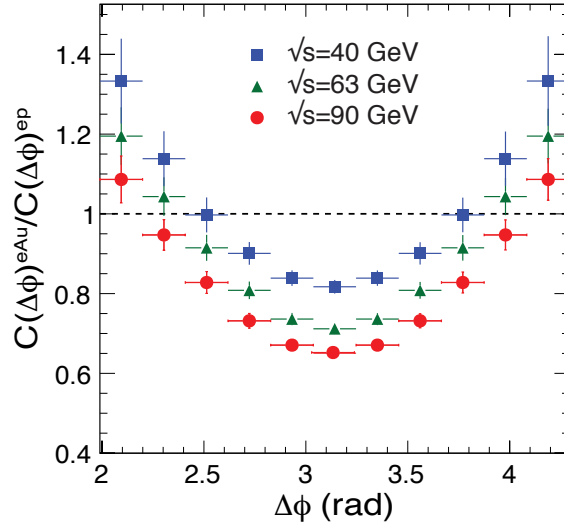


Figure 2.10: Ratio of dihadron correlation functions in e+Au collisions to those in e+p collisions in a simulation study at three different center-of-mass energies. Ratio below 1 implies a suppression or disappearance of hadrons, which is statistically significant (and maximal) at $\Delta\phi = \pi$ radians. Note that the suppression at the highest center-of-mass energy of 90 GeV is almost a factor two larger than that seen at 40 GeV.

azimuthal plane is sensitive to the transverse momentum dependence of gluons as the parton shower develops, and to their interactions amongst themselves—the mechanism that leads to saturation. The experimental signature of saturation is a progressive suppression of the away-side ($\Delta\Phi = \pi$) correlations of hadrons with increasing atomic number A at a fixed value of x . A systematic comparison of the magnitudes and widths in the dihadron azimuthal distribution in $e + p$ and $e + A$ collisions should lead us to the appropriate conclusion about the existence of saturation [41, 60]. In Figure 2.10, we plot the ratio of the correlations functions in $e + Au$ to those in $e + p$ for three energies. The suppression at the highest center-of-mass energy of 90 GeV is almost a factor two larger than that seen at 40 GeV. Since the typical uncertainties in saturation models are approximately equal to what would be a suppression of 20%, a significantly larger suppression ratio would be highly desirable, suggesting the highest possible center-of-mass energy is essential for establishing saturation unambiguously.

Diffraction in $e + A$ scattering is another promising avenue to establish the existence of saturation and study the underlying dynamics. Diffraction entails the exchange of a color neutral object between the virtual photon and the target. A consequence of this is a rapidity gap between the target remnant and the diffractively produced system. Conversely, if the exchanged particle is not color neutral, then in the detector one would observe a broad spray of final state hadrons filling up the rapidity gap. At HERA, these types of diffractive events made up a surprisingly large fraction of the total $e + p$ cross section (10–15%). There are two explanations of such large diffraction cross-sections. One is the physics of saturation. The other is due to nonperturbatively shadowed diffractive structure functions that

satisfy leading twist evolution equations. At EIC, the diffractive DIS off nuclei, saturation models predict that over 20% of the cross-section will be diffractive. In contrast, the perturbative QCD based leading twist shadowing models do not predict any such enhancement. Since diffractive cross sections are proportional to the square of the nuclear gluon distribution, they are very sensitive to the onset of gluon saturation, and are important for the study the gluon saturation.

Machine Parameters For Studies of Gluon Saturation

Highest energy operation of the EIC with the heaviest nuclei will be an essential requirement for discovery of the gluon saturation. A detailed study of saturation beyond its discovery would require a systematic variation of the nuclear size and of the \sqrt{s} to see where the saturation sets in. Di-hadron correlation studies performed with an $10 \text{ fb}^{-1}/A$ integrated luminosity is sufficient to get a clean signature. Such integrated data sets are also sufficient for many diffractive studies, and many of these measurements could be performed simultaneously for a particular nucleus. We conclude that achieving the highest possible energy is the most crucial requirement for this key EIC physics.

2.2.3 Passage of Color Charge Through Cold QCD Matter

Figure 2.11 shows a schematic of an $e + A$ scattering event. The virtual photon transmits the energy from the electron and interacts with a quark inside a nucleon in the nucleus. The struck quark will subsequently traverse the nucleus, interacting with the color charges inside the nucleus and continually lose energy. At some point, this quark will hadronize and form a color neutral hadron. Whether the hadronization process happens inside or outside the nucleus depends on the interplay between the energy of the quark and the atomic number of the nucleus.

If the virtual photon energy (in the nuclear rest frame) is large, the quark that is kicked will have a large energy and produces a jet. Because of its high energy, a jet is a better surrogate for the kicked parton than just the leading hadron. It is also expected that the variability of energy of the collider and the "dialing" of the nuclear size, both of which are possible with the EIC, will allow us to study the emergence of jets as a function of energy, and to study the internal spatial structure of jets systematically as an additional topic of high interest. A comparison of jets in $e + A$ versus $e + p$ collisions is thus a promising avenue to study a broad set of QCD phenomena related to the passage of color through cold QCD matter and the hadronization/fragmentation processes.

At the LHC, jets have been used very effectively in $p+p$, $p+A$, and $A+A$ collisions to study various QCD phenomena. We understand jets much better now than before the beginning of the LHC program. The experience thereby gathered can be gainfully applied to physics at the EIC. Jets are a promising and extremely useful tool for the study of QCD hadronization and parton shower evolution. They also will be an effective tool to be employed to measure and study the hadronic component in high energy photon structure [61] and glu-

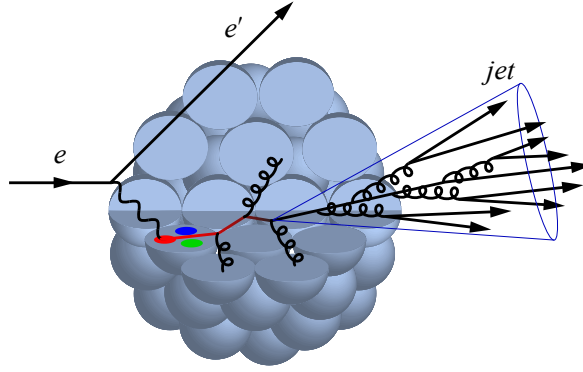


Figure 2.11: Schematic depiction of a struck parton propagating through cold nuclear matter resulting in the formation of a single jet.

ons' helicity in polarized protons. [41].

Machine Design Parameters For Jets Studies

Jets can only be produced and identified cleanly at high enough collider energies. High momentum jets feature higher hadron multiplicity and a more complex internal structure. As such, high center-of-mass energy is vital for jet studies. Nuclear size is an essential control variable in these experiments and a broad range from light to heavy nuclei would be desired for systematic studies of energy loss in a nuclear medium.

2.3 Summary of Machine Design Parameters for the EIC Physics

Having given an overview of the highlights of the EIC science and the machine requirements for achieving them, we summarize them here with additional comments. As summarized in section 1.2 in the EIC White Paper [1], where the important machine design parameters are discussed in detail, the successful scientific outcome of the EIC depends critically on: a) the luminosity, b) the center-of-mass energy, c) the lepton and light ion beam polarization, and d) having ion beams from deuteron to the heaviest nuclei. Two interaction regions are desired to ensure a robust physics program with complementary detector systems.

Luminosity

In the discussion of each physics topic we mentioned, the integrated luminosity needed. eRHIC is being designed to achieve peak luminosities between $10^{33-34} \text{cm}^{-2} \text{sec}^{-1}$. A luminosity of $10^{33} \text{cm}^{-2} \text{sec}^{-1}$ and strong hadron cooling ($L_{\text{peak}} = L_{\text{avg}}$) and an assumed 60%

operations efficiency for the collider complex, as routinely achieved by RHIC, yields an integrated luminosity of 1.5 fb^{-1} per month. Without strong hadron cooling for the same operations parameters, one would get a 30% reduction, as the average luminosity L_{avg} per fill is reduced to 70% of the peak luminosity L_{peak} . Most of the physics topics discussed in the EIC White Paper [1] and here are achievable with an integrated luminosity of 10 fb^{-1} , which corresponds to 30 weeks of operations. The exception is the study of the spatial distributions of quarks and gluons in the proton with polarized beams. These observables require up to a integrated luminosity of 100 fb^{-1} and would therefore benefit from an increased luminosity of $10^{34} \text{ cm}^{-2} \text{ sec}^{-1}$. It should be noted that many measurements can be performed simultaneously by judiciously choosing beam species and their spin orientation appropriately.

Center of Mass Energy

In the EIC White Paper [1], a range of \sqrt{s} of 20 to 140 GeV is suggested. A recent study [41] showed that most of the compelling science goals benefit from higher center-of-mass energy. A $\sqrt{s}_{eN} = 140 \text{ GeV}$ is needed to provide kinematic reach well into the gluon dominated regime. Some measurements require a variation in \sqrt{s} . While the minimum center-of-mass energy in the EIC White Paper [1] was indeed suggested as 20 GeV, recent studies suggest that 40-45 GeV [41] is sufficient. Therefore, the eRHIC design value of 29 GeV is a fine minimum operating energy.

Polarization of beams

EIC Physics involves two types of asymmetries: one is double spin asymmetries, requiring both electron and hadron beams to be polarized, and the other is single spin asymmetries, requiring only one beam—mostly the hadron beam—to be polarized. The statistical uncertainties for double spin asymmetries are $\delta A_{LL} \sim 1 / [P_e P_p \sqrt{N}]$, while for single spin asymmetries $\delta A = 1 / [P \sqrt{N}]$. Therefore high beam polarization is a very effective way to reduce statistical uncertainties. Measurements require longitudinal and transverse polarization orientation for protons, deuterons, ^3He and other polarizable light nuclei, and longitudinal polarization for the electron beam.

Nuclear Beams

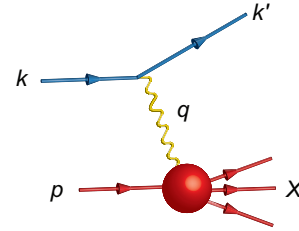
Ion beams of the heaviest nuclei (Gold, Lead, or Uranium) combined with the highest \sqrt{s} , will provide precocious access to the domain of saturated gluon densities and to understand how color propagates through nuclear matter. Light ions are also essential to study how such effects scales with A and for precision studies of the proton structure of short range nuclear interactions.

2.4 Scientific Requirements for the Detectors and IRs

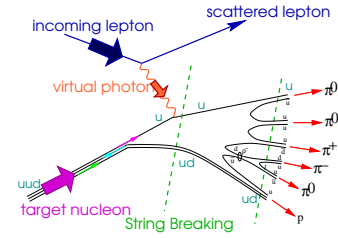
The physics program of an EIC, imposes several challenges on the design of a detector and, more globally the extended interaction region as it spans center-of-mass energies from 29 GeV to 141 GeV, different combinations of both beam energy and particle species, and several distinct physics processes. The EIC science program can be categorized in different experimental measurements as show in Table 2.1.

Table 2.1: Different experimental measurement categories at an EIC.

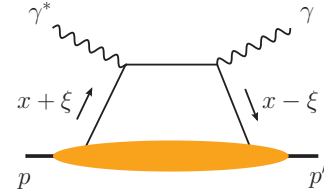
Inclusive DIS: $e + p/A \rightarrow e' + X$; for this process, it is essential to detect the scattered electron with high precision. The scattered electron is critical for all processes to determine the event kinematics.



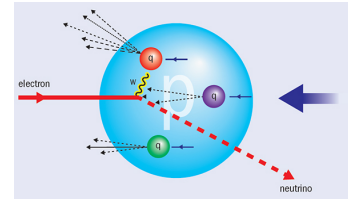
Semi-inclusive DIS: $e + p/A \rightarrow e' + h^{\pm,0} + X$, which requires detection of *at least one* hadron in coincidence with the scattered electron.



Exclusive DIS: $e + p/A \rightarrow e' + p'/A' + \gamma/h^{\pm,0}/VM$, which require the detection of *all* particles in the event with high precision.



electro-weak processes: $e + p/A \rightarrow \nu + X$; at high enough momentum transfer Q^2 , the electron-quark interaction is mediated by the exchange of a W^{\pm} gauge boson instead of the virtual photon. In this case the event kinematic cannot be reconstructed from the scattered electron, but needs to be reconstructed from the final state particles.



The directions of the beams are defined following the HERA@DESY convention: the hadron beam travels in the positive z-direction/pseudo-rapidity and the electron beam travels in the negative z-direction/pseudo-rapidity.

2.5 Scientific Requirements for the Detectors

In this section we will discuss only the scientific requirements on a multipurpose detector fully optimized for EIC physics that have consequences on the design of the interaction region. All the different physics processes to be measured at an EIC require the reconstruction of the event (x, Q^2, y, W) and final state particle kinematics (p_T, z, Φ, θ) with high precision. In order to access the full $x - Q^2$ range at different center-of-mass energies, the detector must be able to reconstruct events over a wide span in pseudo-rapidity.

2.5.1 Inclusive and Semi-inclusive DIS

To minimize the energy loss and multiple scattering of the scattered electron and not to degrade the resolution of the kinematic variables (x, Q^2, y, W) derived from the scattered electron, *the beam pipe needs to be as thin as possible and made from a low mass material, i.e. Beryllium*. As shown in Section 1.1, to study non-linear QCD effects at the largest gluon densities electron-nucleus (i.e. U, Pb, Au) collisions at the highest center-of-mass energies are required. At eRHIC, this means 18 GeV electrons colliding with heavy ion beams of 110 GeV to reach $Q^2 < Q_s^2$ ($\sim 1 \text{ GeV}^2$) at as low x as possible. Figure 2.12 shows the relationship between Q^2 and pseudo-rapidity of the scattered electron. To reach $Q^2 \sim 1 \text{ GeV}^2$, the scattered electron needs to be detected down to a pseudo-rapidity of -4, which corresponds to an angle of 2° off the beam line. The electron scattering angle especially at low Q^2 is independent of the hadron beam energy. *As such, no collider equipment can be installed inside the main detector volume and extend beyond 1.5° .*

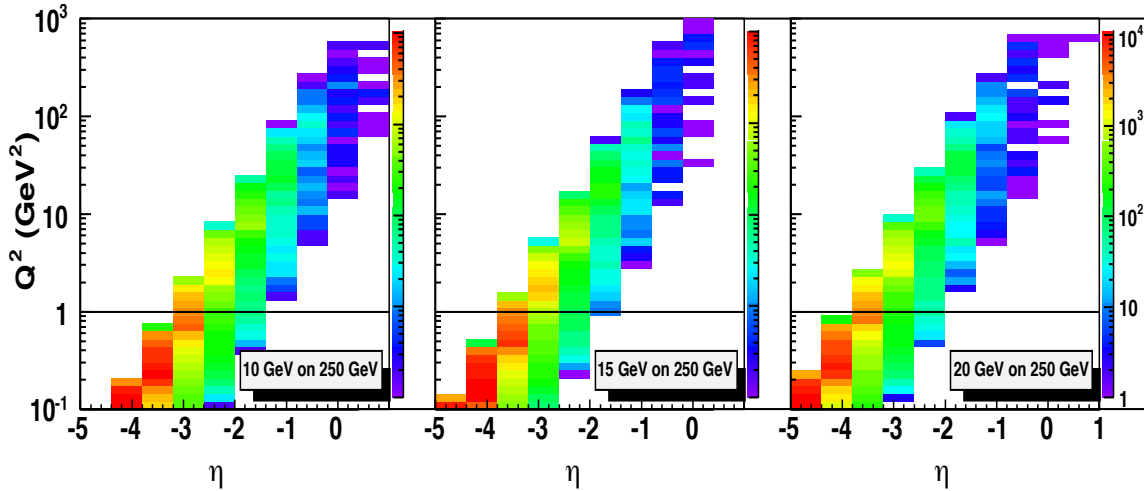


Figure 2.12: Q^2 vs. pseudo-rapidity in the laboratory frame for the scattered electron at different center-of-mass energies. The following cuts have been applied: $0.01 < y < 0.9$, with inelasticity, y , defined as the fraction of the electron's energy lost in the nucleon rest frame. The electron scattering angle especially at low Q^2 is independent of the hadron beam energy.

2.5.2 Exclusive Processes

Exclusive processes require a careful design of the detector and the IR in the outgoing proton/nucleus beam direction. Contrary to exclusive electron-proton events, for electron-nucleus collisions it is not possible to tag the outgoing intact scattered nucleus. Therefore, another technique needs to be realized to ensure exclusivity. One can require a "rapidity gap" in the detector, meaning that there is a region in the detector from the hadron beam towards the center of the detector in which there is no activity from the hadronic final state. The efficiency for detecting exclusive events and their purity therefore depends strongly on the rapidity coverage of the detector. Simulations have shown that a rapidity coverage of -2 to 4 is required to have detection efficiencies $> 90\%$ and a purities $> 90\%$ for exclusive $e + A$ events assuming a cross section ratio of Exclusive-to-DIS events of 10:90 as measured at HERA. *Therefore no collider equipment can be installed inside the main detector volume and/or extend beyond 1.5° in order to not compromise the efficiency and purity of exclusive events that are detected through the rapidity-gap method.*

2.5.3 General Purpose EIC Detectors

A possible baseline detector design, closely following the physics requirements outlined in the EIC White Paper [1], is shown in Figure 2.13. General IR requirements for any detector are similar due to the event geometries expected at the EIC, but details in detector design and technologies may differ. We assume the following characteristics for the present discussion.

The compact tracker, located symmetrically with respect to the IP, consists of a MAPS silicon barrel vertex detector augmented by a set of forward/backward disks, and a two meter long TPC with a gas volume outer radius of 0.8 m and several GEM stations, all placed into a 3 T solenoidal field. The TPC is specifically chosen as the main tracking element because of its small overall material budget as it minimizes the rate of photon conversions in detector components. Besides this, the TPC should provide good charged particle-identification (PID) at central rapidities complementing a DIRC or proximity focusing RICH. The vertex detector covering the central rapidity range $-1 < \eta < 1$ has four layers of high-resolution MAPS sensors with a $20\text{ }\mu\text{m}$ pixel size and an effective thickness of only $\sim 0.3\%$ radiation length per layer. Such a setup enables a momentum resolution better than 3% for scattered electrons and secondary charged hadrons for momenta up to a few tenths of GeV/c in the pseudo-rapidity range $-3 < \eta < 3$. For a compact forward tracker design, it is critical to maintain high spatial resolution. At present, a $20\text{ }\mu\text{m}$ MAPS pixel size, the same as for the vertex detector, is anticipated.

The detector will be equipped with a set of electromagnetic calorimeters, hermetically covering a pseudo-rapidity range of at least $-4 < \eta < 4$. The calorimeter technology choice is driven by the fact that a moderately high-energy resolution in the order of $\sim 2 - 3\%/\sqrt{E}$, is needed only at backward (electron-going) rapidities. Therefore, in the present design the backward endcap calorimeter for the $-4 < \eta < -1$ range is composed of PWO crystals at room temperature. At the very backward rapidities ($\eta < -3$), where tracker momentum

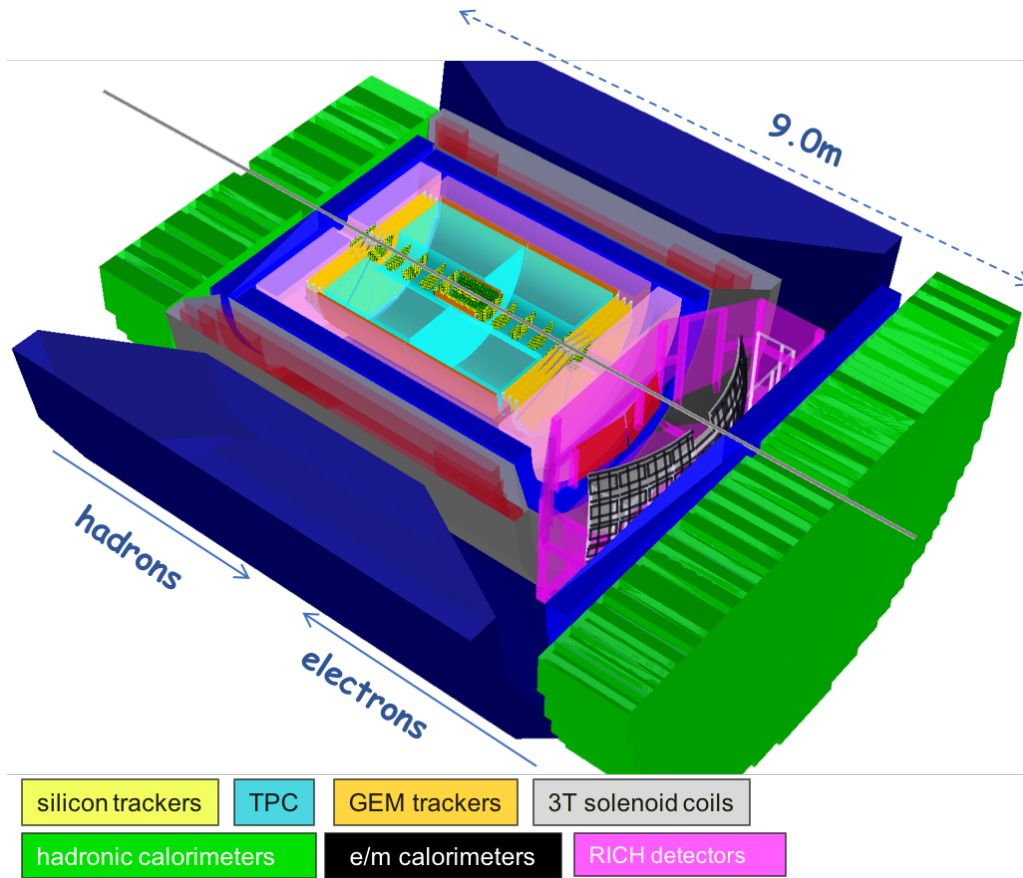


Figure 2.13: A dedicated eRHIC detector with tracker and calorimeter components implemented in the EicRoot GEANT simulation framework [62].

resolution is not sufficient to yield a reliable electron-hadron separation based on E/p , a hadronic calorimeter, installed behind the electromagnetic one, will be used. Both forward and backward hadronic calorimeters are of a sandwich lead scintillator plate sampling type. The calorimeters in the forward and backward directions are preceded by a RICH detector for PID. A compact design will still require ± 4.5 m space around the interaction point (IP). This impacts the required length around the IP that has to be kept free of machine elements, typically referred to as L^* .

2.6 Scientific Requirements for the Interaction Regions

To cover the physics program, as described in earlier sections, it is extremely important to integrate the detector into the interaction region *already during the early design stages* of the collider. In the following, the requirements will be discussed, categorized according to the processes described in Table 2.1.

2.6.1 Exclusive Processes

The detection of forward-going scattered protons from exclusive reactions, as well as of decay neutrons from the breakup of heavy ions in incoherent and non-diffractive reactions, is particularly challenging.

Electron-Proton Scattering: In general, for exclusive reactions, one wishes to map the four-momentum transfer, or Mandelstam variable t ($= p_T^2$ of the scattered proton) of the hadronic system, and then obtain an image of the spatial partonic structure of the proton by a Fourier transform of the (un)polarized cross section as function of t . Figure 2.14 shows what fraction of the beam momentum ($x_L = p'_L / p_{\text{Beam}}$) is carried by these scattered protons as measured by ZEUS at HERA [63] and the correlation between the proton scattering angle and its momentum. This illustrates that the remaining baryonic states go in the very forward proton-beam direction. Even at a proton energy of 50 GeV, the proton scattering angles only range to about 25 mrad. At proton energies of 250 GeV, this number is further reduced by a factor of five. In all cases, the scattering angles are small. As discussed earlier (see section 2.5), the main detector reaches down to a rapidity -4 to 4 , corresponding to 35 mrad from the beam line. Therefore, these protons are not seen in the main detector and need a different technique to be detected, i.e. Roman Pots. Their acceptance strongly depends on the exact interaction region design.

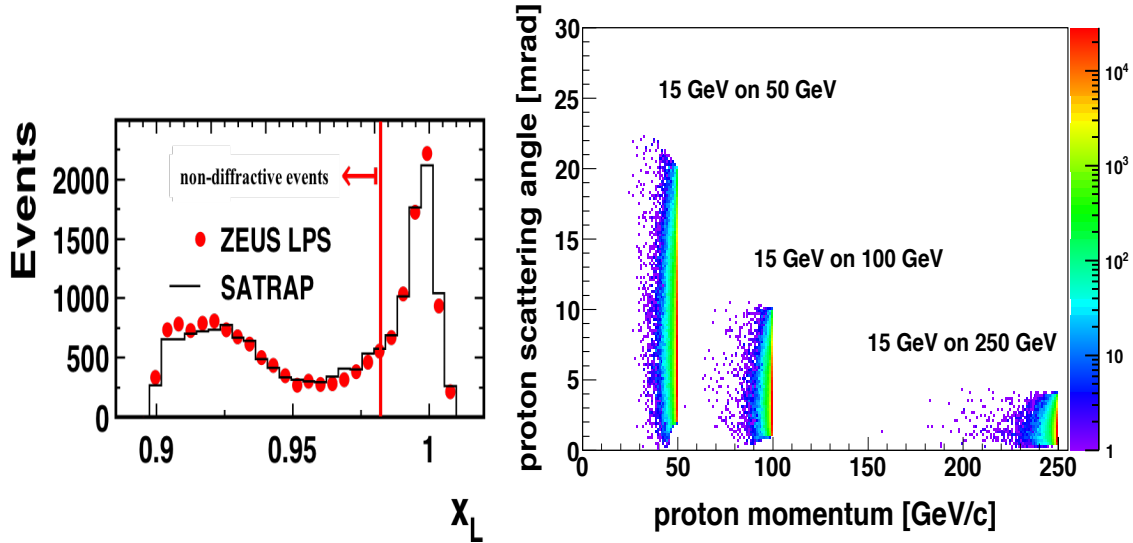


Figure 2.14: Left: Fraction of the beam momentum carried by the scattered protons as measured by ZEUS at HERA. Right: The scattered proton momentum vs. scattering angle in the laboratory frame for DVCS events with different beam energy combinations. The following cuts have been applied: $1 \text{ GeV}^2 < Q^2 < 100 \text{ GeV}^2$, $0.01 < y < 0.85$, $10 - 5 < x < 0.5$ and $0.01 \text{ GeV}^2 < t < 1 \text{ GeV}^2$. The angle of the recoiling hadronic system is directly and inversely correlated with the proton energy. It thus decreases with increasing proton energy.

Figure 2.15 (top) shows the cross section of exclusive real photon production (DVCS: $ep \rightarrow e'p'$) as function of t . The red dots represent the measurements and their statistical precision as obtained at eRHIC for $\sqrt{s} = 141$ GeV and an integrated luminosity of 10 fb^{-1} for $0.03 \text{ GeV}^2 < |t| < 1.6 \text{ GeV}^2$ corresponding to an acceptance in p_T of $0.18 \text{ GeV}/c < p_T < 1.3 \text{ GeV}/c$, which is the nominal requirement from the EIC White Paper. The blue curves represent an exponential fit to the measured points for different regions in t with the width of the band representing the uncertainty of the fit. The different rows show the result for different acceptances in p_T of the scattered protons. The lower row shows the impact parameter dependent PDF obtained from a Fourier transform of the cross section measurement with different p_T acceptances. The bands represent the parametric errors in the fit and the uncertainty from different extrapolations to the regions of unmeasured (very low and very high) p_T of the scattered protons. *Based on these studies and the EIC White Paper, protons with $0.18 \text{ GeV}/c < p_T < 1.3 \text{ GeV}/c$ need to be transported through the IR such that they can be detected as soon as they are separated from the core of the beam.*

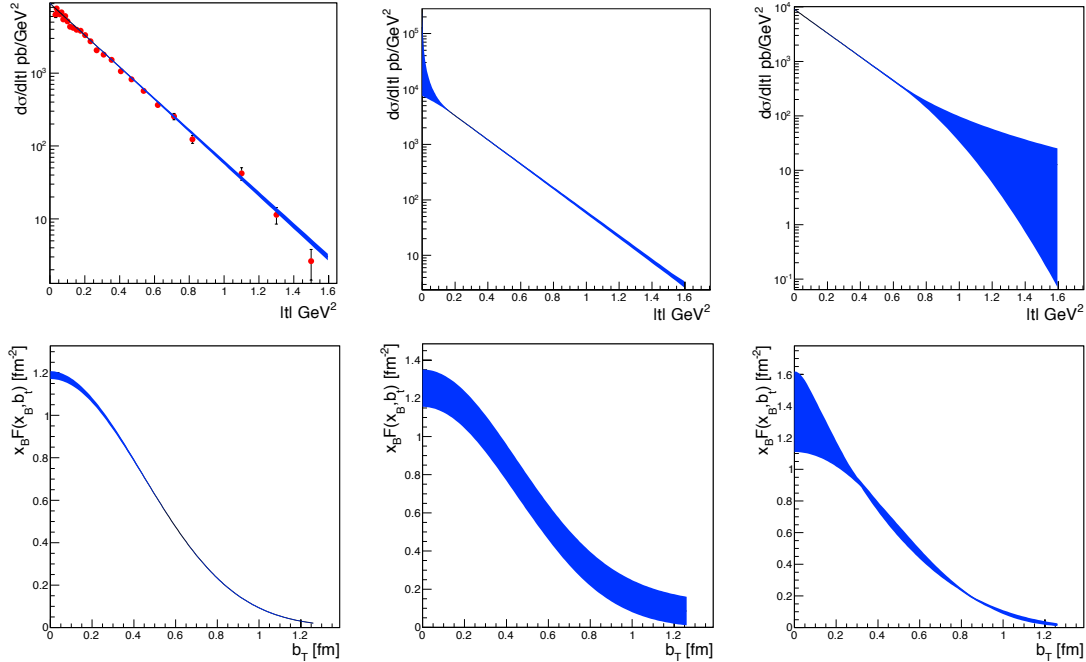


Figure 2.15: Top: The cross section as function of t . The red dots represent the measurements and their statistical precision as obtained at eRHIC for $\sqrt{s} = 141$ GeV and an integrated luminosity of 10 fb^{-1} . The blue curves represent an exponential fit to the measured points for different regions in t with the width of the band representing the uncertainty of the fit. The different rows show the result for different acceptances in p_T of the scattered protons. Bottom: The impact parameter dependent PDF obtained from a Fourier transform of the measured cross section with different p_T acceptances. The bands represent the parametric errors in the fit and the uncertainty from different extrapolations to the regions of unmeasured (very low and very high) p_T of the scattered protons. Left: $0.18 \text{ GeV}/c < p_T < 1.3 \text{ GeV}/c$, $0.03 \text{ GeV}^2 < |t| < 1.6 \text{ GeV}^2$; Middle: $0.44 \text{ GeV}/c < p_T < 1.3 \text{ GeV}/c$; Right: $0.18 \text{ GeV}/c < p_T < 0.8 \text{ GeV}/c$.

To obtain a full picture of the (un)polarized spatial partonic imaging of the proton it is critical to have measurements of the (un)polarized diffractive cross sections of reactions with a charge exchange, like $e + p \rightarrow e' + n$. In this case the four-momentum transfer t is obtained from the forward scattered neutrons. Figure 2.16 shows the correlation of the scattering angle of the neutrons as function of t for two different beam energy combinations. Like for the protons, the neutrons are scattered at very small angles with respect to the outgoing proton beam. *These neutrons with an angular distribution from 9 mrad (at $\sqrt{s} = 141$ GeV) to 26 mrad (at $\sqrt{s} = 32$ GeV) from the hadron beam axis need to be transported through the IR to a zero-degree calorimeter.*

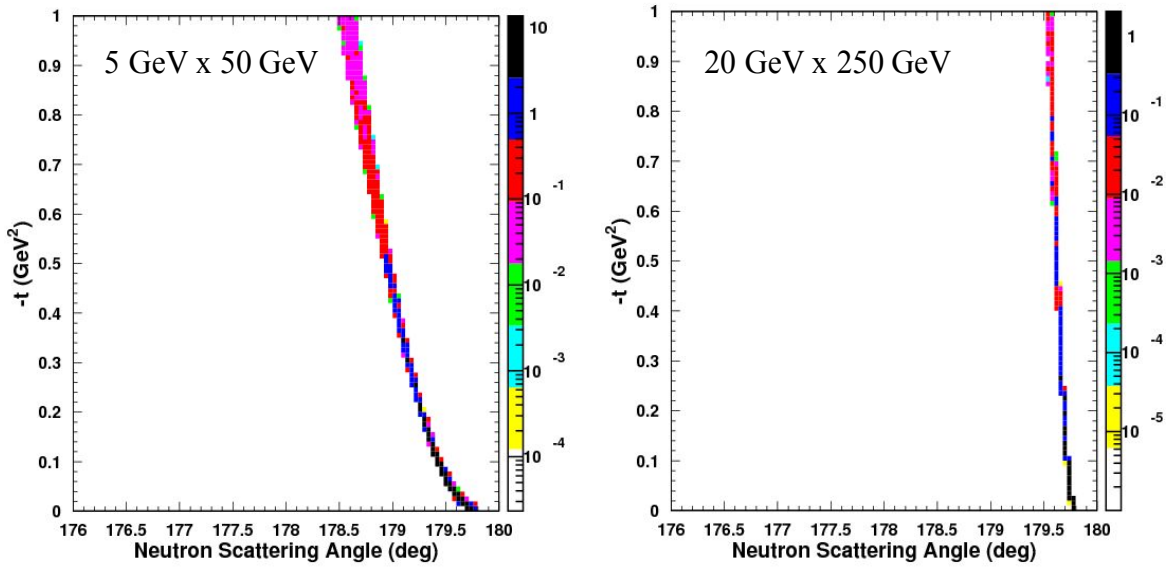


Figure 2.16: The neutron scattering angle as function of t in the laboratory frame for two different beam energy combinations. Note a scattering angle of 180° corresponds to the outgoing proton beam direction in this plot.

Electron-Nucleus Scattering: The only possible way to tag exclusive electron-nucleus events for heavy nuclei is to veto nuclear breakup. For coherent diffractive events the intact nucleus is scattered under very small forward angles in the outgoing beam direction and mainly remains inside the beam envelope. Tagging exclusive events can be realized by requiring no neutrons from the nuclear breakup in a zero-degree calorimeter. Figure 2.17 shows the breakup neutron momentum vs. scattering angle in the laboratory frame for different beam energies. *To achieve a very high tagging efficiency of $\sim 100\%$ for coherent diffractive electron-nuclei scattering events one needs to transport neutrons within a cone of four mrad to six mrad, depending on the beam energy, through the IR to a zero-degree calorimeter.*

For all the different processes, collision geometries in $e + A$ (See Figure 2.18) can be determined by utilizing the ZDC. The number of forward neutrons produced and detected in the ZDC is expected to be sensitive to the path length d of the parton and fragmentation

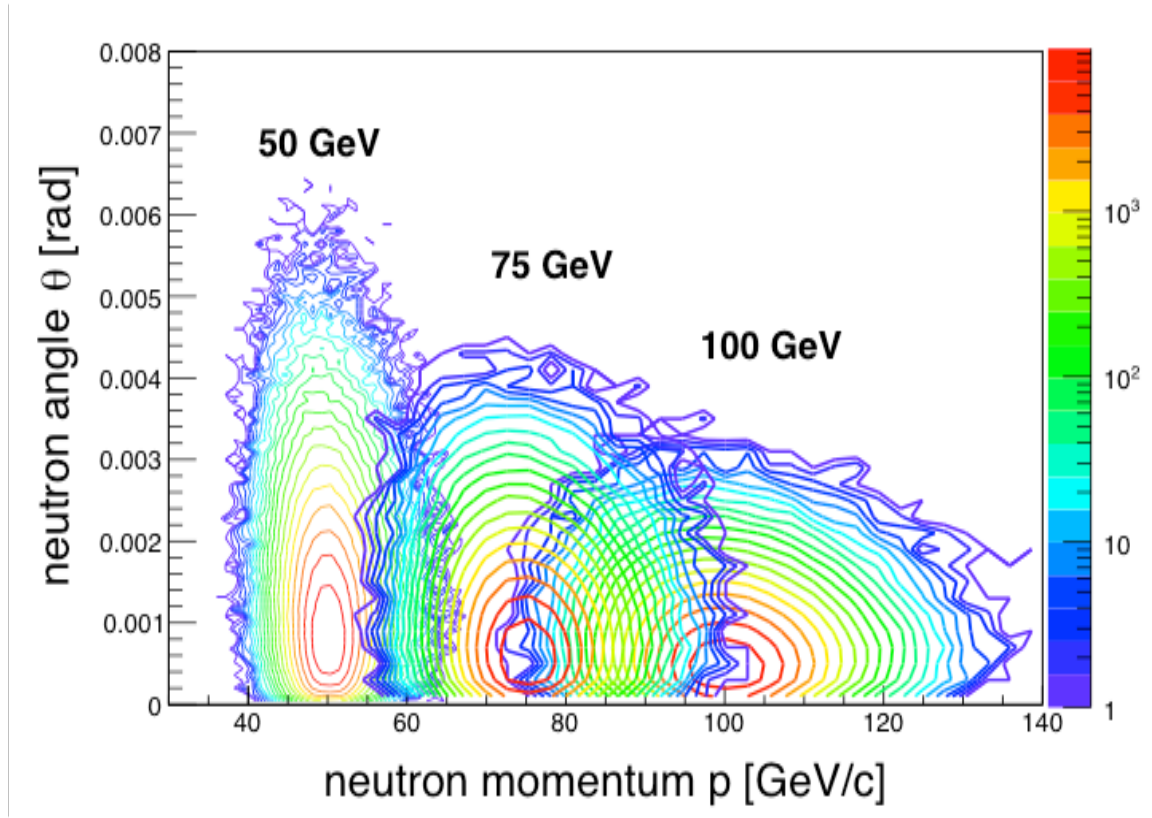


Figure 2.17: The scattered neutron momentum vs. scattering angle in the laboratory frame for different beam energies.

of the colliding nucleon along the virtual photon direction in the nucleus. See Figure 2.18 for the correlation between the number of forward scattered neutrons and the path length. The geometric information is an additional and useful gauge for investigating properties of partonic interactions in nuclei. While the impact parameter b has a correlation with the number of neutrons in the ZDC, the most “central” collision in $e + A$ ($b \sim 0$) can be identified from events with the highest neutron multiplicity since the longest path length of the nucleon fragmentation in the nucleus is expected to be at $b = 0$. This will be an effective tool for selecting events with maximized nuclear effects in SIDIS $e + A$ collisions, like e.g., dihadron correlation studies [60,65].

Recent physics studies showed that selecting on the number of neutrons to reach a centrality of $> 5\%$ enhances the effective A in the reaction, which is crucial for any measurements of non-linear effects in QCD. This, and the requirement that the four-momentum transfer t in diffractive reactions with a charge exchange is obtained from the neutron, requires a ZDC with higher energy resolution ($\approx 30\%/\sqrt{E}$) than is currently achieved at RHIC ($65\%/\sqrt{E} + 15\%$ for a ZDC size of $10\text{ cm} \times 10\text{ cm} \times 60\text{ cm}$). This requires more space in x - y to integrate a ZDC in order to minimize shower leakages in the transverse direction at 30 m from the IR. The required space will depend on the exact detector technology chosen; for examples see [66,67]. The longitudinal size required would be around one meter.

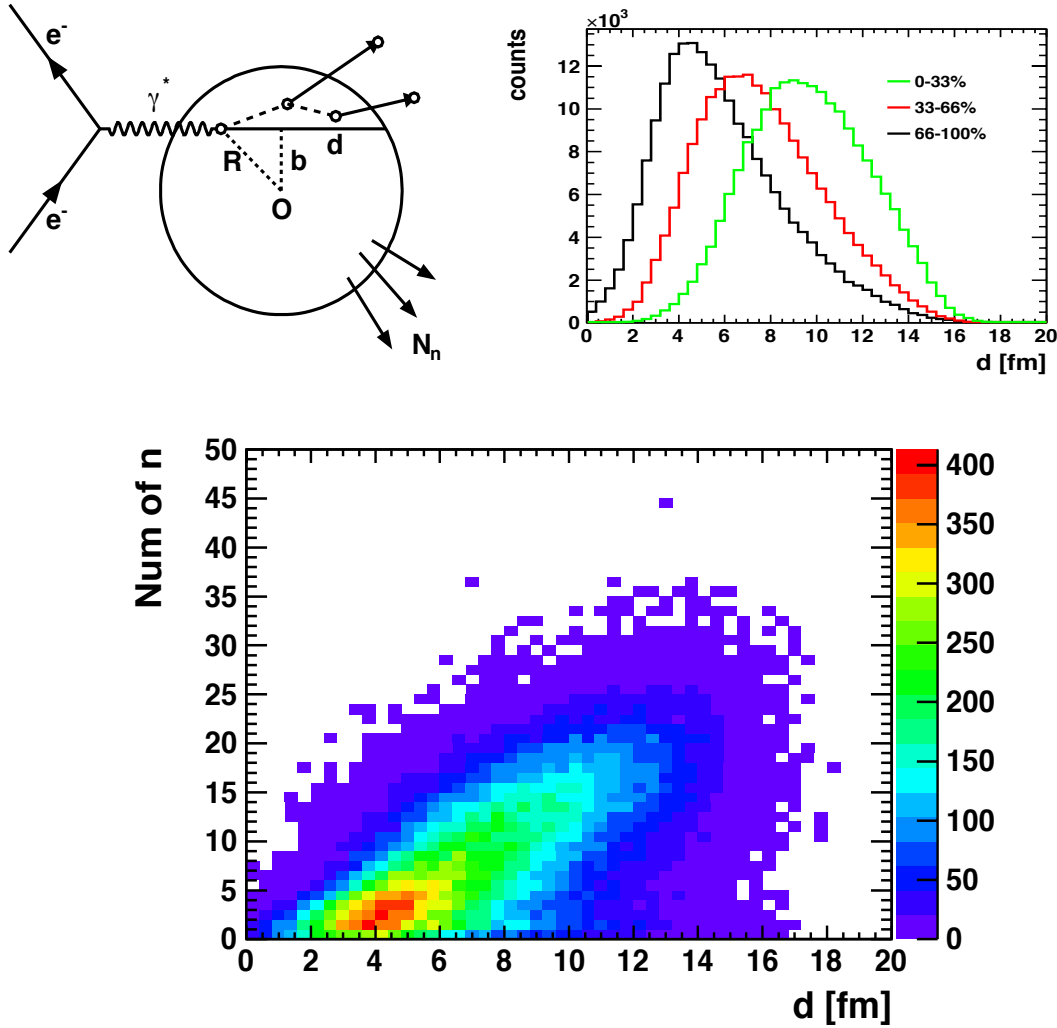


Figure 2.18: Top-left: Collision geometry of $e + A$, showing the path length d of the parton and fragmentation of the struck nucleon along the virtual photon direction. The impact parameter b is defined as the transverse distance between the center of the nucleon and the virtual photon. Top-right: Distribution of the path length as selected by the neutron multiplicity. The estimate done using DPMJet-III [64]. Bottom: Correlation between number of produced forward neutrons vs. path length of parton and fragmentation of the struck nucleon in the nucleus. All the forward neutrons can be detected in the ZDC.

2.6.2 Inclusive Processes

There are many physics topics beyond what was discussed in the EIC White Paper [1] that benefit from tagging the scattered electron at Q^2 values significantly below 1 GeV^2 . An example is the determination of the (un)polarized partonic structure of photons [61]. Scattered electrons with a $Q^2 < 0.5 \text{ GeV}^2$ cannot be detected in the main detector; therefore, as in HERA, a special low- Q^2 tagger is needed. The scattered electrons will be detected

in an electromagnetic calorimeter with several Si-tracking planes in front. Such a device needs to be well-integrated into the IR design and care needs to be taken to separate the scattered electrons from electrons from the bremsstrahlung process, which, due to its high cross section and the high eRHIC luminosity will be dominant. Figures 2.19 and 2.20 show several kinematic relations for the scattered electron, i.e. Q^2 vs. rapidity, Q^2 as function of the electron scattering angle, and its energy.

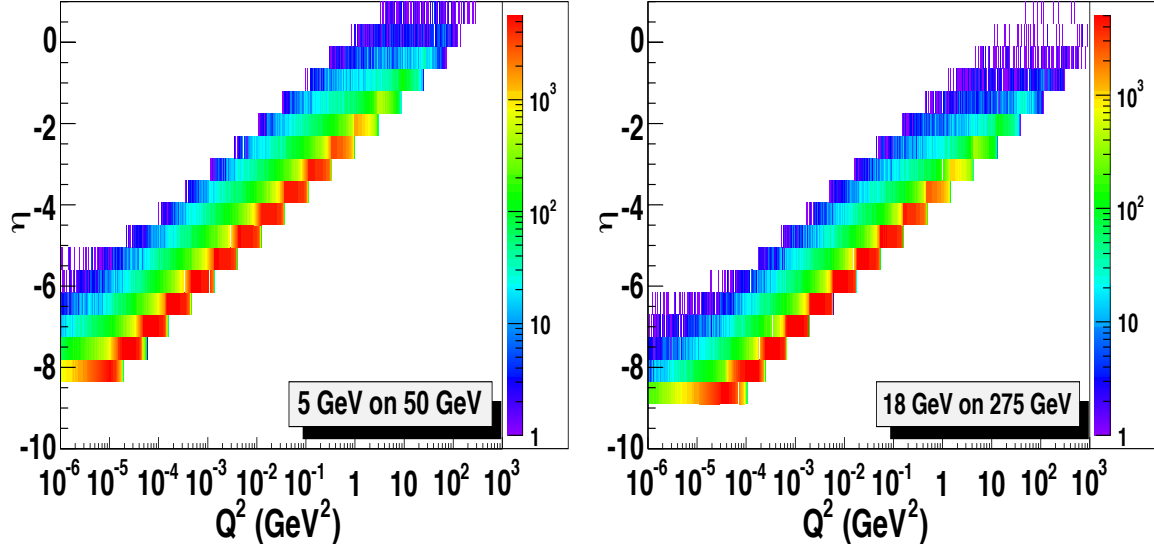


Figure 2.19: Relation between Q^2 of the scattered electron rapidity for 5 GeV and 18 GeV electron beam energy.

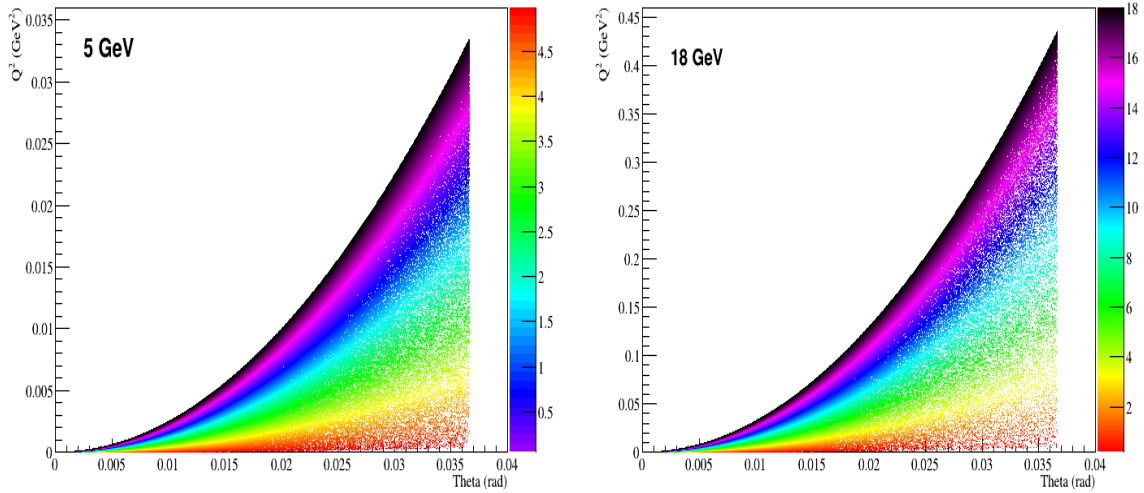


Figure 2.20: The relation between the scattered electron scattering angle and Q^2 for 5 GeV and 18 GeV electron beam energy. The colors indicate the energy of the scattered electron.

2.6.3 Electron-Nucleus Scattering

The physics program of an EIC requires electron-(un)polarized proton and neutron collisions to allow full flavor separation of (un)polarized parton distribution functions. As polarized neutron beams are not feasible, (un)polarized ^3He and deuterium beams constitute effective proxy for a neutron beam. To ensure that the scattering really occurred on the neutron, the spectator proton(s) need to be detected. Figure 2.21 shows the correlation

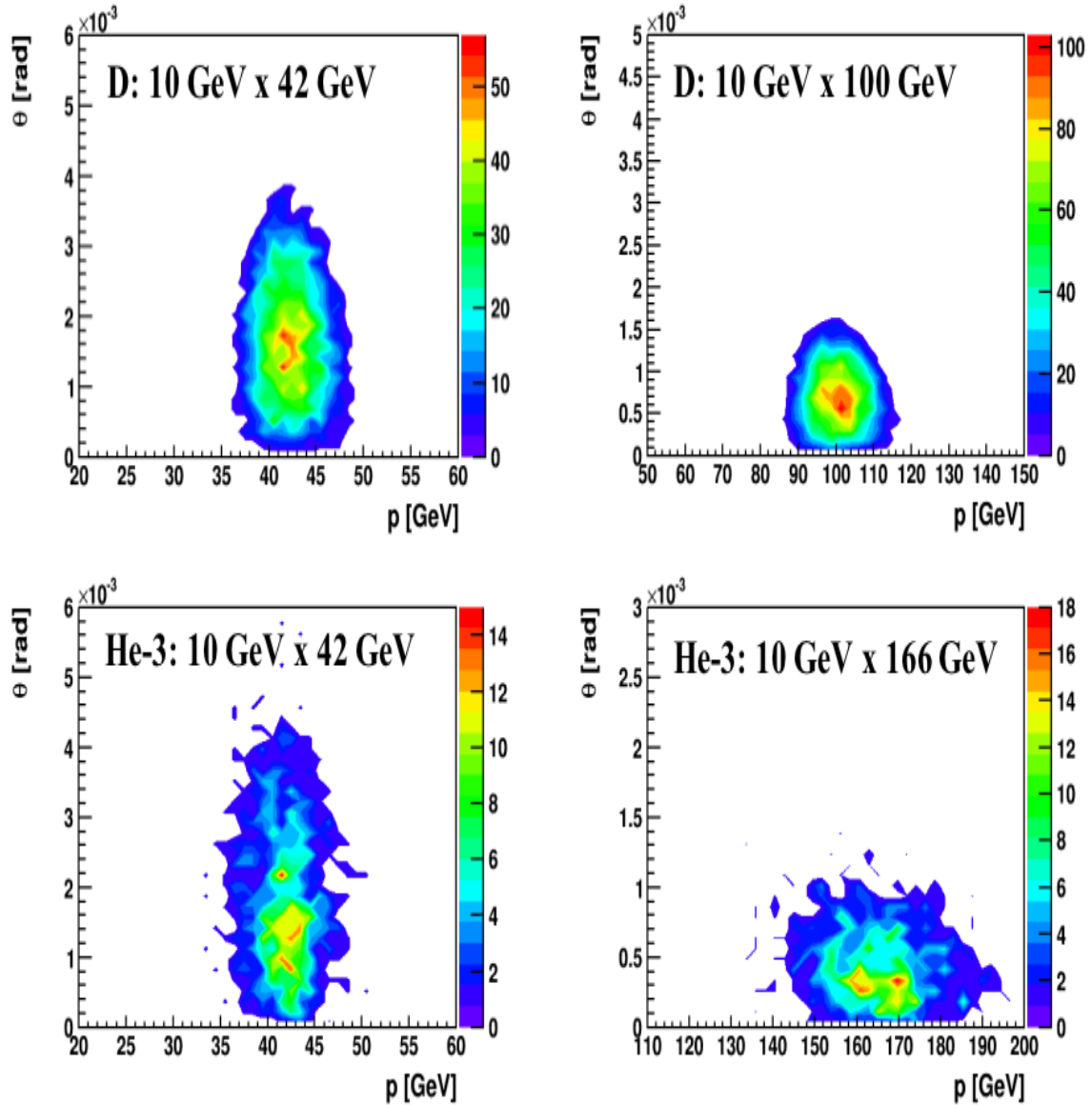


Figure 2.21: The correlation of momentum and scattering angle for the spectator proton in electron-deuteron and electron- ^3He -scattering for two different values of \sqrt{s} .

of momentum and scattering angle for the spectator protons from electron-deuteron and electron- ^3He scattering for two different values of \sqrt{s} . The detection of these spectator protons is challenging as they have small scattering angles and a different rigidity compared to the hadron beam, which leads to stronger bending in the magnets. The (un)polarized ^3He and deuterium beams do not only constitute effective neutron beams, but also provide the possibility to study how the proton structure is modified if bound in a nucleus. For this purpose, the spectator neutron needs to be tagged. These neutrons have the same distribution in scattering angle and momentum as the protons. Therefore, a ZDC with its acceptance optimized for break-up neutrons as described above (see Figure 2.17) will also have a high acceptance for these spectator neutrons.

2.6.4 Auxiliary Detectors

To utilize the full statistical power made possible by the high luminosity of 10^{33} to $10^{34} \text{ cm}^{-2} \text{ sec}^{-1}$, it is indispensable to have high precision measurements of the electron and hadron beam polarizations and the luminosity. Doubly polarized electron-hadron colliders are the best way to unravel the internal structure of the nucleons and are the only tools which will allow us to finally unravel how the spin of the proton is built by its quarks and gluons. Figure 7 in Ref. [45] shows, that for a high precision determination of the gluon contribution to the spin of the proton, the overall systematic uncertainty should be around two percent. An increase of the overall systematic uncertainty of five percent leads to a 30% increase in the uncertainty of the contribution of the gluons to the spin of the protons.

Luminosity

The bremsstrahlung process $e + p \rightarrow e + p + \gamma$ was used successfully for the measurement of luminosity by the HERA collider experiments [68–70]. It has the features of a precisely known large QED cross-section resulting in negligible statistical uncertainty. In contrast to HERA, where only the electron beam was polarized, both the electron and proton/light ion beams will be polarized in eRHIC. In this case the bremsstrahlung rate is sensitive to the polarization dependent term a in the cross section $\sigma_{\text{brems}} = \sigma_0(1 + aP_eP_h)$. Thus, the polarization (P_e, P_h) and luminosity measurements are coupled, and the precision of the luminosity measurement is limited by the precision of the polarization measurement. This also limits the precision of the measurement of double spin asymmetries $A_{LL} = 1/(P_eP_h)(N^{++/--} - RN^{+-/-})/(N^{++/--} + RN^{+-/-})$ through the determination of the relative luminosity $R = L^{++/--}/L^{+-/-}$. The precision needed for the relative luminosity measurement is driven by the magnitude of A_{LL} at low- x and Q^2 , which is typically on the order of 10^{-4} . At RHIC levels of 2 to 4×10^{-4} have been achieved. A factor of 2 to 5 improvement is required for the EIC. As discussed earlier, due to the high luminosity it is critical to minimize the systematic uncertainties; the requirement for the systematic uncertainty is $\delta L/L < 1\%$. The straightforward method for measuring bremsstrahlung is to use a calorimeter at zero degrees in the electron direction counting the resulting photons,

the distribution of which is strongly peaked in the forward direction. The calorimeter is also exposed to the direct synchrotron radiation fan and must be shielded, thus degrading the energy resolution. At peak HERA luminosities, the photon calorimeters were hit by 1-2 photons per HERA bunch crossing. At an EIC luminosity of $10^{33} \text{ cm}^{-2} \text{ s}^{-1}$, the mean number of photons per bunch crossing is over 20 for electron-proton scattering and increases with Z^2 of the target for nuclear beams. The distributions are broad, with a mean proportional to the number of photons per bunch crossing. The counting of bremsstrahlung photons thus is effectively an energy measurement in the photon calorimeter with all of the related systematic uncertainties (e.g. gain stability) of such a measurement. An alternative method to counting bremsstrahlung photons, used effectively by the ZEUS collaboration at HERA, employs a pair spectrometer. A small fraction of photons is converted into e^+e^- pairs in the vacuum chamber exit window. A dipole magnet splits the pairs and each particle hits a separate calorimeter adjacent to the unconverted photon direction. This has several advantages over a zero-degree photon calorimeter:

- The calorimeters are outside of the primary synchrotron radiation fan.
- The exit window conversion fraction reduces the overall rate.
- The spectrometer geometry imposes a low energy cutoff in the photon spectrum, which depends on the magnitude of the dipole field and the transverse location of the calorimeters.

The variable parameters of the last two points (conversion fraction, dipole field and calorimeter locations) may be chosen to reduce the rate to less than or of order one e^+e^- coincidence per bunch crossing even at nominal EIC luminosities. Thus, counting of bremsstrahlung photons is simply counting of e^+e^- coincidences in a pair spectrometer with only small corrections for pileup effects. Such a luminosity detector design needs careful integration into the machine lattice, not only to allow for enough space for the pair spectrometer, but also for the angular acceptance of the photons from the bremsstrahlung process which is especially critical. Figure 2.22 (top) shows the angular distribution of photons from the bremsstrahlung process $e + p \rightarrow e + p + \gamma$. The peak of the distribution sits at 0.03 mrad with a long tail towards higher angles. However, as the angular beam divergence of the electron beam is up to a factor 10 larger, it will completely determine the acceptance for the photons from the bremsstrahlung process. Figure 2.22 (bottom) indicates how the angular distribution is modified, including a crossing angle of 25 mrad, an electron beam angular divergence of 0.1 mrad, and a z-vertex distribution of $\pm 2.5 \text{ cm}$ (black curve), and how a x - y vertex distribution would impact the distribution (red curve).

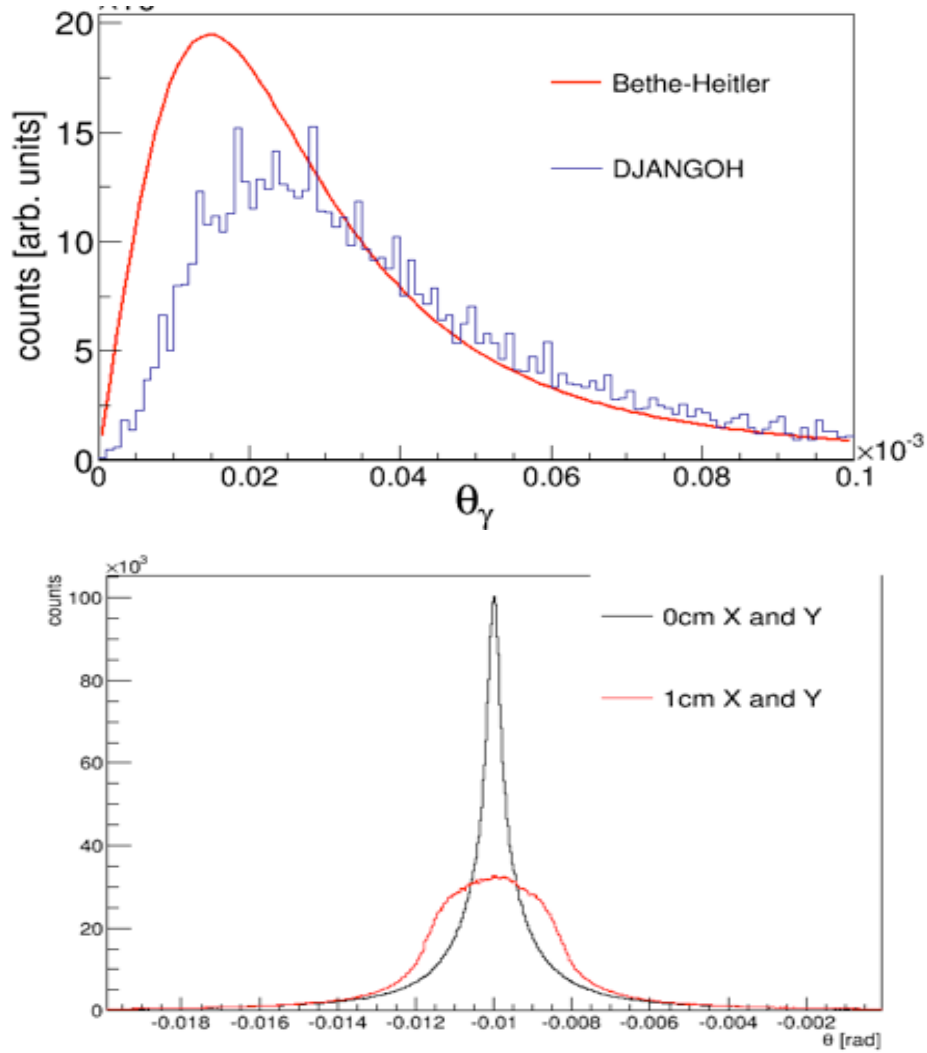


Figure 2.22: Top: The angular distribution of photons from the bremsstrahlung process $e + p \rightarrow e + p + \gamma$ calculated with two different models (DJANGO [71] and a "home-written" MC based on the analytic Bethe-Heitler equations) integrated in Monte Carlo codes. Bottom: The red curve illustrates how the angular distribution would be further modified if the vertex distribution would be spread out in x and y by ± 0.5 cm. The black curve accounts for a crossing angle of 25 mrad, a beam angular divergence of 0.1 mrad and a z -vertex distribution of ± 2.5 cm.

Lepton and Hadron Polarimetry

Lepton Polarization: Compton back-scattering is the established method to measure electron beam polarization in $e - p$ colliders. At HERA, there were two Compton back-scattering polarimeters [72], one measuring the transverse polarization (TPOL) of the beam

through a position asymmetry, and another one measuring the longitudinal polarization (LPOL) of the beam through an energy asymmetry in Compton back-scattered photons. The TPOL and LPOL systematic uncertainties of HERA RUN-I were 3.5% and 1.6% and Run-II 1.9% and 2.0%, respectively. To balance the expected high luminosity at the EIC, these systematic uncertainties should be reduced to $\sim 1\%$. Since it is not foreseen to measure the electron beam polarization at the IR, no constraints need to be considered. More details on eRHIC electron polarimetry can be found in Section ??.

Hadron Polarization: Measuring the hadron beam polarization is significantly more involved. Contrary to the electron case, there is no process that can be calculated from first principles. Therefore, a two-tier measurement is needed: one providing the absolute polarization, which normally has low statistical power, and a high statistical power measurement that measures the relative polarization. At RHIC [73], the single spin asymmetry A_N of the elastically scattered polarized proton beam on a polarized hydrogen jet is used to determine the absolute polarization. This measurement provides the average polarization per fill and for each proton beam with a statistical uncertainty on the order of $\approx 5\%$ and a systematic uncertainty of 3.2%. High-statistics bunch-by-bunch relative polarization measurements are provided by measuring the single spin asymmetry A_N for scattering the polarized proton beam off a carbon fiber target. To obtain absolute measurements, the pC-measurements are cross-normalized to the absolute polarization measurements from the hydrogen-jet polarimeter. The pC-measurements provide the polarization lifetime and the polarization profile per fill with high statistical precision. The achieved total systematic uncertainty for single spin asymmetries until 2015 is 3.4%.

The same concept is currently planned for all polarized hadron beams in the EIC, namely proton, deuterium, and ^3He [74]. It is foreseen to continue to have the absolute and relative hadron polarimeters located at IP12 in eRHIC; therefore, no constraints need to be considered for the IR.

However, there is the requirement for a local polarimeter between the spin rotators to monitor the degree of spin rotation from transverse in the arcs to longitudinal at the experiments. This can be done by integrating a fast, high precision proton-carbon (pC) polarimeter into the extended IR. This pC polarimeter is based on very small angle polarized proton-carbon elastic scattering in the Coulomb-Nuclear Interference region. The analyzing power is maximum for transverse or radial hadron beam polarization and goes to zero for longitudinal polarized hadron beams. The requirements on the extended IR region are purely spatial (~ 0.5 to 0.8 m) to integrate the scattering chamber for the carbon target intercepting the beam and the Si-detectors to measure the elastically scattered carbons. More details on the eRHIC absolute and relative hadron beam polarimetry can be found in Section ??.

2.6.5 Summary of Requirements for the Interaction Regions

Table 2.2 summarizes the requirements for the overall interaction region design derived from the EIC physics discussed in the 2010 INT Report [40], the EIC White Paper [1], and the document assessing the energy dependence of key measurements [41].

Table 2.2: Summary of the requirements from the physics program on the overall IR design.

	Hadron	Lepton
Machine element free region	± 4.5 m main detector beam elements $< 1.5^\circ$ in main detector volume	
Beam Pipe	Low mass material, i.e. Beryllium	
Integration of detectors	Local Polarimeter	
Zero Degree Calorimeter	$40 \text{ cm} \times 40 \text{ cm} \times 1 \text{ m}$ @ $s = 30 \text{ m}$	
scattered proton/neutron acc. all energies for $e + p$	Proton: $0.18 \text{ GeV}/c < p_T < 1.3 \text{ GeV}/c$ Neutron: $p_T < 1.3 \text{ GeV}/c$	
scattered proton/neutron acc. all energies for $e + A$	Proton and Neutron: $\theta < 6 \text{ mrad}$ (for $\sqrt{s} = 50 \text{ GeV}$) $\theta < 4 \text{ mrad}$ (for $\sqrt{s} = 100 \text{ GeV}$)	
Luminosity	Relative Luminosity: $R = L^{++/--}/L^{+-/-+} < 10^{-4}$	
		γ acceptance: $\pm 1 \text{ mrad}$ $\rightarrow \delta L/L < 1\%$
Low Q^2 -Tagger		Acceptance: $Q^2 < 0.1 \text{ GeV}$

Chapter 3

eRHIC Design

3.1 Beam Parameters, Luminosities and Complex Layout

3.1.1 Beam Parameters and Luminosities

Overview

The polarized Electron-Ion Collider eRHIC provides collisions of polarized electrons and polarized protons in the center-of-mass energy region from 20 to 141 GeV, and polarized electron-heavy ion collisions up to 89 GeV/n. This is accomplished by adding an electron storage ring with up to 18 GeV beam energy to the existing RHIC facility, and colliding those electrons with polarized protons or heavy ions stored in the “Yellow” RHIC ring operating at energies between 41 and 275 GeV (protons), or 41 to 110 GeV/nucleon (ions). The high electron energy requires a large bending radius of the electron storage ring, which will therefore be installed in the existing RHIC tunnel. Beams will be brought into collision in up to two interaction regions, namely in IR6 and IR8. Electron-proton luminosities reach $1.0 \times 10^{34} \text{ cm}^{-2}\text{sec}^{-1}$. These high luminosities require strong hadron cooling to counteract emittance growth due to intrabeam scattering, which is very challenging. To mitigate the risk associated with strong hadron cooling, a scenario which uses the existing “Blue” ring as a full-energy injector has been developed (see Appendix ??). In this scheme, the entire hadron fill in the “Yellow” ring is replaced approximately every hour at collision energy, thus keeping the luminosity nearly constant. In addition to this mitigation, a moderate luminosity scenario has been worked out that reaches luminosities of up to $4.3 \times 10^{33} \text{ cm}^{-2}\text{sec}^{-1}$ without cooling (Appendix ??).

These high luminosities are achieved by increasing the number of bunches, from 110 in the present RHIC to 1160 (580 without cooling), and operating both the electron and the hadron storage rings at their respective beam-beam limits. The beam-beam limits assumed in the design are based on parameters achieved - or even slightly exceeded - at RHIC (hadrons) and the e^+e^- collider B-Factories PEP-II and KEKB (electrons). In addition, a maximum synchrotron radiation power of 10 MW is chosen to limit operational costs. It is worthwhile mentioning that this is not a technical limitation; in KEKB, the synchrotron

radiation power loss per unit length, which at 10 kW/meter is state-of-the art, is more than twice as high as the 4 kW/meter in eRHIC.

Luminosity

The luminosity of an electron-ion collider is given as

$$\mathcal{L} = \frac{N_e N_h}{4\pi\sigma_x\sigma_y} H f_{\text{rep}}, \quad (3.1)$$

with N_e and N_h being the electron and hadron bunch intensities, respectively, and σ_x and σ_y the horizontal and vertical RMS beam sizes at the interaction point (IP), which are assumed to be identical for the two beams. H is a factor reflecting the impact of the hourglass effect and the crossing angle; it is near unity if the RMS bunch lengths are smaller than the IP β -functions β_x^* , β_y^* , and the crossing angle is corrected using crab cavities. $f_{\text{rep}} = N_b f_{\text{rev}}$ denotes the bunch repetition rate, with N_b the number of bunches per ring and f_{rev} the revolution frequency of the collider rings.

The numbers of particles per bunch, N_e and N_h , are constrained by the beam-beam parameters $\xi_{e,h,x,y}$ induced by each beam on the other, which are computed as

$$\begin{aligned} \xi_{e,h,x,y} &= \frac{r_{e,h}}{2\pi} \frac{N_{h,e} \beta_{e,h,x,y}^*}{\gamma_{e,h} \sigma_{h,e,x,y} (\sigma_{h,e,x} + \sigma_{h,e,y})} \\ &= \frac{r_{h,e}}{2\pi} \frac{N_{e,h}}{\gamma_{e,h} \epsilon_{h,e,x,y}} \frac{1}{1 + K_{x,y}}, \end{aligned} \quad (3.2)$$

where we have used

$$\sigma_{x,y} = \sqrt{\epsilon_{h,x,y} \beta_{h,x,y}^*} = \sqrt{\epsilon_{e,x,y} \beta_{e,x,y}^*}. \quad (3.3)$$

$r_{h,e}$ are the classical radii of the hadrons or electrons, $K_x = \sigma_x/\sigma_y$, and $K_y = \sigma_y/\sigma_x$, while $\epsilon_{h,x,y}$ and $\epsilon_{e,x,y}$ denote the horizontal and vertical emittances of the hadron and electron beam, respectively.

Expressing the bunch populations through the beam currents,

$$I_{h,e} = N_{h,e} q f_{\text{rep}}, \quad (3.4)$$

and combining Equations (3.1) to (3.4) we re-write the luminosity as

$$\mathcal{L} \propto H \sqrt{\gamma_e \gamma_h I_e I_h (1 + K_x)(1 + K_y)} \left(\frac{\xi_{h,x} \xi_{x,y} \xi_{e,x} \xi_{e,y}}{\beta_{h,x}^* \beta_{h,y}^* \beta_{e,x}^* \beta_{e,y}^*} \right)^{1/4}. \quad (3.5)$$

RHIC has achieved a beam-beam parameter of $\xi_p = 0.015$ in proton-proton collisions; we therefore base the eRHIC design on the same value. Beam-beam tune shift parameters in excess of $\xi_e = 0.1$ have been reached at the e^+e^- collider KEKB. The main parameters of that machine resemble the eRHIC electron ring as shown in Table 3.1, and can therefore

Table 3.1: Key design parameters of CESR-B [75], PEP-II [76,77], KEKB [78], and the eRHIC electron ring. The eRHIC numbers in parentheses correspond to the version without strong hadron cooling.

	CESR-B	PEP-II LER/HER	KEKB LER/HER	eRHIC
Circumference C [m]	768	2200	3000	3834
No. of bunches N_b	36	1588	1584	1160 (580)
Beam current I [A]	0.365	2.45/1.55	1.3/1.6	2.5
Bunch intensity N_e [10^{10}]	16.2	7.0/4.4	5.0/6.2	15 (30)
Beam-beam parameter ξ_e	0.062	0.064/0.055	0.12/0.1	0.1
Transv. damp. decr. δ [10^{-4}]	1.1	1.8/2	2.5	1.25

Table 3.2: Proton beam emittances and intensities achieved during regular RHIC operations.

Parameter	Value
Bunch Intensity [10^{10}]	26
RMS Normalized Emittance, h/v [μm]	2.5/2.5
Longitudinal Bunch Area [$\text{eV} \cdot \text{sec}$]	1.6

serve as a reference for eRHIC.

Taking into account all these constraints, the luminosity is maximized for flat beams with $K_x \gg 1$, as indicated by Equation (3.5). This is realized by both unequal β -functions, $\beta_x^* \gg \beta_y^*$, and unequal emittances, $\epsilon_x > \epsilon_y$. While the latter is achieved naturally in any flat electron storage ring due to the combined effects of synchrotron radiation damping and quantum excitation, the horizontal ion beam emittance needs to be increased intentionally, for instance by application of noise to a transverse kicker. In a well-decoupled, flat storage ring with vanishing vertical dispersion this is also aided by intrabeam-scattering (IBS).

The magnitudes of the hadron design emittances are chosen such that they can be achieved and maintained by the projected strong electron cooling facility, which has to counterbalance the emittance growth rates due to IBS. Without hadron cooling peak luminosities reach up to $4.3 \times 10^{33} \text{ cm}^{-2} \text{ sec}^{-1}$ based on hadron beam emittances close to those achieved during current RHIC operations, which are listed in Table 3.2.

To reach an electron beam-beam parameter $\xi_e = 0.1$, comparable to KEKB, sufficient synchrotron radiation damping is necessary. While the transverse synchrotron radiation damping decrement at KEKB was $\delta = 2.5 \times 10^{-4}$, simulation studies indicate that in eRHIC a transverse damping decrement of $\delta = 1.25 \times 10^{-4}$ is sufficient for stable operation at $\xi_e = 0.1$. This is consistent with the fact that the maximum beam-beam parameter at KEKB reached $\xi_e = 0.12$.

IP β -functions

The minimum achievable IP β -functions β^* are limited by a number of factors. The β -functions and therefore the transverse RMS beam sizes reach their maximum in the low- β quadrupoles which are located at a distance l^* from the interaction point (IP) according to

$$\beta(l^*) = \beta^* + \frac{(l^*)^2}{\beta^*}. \quad (3.6)$$

The eRHIC Physics program requires a machine-element free space of ± 4.5 m around the IP. In practice, due to required vacuum system elements such as warm-to-cold transitions and bellows, the first magnets cannot be installed closer to the IP than approximately at $l^* > 5$ m. The large β -functions resulting from small values of β^* require large apertures in those low- β magnets. As a consequence, for a given gradient requirement in those magnets, the peak field has to increase accordingly. In order to reduce the risk and cost associated with building and operating those magnets, the maximum peak field for the eRHIC IR magnets is kept low enough for conventional NbTi technology. For an electron ion collider IR we must have coil structures that provide large magnetic fields in the hadron beam aperture while shielding the electron beam from these fields, and the eRHIC experimental physics program requires some hadron magnets to have very large apertures.

Large β -functions in the focusing quadrupoles result in large contributions to the chromaticity ζ of the machine lattice,

$$\zeta = \frac{1}{4\pi} \oint k(s)\beta(s) ds, \quad (3.7)$$

where $k(s)$ denotes the quadrupole strength. This chromaticity has to be compensated using sextupole magnets in the arcs. Due to the nonlinear nature of those magnets they limit the dynamic aperture of the machine. Experience at other colliders shows that sufficient dynamic aperture can be achieved as long as the chromatic contribution of the interaction region, ζ_{IR} , does not exceed approximately 1/3 of the chromaticity of the arcs,

$$\zeta_{\text{IR}} < \frac{1}{3}\zeta_{\text{arcs}}. \quad (3.8)$$

In the eRHIC electron ring lattice, this condition is fulfilled as long as the maximum β -functions in the low- β quadrupoles do not exceed $\hat{\beta} \simeq 800$ m.

Small values of β^* in conjunction with long hadron bunches lead to a geometric reduction of the luminosity. Assuming Gaussian beams, this so-called hourglass effect can be expressed as

$$\begin{aligned} R(t_x, t_y) &= \frac{L}{L_0} \\ &= \int_{-\infty}^{\infty} \frac{\exp(-t^2)}{\sqrt{(1 + t^2/t_x^2)(1 + t^2/t_y^2)}} \frac{dt}{\sqrt{\pi}}, \end{aligned} \quad (3.9)$$

with

$$t_x^2 = \frac{2(\sigma_{x,p}^{*2} + \sigma_{x,e}^{*2})}{(\sigma_{z,p}^2 + \sigma_{z,e}^2)(\sigma_{x,p}^{*2}/\beta_{x,p}^{*2} + \sigma_{x,e}^{*2}/\beta_{x,e}^{*2})}. \quad (3.10)$$

In addition, the finite eRHIC crossing angle of $\theta = 25$ mrad causes a further reduction of the luminosity despite the use of crab cavities due to the finite wavelength of the 338 MHz crab cavities, which causes a significant residual offset of the head and the tail of the long hadron bunch w.r.t. the electron bunch. In the limit of short electron bunch length and small crossing angle ($\sin \theta \approx \theta$), the luminosity can be expressed as

$$L = \frac{2f_b N_p N_e}{\sigma_{z,p}(2\pi)^{3/2}} \int_{-\infty}^{\infty} dz \frac{\exp \left\{ -\frac{(\hat{x} \sin(2kz) - \theta z)^2}{2(\sigma_{x,e}^2 + \sigma_{x,p}^2)} - \frac{z^2}{\sigma_{z,p}^2} \right\}}{\sqrt{(\sigma_{x,e}^2 + \sigma_{x,p}^2)(\sigma_{y,e}^2 + \sigma_{y,p}^2)}}, \quad (3.11)$$

where k is the crab cavity RF wavelength, $k = 2\pi f_{\text{crab}}/c$, \hat{x} is the maximum offset at the IP due to the crab cavity, and the z dependence of the transverse beam sizes are included. The luminosity is close to maximum when $2k\hat{x} = \theta$. To limit the geometric luminosity loss due to the hourglass effect and the finite wavelength of the crab cavities, the lowest β^* values should not be significantly smaller than the RMS hadron bunch length. Taking $\sin x \approx x - x^3/6$ the two terms in the exponential of Equation (3.11) are equal at $z = \sigma_{z,p}$ when

$$2\hat{x}k^3\sigma_{z,p}^3 = 3\sqrt{\sigma_{x,p}^2 + \sigma_{x,e}^2}, \quad (3.12)$$

which can be used to judge the relative importance of bunch length and crab wave number as compared to transverse beam size. This shows that short hadron bunch length is important.

Lastly, the EIC physics program requires detection of protons with a transverse momentum as low as $p_{\perp} = 200$ MeV/c. At 275 GeV proton beam energy, for instance, this translates into a scattering angle of 0.72 mrad. In order to detect these scattered particles, the divergence angle of the proton beam itself at the IP has to be smaller than this scattering angle, so the scattered particles travel outside the proton beam envelope where they can be intercepted by dedicated detectors. Experience at HERA has shown that such ‘‘Roman Pots’’ can be operated safely at a transverse distance of about 10σ from the beam center, where σ denotes the RMS beam size at the location of the Roman Pot. This restricts the RMS proton beam divergence at the IP to a tenth of the minimum scattering angle to be detected, $10\sigma' \leq 72$ mrad in at least one transverse plane. For a given proton beam emittance this, in turn, limits the minimum β -function at the IP to

$$\beta^* \geq \epsilon/\sigma'^2 \quad (3.13)$$

The short hadron bunch lengths require small longitudinal emittances in order to limit the resulting momentum spread $\Delta p/p$ for a given bunch length, which would otherwise exceed the off-momentum dynamic aperture of the machine. In conjunction with high bunch intensities, these small hadron beam emittances, on the other hand, result in fast

emittance growth rates of approximately 2 h due to intrabeam scattering (IBS) in the $10^{34} \text{ cm}^{-2} \text{ sec}^{-1}$ luminosity version. This growth needs to be counteracted by strong hadron cooling to achieve typical store lengths of 10-12 hours. In the moderate luminosity scenario, minimum IBS growth times are 8 h, which is comparable to present RHIC and therefore does not require cooling.

Beam heating

While short, intense hadron bunches are desirable to maximize the luminosity, they cause a significant heat load for the cryogenic system due to the resistive wall impedance of the stainless steel vacuum chamber inside the RHIC superconducting magnets, which scales as the product of total beam current, I , and peak bunch current, \hat{I} ,

$$P_{\text{cryo}} \propto I \cdot \hat{I}. \quad (3.14)$$

We will copper-coat the existing RHIC beam pipes in-situ to reduce their resistivity and thus reduce the cryogenic heat load to less than 1 W/m.

With a given machine circumference of $C = 3834 \text{ m}$, the large number of hadron bunches, up to 1160, together with the high bunch intensity may give rise to electron clouds. The threshold for this instability depends strongly on the secondary electron yield (SEY) of the vacuum pipe surfaces. Simulations show that below an SEY of 1.2 the instability does not occur. To reduce the secondary electron yield of the beam pipes to a sufficiently low value, in-situ application of a thin amorphous carbon layer on top of the copper coating is foreseen.

RF system

Together with the reduced longitudinal emittance achieved by bunch splitting, high RF voltages are required to reach the desired short bunch lengths. It is planned to upgrade the present RF system, which consists of 28 and 197 MHz cavities, with a 591 MHz RF system, thus limiting the required RF voltage due to the higher harmonic number.

The total electron beam current $I_e = e \cdot N_e \cdot f_b$, where e is the electron charge, is limited by the available RF power required to restore the synchrotron radiation losses. This radiated power can be expressed as

$$P [\text{kW}] = 88.46 \cdot \frac{E_e [\text{GeV}]^4}{r [\text{m}]} \cdot I_e [\text{A}]. \quad (3.15)$$

Here E_e is the electron beam energy, and r the dipole bending radius of the storage ring. To limit the required investment cost for the storage ring RF system as well as the operating cost, the synchrotron radiation power has been limited to 10 MW. The RF system in the electron storage ring consists of superconducting 591 MHz two-cell cavities. With a voltage of 3 MV per cell, a total of 24 cells are required to provide the necessary voltage at 18 GeV beam energy. The cavities are located in IR10.

Besides the RF power requirement the electron beam intensity is limited by collective ef-

fects, namely the coupled bunch instability (CBI) and the transverse mode coupling instability (TMCI).

Beam polarization

Both the electron and the proton beam in eRHIC require a high degree of polarization. Polarized protons with up to 65% polarization at energies up to 250 GeV have already been routinely achieved using two Siberian Snakes in RHIC. Relocation of the two existing Siberian Snakes from the Blue RHIC ring to the Yellow ring, which will be used for eRHIC, and converting Blue spin rotators into two additional Siberian Snakes for the Yellow ring is expected to increase spin polarization to the 70% level. Additional improvements planned in the AGS will raise this level to 80%.

High polarization with arbitrary spin patterns in the electron ring is achieved by injecting bunches with the desired spin orientation at full collision energy. Bunches with their spin orientation parallel to the main dipole field of the storage ring will slowly reverse their polarization direction due to the Sokolov-Ternov effect. It is therefore necessary to replace entire bunches at a rate significantly faster than the Sokolov-Ternov time constant.

The shortest Sokolov-Ternov (de-)polarization time over the entire energy range of the electron storage ring occurs at 18 GeV, where it reaches $\tau_{S-T} = 28$ min. Replacing individual bunches after approximately 4 min ensures a high level of polarization in either spin orientation. Short bunch trains of 4 individual bunches are replaced at a rate of 1 Hz.

Electron bunches are generated in an SLC-type polarized electron gun. The SLC gun has routinely generated 16 nC electron bunches at a 120 Hz rate with over 80% polarization. This performance is sufficient for eRHIC, which requires 10 nC at 1 Hz and similar polarization levels. After pre-acceleration in a 400 MeV normal-conducting S-band linac these bunches will be injected into a rapid-cycling synchrotron (RCS) in the RHIC tunnel to be accelerated to full collision energy of up to 18 GeV. The RCS is ramped once per second within 200 msec from 400 MeV to 18 GeV.

In order to preserve polarization during acceleration, the RCS lattice has a high superperiodicity. Together with the appropriate choice of the betatron tune this ensures that no intrinsic spin resonances are encountered during the entire ramp to 18 GeV. This high superperiodicity is somewhat broken due to the required bypass around the eRHIC detector. However, spin tracking studies have shown that less than 2% of the initial polarization is lost during the ramp to 18 GeV even with an RMS orbit error of 1 mm. The RF system in the RCS is comprised of normal-conducting 591 MHz cavities with a total voltage of 72 MV.

Polarized protons are injected from the existing AGS at 25.5 GeV, and accelerated to full storage energy in the eRHIC hadron storage ring. With the maximum design bunch intensity and longitudinal emittance being about half the values presently achieved in RHIC, the required values can be reached by longitudinal bunch splitting. This splitting can be performed either in the AGS or in RHIC. In the former case, injecting only one of the resulting two bunches while discarding the second one allows bunch-by-bunch variations of the spin pattern in the eRHIC hadron ring, while splitting bunches in the eRHIC hadron ring leads to spin patterns consisting of pairs of bunches with equal spin orientation.

While the spin orientation in both the electron and the proton beam is vertical in the storage ring arcs, the experiments require longitudinally polarized beams. The necessary spin rotation is accomplished by the existing helical dipole rotators in the proton ring, and by solenoid-based spin rotators in the electron machine. Spin matching is required to preserve spin polarization in the presence of these solenoids.

Interaction region

The beams are brought into collision in either one or two interaction regions (IRs), at 6 o'clock (present STAR location) and 8 o'clock (PHENIX/sPHENIX). The two beams collide at a total crossing angle of 25 mrad, which provides early beam separation to avoid parasitic collisions, and allows low- β quadrupoles for the two beams to be installed close to the interaction point, with the first magnet located just outside the ± 4.5 long detector. The crossing angle is compensated by sets of crab cavities in each beam. These 394 MHz double quarter-wave crab cavities are scaled versions of the 400 MHz HL-LHC prototype crab cavities.

Beam parameters

The beam parameters with and without strong hadron cooling and the resulting luminosities of electron-proton collisions at different center-of-mass energies \sqrt{s} are listed in Tables 3.3 to 3.4. The required bunch intensities and longitudinal emittances can be achieved by longitudinal splitting of bunches with parameters very similar to present RHIC (see Table 3.2), assuming a moderate increase of the bunch intensity listed in the Table from 26×10^{10} to 30×10^{10} protons/bunch. The horizontal design emittances with strong hadron cooling are very close to the ones already achieved, while the much smaller vertical emittances are achieved and maintained by cooling. Depending on the actual cooling scheme, this process may also affect the horizontal plane where cooling is not desirable. The details of how to overcome this conundrum still need to be worked out.

Without hadron cooling, the vertical design emittances are identical to the ones achieved in RHIC, except for the case of highest center-of-mass energy $\sqrt{s} = 141$ GeV, which requires a slightly smaller vertical emittance that can be achieved by scraping in the AGS. The horizontal emittances without cooling are about twice as large as in present RHIC and can be easily achieved by application of noise to a broadband kicker or a deliberate injection mismatch.

Tables 3.5 and 3.6 show parameters and luminosities for collisions of electrons with fully stripped gold ions ($Z = 79$, $A = 197$). Without strong hadron cooling stochastic cooling can be used to maximize the luminosities. The existing RHIC stochastic cooling system needs to be upgraded for efficient operation with reduced bunch spacing between ion bunches (in 660 bunch mode). This upgrade is expected to be straightforward.

Table 3.3: eRHIC beam parameters for different center-of-mass energies \sqrt{s} , with strong hadron cooling. High divergence configuration.

Species	proton		electron		proton		electron		proton		electron	
Energy [GeV]	275	18	275	10	100	10	100	5	41	5	28.6	
CM energy [GeV]	63.2											
Bunch intensity [10^{10}]	20.5	6.2	6.9	17.2	6.9	17.2	4.7	17.2	2.6	13.3		
No. of bunches	290		1160		1160		1160		1160			
Beam current [A]	0.74	0.227	1	2.5	1	2.5	0.68	2.5	0.38	1.93		
RMS norm. emit, h/v [μm]	4.6/0.75	845/72	2.8/0.45	391/24	4.0/0.22	391/25	2.7/0.27	196/20	1.9/0.45	196/34		
RMS emittance, h/v [nm]	16/2.6	24/2.0	9.6/1.5	20/1.2	37/2.1	20/1.3	25/2.6	20/2.0	44/10	20/3.5		
β^* , h/v [cm]]	90/4.0	59/5.0	90/4.0	43/5.0	90/4.0	167/6.4	90/4.0	113/5.0	90/7.1	196/21.0		
IP RMS beam size, h/v [μm]	119/10		93/7.8		183/9.1		150/10		198/27			
K_x	11.8		11.9		20.0		14.9		7.3			
RMS $\Delta\theta$, h/v [μrad]	132/253	202/202	103/195	215/156	203/227	109/143	167/253	133/202	220/380	101/129		
BB parameter, h/v [10^{-3}]	3/2	100/100	14/7	73/100	10/9	75/57	15/10	100/66	15/9	53/42		
RMS long. emittance [10^{-3} , eV $\cdot\text{sec}$]	36		36		21		21		11			
RMS bunch length [cm]	6	0.9	6	2	7	2	7	2	7.5	2		
RMS $\Delta p/p$ [10^{-4}]	6.8	10.9	6.8	5.8	9.7	5.8	9.7	6.8	10.3	6.8		
Max. space charge	0.006	neglig.	0.003	neglig.	0.028	neglig.	0.019	neglig.	0.05	neglig.		
Piwinski angle [rad]	5.6	0.8	7.1	2.4	4.2	1.2	5.1	1.5	4.2	1.1		
Long. IBS time [h]	2.1		3.4		2		2.6		3.8			
Transv. IBS time [h]	2		2		2.3/2.4		2/4.8		3.4/2.1			
Hourglass factor H	0.86		0.86		0.85		0.83		0.93			
Luminosity [$10^{33}\text{cm}^{-2}\text{sec}^{-1}$]	1.65		10.05		4.35		3.16		0.44			

Table 3.4: eRHIC beam parameters for different center-of-mass energies \sqrt{s} , with strong hadron cooling. High acceptance configuration.

Species	proton electron		proton electron		proton electron		proton electron		proton electron	
Energy [GeV]	275	18	275	10	100	10	100	5	41	5
CM energy [GeV]	140.7		104.9		63.2		44.7		28.6	
Bunch intensity [10^{10}]	19.53	6.248	6.9	17.2	6.9	17.2	4.7	17.2	2.6	13.3
No. of bunches	290		1160		1160		1160		1160	
Beam current [A]	0.71	0.227	1	2.5	1	2.5	0.68	2.5	0.38	1.93
RMS norm. emit., h/v [μm]	4.9/0.62	845/42.3	2.8/0.45	391/22	3.5/0.25	391/27	2.7/0.27	196/20	1.9/0.45	196/34
RMS emittance, h/v [nm]	16.7/2.1	24.0/1.2	9.6/1.5	20/1.1	33/2.4	20/1.4	25/2.6	20/2.0	44/10	20/3.5
β^* , h/v [cm]	395/4.0	274/7.0	227/4.0	109/5.5	102/4.0	169/6.8	90/4.0	113/5.0	90/7.1	196/21
IP RMS beam size, h/v [μm]	256/9.2		148/7.8		184/9.7		150/10		198/27	
K_x	0.036		18.9		18.9		14.9		7.3	
RMS $\Delta\theta$, h/v [μrad]	65/229	94/131	65/196	135/143	180/243	109/143	167/253	133/202	220/380	101/129
BB parameter, h/v [10^{-3}]	3/1	100/71	14/5	75/71	11/8	75/57	15/10	100/66	15/9	53/42
RMS long. emittance [10^{-3} , eV·sec]	36		36		21		21		11	
RMS bunch length [cm]	6	0.9	6	2	7	2	7	2	7.5	2
RMS $\Delta p/p$ [10^{-4}]	6.8	10.9	6.8	5.8	9.7	5.8	9.7	6.8	10.3	6.8
Max. space charge	0.006	neglig.	0.003	neglig.	0.027	neglig.	0.019	neglig.	0.05	neglig.
Piwnski angle [rad]	2.6	0.4	4.5	1.5	4.2	1.2	5.1	1.5	4.2	1.1
Long. IBS time [h]	2		3.4		2		2.6		3.8	
Transv. IBS time [h]	2		2		2.0/3.0		2/4.8		3.4/2.1	
Hourglass factor H	0.88		0.87		0.85		0.83		0.93	
Luminosity [$10^{33} \text{ cm}^{-2} \text{ sec}^{-1}$]	0.83		6.4		4.07		3.16		0.44	

Table 3.5: eRHIC beam parameters for e-Au operation for different center-of-mass energies \sqrt{s} , with strong hadron cooling.

Species	Au ion		electron		Au ion		electron		Au ion		electron		Au ion		electron	
Energy [GeV]	110	18	110	10	110	110	5	46.9	110	110	5	28.6	41	41	5	5
CM energy [GeV]	89.0		66.3		66.3		46.9		46.9		28.6		28.6		28.6	
Bunch intensity [10^{10}]	0.08	7.29	0.05	17.2	0.05	0.05	17.2	0.05	0.05	17.2	0.036	17.2	0.036	0.036	17.2	17.2
No. of bunches	290		1160		1160		1160		1160		1160		1160		1160	
Beam current [A]	0.23	0.26	0.57	2.50	0.57	0.57	2.50	0.57	0.57	2.50	0.41	2.50	0.41	0.41	2.50	2.50
RMS norm. emit., h/v [μm]	5.1/0.7	705/20	5.0/0.4	391/20	5.0/0.4	5.0/0.4	196/20	5.0/0.4	5.0/0.4	196/20	3.0/0.3	196/20	3.0/0.3	3.0/0.3	196/20	196/20
RMS emittance, h/v [nm]	43.2/5.8	20.0/0.6	42.3/3.0	20.0/1.0	42.3/3.0	42.3/3.0	20.0/2.0	42.3/3.0	42.3/3.0	20.0/2.0	68.1/5.7	20.0/2.0	68.1/5.7	68.1/5.7	20.0/2.0	20.0/2.0
β^* , h/v [cm]]	91/4	196/41	91/4	193/12	91/4	91/4	193/6	91/4	91/4	193/6	90/4	307/11	90/4	90/4	307/11	307/11
IP RMS beam size, h/v [μm]	198/15		196/11		196/11	196/11		197/11	197/11		248/15		248/15	248/15		
K_x	0.077		0.057		0.057	0.057		0.056	0.056		0.061		0.061	0.061		
RMS $\Delta\theta$, h/v [μrad]	218/379	101/37	216/274	102/92	216/274	215/275	102/185	215/275	215/275	102/185	275/377	81/136	275/377	275/377	81/136	81/136
BB parameter, h/v [10^{-3}]	1/1	37/100	3/3	43/47	3/3	3/2	86/47	3/2	3/2	86/47	5/4	61/37	5/4	5/4	61/37	61/37
RMS long. emittance [10^{-3} , eV·sec]	16		16		16	16		16	16		16		16	16		
RMS bunch length [cm]	7	0.9	7	2	7	7	2	7	7	2	11.6	2	11.6	11.6	2	2
RMS $\Delta p/p$ [10^{-4}]	6.2	10.9	6.2	5.8	6.2	6.2	6.8	6.2	6.2	6.8	10	6.8	10	10	6.8	6.8
Max. space charge	0.007	neglig.	0.008	neglig.	0.008	0.008	neglig.	0.008	0.008	neglig.	0.038	neglig.	0.038	0.038	neglig.	neglig.
Piwnski angle [rad]	4.4	1.1	4.5	1.2	4.5	4.5	1.5	4.5	4.5	1.5	5.8	1.2	5.8	5.8	1.2	1.2
Long. IBS time [h]	0.33		0.36		0.36	0.36		0.36	0.36		0.85		0.85	0.85		
Transv. IBS time [h]	0.81		0.89		0.89	0.89		0.89	0.89		0.16		0.16	0.16		
Hourglass factor H	0.85		0.85		0.85	0.85		0.85	0.85		0.71		0.71	0.71		
Luminosity [$10^{33} \text{cm}^{-2} \text{sec}^{-1}$]	0.59		4.76		4.76	4.77		4.77	4.77		1.67		1.67	1.67		

Table 3.6: eRHIC beam parameters for e-Au operation for different center-of-mass energies \sqrt{s} , with stochastic cooling.

Species	Au ion	electron	Au ion	electron	Au ion	electron	Au ion	electron
Energy [GeV]	110	18	110	10	110	5	41	5
CM energy [GeV]	89.0		66.3		46.9		28.6	
Bunch intensity [10^{10}]	0.10	7.29	0.10	30	0.08	30	0.09	30
No. of bunches	290		580		580		580	
Beam current [A]	0.29	0.26	0.57	2.18	0.44	2.18	0.50	2.18
RMS norm. emit, h/v [μm]	2.0/2.0	845/60	2.0/2.0	391/102	2.0/2.0	196/63	2.0/2.0	196/113
RMS emittance, h/v [nm]	16.9/16.9	24.0/1.7	16.9/16.9	20.0/5.2	16.9/16.9	20.0/6.4	45.4/45.4	20.0/11.5
β^* , h/v [cm]	288/12	203/116	91/12	77/39	146/12	113/31	149/50	339/196
IP RMS beam size, h/v [μm]	221/45		124/45		157/45		261/150	
K_x	0.202		0.363		0.284		0.577	
RMS $\Delta\theta$, h/v [μrad]	77/380	109/38	136/376	161/116	108/380	127/144	174/302	77/77
BB parameter, h/v [10^{-3}]	3/1	35/100	11/4	66/93	11/3	100/96	9/5	100/100
RMS long. emittance [10^{-3} , eV $\cdot\text{sec}$]	64	0.9	64	2	64	2	64	2
RMS bunch length [cm]	15	0.9	18	5.8	18	6.8	18	6.8
RMS $\Delta p/p$ [10^{-4}]	10	10.9	10	5.8	10	6.8	13	6.8
Max. space charge	0.001	neglig.	0.001	neglig.	0.001	neglig.	0.007	neglig.
Piwinski angle [rad]	8.5	0.5	18.1	2.0	14.3	1.6	8.6	1.0
Long. IBS time [h]	2.65		2.65		3.39		2.02	
Transv. IBS time [h]	1.02		0.80		1.32		0.93	
Hourglass factor H	0.54		0.54		0.54		0.65	
Luminosity [$10^{33}\text{cm}^{-2}\text{sec}^{-1}$]	0.14		2.06		1.27		0.31	

3.1.2 Layout of eRHIC Accelerator Systems

The eRHIC accelerator complex is composed of the existing systems that constitute present RHIC and some systems which have been added. The most important existing system is the RHIC storage ring with its superconducting magnets inside the RHIC tunnel. Only one of the two superconducting rings, the “Yellow” ring, is used for eRHIC. The ring is composed of six sextants separated by straight sections. The straight sections are labeled as “2, 4, 6, 8, 10 and 12 o’clock”, with 12 o’clock being in the northernmost part of the ring, or, alternatively, as IR2 to IR12. The ring complex also includes the hadron injector chain with the AGS synchrotron, the Booster synchrotron, the injector linacs and the particle sources. Furthermore there is a large cryogenic 4 K liquid helium plant located near IR6 that feeds the superconducting magnets.

New systems are the electron beam complex consisting of the electron storage ring, the electron injector synchrotron, and the electron injector. The storage ring and the injection synchrotron are located in the RHIC tunnel. In addition there is a 150 MeV energy recovery linac which provides electrons for strong hadron cooling.

The utility space of the present RHIC complex is not sufficient to host the equipment. A number of new buildings is required. These are described in Sections ?? and ??.

Figure 3.1 provides an overview of the layout of the eRHIC facility. The diagram shows the RHIC tunnel and labels indicate which of the new systems are located at or near which straight section. The new systems are summarized as follows:

- IR6 and 8:
IR6 and IR8 accommodate the eRHIC colliding beam detectors and the magnetic lattices required for the interaction regions. The interaction region straights also host the spin rotators for electron and hadron beams, and the crab cavities for both beams. For the hadron beam two times two crab cavities are required. The spin rotators of the hadrons are identical to present RHIC. The crab cavities require a small 2 K liquid He plant.
- IR4:
The hadrons traveling from the injection line via the “Blue” arc from IR6 to IR4 are injected in IR4 and the new fast injection kickers of 25 m total length are located there. This straight section also accommodates the room temperature RF for hadrons. The hadron storage RF system needs an upgrade for splitting each bunch into 4 bunches and to provide short bunches for collisions. These systems, consisting of 49 MHz and 98 MHz cavities for splitting, and 591 MHz storage cavities, are placed there as well.
- IR2:
This straight section hosts instrumentation, feedback systems, the electron source, the 400 MeV S-band injector linac, and the beam dumps.
- IR12:
This straight section accommodates the polarimeters for both electron and hadron

beams. The section will also contain the set up for electron cooling. At this location a small 2 K liquid He plant is needed for the superconducting ERL.

- IR10:
IR10 hosts the hadron beam abort and the electron RF systems for storage ring and rapid cycling synchrotron.

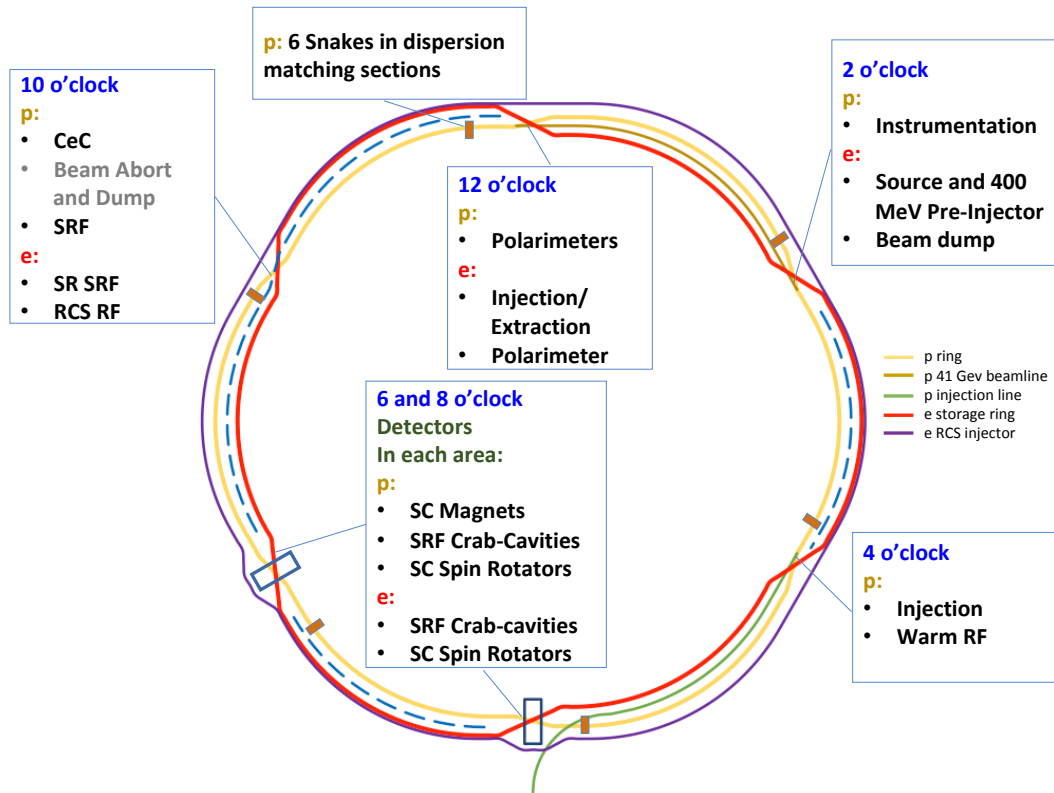


Figure 3.1: Schematic layout of locations of eRHIC Accelerator Hardware Systems. The yellow lines represent the “Yellow” ring for hadrons. The brown line indicates the hadron injection line using the “Blue” arc, and the Blue arc in sector 2-12 which is used for 41 GeV operation of hadrons, which requires a shorter circumference. The red line represents the electron storage ring and the blue line the rapid cycling injector synchrotron. The dashed line is the unused part of the “Blue” ring which will stay in place. Note that the lattice and simulations described in this document are for the case of a single detector at the 6 o'clock area. Calculations with a second detector at the 8 o'clock area are in progress. Initial studies for the two-detector configuration are described in Sections ?? and ??.

3.2 Interaction Region Development

3.2.1 Interaction Region Design Concept

The design parameters of eRHIC and their rationale have been discussed in Sections 3.1.1. Some parameters relevant for the interaction region design are repeated in Table 3.7 for convenience.

Table 3.7: Key beam parameters at the energy point of highest luminosity relevant for the interaction region design.

E_{CM} [GeV]	Proton 105	Electron	Proton 140	Electron	Proton 29	Electron
Energy [GeV]	275	10	275	18	41	5
ϵ_x [nm]	9.6	20.0	15.8	24.0	43.6	20.0
ϵ_y [nm]	1.5	1.2	2.5	2.0	10.3	3.5
β_x^* [cm]	90	43	90	59	90	196
β_y^* [cm]	4.0	5.0	4.0	5.0	7.1	21.0

The purpose of the interaction region (IR) is to focus the beams to small spot sizes at the collision point and to separate them into their respective beam lines while providing the space and geometry required by the physics program for the detector. The separation is accomplished by a total crossing angle of 25 mrad between the two beams, which has the advantage of avoiding the introduction of separator dipoles in the detector vicinity that would generate huge amounts of synchrotron radiation. The detrimental effects of this crossing angle on the luminosity and beam dynamics are compensated by a crab-crossing scheme. Figure 3.2 shows a zoom in of the rear and forward side of the IR.

The layout of the interaction region (IR) fulfills the following requirements:

- To achieve high luminosity, small beam cross sections are required. The beams are strongly focused at the interaction point (small β^*) by low- β -quadrupole magnets (also referred to as final focusing quadrupoles).
- The final focusing quadrupoles must have sufficient aperture for the large beam size at their location.
- Large contributions to the chromaticity, which is a set of parameters characterizing the energy sensitivity of the beam optics, are generated in the low- β quadrupoles. Chromaticity needs to be compensated by nonlinear sextupole fields which, in turn, limit the dynamic aperture. The IR design balances small β^* and tolerable values of chromaticity.

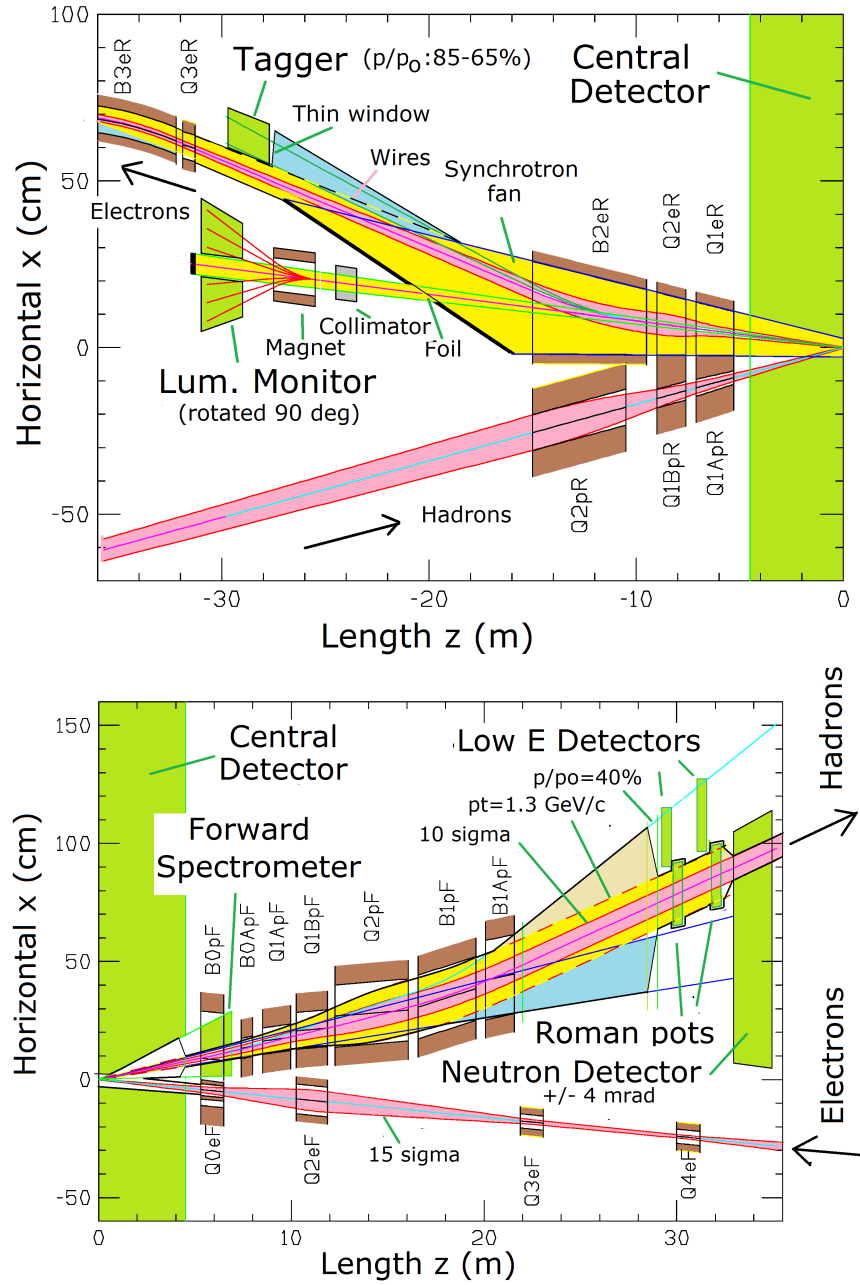


Figure 3.2: A zoom of the interaction region layout in the rear (top) and forward (bottom) directions.

- The colliding beam detector requires a large acceptance of protons scattered off the collision point. Therefore, we do not place accelerator components inside the detector (± 4.5 m from the IP). Some of the low- β quadrupoles have even larger apertures so that scattered protons and neutrons can be detected by detector elements placed further downstream.

- The beam divergence (and the minimum β^*) is restricted to enable detection of forward scattered protons with transverse momentum as small as $p_t = 200 \text{ MeV}/c$. These particles are then outside the 10σ proton beam envelope and are detectable by near-beam-detectors, “Roman Pots”, which are placed along the forward hadron beam pipe.
- The beams collide under a crossing angle of 25 mrad to separate the electron and proton beams quickly, to avoid parasitic collisions and to provide space for a neutron detector at zero degree in the forward ¹ direction and the luminosity detector in the rear side where the electron exit. An important factor is the large bunch frequency (up to 99 MHz , which corresponds to only 10 ns bunch spacing) required for high luminosity. The crossing angle effects (enlarged transverse beam size and excitation of synchro-betatron resonances) must be compensated for by using crab cavities, transverse RF resonators which kick the head and the tail of the proton (and electron) bunches in opposite directions in the plane of the crossing angle. These cavities are placed at a horizontal betatron phase advance of $\pi/2$ from the interaction point (IP) on both the rear- and the forward sides, forming a 180° bump. This causes the bunches to be tilted in the horizontal plane by exactly half the crossing angle at the IP, and provides (ideally) the same collision geometry as head-on collisions and thereby avoids synchrobetatron coupling.
- Strong synchrotron radiation, which might be generated by the electron beam, can destroy sensitive detector equipment and make data-taking impossible. Therefore, we argue that the electron beam must not experience dipole fields in the interaction region (IR), and certainly not upstream of the IP (we use the term forward side). This is another strong reason why the two beams must collide at a crossing angle. Synchrotron radiation generated in the low- β quadrupoles on the rear-electron side should be absorbed on the rear side of the IR as far as possible from the detector so as to minimize backscattered photons. This requires an extra large aperture for the electron low- β quadrupole magnets on the downstream side of the IP.
- Both the light hadron and electron beams are spin polarized. Polarization is only stable if the polarization direction coincides with the direction of the guide field in the arc. In collisions, the spins of the electron beam are oriented longitudinally and the ones for the hadron beam either longitudinally or transverse. Thus the IR design accommodates pairs of spin rotators, which ensures longitudinal spin at the IP and vertical spin in the arcs. The spin rotators in the hadron ring already exist and are unchanged in this design. The spin rotators for the electron beam consist of two pairs of strong solenoids with quadrupole magnets in-between each pair which are tuned such that the x - y coupling by the two solenoids cancels. This set of four solenoids is required on both sides of the IP. The beam transport between the rotators is “spin transparent”. This means that the magnetic fields in quadrupole magnets experienced by a particle performing betatron and synchrotron oscillations cancel between the spin rotators.

¹The IP separates the IR into a forward and a rear side or direction. The forward side is the side of the proton beam coming from the IP and the rear side is the side of protons going to the IP.

- The IR layout must provide room for a luminosity monitor on the rear side. This monitor detects hard γ -rays that are generated in the Bethe-Heitler process and exploited for luminosity measurement. The dipole magnet bending the electrons away from the path of the γ beam is at the same time a spectrometer magnet for the off-momentum electrons generated at low Q^2 .
- On the forward proton side, a neutron spectrometer is required. A dipole magnet bends the hadron beam away from the collision axis to provide space for this element. It also generates dispersion which helps to detect forward scattered protons in detectors that are integrated into the hadron beam pipe (called “Roman Pots”)

The small β -functions at the IP necessitate focusing elements as close as possible to the IP. This is accomplished by a combination of dual-aperture magnets and single-aperture quadrupoles with field-free regions for the electron beam, as shown in Figures 3.3. Design magnet apertures are chosen such that a minimum aperture radius of 10σ for protons and 15σ for electrons is ensured in all operating modes. Tables 3.8 to 3.10 list the magnet parameters in the electron and proton beam lines and their positions, beginning from the interaction point (IP).

Table 3.8: Forward hadron magnets, the settings are for 275 GeV.

FORWARD DIRECTION	Hadron Magnets						
	B0PF	B0APF	Q1APF	Q1BPF	Q2PF	B1PF	B1APF
Center position [m]	5.9	7.7	9.23	11.065	14.170	18.070	20.820
Length [m]	1.2	0.6	1.46	1.6	3.8	3.0	1.5
Center position w.r.t. to x-axis [cm]	-1.50	5.5	1.40	2.38	4.07	3.90	8.00
Angle w.r.t. to z-axis [mrad]	-25.0	0.0	-5.5	-10.0	-10.2	9.0	0.0
Inner radius [cm]	20.0	4.3	5.6	7.8	13.1	13.5	16.8
Peak field [T]	-1.3	-3.3	0.0	0.0	0.0	-3.4	-2.7
Gradient [T/m]	0.0	0.0	-72.608	-66.180	40.737	0.0	0.0

Since for both beams the vertical IP β -function is much smaller than the horizontal one, $\beta_y^* \ll \beta_x^*$, the innermost quadrupoles on both beam lines are vertically focusing. In the hadron ring this limits the maximum vertical β -function in those magnets to about 1600 m at a proton beam energy of 275 GeV, resulting in moderate contributions to the overall chromaticity of the machine. The horizontal β -function is intentionally increased to about 1300 m in the region of the crab cavities. This limits the required voltage of those devices, which scales as $1/\sqrt{\beta_x^* \beta_{\text{crab},x}}$, to about $U_{\text{crab}} = 12$ MV. At lower energies the IP β -functions are increased, resulting in lower β -functions in the low- β magnets as well as at the crab cavities. However, due to the lower beam rigidity the required crab cavity voltage does not exceed 14 MV at any energy.

The focusing scheme for the electrons is conceptually the same as for the hadrons. The vertical β -function reaches a maximum of about 500 m in the low- β quadrupoles, while

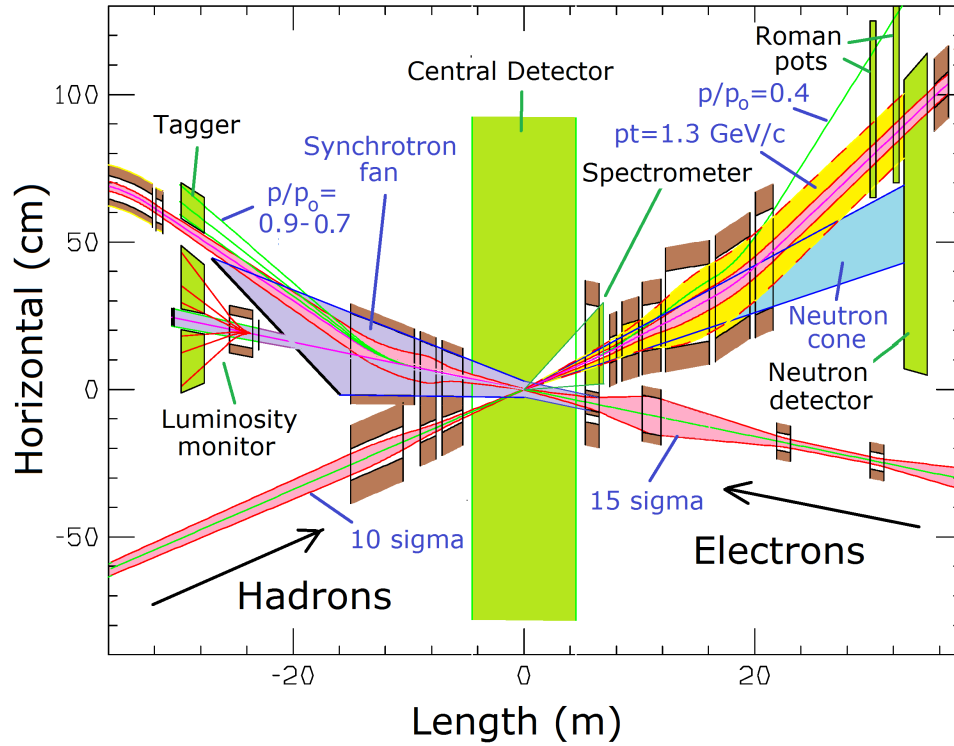


Figure 3.3: Schematic layout of the interaction region (top view, as simulated for high divergence, no cooling). Beams cross with a crossing angle of 25 mrad. Note the length scales for the horizontal and vertical axis are very different. The IR design integrates focusing magnets for both beams, luminosity and neutron detectors, electron taggers, spectrometer magnets, near-beam detectors (Roman pots for hadrons), crab cavities, and spin rotators for both beams. The two beams are both focused by quadrupole doublets. On the hadron-forward side, there are separate focusing magnets which are longitudinally interleaved. The first quadrupole magnet for electrons is integrated into a hadron spectrometer dipole. On the rear side, hadrons and electrons are focused by quadrupoles which are installed side-by-side in the same cryostat. The maximum β -functions in the IR for hadrons of 2000 m remain within the operating range of RHIC, while the maximum β -functions for electrons remain below 500 m.

the horizontal β is intentionally increased to about 200 m at the crab cavities to limit their required voltage.

The forward hadron magnet apertures are completely dominated by experimental acceptance requirements, and the 10σ outline shown for the circulating beam only uses the small central regions of the magnet apertures. This allows particles scattered at small angles to pass through the apertures of the innermost magnets so they can be detected by detectors which are integrated into the hadron beam vacuum system (“Roman Pots”) further down the beamline.

The B0 spectrometer magnet shown in Figure 3.4 is used to cover an intermediate experimental acceptance region below what can be detected in the main solenoid detector and

Table 3.9: Forward electron magnets, the settings are for 18 GeV electron beam energy.

FORWARD DIRECTION	Electron Magnets				
	Q0eF	Q2eF	Q3eF	Q4eF	Q5eF
Center position [m]	5.9	11.065	22.470	30.60	39.50
Length [m]	1.2	1.61	1.2	1.2	1.2
Center position w.r.t. to x-axis [cm]	-14.75	-27.66	-56.17	-76.5	-98.75
Angle w.r.t. to z-axis [mrad]	25.0	25.0	25.0	25.0	25.0
Inner radius [cm]	2.50	6.3	3.0	3.0	3.0
Peak field [T]	0.0	0.0	0.0	0.0	0.0
Gradient [T/m]	-13.54	8.008	-11.627	-15.400	4.023

Table 3.10: Rear hadron and electron quadrupoles with their apertures tapered in proportion to their distance to the IP for 275 GeV and 18 GeV, respectively.

REARWARD DIRECTION	Hadron Magnets			Electron Magnets		
	Q1APR	Q1BPR	Q2PR	Q1eR	Q2eR	B2ER
Center position [m]	-6.2	-8.30	-12.75	-6.2	-8.30	-12.25
Length [m]	1.80	1.40	4.50	1.80	1.4	5.50
Center position w.r.t. to x-axis [cm]	0.0	0.0	0.0	15.5	20.75	30.63
Angle w.r.t. to z-axis [mrad]	0.0	0.0	0.0	25.0	25.0	25.0
Entrance radius [cm]	2.00	2.80	5.40	6.60	8.30	9.70
Peak field [T]	0.0	0.0	0.0	0.0	0.0	-0.198
Gradient [T/m]	-78.375	-78.375	33.843	-13.980	14.100	0.0

above particle angles that will exit through the IR magnets. Inside its aperture the electron beam is shielded by a 2 m long superconducting bucking coil (dipole active shield magnet) with an outside diameter of 10 cm and a field of 1.3 T. This bucking coil houses the vertically focusing superconducting electron low- β quadrupole Q1EF, as shown on Figure 3.5.

The B1PF and B1APF dipoles separate the hadron beam from the outgoing 4 mrad neutron cone, and create dispersion at the Roman Pots to allow determination of the forward momentum of the scattered particles.

The electron beamline on the forward side does not contain any bending magnets within 80 m upstream of the IP. Within this region the only source of synchrotron radiation is focusing in quadrupole magnets. The synchrotron radiation fan generated in the far away arc dipoles can be easily collimated such that it is completely contained within the radiation fan produced by the quadrupoles in the straight. This fan has finite maximum diver-

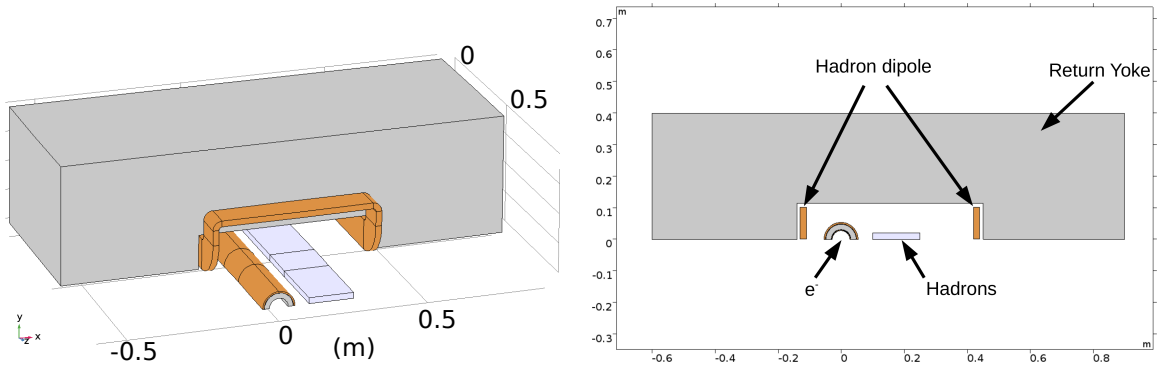


Figure 3.4: Schematic drawing of the warm iron B0 spectrometer dipole with the superconducting 1.3 T bucking coil shielding the electron beam, and the electron quadrupole Q1EF inside that bucking coil

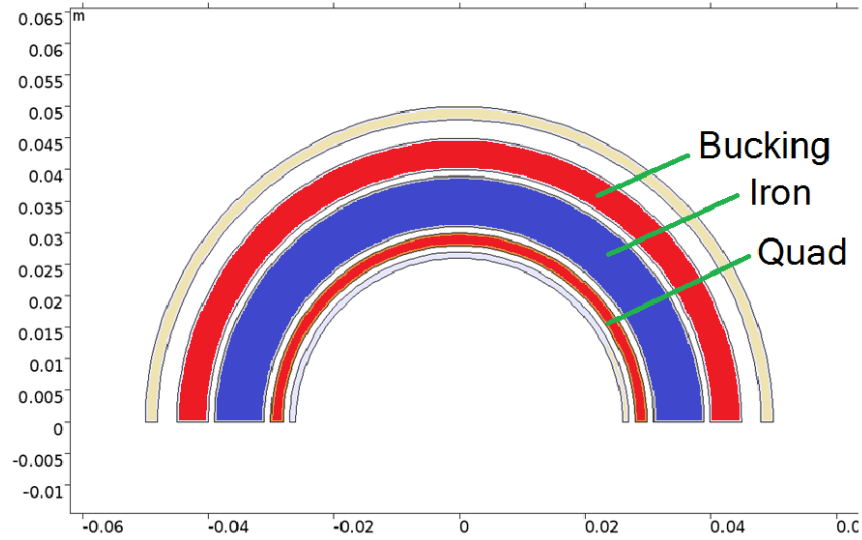


Figure 3.5: Design of the electron quadrupole Q1EF with its 1.3 T bucking coil to shield the electron beam from the B0 spectrometer magnet.

gences, collimated to 13σ bounds, that are allowed to pass without interference through the beam pipe and following magnets, thus allowing for installation of detector components close to the beam. This is discussed in detail in Section 3.2.7.

On the rearward side, no dipoles are introduced into the proton beam line, which allows placement of the low- β quadrupoles even closer to the IP than on the forward side. The electron beamline contains a bending magnet that bends the electrons away from the γ -beam generated by scattering of electrons at the hadrons (Bethe-Heitler process) which is used to measure luminosity in the luminosity monitor placed in this area. The bending magnet also serves as a spectrometer to tag scattered electrons that lost energy in the Bethe-Heitler process, but most importantly for the scattered electrons with low Q^2 . However, since this magnet is introduced downstream of the main detector the associated

synchrotron radiation fan does not pass through the experiment.

The vertically focusing low- β quadrupoles Q1ER and Q1APR as well as Q2ER and Q1BPR are realized as superconducting dual-aperture magnets sharing the same iron yoke, as shown in Figure 3.6 (left). The apertures for both beams are tapered and angled with respect to each other, following the divergent proton beam and synchrotron radiation fan as they emerge from the central detector, as depicted in Figure 3.6 (right). The tapering is needed to minimize the initial magnet apertures and to allow enough iron between the beams in order to limit the magnetic fields for each of them effecting the other section.

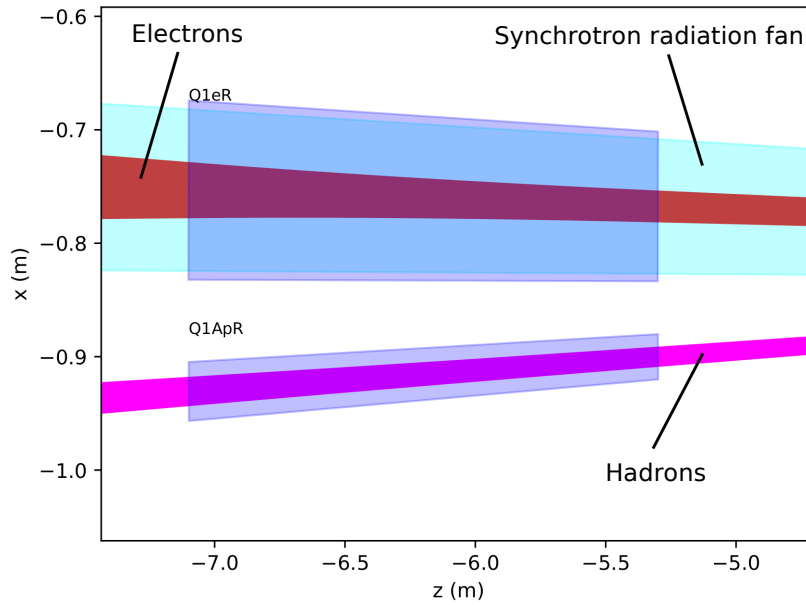


Figure 3.6: Cross section and top view of the first rear quadrupoles Q1ER and Q1PR, sharing the same iron yoke. The apertures are tapered around the synchrotron radiation fan and the proton beam envelope, respectively.

The required horizontal aperture radius x_{synch} to accommodate the synchrotron radiation fan from the 15σ electron beam at distance s from the IP is parametrized as

$$x_{\text{synch}}(s) = 6.75 \times 10^{-3}(s + 3.5) \quad (3.16)$$

The vertical size of the synchrotron radiation fan y_{synch} is significantly smaller than the horizontal one. The horizontally focusing quadrupoles Q2ER (tapered) and Q2PR (not tapered) are conceptually similar to Q1ER and Q1APR. With these apertures, the entire synchrotron radiation fan is transported safely through the interaction region until it hits a dedicated absorber 23 m from the IP.

3.2.2 IR Vacuum Design

The interface requirements within the IR present several complex challenges, which require close attention to detail. The vacuum chamber in this region will become the primary interface between the particle beams and the different detector components.

One of the first challenges is to meet all of the geometrical requirements of the region. First and foremost the vacuum chamber must be designed to allow clear passage of the two high energy particle beams. Space constraints for the synchrotron radiation (SR) fan resulting from the strong focusing electron quadrupoles also need to be taken into account. Designing the central vacuum pipe with a large diameter would easily meet these requirements and it would provide a large conductance to the vacuum pumps that are required to achieve the lowest possible pressure in the detector region. However, to ensure large acceptance for all the collisions products, detectors must be placed as close as possible to the interaction point. Since these particles must pass through the walls of the beam pipe, every effort must be made to minimize their thickness.

The design is further complicated by the fact that the charged particle beams induce electromagnetic fields in the walls of the vacuum chambers. These induced fields create an image current inside the vacuum chamber walls, which travels with the particle bunches as they move through the accelerator. Changes in the material resistivity or abrupt steps result in wake fields, which can retard the image current and lead to energy loss and heating of the vacuum system.

Every effort must be made to reduce the dynamic pressure inside the IR vacuum chamber in order to minimize beam-gas interactions. The particles in the circulating beams can scatter on the residual gas molecules, which can result in high detector backgrounds. Any synchrotron radiation (direct or scattered) impinging on surfaces will result in a high dynamic pressure, because of photon induced desorption and surface heating. This further increases the beam-gas interaction problem and the backgrounds in the detector.

Geometry

In order to define an initial acceptable envelope for the IR vacuum chamber, a full scale layout of the central detector region was developed (see Figure 3.7). It soon became clear that as a result of the shallow crossing angle between the beams, there was no adequate space for two independent beam pipes leading up to the inner detector region. In order to proceed the decision was made to combine the two pipes into one common vacuum flange in order to save space. It also became clear that insufficient space was reserved between the start of the detector region and the focusing quads in the forward hadron beam direction. The superconducting bucking coil for the electrons only leaves 10 cm of longitudinal space for a cold to warm transition, bellows to accommodate misalignment and thermal expansion and beam position monitors, this issue will be addressed in future iterations.

In addition to the crossing angle, one of the main parameters driving the size of the central

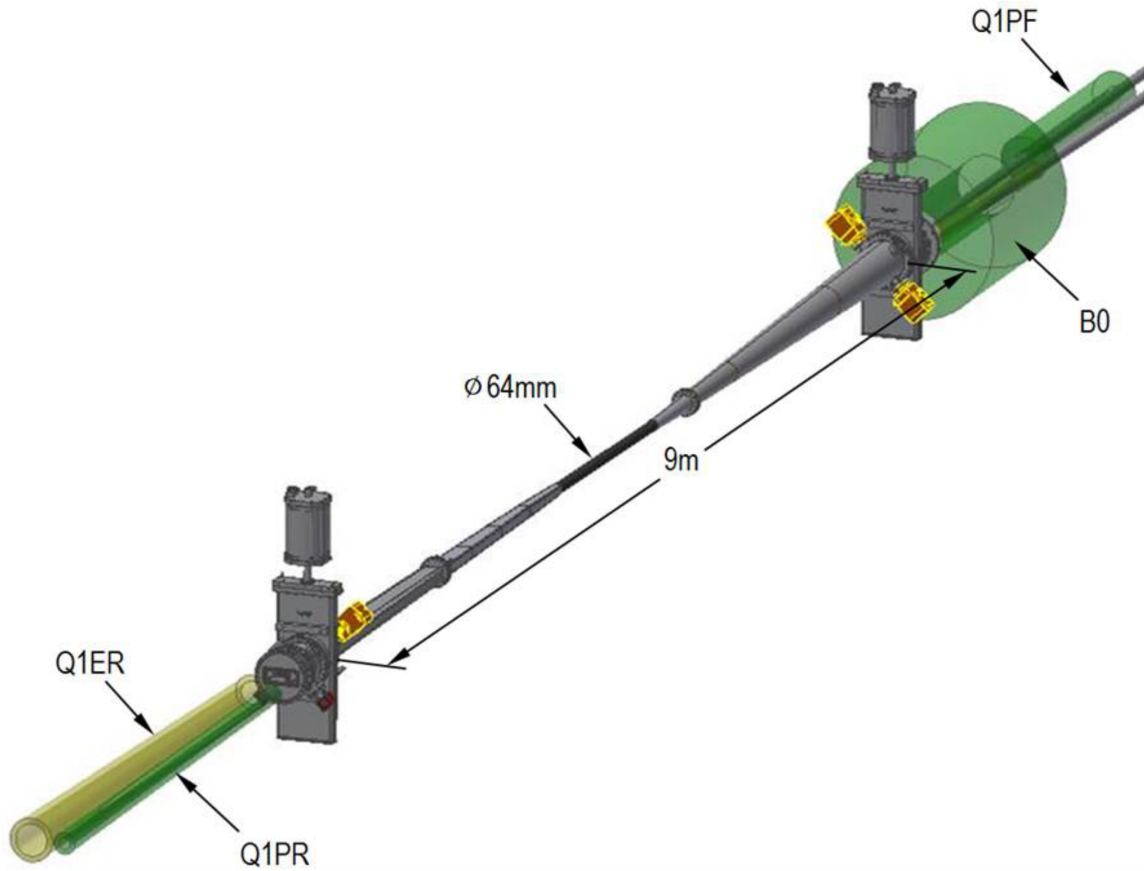


Figure 3.7: Interaction region layout with magnets. The incorporation of gate valves is still under consideration

beam pipe is synchrotron radiation. This radiation is produced when relativistic electrons are accelerated radially, or perpendicular to their velocity. To minimize this problem the electron dipole magnets have been located as far as possible (> 50 m) from the IR leaving adequate space to collimate the radiation produced. While the dipole magnets are responsible for the majority of the synchrotron radiation, the final strong focusing electron quadrupoles located just upstream of the detector need to be taken into account. In order to study the resulting radiation (see Figure 3.8) a simulation study was performed using the SynRad software package developed at CERN [79]. A stay-clear envelope was established based on the final magnet and beam parameters.

Considering the central portion of the beam pipe will be made from beryllium and taking into account its limited fabrication possibilities, a diameter of 62 mm was defined. This value provides additional clearances for mechanical and positioning tolerances. In the outgoing electron beam direction, the beam pipe will continue to increase in size to ensure the synchrotron radiation can travel through the IR without impinging on the chamber walls. In the forward hadron beam direction the beam pipe has a conical cross section in order to provide an unobstructed path to the forward spectrometer located in the B0

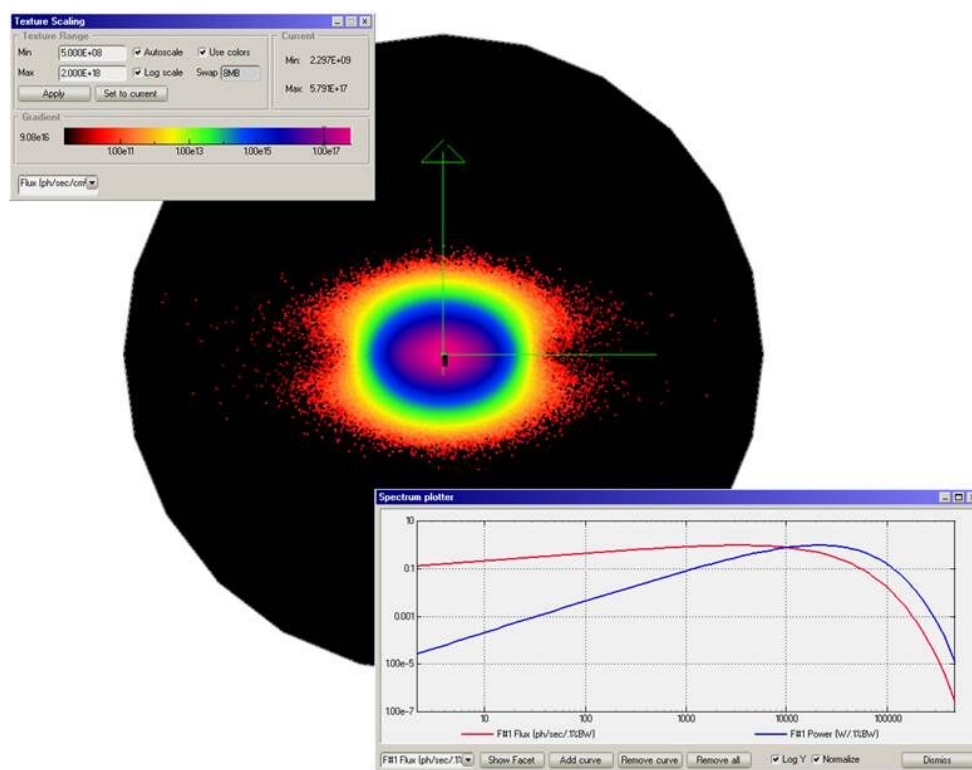


Figure 3.8: SynRad code simulation showing the resulting synchrotron radiation from the electron focusing quadrupoles Q1EF and Q2EF

magnet bore. To minimize the beam impedance for the electrons, a conducting screen will be installed providing a controlled path for the induced image currents. Once outside the central detector region the forward traveling particles will pass through a vacuum-air interface made of thin aluminum or stainless steel before entering the B0 spectrometer. The design and position of the required chamber supports will need additional care. These supports must ensure that the chamber does not encroach into the stay clear area and must also guarantee the mechanical stability of the chamber during operations and bake out. Careful consideration of the mechanical eigenfrequencies must be taken to avoid large amplitude vibrations, which can lead to stress and fatigue of the chamber. Where possible, natural vibration frequencies will be kept above 100 Hz.

Material Considerations

To minimize the interaction of the collision products in the vacuum chamber walls, their thickness has to be kept at a minimum. The 'transparency' of a material is usually quantified through the radiation length (χ_0) for elastic collisions and the interaction length (l_T) for inelastic hadron collisions.

The radiation length is defined as the mean distance over which a high-energy electron

loses all but $1/e$ of its energy by bremsstrahlung radiation. This property is inversely proportional to the density and atomic number of the material. The interaction length is the mean distance traveled before experiencing an inelastic nuclear interaction.

In order to reduce the background produced by these material properties, the walls of the vacuum chamber should be made as thin as possible. A limit is clearly defined by the mechanical integrity of the vacuum chamber. If the chamber is too thin, the vessel will collapse under the outside atmospheric pressure or fail to meet the tight mechanical tolerances required to stay clear of sensitive instrumentation. To compare the nuclear and mechanical performances of various materials, $\chi_0 E^{-1/3}$ has been used to define the figure-of-merit, with E being the Young's modulus. The required chamber wall thickness is directly proportional to $E^{-1/3}$, the properties of several materials are listed in Table 3.11.

Table 3.11: Table of material properties considered for the IR vacuum pipe.

Material	χ_0 [cm]	l_T [cm]	E [GPa]	$\chi_0 E^{-1/3}$
Beryllium	35.3	41.8	290	2.34
Carbon fiber	27.0	40.0	200	1.58
Aluminum	8.9	28.7	70	0.37
Titanium	3.6	21.4	110	0.17

While beryllium would seem to be the best choice it has several drawbacks including fabrication difficulties and safety concerns as well as having very high cost. For these reasons, only the central portion of the IR chamber will be made from beryllium. Additional aluminum sections made from AA2219 will be electron beam welded to the center section to complete the approximately 9 m long vacuum section. This particular aluminum alloy can be used at operating temperatures up to 250° C and is weldable using conventional techniques. Three separate vacuum pipes are envisioned with flange joints located at positions compatible with the central detector. The shorter pipe sections will not only simplify the fabrication, transportation and handling of the fragile chambers and also facilitate NEG coating on the interior vacuum surfaces.

The magnetic properties of materials used in the interaction region must be carefully considered. Most of the vacuum chamber components will be made of beryllium, aluminum and copper which are non-magnetic. Any stainless steel used in this region will be 316LN. This austenitic stainless steel maintains its very low magnetic permeability after welding or cold working. In general the use of stainless steel in the IR will be avoided due to the presence of cobalt in the material and the possible formation of ^{60}Co due to neutron activation. Once formed, this radioactive isotope has a half-life of 5.3 years, severely limiting the serviceability of the area.

Impedance and Instabilities

From an electromagnetic standpoint, the ultimate beam pipe would be a perfectly smooth flawless conductor. This would allow the induced image currents to travel along the cham-

ber walls without losses or forces acting back on the particle beam. In reality this is not possible and one has resulting electromagnetic interactions, called wake fields. Longitudinal and transverse fields are generated when a bunch passes a sudden change in geometry or wall resistivity. These transverse fields can deflect the beam and lead to instabilities while the longitudinal wake fields lead to energy loss of the particles and localized heating of vacuum components.

In order to reduce effects related to resistivity changes, materials such as stainless steel pipes with small diameters need to be copper plated. The required copper thickness depends on the shape of the beam pipe and simulation results. To minimize detrimental effects from sudden geometry changes a radial tapering of 10:1 will be followed, unless absolutely not possible. This means a 1 mm change in the radial distance between the particle beam and the chamber wall will occur over at least 10 mm of longitudinal space. RF shielding will be used to bridge all vacuum flange joints to prevent trapped modes and to help maintain uniform wall geometry. Even a few watts of deposited power on an uncooled vacuum surface can result in an extremely high temperature rise. Bellows, which need to be installed to compensate for mechanical misalignment and provide room for thermal expansion during bake outs, will also be internally shielded to avoid trapped modes. Steps inside the bellows RF shielding will be kept to a minimum. Figure 3.9 shows an example of a dual aperture RF shielded bellows.

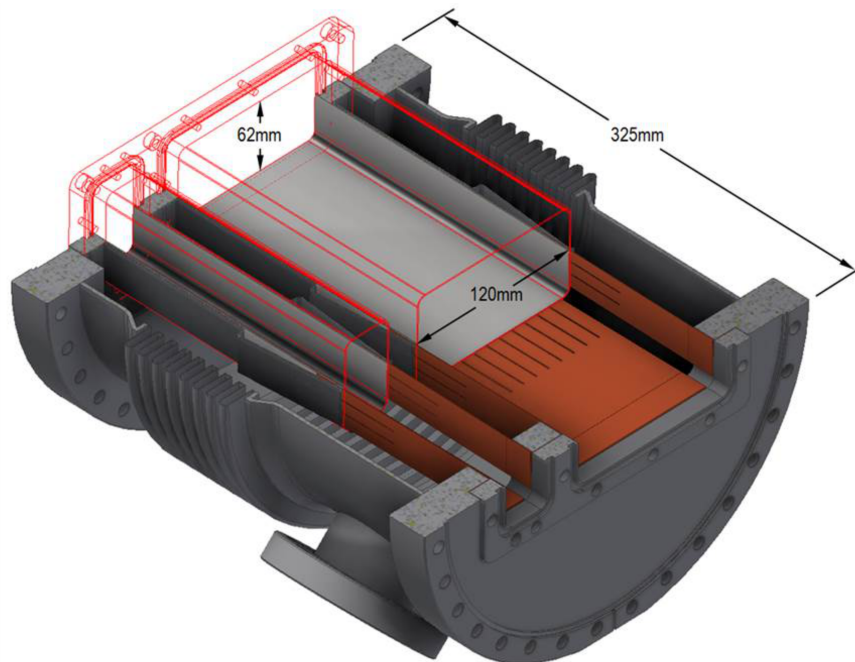


Figure 3.9: Dual aperture RF shielded bellows

Vacuum Requirements

Every effort must be made to reduce the residual gas pressure in the interaction region to minimize beam-gas interactions. The first concern is related to scattering, both elastic (Coulomb) and inelastic (Bremsstrahlung). Particles in the beam which are scattered off of the remaining gas molecules can further interact with vacuum chamber walls. This in turn leads to a 'positive feedback' loop which can quickly turn catastrophic. The second concern is related to phenomena such as ion induced desorption and electron multipacting. In both of these cases charged particles, freed electrons or ionized residual gas molecules are accelerated by the electric fields resulting from the charged particle beams. These accelerated particles can bombard the vacuum chamber walls and lead to large localized pressure rises and additional scattering. This is another self-feeding process. All of these aspects decrease the beam lifetime and intensity and have direct impact on the luminosity.

In order to eliminate the potential of unwanted contamination and ensure the lowest possible base pressure, best UHV practices will be followed from start to finish. This entails special processing of fabricated parts, careful surface treatment and minimizing the surface area exposed to vacuum. All parts will be chemically cleaned and/or vacuum baked prior to welding or assembly. After cleaning, no vacuum surfaces will be touched with bare hands and all openings to vacuum surfaces will be wrapped in clean vacuum grade aluminum foil.

Given the limited space for lumped pumping as well as the need for ultra-high vacuum throughout the entire interaction region, the vacuum chamber will be coated with a non-evaporative getter (NEG) layer. This coating will be magnetron sputtered directly onto the interior surfaces of the IR vacuum chambers. NEG layers are a composition of active metals (Ti, Zr and V) which chemically pump most of the gases found in a UHV system (N_2 , CO and CO_2). It also has a high diffusivity for H_2 which is the predominant gas in a baked leak tight vacuum section. The film also creates a hydrogen barrier on the interior surfaces which limits the permeation of H_2 into the system. In addition to all of these benefits the film has a low secondary electron yield, which reduces the risk of electron cloud formation, and being in the order of microns, adds negligible mass between the experiment and the detectors.

Incorporating NEG coating into the design has two implications. First is the degradation of the pumping performance after successive regenerations. Anytime the vacuum section is vented for maintenance, the NEG layer becomes completely saturated and needs to be regenerated to regain its pumping characteristics. Regenerating the layer requires dissolving the surface oxides and nitrides into the bulk material which creates a new metallic surface facing the vacuum system. Since the film is thin, it has a limited storage capacity. Some of the pumping capacity can be regained by activating at higher temperatures but the upper bound is limited by the material choices for the vacuum chambers. To increase the potential number of activations, the vacuum section will be vented with an extremely pure noble gas which is not pumped by NEG's.

Given the limited access inside the central detector region, permanently mounted heaters are envisioned to facilitate baking. Thin polyamide heaters which are made from thin

metal foils sandwiched between Kapton films will be used. These heaters can be made in almost any size or shape with varying watt densities to ensure adequate heating and activation of the NEG coatings. While adding some radiation length, these are a good compromise considering the alternatives. Depending on the final design of the detector, additional insulation may be required to protect sensitive components located close to the beam pipe.

Since NEG coatings only pump active gases, ion pumps will be installed at either side of the interaction region for residual noble gases. Ion pumps are Penning traps with crossed electrical and magnetic fields. The magnetic field increases the flight time of free electrons which ionize incoming gas molecules. These ions are then accelerated in the presence of the electric field and impact on a metallic cathode typically made of titanium or tantalum. This freshly sputtered material can physically or chemically react with gas present in the system.

3.2.3 Interaction Region Performance for Scientific Requirements

The physics program of an EIC and the resulting requirements for the detector and the IR have been discussed in sections 2.1 and 3.2. In order to verify that the IR design fulfills all the requirements as summarized in Table 2.2, an eRHIC general purpose detector, the auxiliary detectors, the vacuum chamber, and the machine components up to the crab cavities, have been implemented in the EicRoot GEANT simulation framework [62]. To make the simulations as realistic as possible the beam line element 3-dimensional locations and magnetic fields are directly taken from the MADX files used for optics calculations. Their apertures precisely reflect our present understanding of how these magnets can be built in reality. The vacuum system is modeled by importing the essential part of the engineering design into GEANT.

In the following, results from these simulations will be presented. The IR setup, which has been used in the simulations is one version earlier than what is described in section 3.2.1. The main differences are the increased crossing angle (22 mrad used in the simulations, since increased to 25 mrad) and optimized bore sizes of the magnets in the outgoing hadron and electron beam directions to increase the acceptance for small angle scattered particles. So the results presented here can be seen as the "worst case" scenario for the results one would get with the current IR.

Realization of the Scientific Requirements for the Central Detector

As shown in figure 3.2, the beam element free region L^* along the beam lines is ± 4.5 m from the IP. In order to have the acceptance required for inclusive and semi-inclusive DIS as well as exclusive reactions it is critical to reconstruct events over a wide span in pseudorapidity ($-4 \leq \eta \leq 4$), as discussed in section 2.1. Therefore the design of the vacuum system in the detector volume (see Figure 3.7) needs to fulfill these specifications:

- Provide enough space to pass the synchrotron radiation fan through the detector.
- Do not extend beyond a 2° opening angle from the interaction point.

Figure 3.10 shows the integration of the various detector components around the beam pipe elements in the outgoing hadron beam direction, overlaid by a deep inelastic electron-deuteron scattering event with the secondary particle tracks and hits in the TPC and the silicon trackers.

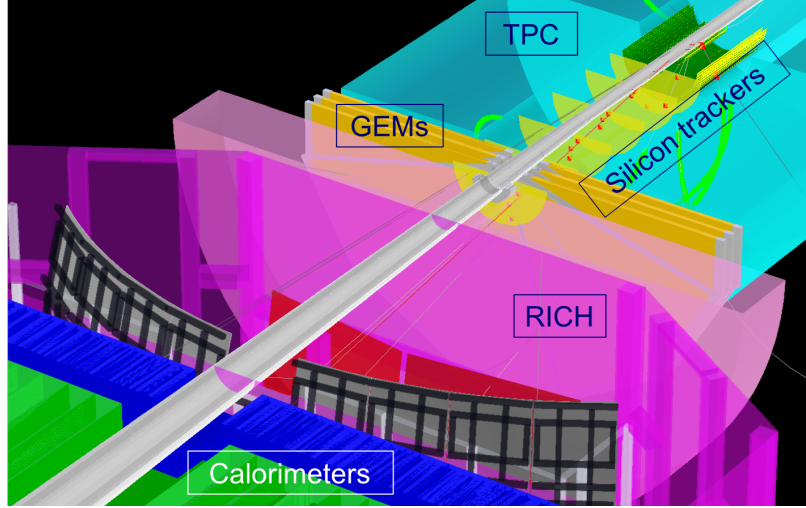


Figure 3.10: The integration of the beam pipe and various detector components in the outgoing hadron beam direction.

To illustrate that the tracker acceptance at large rapidities as shown in Fig. 3.10 provides enough points along the particle trajectory to obtain excellent momentum resolutions up to the highest rapidities, Fig. 3.11 shows the expected momentum resolution σ_p/p as function of particle rapidity for four different particle momenta.

Realization of the Scientific Requirements for the Interaction Region

Exclusive Processes

As emphasized below the detection of forward-going scattered protons from exclusive reactions as well as of neutrons from the breakup of heavy ions in incoherent and non-diffractive reactions is particularly challenging.

Electron-Proton Scattering: Extreme care has been taken to transport protons with $0.2 \text{ GeV}/c < p_T < 1.3 \text{ GeV}/c$ through the IR such that they can be detected as soon as they can be separated from the core of the beam. To achieve this p_T coverage over a wide range of center-of-mass energies a multi-prong approach is required. Protons with scattering angles up to 5 mrad are detected in the Roman Pots, while the range from 7 to 20 mrad

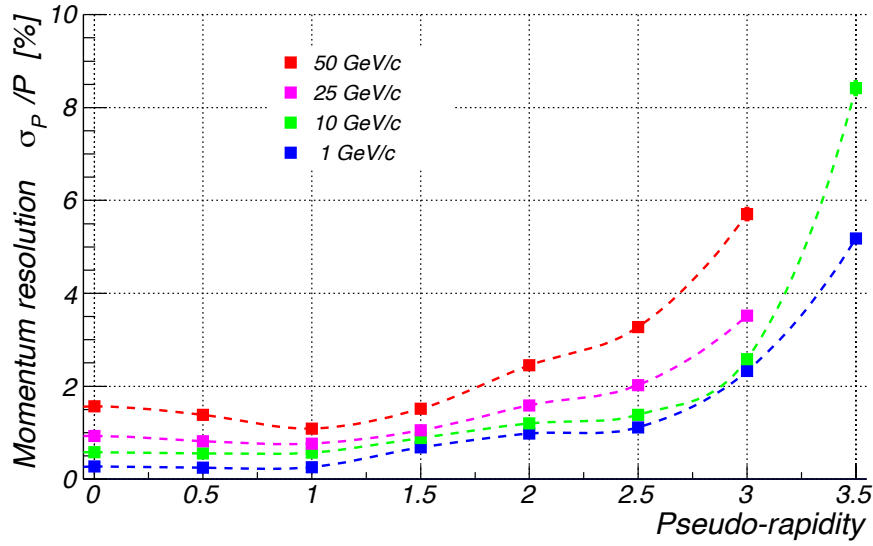


Figure 3.11: Momentum resolution σ_p/p as function of η for a wide range of particle momenta

is covered by the B0 large-acceptance spectrometer (see Figure 3.12). In general the main detector starts seeing secondary particles above ~ 30 mrad ($\eta \sim 4$), and bending power of the 3 T solenoid is sufficient for momentum measurement above ~ 50 mrad ($\eta \sim 3.5$ or so).

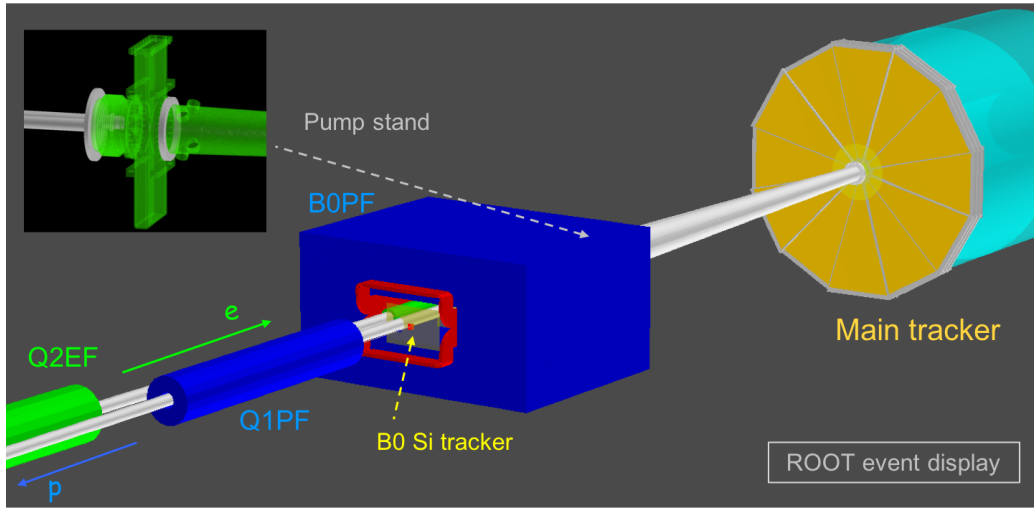


Figure 3.12: An EicRoot view of the B0 large-acceptance spectrometer and other equipment around it, as implemented in GEANT.

The current Roman Pot configuration has a single station with two silicon planes at ~ 28 m downstream of the IP, with a relatively modest single point XY-resolution. As shown later, even this very basic setup provides sufficient acceptance and a good momentum and

scattering angle measurement.

There are several effects influencing the low p_T acceptance. We have been following the general rule of thumb that the distance between the edge of the Roman Pot silicon sensors and the beam orbit should be 10σ in X and Y . The physical size of the separation $\sigma_{x,y} = \sqrt{(\beta_{x,y}\epsilon_n)/\gamma}$ is driven by the normalized beam emittance ϵ_n and the β -functions $\beta_{x,y}$ at the location of the Roman Pots. The acceptance at large p_T is mainly constrained by the magnet apertures.

Figure 3.13 summarizes the p_T acceptance for three different proton beam energies, $E_p = 41$ GeV, 100 GeV, and 275 GeV for the “high beam divergence optics” (see Table ??) for eRHIC. The figures illustrate the need for a multi-prong detector approach to provide the full p_T acceptance over a wide range of hadron beam energies. For $E_p = 41$ GeV the limiting factor in acceptance at high p_T is the inner dimension of the vacuum chamber and the magnet apertures. At $E_p = 100$ GeV one in general has full acceptance in p_T but there exists some “grey” (transition) area separating the forward scattered proton acceptances in the B0 spectrometer and the Roman Pots. We are currently investigating how much of this “grey” area can be filled by optimizing the layout of the outgoing vacuum beam pipe and/or by installation of additional Roman Pots closer to the IP. For $E_p = 275$ GeV the acceptance is mainly limited at low p_T , however this region can be partly filled by taking data with the “high acceptance beam optics” (see Table ??) for eRHIC, which is supposed to reduce the beam envelope size at the Roman Pot location and consequently relieve the 10σ separation cut.

The p_T resolution of these forward scattered particles is of equal importance as their acceptance. There are several effects that can influence the momentum resolution and need to be mitigated:

- The finite width of the vertex distribution at the IP adds uncertainty in the angle determination. This uncertainty can be eliminated by determining the vertex of the event through other tracks in the event being registered in the main detector and benefit from the excellent vertex definition from the μ -vertex detector.
- The angular divergence $\sigma_\theta = \sqrt{\epsilon_n/(\beta^*\gamma)}$ of the beam, which directly leads to a smearing of the scattering angle.
- The hadron bunch “rotation” at the IP due to the crab cavities. Crabbing implies a transverse momentum kick $p_x(z)$ to the particle bunch, with the kicking strength proportional to the longitudinal position z of particles in the bunch. Therefore at the IP particles at the “head” of the bunch will have a slightly different orientation and/or transverse offset compared to the ones in the “tail” of the bunch, which leads to additional smearing of the apparent scattering angle. The z -vertex determination of the event provided by the main tracker as well as high-resolution timing of the Roman Pot silicon sensors (of an order of ~ 10 psec or so) is able to mitigate this effect to a large extent, but more studies are needed.
- The spread in the beam energy, which normally has a width (RMS) of $\sim 10^{-4}$.

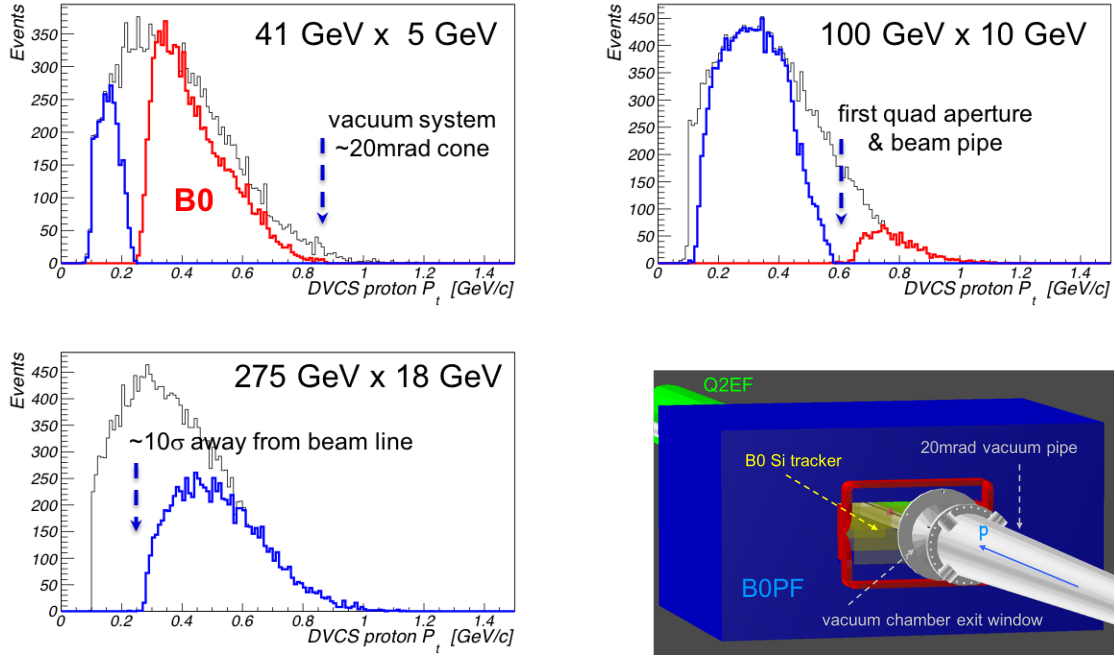


Figure 3.13: The p_T acceptance of forward scattered protons from the DVCS (Deep-Virtual Compton Scattering) process at different combinations of beam energies. The blue curves represent the acceptance of the RPs and the red ones of the B0 spectrometer. A view in the outgoing proton beam direction z of the B0-spectrometer.

Currently the setup to detect the forward scattered protons is four silicon planes placed inside the bore of the 1.2 m long B0 magnet with a ~ 1.3 Tesla field and a single Roman Pot station with two silicon detector planes with a relative separation of 20 cm, at ~ 28 m from the IP. The silicon detectors are supposed to have $20 \mu\text{m}$ hit resolution in both X and Y . The track reconstruction is based on a Kalman filter (either with or without the vertex constraint) for the protons registered in the B0 spectrometer and a matrix transport method (with the realistic beam envelope size at the IP) for the protons registered in the Roman Pots. Under relatively conservative assumptions one obtains a p_T resolution $\sim 15 \text{ MeV}/c$ for the protons measured in the B0 spectrometer and $\sim 20 \text{ MeV}/c$ ($10 \text{ MeV}/c$) for protons measured in the Roman Pots in the horizontal (vertical) plane. The effect of the beam angular divergence still needs to be fully investigated.

Electron-Nuclei Scattering: The only possible way to tag exclusive electron-nucleus events for heavy nuclei is to veto the nuclear break-up. Figure 2.17 shows the break-up neutron momentum vs. scattering angle in the laboratory frame for different beam energies. One needs to transport neutrons within a cone of 4 mrad to 6 mrad, depending on the beam energy, through the IR to a Zero-Degree Calorimeter (ZDC). The ZDC is placed right in front of the B2APF magnet at ~ 30 m from the IP. Figure 3.14 (left) shows the layout of the beam elements towards the ZDC. The picture illustrates that currently neutrons are not

really well centered at the $60 \times 60 \text{ cm}^2$ ZDC front surface. This is improved by the new IR design. Preliminary estimates show that the new option provides sufficient containment of the hadronic shower for the whole ZDC angular acceptance from 0 to 4 mrad.

Figure 3.14 (right) shows the resulting acceptance for neutrons from nuclear break-up. The required angular acceptance of $\pm 4 \text{ mrad}$ has been achieved and even extended beyond that (blue line) by careful consideration of machine beam line element apertures.

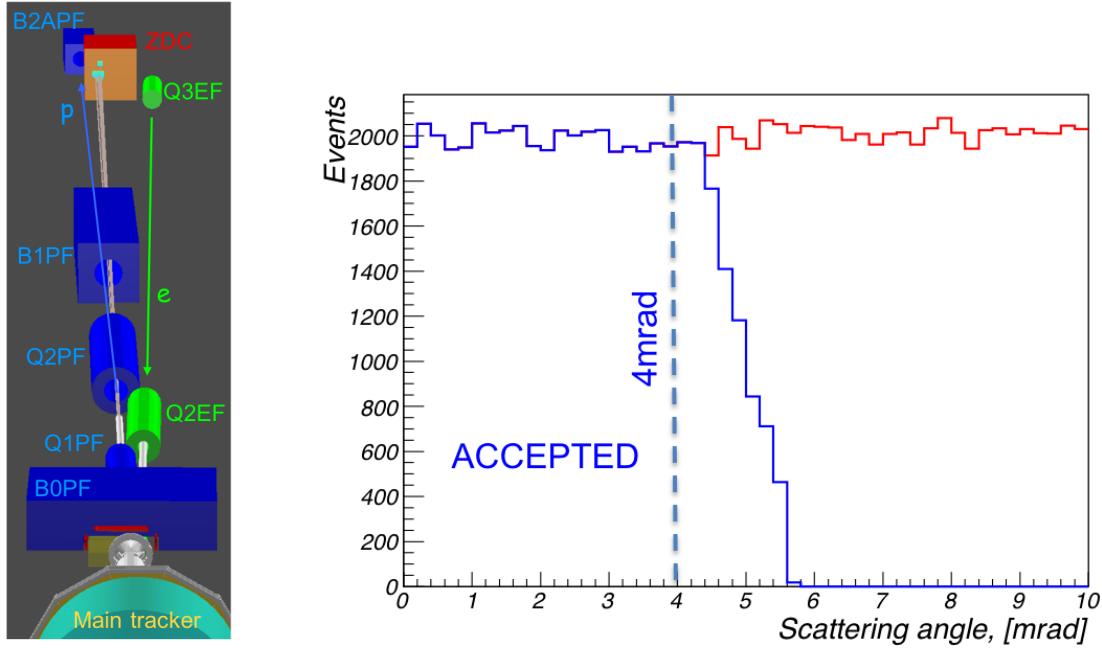


Figure 3.14: A view along the beam elements towards the Zero Degree Calorimeter (left). The acceptance for neutrons from nuclear break-up (right). For simplicity the neutrons have been simulated with a flat distribution in polar scattering angle.

Electron-Nucleus Scattering:

The physics program of an EIC requires proton and neutron collisions to allow for a full flavor separation of parton distribution functions. As neutron beams are not feasible, (un)polarized ^3He and deuteron beams are used for these purposes. To ensure the scattering really occurred off the neutron the spectator proton(s) need to be detected. Figure 2.21 shows the correlation of momentum and scattering angle for the spectator protons from electron-deuteron and electron- ^3He scattering for two different values of \sqrt{s} . Figure 3.15 shows the angular and momentum acceptance for spectator protons from inelastic electron-deuteron collisions as simulated with the Monte Carlo generator DPMJET [64] and passed through the complete simulation of the interaction region. For both beam energies E_p of 41 GeV and 100 GeV full acceptance is achieved. The response for spectator protons from ^3He will be identical as the angular momentum distribution for spectator protons is practically the same and their rigidity is closer to the beam rigidity.

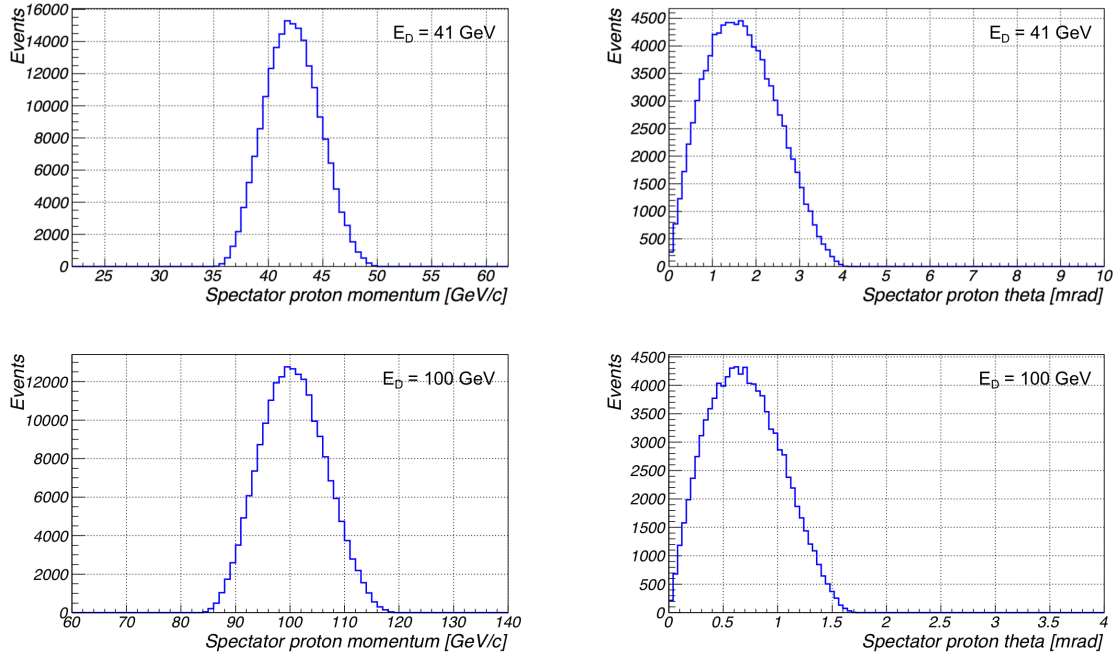


Figure 3.15: The momentum and angular acceptance for spectator protons from inelastic electron-deuteron collisions for beam energies E_D of 41 GeV (top) and 100 GeV (bottom) per nucleon, respectively.

Inclusive Processes:

Many physics topics beyond the ones discussed in the EIC White Paper [1] benefit from tagging the scattered electrons at Q^2 values significantly below 1 GeV^2 . Scattered electrons with $Q^2 < 0.5 \text{ GeV}^2$ cannot be detected in the main detector. Therefore, similar to the HERA collider detectors, a special low- Q^2 tagger is needed. An electromagnetic calorimeter with a number of silicon tracking planes in front of it needs to be integrated into the IR design to detect the scattered electrons with low Q^2 .

Figure 3.16 shows a view along the outgoing electron beam from the main detector towards the low Q^2 -tagger. As shown in Figure 3.2 (left) the magnet apertures need to be large enough to pass the synchrotron radiation fan as well as scattered electrons with low Q^2 .

Figure 3.17 shows the Q^2 acceptance of the low Q^2 -tagger for the highest eRHIC electron-proton energies of $18 \text{ GeV} \times 275 \text{ GeV}$. The black histograms are events generated using PYTHIA. The green curve shows the same events after taking the apertures of the quadrupoles and dipoles into account. If one also considers that (similar to the Roman Pots) one needs to keep a 10σ clearance between the beam central trajectory and the detector one obtains the Q^2 acceptance as shown in the blue histogram. Currently the magnet apertures limit the acceptance at high Q^2 to $\sim 0.001 (\text{GeV}/c)^2$ and at low Q^2 the acceptance is constrained by the 10σ clearance requirement.

The preliminary conclusion of these physics simulation studies is that the current IR design

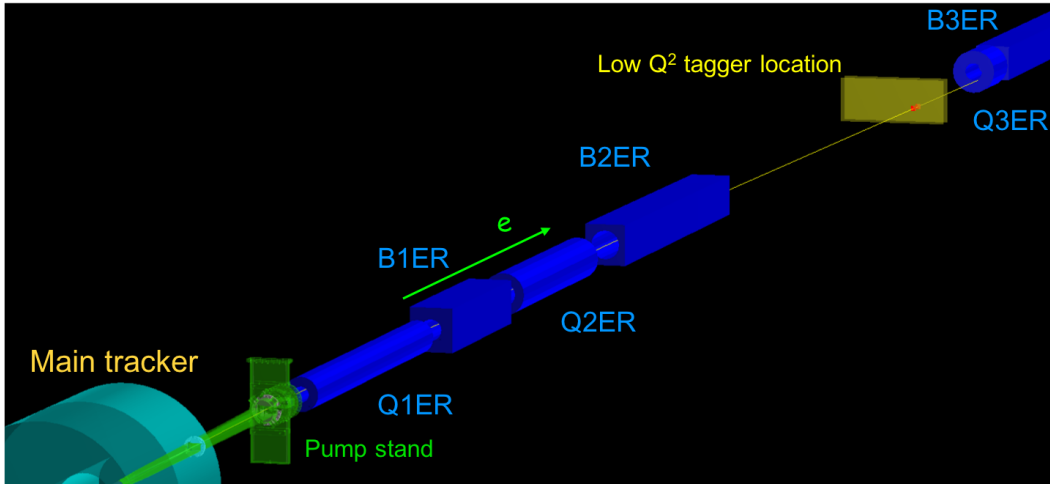


Figure 3.16: A view along the outgoing electron beam from the main detector towards the low- Q^2 tagger.

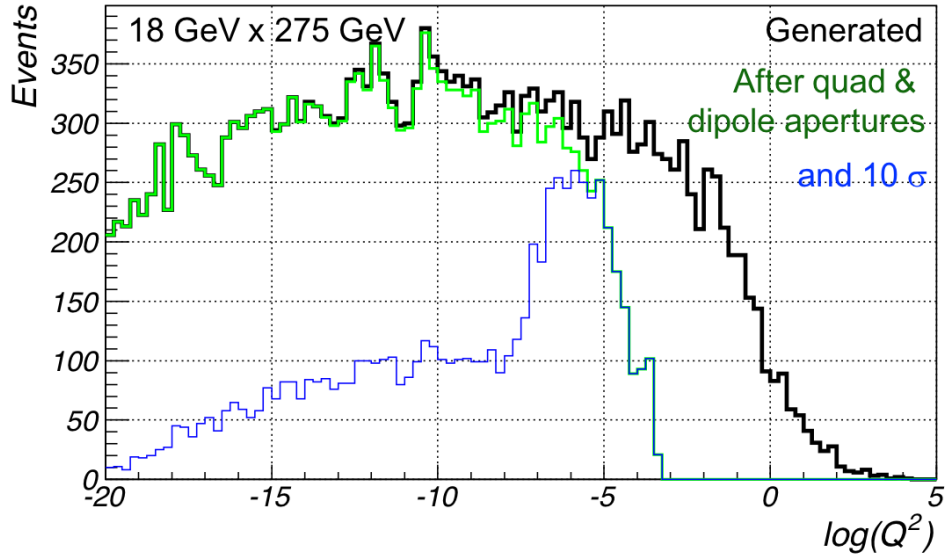


Figure 3.17: The Q^2 acceptance of the low Q^2 -tagger after accounting for the apertures of the quadrupoles and dipoles (green histogram) as well as that of a 10σ distance separation, which needs to be kept between the low Q^2 -tagger tracker and the core of the electron beam (blue histogram). The spectra are for $e + p$ collisions at $18 \text{ GeV} \times 275 \text{ GeV}$.

fulfills most of the requirements summarized in Table 2.2. Several potential improvements to the design are identified already, which will extend the eRHIC physics reach even further.

3.2.4 Crab Cavity Requirement and Specifications

eRHIC Crab Cavity Introduction

The concept of crab cavities as a countermeasure to the geometric reduction in luminosity caused by the crossing angle in colliders was introduced in 1988 [17]. A crab cavity imparts a transverse momentum kick $p_x(z)$ to the particle bunch, with the kicking strength proportional to the longitudinal position z of the particle. At the right phase, the bunch arrives at the cavity with its particles at the center receiving an accumulative zero deflection. The transverse momentum kick can be expressed as

$$p_x(z) = \frac{eE_0}{\omega} \sin(kz) \sin\left(\frac{kL}{2}\right) \approx \frac{eE_0 z}{c} \sin\left(\frac{kL}{2}\right)$$

where E_0 is the amplitude of the electric field acting on the bunch, ω and k are the angular frequency and the wave number of the crab cavity respectively, and L is the bunch length. The longitudinal coordinate z is referencing to the center of the bunch, where $z = 0$.

Transverse oscillation translates the longitudinally dependent kick p_x to a transverse offset x_{IP} at the interaction point (IP), which gives

$$x_{IP} = R_{12} \frac{p_x c}{E_b} = \sqrt{\beta_{\text{crab}} \beta^*} \frac{eE_0 z \sin\left(\frac{kL}{2}\right)}{E_b}$$

where R_{12} is the element of transverse transfer matrix from the crab cavity to the IP, β_{crab} and β^* are the beta functions at the crab cavity and IP.

At the desired cavity voltage, the transverse offset will cancel the crossing angle in the optics and restore the head-on collision. The requirement to the transverse offset can be exchanged with the crossing angle as

$$\theta_c = \frac{2x_{IP}(z)}{z} = \sqrt{\beta_{\text{crab}} \beta^*} \frac{2eE_0 \sin\left(\frac{kL}{2}\right)}{E_b}.$$

For the beam energy E_b , the desired voltage should be

$$V = \frac{cE_b \theta_c}{2e\omega \sqrt{\beta_{\text{crab}} \beta^*}}.$$

Here we assume that the phase advance between the crab cavity location and IP is exactly $\frac{\pi}{2}$.

eRHIC Crab Cavity Requirement and Specifications

The eRHIC crossing angle is 25 mrad horizontally. Based on the bunch length and feasibility of fabrication, the crab cavity frequency of the eRHIC ion beam is chosen to be 394.118 MHz, which is the 16th harmonic of the bunch frequency. To minimize the design risk and single cavity fabrication cost, the electron beam will use the same design of crab cavity as the ions. With shorter bunch length and lower energy, the requirements to the crab cavity system from the electron beam are below 80% of the requirements from the ion beam. Thus, the crab cavity system development focused on the ion beam requirement, which would fulfill both beams. Table 3.12 shows the crab cavity related lattice parameters and the calculated voltage requirement for each scenario. The table also compares the eRHIC crab cavity with the existing crab cavities from KEKB and Hi-Lumi LHC [80–82]. The frequency difference between the Hi-Lumi LHC and eRHIC crab cavities is 1.5%, with the operational deflecting voltage difference less than 1%. Therefore, eRHIC can directly benefit from the experience from the LHC crab cavity program in most of aspects.

Table 3.12: Comparison of crab cavity parameters.

	KEKB		LHC	eRHIC		eRHIC	
			Hi-Lumi	no cooling		with cooling	
Parameter	LER	HER	both	ion	e	ion	e
Full crossing angle [mrad]	22	22	0.59	25	25	25	25
Energy [GeV]	3.5	8	7000	250	18	250	18
RMS L_{bunch} [cm]	0.7	0.6	7	7	0.9	6	0.9
Frequency [MHz]	509	509	400	394	394	394	394
Wave number	10.6679	10.6679	8.3834	8.26	8.26	8.26	8.26
Wave length [m]	0.5890	0.5890	0.7495	0.76	0.76	0.76	0.76
Scheme	global		local	local	local	local	local
6σ of wavelength	0.07	0.06	0.56	0.55	0.07	0.47	0.07
β at IP [m]	1.2	1.2	0.15	0.92	0.76	0.92	0.59
β at crab cavity [m]	51	122	2616	1300	200	1300	200
Hor. beam size [μm]	110	110	7	135	135	119	119
Piwinski angle [rad]	0.70	0.60	2.95	9.17	0.79	10.40	0.89
Voltage [MV]	0.92	1.36	12.43	12.03	2.21	12.03	2.51

The location of the crab cavity is chosen with consideration of minimizing the voltage, i.e. maximizing the β -function. However, the dispersion functions at the crab cavity locations are non zero for both rings, which would generate linear and non-linear instabilities with beam-beam interaction. Analysis of the detailed beam dynamics with crab crossing is

discussed in Section ??.

The spacial allowance for crab cavity system installation is limited by the distance between the electron and the ion beam lines in horizontal direction, and the local structures in the vertical plane, e.g. cable trays, cryogenic transfer lines, and the tunnel floor, but the limitation is much more relaxed compared to the LHC requirement. The parallel beam lines can accommodate the crab cavity cryomodules with 70 cm radius. In addition the IR is populated with various species of magnets, instrumentation devices, along with their auxiliaries. With the current matching lattice, the crab cavity systems are given 31 meters longitudinally on both sides of the IP for the hadron beam to provide a deflecting voltage of 12.03 MV, and more than 7 m for electron beam. Figure 3.18 shows the crab cavity cryomodules installed in both rings on one side of the IP, and the RCS ring is also shown in the picture. The red tunnel illustrates the injection line tunnel for the hadron beam. The location of the crab cavity cryomodule starts from 50 m on both sides to the interaction point (IP) for the hadron beam, and 40 m for the electron beam. These limits are carefully considered at the beginning of the cavity, coupler, helium vessel, tuner and cryomodule development to avoid any significant change in the future.

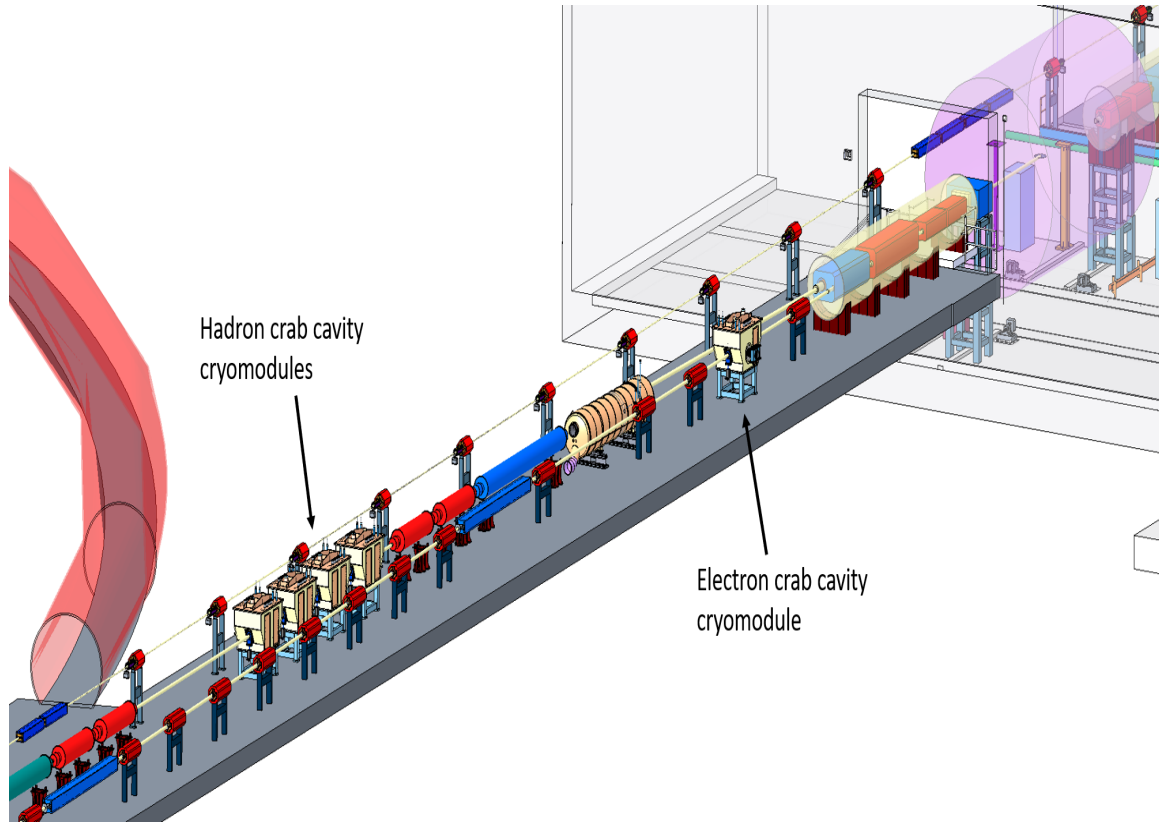


Figure 3.18: Schematic drawing of the local configuration of all beam lines near the crab cavity installation region, vertical.

3.2.5 Impedance Modeling

The main parameters used to evaluate the collective effects of the electron beam are given in Table 3.13. To estimate instability thresholds, the wake-potential for a 0.3 mm bunch length was used for beam dynamics simulations in the SPACE particle tracking code [83]. This simulated length is much shorter than the expected nominal bunch length of 19 mm for the unperturbed circulating beam.

Table 3.13: Parameters used for threshold calculation.

Parameter	Value
Energy E [GeV]	10
Revolution period T_0 [μ s]	12.79
Momentum compaction α	1.45×10^{-3}
Energy loss U [keV]	9100
RF voltage V [MV]	41
Synchrotron tune ν_s	0.0815
Damping time τ_x, τ_s [ms]	70, 35
Energy spread σ_δ	5.5×10^{-4}
Bunch length σ_s [mm]	19

IR Chamber

The vacuum chamber geometry for the interaction region (IR) is very complex with abrupt changes in the cross section as the particle beams cross each other. A cross-sectional top view of the preliminary IR chamber is shown in Figure 3.19 (upstream) and Figure 3.20 (downstream). Figure 3.21 shows a sectional view of the upstream section of the IR chamber.

An impedance analysis of this geometry has been performed using the GdfidL code [84]. The results of the numerical simulations are shown in Figure 3.22 and Figure 3.23. Using the machine parameters presented in Table 3.13 and the simulated results, the heat load due to multiple passes of the bunch train through the structure can be estimated by

$$P_{\text{loss}} = \kappa_{\text{loss}} I_{\text{av}}^2 T_0 / M, \quad (3.17)$$

where M is the number of bunches, T_0 is the revolution period, and I_{av} is the average current. Using the simulated geometric loss factor $k_{\text{loss}} = 0.2 \text{ V/pC}$, the power loss is $P_{\text{loss}} = 22.6 \text{ kW}$ for $M = 660$ bunches and $I_{\text{av}} = 2.48 \text{ A}$. Most of this heating is a result of the large step transitions which needs to be optimized from the impedance point of view. Reducing the abruptness of the transitions and providing better RF bridging will significantly reduce the heat load on the chamber walls.

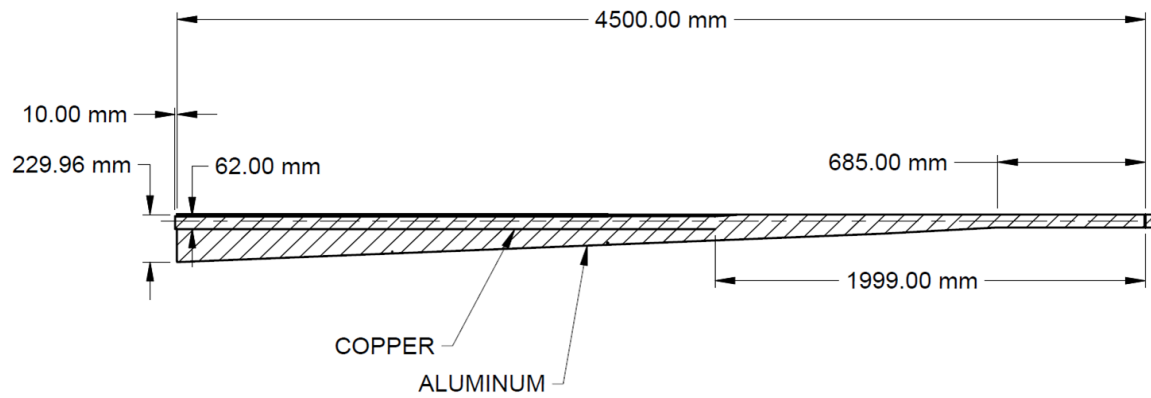


Figure 3.19: Cross-sectional top view of the upstream IR chamber.

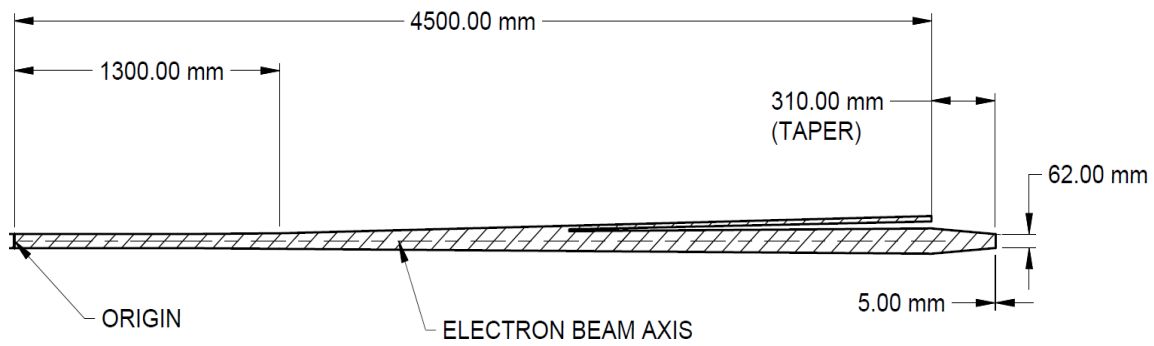


Figure 3.20: Cross-sectional top view of the downstream IR chamber.

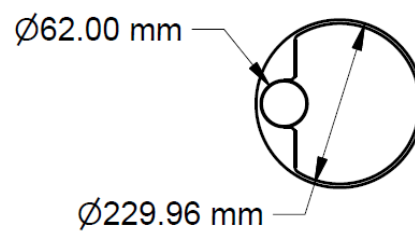


Figure 3.21: Section view of the upstream IR chamber entrance. The electron beam chamber with a 62 mm diameter.

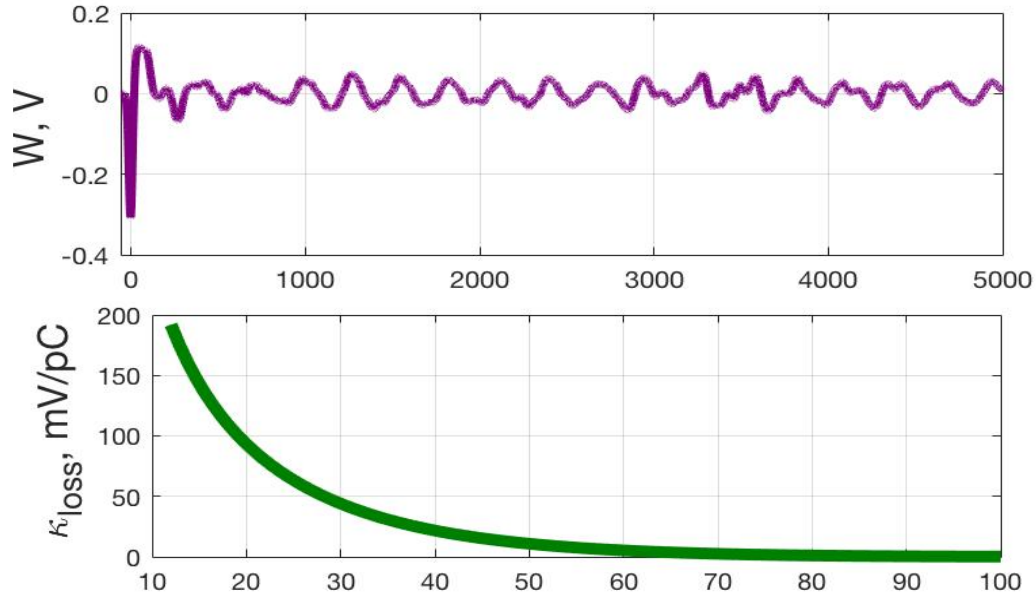


Figure 3.22: Numerically simulated data for the IR chamber. Top: Longitudinal wakepotential $W_{||}(s)$ simulated for a $\sigma_s = 12$ mm. Bottom: Loss factor as function of the bunch length σ_s .

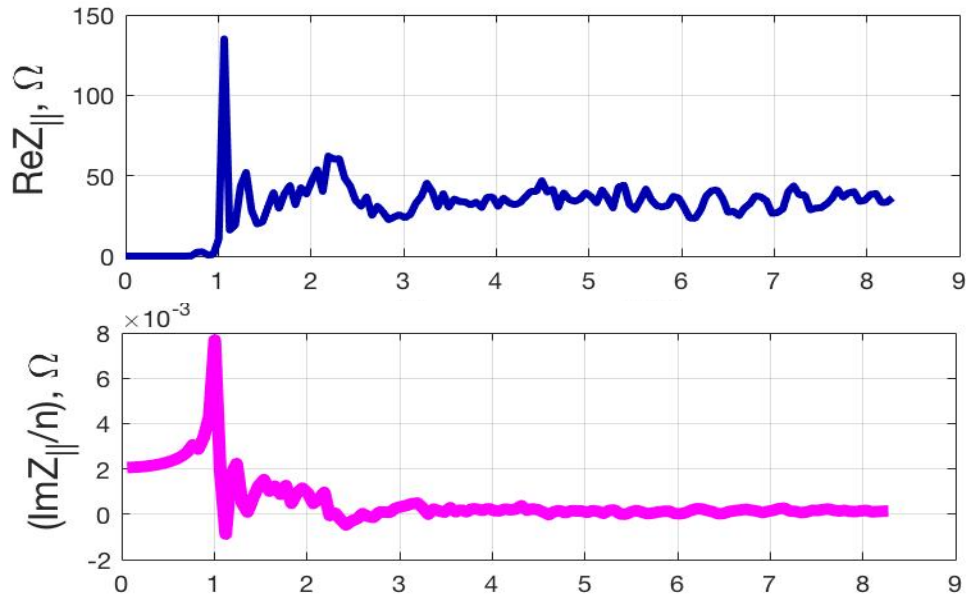


Figure 3.23: Top: Real part of the longitudinal impedance. Bottom: Imaginary part of the longitudinal impedance divided by $n = \omega/\omega_0$, where $\omega_0 = 2\pi \times 78.186$ kHz.

Longitudinal Impedance Model

By passing through the vacuum chamber, the electron beam generates electromagnetic fields, which can affect the beam stability. This makes it important to determine the impedance/wakepotential for all of the vacuum components distributed around the ring. A list of preliminary vacuum components is presented in Table 3.14. The exact geometric dimensions and surface resistivity of many of the vacuum components have not been finalized yet. For a first pass analysis the wakepotential and impedances simulated for several of the NSLS-II vacuum components have been scaled using the eRHIC lattice parameters to study the instability thresholds. The geometric impedance due to the cross-sectional changes of the vacuum components has been calculated by the GdfidL code. Table 3.14 indicates the origin of the data which is being used for the applied wakepotential. As the storage ring geometry is finalized, updates to the simulations will be performed and used to generate the total impedance budget for particle tracking simulations and analyt-

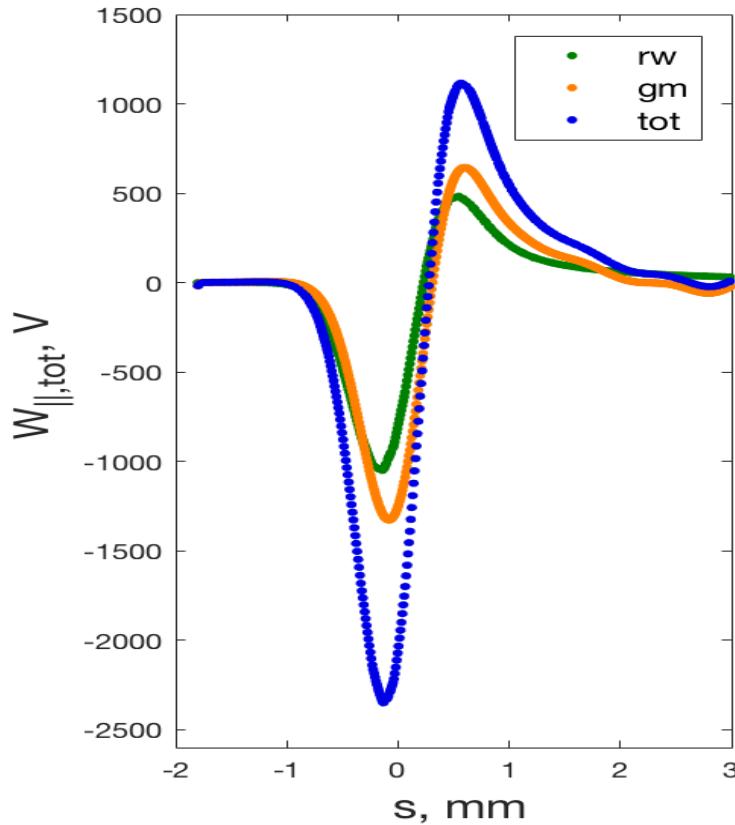


Figure 3.24: Longitudinal short-range wakepotential calculated for a bunch length of $\sigma_s = 0.3$ mm. The total longitudinal wakepotential of the eRHIC project (blue trace) is a sum of the resistive wall contribution (green trace) calculated analytically (Equation 3.18) and the geometric wakepotentials (orange trace).

Table 3.14: List of the vacuum components contributing to the total impedance of the electron storage ring.

Object	Abbreviation	Qty	Project
Bellows	BLW	380	NSLS-II
LA BPM	LABPM	494	NSLS-II
Stripline	SL	18	NSLS-II
Gate Valve	GV	45	NSLS-II
Flange Absorber	FABS	200	NSLS-II
RF Cavity	CAV	23	NSLS-II
RF Tapered Transition	TPRDRF		NSLS-II
IR Chamber	IRCHM	1	eRHIC

ical evaluation. The contribution of the resistive wall to the total impedance is calculated separately by applying the analytical approach derived by Bane and Sands [85]:

$$W_{\parallel}(\tau) = \frac{r_e mc^2 N_e}{2b \sqrt{2\mu_r Z_0 \sigma_{\text{con}}}} i \left| \frac{\tau}{\sigma} \right|^{3/2} e^{-\tau^2/4\sigma^2} \times \left[I_{1/4} \left(\frac{\tau^2}{4\sigma^2} \right) - I_{-3/4} \left(\frac{\tau^2}{4\sigma^2} \right) - \text{sgn}(\tau) I_{-1/4} \left(\frac{\tau^2}{4\sigma^2} \right) + \text{sgn}(\tau) I_{3/4} \left(\frac{\tau^2}{4\sigma^2} \right) \right] \quad (3.18)$$

where b is the vacuum chamber radius, $Z_0 = 120\pi$ is the impedance of free space, σ is the electrical conductivity and μ_r is the relative permeability of the chamber surface. As a preliminary estimate for the resistive wall surface, six 257 m long arc sections and twelve 123 m long copper straight sections with a radius of 20 mm are assumed.

The total longitudinal wakepotential, which is a sum of the short-range geometric and resistive-wall longitudinal wakepotentials, is shown in Figure 3.24. The real part of the frequency spectrum of the total longitudinal impedance is presented in Figure 3.25 up to 350 GHz. The total longitudinal wakepotential $W_{\parallel, \text{tot}}$ was used as an input file for the SPACE particle tracking code along with the parameters presented in Table 3.13. Numerical simulations were done using 30 million macro-particles and 800 grid points in order to accurately determine the first microwave instability threshold and to characterize the microwave dynamics. The energy spread of the unperturbed Gaussian bunch at low current is estimated at $\sigma_{\delta} = 5.5 \times 10^{-4}$. From this the first microwave instability threshold is observed at $I_{\text{th}} = 4.5$ mA (see Figure 3.26), which is above the single bunch current of 3.8 mA. The bunch lengthening effect due to potential-well distortion (see Figure 3.26) is small enough up to 4 mA for the applied total longitudinal wakepotential.

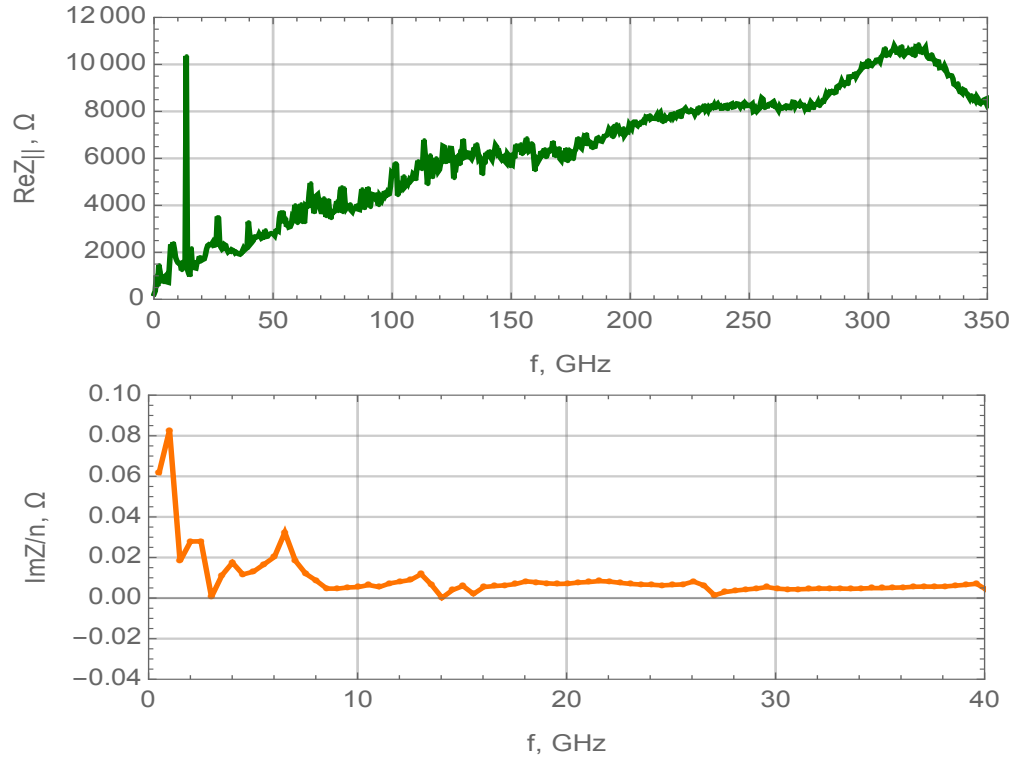


Figure 3.25: Top: Real part of the longitudinal impedance. Bottom: Imaginary part of the longitudinal impedance divided by $n = \omega/\omega_0$, where $\omega_0 = 2\pi \times 78.186 \text{ kHz}$.

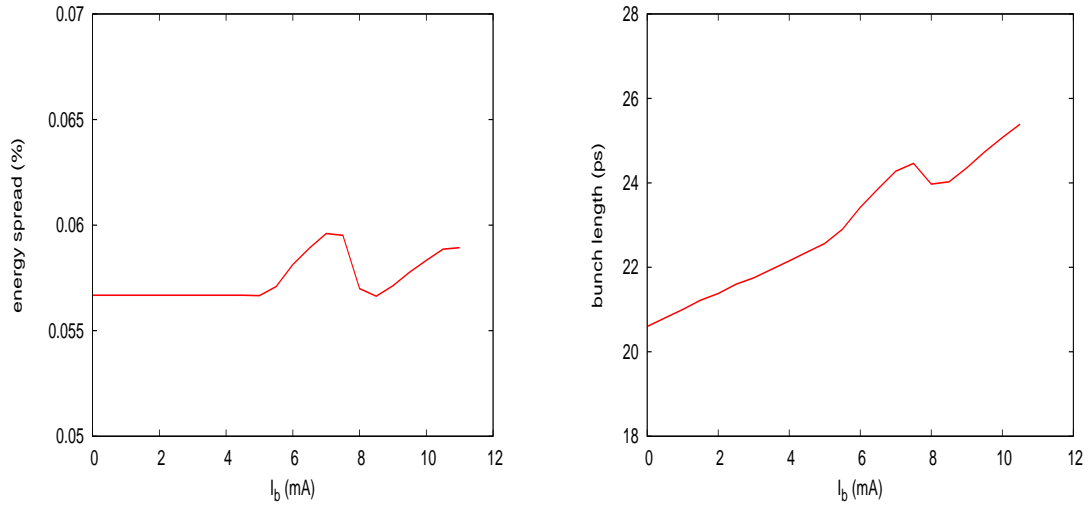


Figure 3.26: Left: Energy spread as a function of single bunch current. Right: Bunch lengthening dependence on the single-bunch current.

3.2.6 Betatron Tune Dependence on Electron Beam Intensity

For the octagonal shape of the dipole vacuum chamber with a half-aperture $b = 20$ mm and dipole magnet half-gap $d = 26$ mm, the multi-bunch current dependent betatron tune shift induced by the quadrupole impedance of the dipole magnets at frequency $\omega \rightarrow 0$ is given by

$$\Delta\nu_{x,y} = \frac{I_{av}L}{4\pi E/e} \beta_{x,y} \text{Im}Z_{Q_{x,y}}(0) \quad (3.19)$$

where $L = 192 \times 6.064$ m is the total length of the dipole magnets, $I_{av} = 2.48$ A is the average current, $\beta_x = 17$ m and $\beta_y = 18$ m are the local horizontal and vertical average β -functions, $E = 10$ GeV is the electron beam energy and $\text{Im}Z_{Q_{x,y}}$ is the imaginary part of the quadrupole impedance. For the dipole magnets, the quadrupole impedance $\text{Im}Z_{Q_{x,y}}$ is analytically approximated by a multi-parallel plates model [86]

$$\Re Z_{Q_{x,y}}(0) = \pm \frac{\pi^2}{12cb^2} \left(1 + 2\frac{b^2}{d^2} f(\eta) \right), \quad (3.20)$$

where

$$f(\eta) = \frac{6}{\pi^2} \text{Li}_2(\eta) \quad (3.21)$$

and

$$\eta = \frac{\mu_r - 1}{\mu_r + 1} \quad (3.22)$$

With relative permeability $\mu_r \rightarrow 0$ (perfect magnets) $f(\eta) = 1$. We notice that Equation 3.20 differs by a factor of 2 from the formula for the resistive wall impedance derived by Chao, Heifets and Zotter in Ref. [87] using the well known Laslett coefficients [88]. The validity of Equation 3.19, where the only contribution to the betatron tune shift is given by the quadrupole impedance evaluated at zero frequency, is justified by the fact that the first contribution from the dipole impedance, which is given by the impedance evaluated at $\nu_{\perp} f_0$, where ν_{\perp} is the fractional betatron tune and $\perp = x$ or y , is negligible, as shown in Figure 3.27 for the nominal fractional betatron tunes $\nu_x = 0.08$ and $\nu_y = 0.06$.

The calculated betatron tunes ν_x and ν_y as a function of average current I_{av} are presented in Figure 3.28. At the nominal $I_{av} = 2.48$ A, the estimated tune shifts $\Delta\nu_x = 0.05$ and $\Delta\nu_y = -0.05$ might affect the lattice optimization to mitigate the beam-beam effects. To eliminate the effect of the quadrupole impedance on the multi-bunch tune shift dependence vs. the average current, the dipole vacuum chamber should be considered with a circular profile.

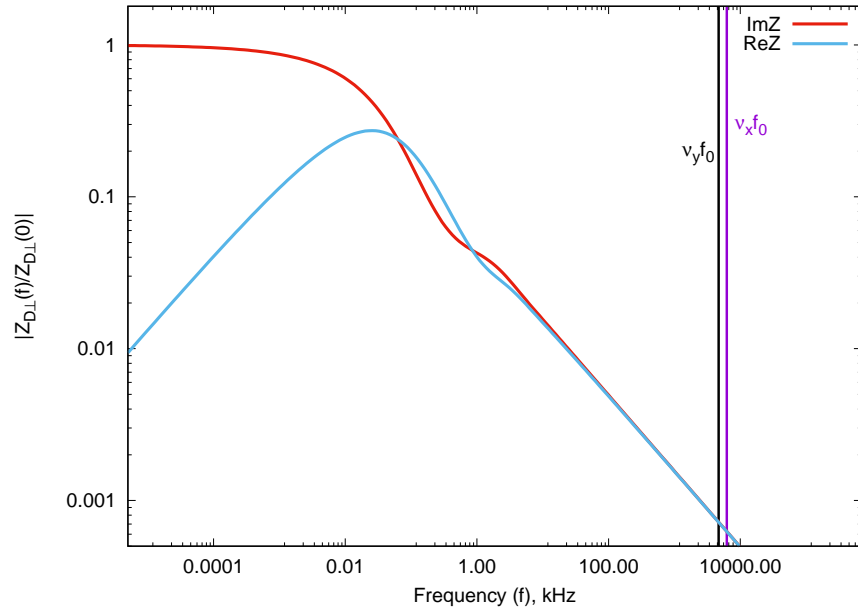


Figure 3.27: Absolute value of the ratio of the transverse dipole impedance to the quadrupole impedance evaluated at zero frequency. Here \perp is either x or y . The dipole and quadrupole impedances are related as follows: $Z_{D_x}(f) = -Z_{Q_x}(f)$, $Z_{D_y}(f) = Z_{Q_y}(f)$. The dipole impedance is obtained numerically by the standard field matching technique as applied in [86], with dipole chamber conductivity $\sigma_{Cu} = 54 \text{ S/m}$ and thickness $t = 4 \text{ mm}$. The dipole impedance, evaluated at $f = \nu_{\perp} f_0$ with parameters $\nu_x = 0.08$, $\nu_y = 0.06$ and $f_0 = 78196.5 \text{ kHz}$ is negligible with respect to the quadrupole impedance evaluated at $f = 0$, thus justifying the validity of Equation 3.19.

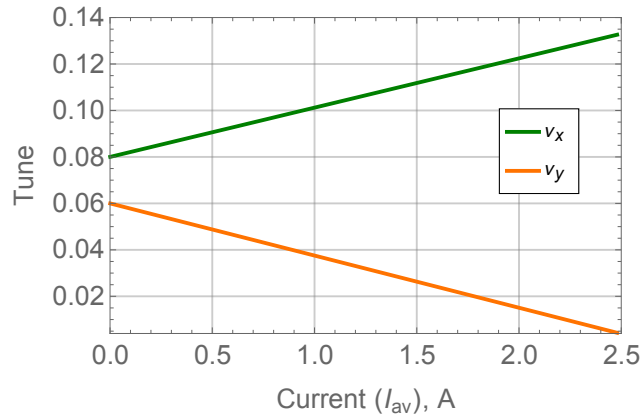


Figure 3.28: Horizontal and vertical betatron tune shifts as a function of average current estimated using Equation 3.19.

3.2.7 Synchrotron Radiation Analysis

The IR crossing angle scheme avoids the necessity of separator dipoles in or near the detector, which would generate a wide fan of hard synchrotron radiation photons. However, the nearby low- β quadrupoles generate a synchrotron radiation cone that can be equally harmful for different detector components, if not handled appropriately.

In contrast to the homogeneous fan produced by dipole magnets, the photon cone generated by quadrupoles consists of a huge number of weak photons in its center, and a comparatively small number of very high energy photons with increasing distance from the center. These high energy photons stem from electrons in the transverse tails of the beam distribution that experience strong magnetic fields at large amplitudes in these low- β quadrupoles. Additionally, since the beam-beam interaction tends to cause an overpopulation of the transverse electron beam tails, especially in the vertical plane, the number of hard photons produced in the quadrupoles by large-amplitude electrons can be significantly higher than expected for a pure Gaussian distribution. Therefore it is important to take all these factors into account when evaluating the synchrotron radiation background in the detector, and designing a masking scheme.

Nonlinear effects in the beam-beam interaction lead to the formation of non-Gaussian tails with an enhanced electron density. Figure 3.29 illustrates this. The colliding electron beam requires about 50% larger aperture than without beam-beam interactions. The magnets and synchrotron radiation masks have to provide sufficient aperture for these tails to pass through in order to provide beam lifetimes of several hours.

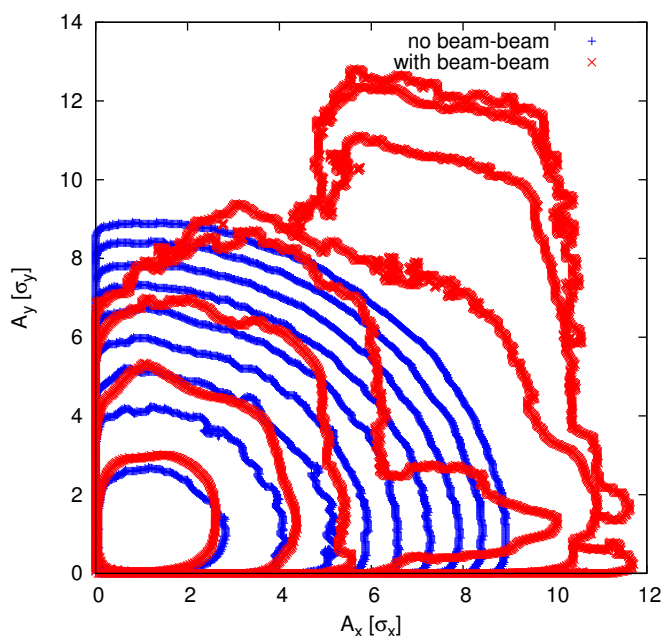


Figure 3.29: Transverse electron density distribution with (red) and without (blue) beam-beam interaction. The contour lines are spaced by a factor 10.

The design of an eRHIC general purpose detector requires a machine element free region of ± 4.5 m around the IP. As a consequence, any synchrotron radiation mask that gets hit by direct radiation can only be installed outside the detector volume in the incoming electron beam direction. The aperture of those masks has to be sufficiently large to ensure beam lifetimes on the order of several hours. As shown in Figure 3.29 the electron density at 13σ is about the same as at 8σ without beam-beam. Therefore, one expects a beam lifetime of more than 20 hours [89] with a 13σ aperture and beam-beam effects.

The first focusing element (quadrupole Q1EF) starts at a distance of 5.0 m from the IP. In order to reduce the peak magnetic fields encountered by electrons in the transverse tails, this magnet as well as the following quadrupole Q2EF are comparatively long; the length is limited by the requirement to interleave focusing elements in the hadron beam line [90]. Table 3.15 lists the design parameters of the last two quadrupoles upstream of the IP.

A dual stage masking scheme is what is required to limit the synchrotron radiation fan through the central detector. On the incoming side, its cross section will be identical to that of the masks before the central detector. Their size is determined by the 13σ beam size requirement at their specific location. Assuming radii of the upstream ellipse of 11 mm in the horizontal plane, and 10 mm vertically, at the downstream end of the central detector, the cone radii will have substantially increased, to 71 mm horizontally, and 19 mm vertically. This growth of the synchrotron radiation fan determines the minimum dimensions of the detector beam pipe that ensure strongly reduced background from primary photons generated by the electron beam.

In the next step, the impact of potentially backscattered photons on the detector is simulated using the code DESYNC [91].

The focusing upstream of the detector is designed to minimize the magnetic fields of the last two quadrupoles seen by electrons in the transverse tails of the beam. This is accomplished by designing quadrupoles Q1EF and Q2EF with a low gradient and an extended length. Even at the highest electron beam energy of 18 GeV this results in peak fields of only 0.3 T at the 15σ design aperture of these magnets. However, since the movable upstream mask at $s = 4.5$ m has an aperture radius of only 10σ , no electrons are present in the beam beyond this limit. Therefore, the maximum magnetic field sampled is only $2/3$ of the peak field of those quadrupoles, namely $B_{\max} = 0.2$ T. The corresponding critical energy of the synchrotron radiation generated by the small number of electrons at the outer edges

Table 3.15: Electron IR magnet parameters on the upstream side of the detector, for the highest design energy of 18 GeV.

Magnet	s_i [m]	l [m]	IR [cm]	B [T]	g [T/m]
Q1EF	5.00	1.2	2.2	0.309	-14.1
Q2EF	8.74	1.72	4.85	0.282	6.0

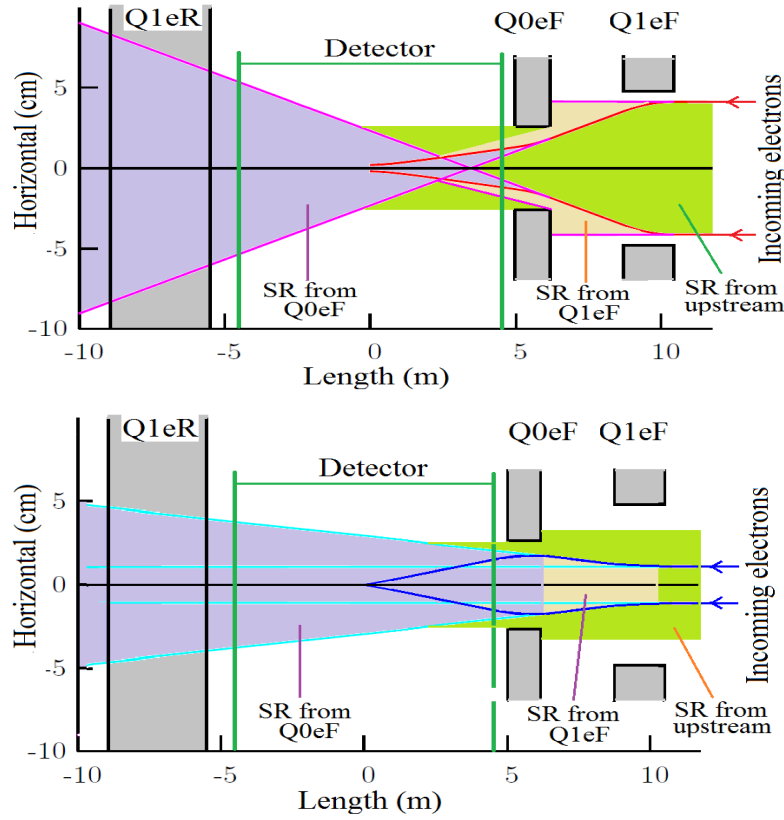


Figure 3.30: Synchrotron radiation fans from the low- β quadrupole doublet through the IR. Top: top view; Bottom: side view.

of the beam is therefore reduced to

$$\begin{aligned}
 E_c &= \frac{3 \hbar c^2 e E^2 B}{2 E_0^3} \\
 &= 43.2 \text{ keV},
 \end{aligned}
 \tag{3.23}$$

at 18 GeV, or $E_c = 13.3 \text{ keV}$ at $E = 10 \text{ GeV}$. Here $E_0 = m_e c^2$ is the electron energy at rest.

Photon scattering in the IR geometry described above has been simulated with the code DESYNC [91]. Assuming a detector beam pipe that is tailored to accommodate the primary synchrotron radiation fan according to Figure 3.30 the radiation load outside the 1 mm thick beryllium detector pipe reaches a maximum of 2.2 rad/hour at 18 GeV in the 1 m long section right after the mask, and less than a $\mu\text{rad/hour}$ everywhere else throughout the central detector. At a beam energy of 10 GeV the maximum rate reduces by 2-3 orders of magnitude.

While these radiation levels are likely acceptable more detailed simulations including the actual eRHIC detector are required. These simulations are beyond the capabilities of DESYNC and will therefore be carried out using a simulation code such as GEANT4 [92].

Glossary of Acronyms

Name	Description
ACS	Access Control Systems
ADC	Analog to Digital Converter
ADO	Accelerator Device Object, device software manager in C++ programming
AGS	Alternating Gradient Synchrotron: an accelerator at BNL that serves as injector to RHIC
ANL	Argonne National Laboratory
API	Application (Program) Interface
APS	Argonne Photon Source: a light source facility at Argonne National Lab
ARR	Accelerator Readiness Review
ATLAS	A colliding beams detector at the CERN Large Hadron Collider
ATR or AtR	AGS to RHIC beam transfer line
AWG	American Wire Gauge
B-factory	A particle collider designed to produce large numbers of B mesons
B-field	Magnetic field
BLA	Beam Line Absorbers
BLM	Beam Loss Monitor
BNL	Brookhaven National Laboratory
BPM	Beam Position Monitor
CAD	Computer Aided Design
C-AD	Collider-Accelerator Department, Brookhaven National Lab
CBI	Coupled bunch instability
CBM	Coupled bunch modes
CC	Crab Cavity
CCD	Charged Coupled Device: a silicon chip for capturing and manipulating digital data
CCG	Cold cathode ion gauge
CDEV	Common Device interface
CDR	Conceptual Design Report
CDS	Computers, Devices, and Software
CEBAF	Continuous Electron Beam Accelerator Facility at Jefferson Laboratory, Virginia
CeC or CEC	Coherent Electron Cooling

CEM	Channeled Electron Multiplier
CERN	European Organization for Nuclear Research: accelerator laboratory in Switzerland
CESR	Cornell Electron Storage Ring facility
CM or c.m.	Center of mass
CME	Center of mass energy
CMOS	Complementary Metal-Oxide-Semiconductor: a silicon chip for manipulating digital data
CNS	Controls Name Server
COMPASS	An experiment at CERN utilizing muon and proton beams
COTS	Commercial off-the-shelf
CSR	Coherent synchrotron radiation
CVD	Chemical Vapor Deposition
DAC	Digital to Analog Converter
DAFNE	An accelerator facility in Frascati, Italy
DCCT	Direct Current Current Transformer, a precision DC current transducer
DESY	Deutsche Elektronen Synchrotron Laboratory: an accelerator facility in Hamburg, Germany
DOE	U.S. Department of Energy
DoS	Density of State
DQW	Double quarter wave
DQWCC	Double quarter wave crab cavity
DVCS	Deeply Virtual Compton Scattering
DVVM	Deeply Virtual Vector Meson
EBIS	Electron Beam Ion Source
EBW	Electron Beam Welding
EH&S	Environment Health and Safety
EHS&Q	Environment Health Safety and Quality
EIC	Electron Ion Collider
EIS	Environmental Impact Statement
EMC	European Muon Collaboration experiment at CERN
EOM	Electro-Optic Modulator
EPS	Equipment control and Protection System at RHIC
eRHIC	Electron Ion Collider at BNL utilizing RHIC
ERL	Energy Recovery LINAC
eSR	Electron Storage Ring
eSTAR	A proposed eRHIC detector based on the existing STAR detector at RHIC
FCT	Fast Current Transformer
FEC	Front End Controller/Computer
FEL	Free Electron Laser
FHA	Fire Hazard Analysis
FODO	A particular grouping of focusing and defocusing magnets used in accelerator beams

FONSI	Finding of No Significant Impact
FPC	Fundamental Power Coupler
FPGA	Field-Programmable Gate Array
FRIB	Facility for Rare Isotope Beams under construction at Michigan State University
FSAD	Final Safety Analysis Document
FY	Fiscal Year
GEMA	planar multi-electrode array used to measure particle trajectories in gas-filled detectors
GPIB	General Purpose Interface Bus, IEEE-488
GPM	General Purpose Monitor
HEBT	High Energy Beam Transport
HERA	Hadron-Electron Ring Accelerator at DESY in Hamburg, Germany
HERMES	A fixed-target experiment at HERA facility
HOM	Higher Order Modes
HTTP	Hypertext Transfer Protocol
IBS	Intrabeam Scattering
ICT	Integrating Current Transformer
IEEE	Institute of Electrical and Electronics Engineers
ILC	International Linear Collider
INT	Institute for Nuclear Theory at the University of Washington, Seattle
IOT	Inductive Output Tube, a vacuum tube used as a high power RF amplifier
IP	Interaction Point
IAD	Ion Assisted Deposition
IPM	Ionization Profile Monitor
IR	Interaction Region
ISO	Optical isolator, , or International Standards Organization
IVA	Inductive Voltage Adder
JFT	A Japanese tokamak fusion research facility
JLab	Thomas Jefferson National Accelerator Facility, Newport News, Virginia
KEK	High Energy Accelerator Research Laboratory, Tsukuba, Japan
KEKB	A particle accelerator operating as a B-factory at KEK
LARP	Large Hadron Collider (LHC) Accelerator Research Program
LBNL	Lawrence Berkeley National Laboratory in California
LDRD	Laboratory Directed Research and Development
LEP	Large Electron Positron collider, predecessor to the LHC at CERN
LEReC	Low Energy RHIC electron Cooling
LHC	Large Hadron Collider at CERN in Geneva, Switzerland
LINAC	Linear Accelerator
LLRF	Low Level Radio Frequency
LPOL	Longitudinal polarization measurement of the electron beam at HERA
LTR or LtR	LINAC to RCS transfer line
MAPS	A planar multi-electrode array on a microchip, used to measure charged particle trajectories in compact gas-filled detectors

MBEC	Micro-bunched electron beams
MCP	Micro Channel Plate detector
NAS	National Academy of Science and Network Attached Storage system
NCRF	Normal Conducting Radio Frequency
NEA	Negative Electron Affinity
NEG	Non-Evaporation Getter
NEPA	National Environmental Policy Act
NPCT	New Parametric Current Transformer
NSAC	Nuclear Science Advisory Committee for U.S. Department of Energy
NSLS-II	National Synchrotron Light Source-II at BNL
NSRL	NASA Space Radiation Laboratory at BNL
ODH	Oxygen Deficiency Hazard
OFHC	Oxygen-Free High Conductivity copper
PPM	Office of Project Management
OPPIS	A polarized ion source used for injection of polarized protons into RHIC
OTR	Optical Transition Radiation
PASS	Personnel Access Safety System
PDF	Particle Distribution Function
PED	Project Engineering and Design
PEP-II	Positron-Electron Project, a colliding beams facility at SLAC
PETRA	A high energy electron-positron accelerator facility at DESY, now operating as a light source
PFL	Pulse Forming Line
PHENIX	A large colliding-beams detector at RHIC
PID	Particle Identification
PLC	Programmable Logic Controller
PLL	Phase-Locked Loop
PoP	Proof of Principle
PPS	Personnel Protection System
PSAD	Preliminary Safety Assessment Document
PSD	Photon Stimulated Desorption, or Power Spectrum Density
PSEG	A local utility company providing electrical power to BNL
PSI	Power Supply Interface
PVD	Physical Vapor Deposition
PWO	Lead Tungstate crystal
QCD	Quantum Chromodynamics
QE	Quantum Efficiency
QWR	Quarter-Wave Resonator
RACF	RHIC and ATLAS Computing Facility at BNL
R&D	Research and Development
RCS	Rapid Cycling Synchrotron for eRHIC
RCStSR	The beam transfer line from RCS to the eRHIC Storage Ring
REST	Representational State Transfer protocol

RF	Radio Frequency
RG	Residual Gas Analyzer
RHIC	Relativistic Heavy Ion Collider at Brookhaven National Laboratory
RICH	Ring Imaging Cherenkov detector
RMS	Root Mean Square
RTD	Resistance Temperature Detector
RTDL	Real Time Data Link
RtS	RCS to Storage Ring
SAD	Safety Assessment Document
SBEND	Sector Bend in RCS ring lattice
SBMS	Standards-Based Management System
SCCR	Short Circuit Current Rating
SEY	Secondary Emission Yield
SIDIS	Semi-Inclusive Deep Inelastic Scattering (of high energy electrons)
SIL	Safety Integrated Level
Sindi	Synoptic Display tool
SIP	Sputtering Ion Pump
SLAC	Stanford Linear Accelerator Center in California SLC SLAC Linear Collider
SLM	Synchrotron Light Monitor
SM	Standard Model of particle physics
sPHENIX	A proposed new RHIC detector to replace PHENIX
SPS	Super Proton Synchrotron, and accelerator at CERN
SR	Synchrotron Radiation
SRF	Superconducting Radio-Frequency
SRP/CS	Safety Related Parts of Control Systems
SW	Standing Wave
SOC or SoC	System on a Chip
Tape	Tool for Automated Procedure Execution
T-BMT	Thomas-BMT equation, named after Thomas, Bargmann-Michel-Telegdi
TAL	Triplet Achromat Lattice
TBA	Triple Bend Achromat
TEC	Total Estimated Cost
TIG	Tungsten Inert Gas (a specialized form of welding)
TMCI	Transverse Mode Coupling Instability
TMD	Transverse Momentum Distribution
TMP	Turbomolecular Pump
TPC	Time Projection Chamber
TPOL	Transverse Polarization measured for the electron beam at HERA
TSP	Titanium Sublimation Pumps
TWP	Traveling Wave Plates
UHV	Ultra-High Vacuum
UPC	Ultra-Peripheral Collisions

UPS	Uninterruptable Power Supply
VME	VERSAModule Europa, IEEE-1014-1987, chassis for electronic control modules
WCM	Wall Current Monitor
XDB	Xray Diagnostic Beamline
XHV	Extremely High Vacuum
YAG	A type of laser using a Yttrium-Aluminum-Garnet crystal
ZDC	Zero Degree Calorimeter
ZEUS	A large detector at the HERA collider
ZFCT	Zero Flux Current Transformer, a type of DCCT

References

- [1] A. Accardi *et al.*, “Electron Ion Collider: The Next QCD Frontier,” *Eur. Phys. J.*, vol. A52, no. 9, p. 268, 2016.
- [2] A. Aprahamian *et al.*, “Reaching for the horizon: The 2015 long range plan for nuclear science.” DOE/NSF Nuclear Science Advisory Panel (NSAC) Report, 2015.
- [3] National Academies of Sciences, Engineering, and Medicine, “An Assessment of U.S.-Based Electron-Ion Collider Science.” The National Academies Press, Washington DC, 2018. <https://doi.org/10.17226/25171>.
- [4] Harrison, M. and Ludlam, T. and Ozaki, S., “RHIC Project Overview,” *Nucl. Instr. Meth. A*, vol. 499 (2-3), p. 235, 2003.
- [5] O. S. Bruning, P. Collier, P. Lebrun, S. Myers, R. Ostojic, J. Poole, and P. Proudlock, “LHC Design Report Vol.1: The LHC Main Ring,” 2004.
- [6] W. Busza, K. Rajagopal, and W. van der Schee, “Heavy Ion Collisions: The Big Picture, and the Big Questions,” *Annual Review of Nuclear and Particle Science*, vol. 68, pp. 1 – 49, 2018.
- [7] P. Schmüser and F. Willeke, *The Electron-Proton Collider HERA, Accelerators and Colliders, Landolt-Börnstein - Group I Elementary Particles, Nuclei and Atoms*, vol. 21. Springer-Verlag, Berlin Heidelberg, 2013.
- [8] A. Lung, “Future plans at Jefferson Lab: 12-GeV CEBAF upgrade and electron-ion collider (EIC),” in *Proceedings, 16th International Workshop on Deep Inelastic Scattering and Related Subjects (DIS 2008): London, UK, April 7-11, 2008*, p. 230, 2008.
- [9] F. Bradamante, “The COMPASS experiment at CERN,” *Nucl. Phys.*, vol. A622, pp. 50C–65C, 1997.
- [10] K. H. Ackermann *et al.*, “STAR detector overview,” *Nucl. Instrum. Meth.*, vol. A499, pp. 624–632, 2003.
- [11] M. Connors, “Design, status and schedule of the sPHENIX experiment at RHIC,” *Nucl. Phys.*, vol. A967, pp. 548–551, 2017.

- [12] F. Willeke, "Overcoming performance limitations due to synchro-betatron resonances in the HERA electron ring," in *9th European Particle Accelerator Conference (EPAC 2004) Lucerne, Switzerland, July 5-9, 2004*, 2004.
- [13] A. Piwinski, "Intra-beam-Scattering," in *Proceedings, 9th International Conference on the High-Energy Accelerators (HEACC 1974): Stanford, California, May 2-7, 1974*, pp. 405–409, 1974.
- [14] D. Kayran *et al.*, "Proof-of-principle experiment for FEL-based coherent electron cooling," *Conf. Proc.*, vol. C110328, pp. 2064–2066, 2011.
- [15] A. Sokolov and I. Ternov, "Polarization and Spin Effects in the Theory of Synchrotron Radiation," *Doklady Akademii Nauk SSSR (USSR)*, vol. 153, 1963.
- [16] D. Sagan, "Beam-beam effects with errors in the crab compensation," *Conf. Proc.*, vol. C930517, pp. 3470–3472, 1993.
- [17] R. B. Palmer, "Energy Scaling, Crab Crossing, and the Pair Problem," in *High energy physics in the 1990's: Proceedings*, vol. C8806271, pp. 613–619, 1988.
- [18] KEK, "KEKB B factory design report," 1995.
- [19] "PEP-II: An Asymmetric B Factory. Conceptual Design Report.," 1994.
- [20] Ya. S. Derbenev and A. M. Kondratenko, "Acceleration of Polarized Particles to High-Energies in Synchrotrons," in *Proceedings: 10th International Conference on High-Energy Accelerators, Protvino, Jul 1977. 1.*, vol. 2, pp. 70–75, 1977.
- [21] V. Schoefer *et al.*, "RHIC Polarized Proton-Proton Operation at 100 GeV in Run 15," in *Proceedings, 6th International Particle Accelerator Conference (IPAC 2015): Richmond, Virginia, USA, May 3-8, 2015*, p. TUPWI060, 2015.
- [22] V. N. Litvinenko and Y. S. Derbenev, "Coherent Electron Cooling," *Phys. Rev. Lett.*, vol. 102, p. 114801, 2009.
- [23] K. Ohmi, "Simulation of beam-beam effects in a circular $e^+ e^-$ collider," *Phys. Rev.*, vol. E62, pp. 7287–7294, 2000.
- [24] J. Qiang, M. A. Furman, and R. D. Ryne, "A parallel particle-in-cell model for beam-beam interaction in high energy ring colliders," *J. Comput. Phys.*, vol. 198, pp. 278–294, 2004.
- [25] V. Ptitsin and Yu. M. Shatunov, "Helical spin rotators and snakes," *Nucl. Instrum. Meth.*, vol. A398, pp. 126–130, 1997.
- [26] I. Alekseev *et al.*, "Polarized proton collider at RHIC," *Nucl. Instrum. Meth.*, vol. A499, pp. 392–414, 2003.
- [27] D. P. Barber *et al.*, "The First achievement of longitudinal spin polarization in a high-energy electron storage ring," *Phys. Lett.*, vol. B343, pp. 436–443, 1995.

- [28] Y. Shatunov and V. Ptitsin, "Siberian Snakes for Electron Storage Rings," in *17th IEEE Particle Accelerator Conference (PAC 97): Accelerator Science, Technology and Applications Vancouver, British Columbia, Canada, May 12-16, 1997*, vol. C970512, p. 3500, 1997.
- [29] I. Borchardt, E. Karantzoulis, H. Mais, and G. Ripken, "Calculation of Beam Envelopes in Storage Rings and Transport Systems in the Presence of Transverse Space Charge Effects and Coupling," *Z. Phys.*, vol. C39, p. 339, 1988.
- [30] D. P. Barber, F. Brinker, W. Decking, E. Gianfelice-Wendt, J. Keil, M. Vogt, and F. J. Willeke, "Longitudinal Positron Polarisation in HERA-II," in *9th European Particle Accelerator Conference (EPAC 2004) Lucerne, Switzerland, July 5-9, 2004*.
- [31] Ya. S. Derbenev and A. M. Kondratenko, "Diffusion of particle spins in storage elements," *Sov. Phys. JETP*, vol. 35, p. 230, 1972.
- [32] R. Assmann, A. Blondel, B. Dehning, P. Grosse-Wiesmann, R. Jacobsen, J. P. Koutchouck, J. Miles, M. Placidi, R. Schmidt, and J. Wenninger, "Deterministic harmonic spin matching in LEP," in *4th European Particle Accelerator Conference (EPAC 94) London, England, June 27-July 1, 1994*, vol. C940627, pp. 932–934, 1994.
- [33] D. P. Barber, E. Gianfelice-Wendt, and M. Vogt, "Spin polarisation at DESY," *ICFA Beam Dyn. Newslett.*, vol. 37, pp. 88–93, 2005.
- [34] M. Blaskiewicz, "A multipurpose coherent instability simulation code," in *Particle Accelerator Conference, 2007. PAC. IEEE*, pp. 3690–3692, IEEE, 2007.
- [35] O. S. Bruning *et al.*, "Electron cloud and beam scrubbing in the LHC," in *Proceedings, 1999 Particle Accelerator Conference (PAC'99): New York, New York, March 29-April 2, 1999*, pp. 2629–2631, 1999.
- [36] M. Blaskiewicz and U. Iriso, "How To Use CSEC," Tech. Rep. BNL-99410-2013-IR, Brookhaven National Laboratory, 2006.
- [37] D. Ratner, "Microbunched Electron Cooling for High-Energy Hadron Beams," *Phys. Rev. Lett.*, vol. 111, no. 8, p. 084802, 2013.
- [38] M. Woods, J. Clendenin, J. Frisch, A. Kulikov, P. Saez, D. Schultz, J. Turner, K. Witte, and M. Zolotarev, "Observation of a charge limit for semiconductor photocathodes," *J. Appl. Phys.*, vol. 73, pp. 8531–8535, 1993.
- [39] "Computer Simulation Technology." <http://www.cst.com>.
- [40] D. Boer *et al.*, "Gluons and the quark sea at high energies: Distributions, polarization, tomography," *arXiv preprint arXiv:1108.1713*, 2011.
- [41] E. C. Aschenauer, S. Fazio, J. H. Lee, H. Mantysaari, B. S. Page, B. Schenke, T. Ullrich, R. Venugopalan, and P. Zurita, "The Electron-Ion Collider: Assessing the Energy Dependence of Key Measurements," *arXiv preprint arXiv:1708.01527*, 2017.
- [42] R. L. Jaffe and A. Manohar, "The G(1) Problem: Fact and Fantasy on the Spin of the Proton," *Nucl. Phys.*, vol. B337, pp. 509–546, 1990.

- [43] E.-C. Aschenauer *et al.*, “The RHIC SPIN Program: Achievements and Future Opportunities,” *arXive preprint arXive:1501.01220*, 2015.
- [44] E. C. Aschenauer, R. Sassot, and M. Stratmann, “Unveiling the Proton Spin Decomposition at a Future Electron-Ion Collider,” *Phys. Rev.*, vol. D92, no. 9, p. 094030, 2015.
- [45] E. C. Aschenauer, R. Sassot, and M. Stratmann, “Helicity Parton Distributions at a Future Electron-Ion Collider: A Quantitative Appraisal,” *Phys. Rev.*, vol. D86, p. 054020, 2012.
- [46] D. Boer and P. J. Mulders, “Time reversal odd distribution functions in lepton production,” *Phys. Rev.*, vol. D57, pp. 5780–5786, 1998.
- [47] L. Zheng, E. C. Aschenauer, J. H. Lee, B.-W. Xiao, and Z.-B. Yin, “Accessing the Gluon Sivers Function at a future Electron-Ion Collider,” *arXive preprint arXive:1805.05290*, 2018.
- [48] D. W. Sivers, “Hard scattering scaling laws for single spin production asymmetries,” *Phys. Rev.*, vol. D43, pp. 261–263, 1991.
- [49] D. W. Sivers, “Single Spin Production Asymmetries from the Hard Scattering of Point-Like Constituents,” *Phys. Rev.*, vol. D41, p. 83, 1990.
- [50] D. Boer, C. Lorcé, C. Pisano, and J. Zhou, “The gluon Sivers distribution: status and future prospects,” *Adv. High Energy Phys.*, vol. 2015, p. 371396, 2015.
- [51] D. Müller, D. Robaschik, B. Geyer, F. M. Dittes, and J. Hořejši, “Wave functions, evolution equations and evolution kernels from light ray operators of QCD,” *Fortsch. Phys.*, vol. 42, pp. 101–141, 1994.
- [52] A. V. Radyushkin, “Scaling limit of deeply virtual Compton scattering,” *Phys. Lett.*, vol. B380, pp. 417–425, 1996.
- [53] X.-D. Ji, “Deeply virtual Compton scattering,” *Phys. Rev.*, vol. D55, pp. 7114–7125, 1997.
- [54] X.-D. Ji, “Gauge invariant decomposition of nucleon spin,” *Phys. Rev. Lett.*, vol. 78, pp. 610–613, 1997.
- [55] E.-C. Aschenauer, S. Fazio, K. Kumericki, and D. Mueller, “Deeply Virtual Compton Scattering at a Proposed High-Luminosity Electron-Ion Collider,” *JHEP*, vol. 09, p. 093, 2013.
- [56] K. J. Eskola, P. Paakkinen, H. Paukkunen, and C. A. Salgado, “EPPS16: Nuclear parton distributions with LHC data,” *Eur. Phys. J.*, vol. C77, no. 3, p. 163, 2017.
- [57] A. H. Mueller and J.-W. Qiu, “Gluon Recombination and Shadowing at Small Values of x ,” *Nucl. Phys.*, vol. B268, p. 427, 1986.

- [58] E. C. Aschenauer, S. Fazio, M. A. C. Lamont, H. Paukkunen, and P. Zurita, “Nuclear Structure Functions at a Future Electron-Ion Collider,” *Phys. Rev.*, vol. D96, no. 11, p. 114005, 2017.
- [59] F. Gelis, E. Iancu, J. Jalilian-Marian, and R. Venugopalan, “The Color Glass Condensate,” *Ann. Rev. Nucl. Part. Sci.*, vol. 60, pp. 463–489, 2010.
- [60] L. Zheng, E. C. Aschenauer, J. H. Lee, and B.-W. Xiao, “Probing Gluon Saturation through Dihadron Correlations at an Electron-Ion Collider,” *Phys. Rev.*, vol. D89, no. 7, p. 074037, 2014.
- [61] X. Chu, E.-C. Aschenauer, J.-H. Lee, and L. Zheng, “Photon structure studied at an Electron Ion Collider,” *arXiv preprint arXiv:1705.08831*, 2017.
- [62] EicRoot simulation framework, <http://svn.racf.bnl.gov/svn/eic/eicroot>.
- [63] S. Chekanov *et al.*, “Leading proton production in deep inelastic scattering at HERA,” *JHEP*, vol. 06, p. 074, 2009.
- [64] S. Roesler, R. Engel, and J. Ranft, “The Monte Carlo event generator DPMJET-III,” in *Advanced Monte Carlo for radiation physics, particle transport simulation and applications. Proceedings, Conference, MC2000, Lisbon, Portugal, October 23-26, 2000*, pp. 1033–1038, 2000.
- [65] L. Zheng, E. C. Aschenauer, and J. H. Lee, “Determination of electron-nucleus collision geometry with forward neutrons,” *Eur. Phys. J.*, vol. A50, no. 12, p. 189, 2014.
- [66] G. R. Young *et al.*, “The 0-degree calorimeter for the relativistic heavy ion experiment WA80 at CERN,” *Nucl. Instrum. Meth.*, vol. A279, pp. 503–517, 1989.
- [67] Zero-degree High-Precision Hadronic Calorimetry, https://wiki.bnl.gov/conferences/images/9/97/ZDC-2014-EIC-RD_2.pdf.
- [68] F. D. Aaron *et al.*, “Determination of the Integrated Luminosity at HERA using Elastic QED Compton Events,” *Eur. Phys. J.*, vol. C72, p. 2163, 2012. [Erratum: *Eur. Phys. J.*C74,2733(2012)].
- [69] H1 Luminosity Monitor, <http://www-h1.desy.de/h1/www/h1det/lumi/>.
- [70] Zeus Luminosity Monitor, http://www-zeus.desy.de/zeus_det_papers/zeus_det_papers.html.
- [71] G. Schuler and H. Spiesberger, “DJANGO: the interface for the event generators HERACLES and LEPTO,” In *Ingelman, G. (Ed.). Physics at HERA Proceedings*, vol. 3, p. 422, 1982. <https://wiki.bnl.gov/eic/index.php/DJANGO>.
- [72] <http://www.desy.de/~pol2000/Welcome.html>.
- [73] <https://wiki.bnl.gov/rhicspin/Polarimetry>.

- [74] Workshop on Opportunities for Polarized He-3 in RHIC and EIC, <https://indico.bnl.gov/conferenceDisplay.py?ovw=True&confId=405>.
- [75] “CESR operating parameters.” <https://www.classe.cornell.edu/Research/CESR/OperatingParameters.html>.
- [76] E. D. Bloom *et al.*, “The PEP-II asymmetric B factory: Design details and R & D results,” in *4th European Particle Accelerator Conference (EPAC 94) London, England, June 27-July 1, 1994*, vol. C940627, pp. 464–466, 1994.
- [77] J. Seeman *et al.*, “Performance of the PEP-II B-Factory collider at SLAC,” in *Proceedings, Particle Accelerator Conference, PAC’05, Knoxville, USA, May 16-20, 2005*, vol. C0505161, p. 2369, 2005.
- [78] K. Oide, “KEKB B-factory, the luminosity frontier,” *Prog. Theor. Phys.*, vol. 122, pp. 69–80, 2009.
- [79] “SynRad+ is part of the MolFlow+ code from CERN, which traces photons to calculate flux and power distribution on a surface caused by synchrotron radiation.”
- [80] T. Abe *et al.*, “Beam operation with crab cavities at KEKB,” in *Proceedings, 22nd Particle Accelerator Conference, PAC’07, Albuquerque, USA, June 25-29, 2007*, vol. C070625, p. 1487, 2007.
- [81] K. Akai *et al.*, “Commissioning and Beam Operation of KEKB Crab RF System,” in *RF superconductivity. Proceedings, 13th International Workshop, SRF 2007, Beijing, China, October 14-19, 2007*, 2007.
- [82] P. Baudrenghien, A. Macpherson, R. Calaga, V. Parma, E. Jensen, E. Montesinos, O. Capatina, and K. Brodzinski, “Functional Specifications of the LHC Prototype Crab Cavity System,” Tech. Rep. CERN-ACC-NOTE-2013-003, 2013.
- [83] G. Bassi, A. Blednykh, and V. Smaluk, “Self-consistent simulations and analysis of the coupled-bunch instability for arbitrary multibunch configurations,” *Phys. Rev. Accel. Beams*, vol. 19, no. 2, p. 024401, 2016.
- [84] W. Bruns, <http://www.gdfidl.de>.
- [85] K. L. F. Bane and M. Sands, “The Short-Range Resistive Wall Wakefields,” *AIP Conf. Proc.*, vol. 367, pp. 131–149, 1996.
- [86] A. Blednykh, G. Bassi, Y. Hidaka, V. Smaluk, and G. Stupakov, “Low-frequency quadrupole impedance of undulators and wigglers,” *Phys. Rev. Accel. Beams*, vol. 19, no. 10, p. 104401, 2016.
- [87] A. Chao, S. Heifets, and B. Zotter, “Tune shifts of bunch trains due to resistive vacuum chambers without circular symmetry,” *Phys. Rev. ST Accel. Beams*, vol. 5, p. 111001, 2002.

- [88] J. Laslett, "On Intensity Limitations Imposed by Transverse Space-Charge Effects in Circular Particle Accelerators," in *Proceedings of the Summer Study on Storage Rings, Brookhaven*, pp. 324–367, 1963.
- [89] Piwinski, A, "Beam losses and lifetime," in *CERN Accelerator School*, CERN, 1985.
- [90] C. Montag *et al.*, "Overview of the eRHIC Ring-Ring Design," in *Proceedings, 8th International Particle Accelerator Conference (IPAC 2017): Copenhagen, Denmark, May 14-19, 2017*, p. WEPIK049, 2017.
- [91] S. Khan, unpublished.
- [92] S. Agostinelli *et al.*, "GEANT4: A Simulation toolkit," *Nucl. Instrum. Meth.*, vol. A506, pp. 250–303, 2003.